Probing the Early Universe through Large-Scale Magnetic Fields and Secondary Gravitational Waves

A thesis submitted in fulfillment of the requirements
for the degree of

Doctor of Philosophy

in

Physics

by

Subhasis Maiti

Supervisor:
Prof. Debaprasad Maity

Department of Physics
Indian Institute of Technology Guwahati

2026

Statement

.

The work contained in the thesis entitled "**Probing the Early Universe through Large-Scale Magnetic Fields and Secondary Gravitational Waves**" has been carried out at the Department of Physics, Indian Institute of Technology Guwahati, India, by me, under the supervision of Prof. Debaprasad Maity. The content of this thesis is original and has not been submitted elsewhere for any other degree or diploma. Works presented in the thesis are all my own unless referenced to the contrary in the text.

Subhasis Maiti
Roll Number: 206121111
PhD student
Department of Physics
Indian Institute of Technology Guwahati
Guwahati, Assam, India-781039
Date: 26/03/2026

Disclaimer

.

The bibliography included in this thesis is, by no means, complete; rather, it contains the ones I went through thoroughly. I apologize for inadvertently missing out on some of the research papers, review articles, and other scientific documents relevant to this thesis, which also should have been cited. For the sake of illustration, some of the figures in this thesis are excerpted from other sources, which are properly cited.

Certificate

.

It is certified that the work contained in the thesis entitled "**Probing the Early Universe through Large-Scale Magnetic Fields and Secondary Gravitational Waves**" by Subhasis Maiti (Roll number-206121111), a PhD student of the Department of Physics, IIT Guwahati, was carried out under my supervision. The content of this thesis is original and has not been submitted elsewhere for any other degree or diploma.

....
(Signature of the supervisor)

Prof. Debaprasad Maity
Professor,
Indian Institute of Technology Guwahati,
Guwahati-781039, Assam, India
Date: 01/01/2026

Acknowledgements

.

I would like to express my sincere gratitude to my PhD advisor, Prof. Debaprasad Maity, for his continuous guidance, insightful discussions, and unwavering support throughout the course of this research programme. His encouragement, critical perspective, and intuitive insights have been invaluable in shaping both the direction and depth of this work.

I am grateful to the members of my doctoral advisory committee, Prof. Santabrata Das, Dr. Sovan Chakraborty, and Dr. Sayan Chakrabarti, for their encouragement and insightful comments, which greatly helped me improve both my presentation skills and my understanding of my research. I also extend my thanks to all the faculty members and non-teaching staff of the Department of Physics, Indian Institute of Technology Guwahati, for their constructive feedback and academic support at various stages of my doctoral journey. I sincerely acknowledge the stimulating research environment provided by the department, which greatly contributed to the development of this thesis.

I would like to sincerely thank my collaborators, Prof. L. Sriramkumar, Dr. Ayan Chakraborty, Dr. Sovan Sau, Dr. Alberto Roper Pol, and Dr. Sohel Dey, for many fruitful discussions, technical support, and for creating a collegial atmosphere that made this research experience both productive and enjoyable. I would like to express my special gratitude to Prof. L. Sriramkumar. Beyond being a collaborator, he has continuously guided me on how to think about problems and how to write scientific papers from the very beginning, which has been immensely valuable for my growth as a researcher.

I would also like to express my gratitude to my senior and current PhD group members, Dr. Mousumi Maitra, Dr. Rajesh Karmakar, Dr. Md Riajul Haque, Dr. Banarshree Baishya, Dr. Sourav Pal, Gargi Sen, Dr. Sovan Sau, Dr. Rajesh Mondal, Dr. Ayan Chakraborty, Jitumani Kalita, and Sitesh Kumar Panda, for the many enriching discussions we shared. I extend my special thanks to Ayan and Dr. Sovan for their constant support, stimulating physics discussions, and the warm companionship we shared throughout this long journey. I consider myself fortunate to have a companion like Ayan, who has always treated me like a brother and stood beside me during both joyful and difficult times in this academic journey. I thank him from the bottom of my heart.

My heartfelt thanks also go to my dear friends, juniors, and seniors, including Niloy, Abhik, Sourav, Indrajit, Nayan, Sanjib, Amit, Dipendu Bhandari, Dipankar, Shubhankar, Pratim, Sanket da, Surajit da, Sovan da, Shantanu da, Disha, Sounak, Debalina, Sonakshi, and Suchanda. I will always cherish the wonderful memories created during this long association with all of them. I would like to express my very special gratitude to Debalina for her constant support and encouragement. She has always stood by me, motivating me and lifting my spirits whenever I felt discouraged. Her belief in me has meant more than words can express, and I am deeply thankful for her presence throughout this journey.

I express my deepest gratitude to my parents and my elder sisters for their constant encouragement, patience, and understanding throughout this journey. I am especially indebted to my mother and father, whose unwavering support, sacrifices, and belief in me made it possible for me to pursue and complete this degree. Without their steadfast guidance and encouragement, this achievement would not have been possible. Their unconditional love has been a constant source of strength and motivation, particularly during challenging times. Whenever I doubted my ability to overcome difficulties, their reassuring words reminded me to remain strong and hopeful, and to believe that there is always a silver lining behind every cloud. I will remain eternally grateful to them.

Finally, I humbly offer my gratitude to the Almighty for blessing me with the opportunity to undertake this journey and for bringing such wonderful people into my life.

Abstract

Over the past few decades, remarkable advances in precision observational cosmology have significantly deepened our understanding of the early Universe. Observations of the cosmic microwave background (CMB) have firmly established the inflationary paradigm, which successfully resolves the horizon and homogeneity problems and explains the origin of the nearly scale-invariant spectrum of primordial curvature perturbations. In contrast, the post-inflationary reheating phase remains poorly constrained, primarily because its dynamics occur at small, currently unobservable scales by the CMB. Nevertheless, reheating plays a pivotal role in cosmic history, as it bridges the vast gap in energy and time scales between the end of inflation and the onset of hot Big-Bang nucleosynthesis (BBN). Moreover, reheating sets the initial conditions for BBN and can generate a variety of cosmological relics, including gravitational waves (GWs), dark matter (DM), and large-scale magnetic fields. The imprints left by reheating on these relics, therefore, provide a promising avenue to probe this otherwise elusive epoch through cosmological observations.

At the same time, the origin of large-scale magnetic fields observed in the intergalactic medium and cosmic voids remains one of the longstanding open problems in modern cosmology. Astrophysical mechanisms alone fail to explain the presence of non-vanishing magnetic fields in such low-density environments, strongly motivating a primordial origin. In this thesis, we investigate the interplay between non-instantaneous reheating scenarios and primordial magnetogenesis, with the goal of understanding how reheating dynamics influence present-day cosmological relics and their observational signatures, particularly in gravitational waves.

Among the various magnetogenesis mechanisms, inflationary magnetogenesis has been extensively studied as a viable source of large-scale magnetic fields. However, such scenarios often suffer from severe strong-coupling and backreaction problems. In this thesis, we demonstrate that the post-inflationary evolution of electromagnetic fields—especially during the reheating era—plays a crucial role in alleviating these issues. By analyzing different limits of the electrical conductivity, we show that both the strong-coupling and backreaction problems can be significantly relaxed. In particular, in the zero-conductivity limit, an efficient conversion between electric and magnetic energy densities takes place, with the effect being most pronounced for modes that remain outside the horizon during reheating. Depending on the duration and dynamics of the reheating phase, this energy transfer can substantially enhance the magnetic field strength, leading to present-day values consistent with current observational bounds. Furthermore, we find that within certain regions of parameter space, the secondary gravitational waves sourced by electromagnetic fields can dominate over the primary inflationary contribution and can be probed by future GW detectors such as LISA, DECIGO, and BBO. Although the electromagnetic spectra are blue-tilted, the resulting present-day GW spectrum exhibits multiple spectral breaks, whose shape and location sensitively depend on the detailed dynamics of reheating.

We then extend our analysis to post-inflationary magnetogenesis scenarios in which the

gauge-field coupling remains active after the end of inflation and continues to source magnetic fields during reheating. Even in the presence of a matter-like evolution during reheating, we find that a significant large-scale magnetic field can be generated. Notably, although these scenarios typically produce strongly blue-tilted magnetic spectra, the late-time production of magnetic fields allows the present-day magnetic field strength observed in cosmic voids to be explained without encountering strong-coupling or backreaction issues. We further show that these models naturally generate a sizable secondary GW background in the intermediate frequency range, characterized by a broken power-law spectrum. The slope and amplitude of the GW signal are governed by the magnetic spectral index as well as the reheating parameters, including the equation of state $w_{\rm re}$ and reheating temperature $T_{\rm re}$, making them potentially testable with future GW observations.

We also explore an alternative magnetogenesis mechanism involving axion-like particles (ALPs) during the post-recombination epoch, when the Universe is dominated by neutral hydrogen and the electrical conductivity drops significantly. In this regime, ultra-light ALPs can efficiently transfer their energy to gauge fields, particularly for modes that reenter the horizon during the early oscillatory phase of the axion field. We find that this mechanism can generate large-scale magnetic fields on length scales exceeding $1,\mathrm{Mpc}$, along with distinctive secondary GW signatures. Since the generated magnetic fields are inherently helical, the resulting GWs are also chiral in nature. Consequently, future observations of B-mode polarization, for instance by CMB-S4 experiments, could place meaningful constraints on the axion mass and axion–gauge-field coupling.

Finally, we propose a novel pathway for the formation of primordial black holes (PBHs) within post-inflationary magnetogenesis scenarios. PBHs are well-motivated dark matter candidates, especially given that the fundamental nature of dark matter remains unknown despite extensive experimental and theoretical efforts. We demonstrate that magnetic-field-induced density perturbations generated during reheating can collapse to form PBHs in a mass range consistent with cold dark matter. The resulting PBH mass spectrum is primarily governed by the reheating dynamics, and by appropriately tuning the reheating parameters $(w_{\rm re}, T_{\rm re})$, we identify regions of parameter space in which PBHs can account for the entire observed dark matter abundance. Since strong magnetic fields also efficiently source secondary gravitational waves, these scenarios predict correlated GW signals that may be observable in future experiments. In this way, our work provides a unified framework that connects two longstanding open problems in cosmology: the origin of large-scale magnetic fields and the nature of dark matter.

Overall, this thesis establishes a comprehensive connection between reheating dynamics, primordial and post-inflationary magnetogenesis, and their observational imprints on gravitational waves, offering new avenues to probe the physics of the early Universe.

List of Publications

Thesis Works :

1. **S.Maiti**, D. Maity, R. Srikanth, *"Minimal Magnetogenesis: The Role of Inflationary Perturbations and ALPs, and Its Gravitational Wave Signatures"*.
   Journal: Physical Review D 112, 043535 (2025);
   arXiv:arXiv.2504.15400 [astro-ph.CO]

2. **S.Maiti**, D. Maity, R. Srikanth,
   Probing Reheating Phase via Non-Helical Magnetogenesis and Secondary Gravitational Waves,
   Journal: Phys.Rev.D 112 (2025) 6, 063552
   arXiv:arXiv.2505.13623 [astro-ph.CO]

3. **S.Maiti**
   Magnetogenesis from Sawtooth Coupling: Gravitational Wave Probe of Reheating,
   Journal: Physical Review D 112, 043536 (2025).
   arXiv:arXiv.2506.06183 [astro-ph.CO]

4. **S.Maiti**, D. Maity
   The Magnetic Origin of Primordial Black Holes: A Viable Dark Matter Scenario,
   Journal: Accepted in JCAP;
   arXiv:arXiv. 2508.19217 [astro-ph.CO]

Other Works :

1. **S. Maiti** and D. Maity, L. Sriramkumar
   Constraining inflationary magnetogenesis and reheating via GWs in light of PTA data,
   arXiv:arXiv.2401.01864 [gr-qc]

2. Ayan Chakraborty, **S. Maiti**, Debaprasad Maity, *"Probing non-minimal coupling through super-horizon instability and secondary gravitational waves"*.
   Journal: Phys. Rev. D 111, 083505 (2025)
   arXiv:arXiv: 2408.07767 [astro-ph.CO]

Notations and Conventions

.

- Throughout this thesis, we use natural units $\hbar$=c=k_B=1. In this unit, Reduced Planck mass is given by $M_\mathrm{P} = \frac{1}{\sqrt{8\pi G}} = 2.435 \times 10^{18}$ GeV.

- Greek indices μ,ν and so on go over the four space-time co-ordinates $x^\mu = [x^0, x^1, x^2, x^3]^T$ with x^0 for the time coordinate.

- Minkowski metric is given by $\eta_{\mu\nu} = diag[-1, 1, 1, 1]$.

- Latin labels i, j, k and so on go over the three spatial co-ordinates.

- The Ricci tensor, defined in terms of the Christoffel symbols, is

$$R_{\mu\nu} = \partial_\lambda \Gamma^\lambda_{\mu\nu} - \partial_\nu \Gamma^\lambda_{\mu\lambda} + \Gamma^\lambda_{\lambda\rho}\Gamma^\rho_{\mu\nu} - \Gamma^\rho_{\mu\lambda}\Gamma^\lambda_{\nu\rho}, \tag{1}$$

and the Ricci scalar is $R = g^{\mu\nu} R_{\mu\nu}$

Cosmological Parameters	
Symbol	**Definition**
a	Scale factor of the Universe (dimensionless)
H	Hubble parameter (s^{-1})
η	Conformal time (s)
w	Equation of state parameter, $p = w\rho$ (dimensionless)
N_e	Number of e-folds (dimensionless)
Ω_{rad}	Radiation density parameter (dimensionless)
Ω_m	Total matter density (dimensionless)
$\Omega_b h^2$	Baryon density
$\Omega_c h^2$	Cold dark matter (CDM)
t_0	Age of the Universe
T_{CMB}	CMB temperature
z_{rec}	Recombination redshift
n_s	Scalar spectral index
σ_8	Density fluctuation amplitude
D/H	Primordial deuterium abundance
Y_P	Helium-4 mass fraction
N_{eff}	Effective number of relativistic species
Ω_Λ	Dark energy density parameter (dimensionless)
H_0	Present-day Hubble constant
Fields and Particles	
Symbol	**Definition**
φ	Inflaton field
$V(\varphi)$	Inflaton potential (GeV^4)
χ	Secondary scalar field (GeV)
$A_{\mathbf{k}}$	Gauge field mode function
$F_{\mu\nu}$	Electromagnetic field strength tensor (GeV^2)
$\tilde{F}_{\mu\nu}$	Dual of gauge field tensor (GeV^2)
Inflationary Parameters	
Symbol	**Definition**
ϵ_φ	First slow-roll parameter (dimensionless)
η_φ	Second slow-roll parameter (dimensionless)
H_{e}	Hubble parameter during inflation
N_{end}	e-folding number of the inflationary period
$f_{\mathrm{end}} = k_{\mathrm{e}}/2\pi$	Highest comoving frequency associated with the horizon size at the end of inflation

Table 1: List of cosmological, field, and inflationary parameters.

Reheating Parameters	
Symbol	**Definition**
$w_{\rm re}(=P/\rho)$	Average equation of state during reheating
$T_{\rm re}$	Reheating temperature
$k_{\rm re}$	Comoving wavenumber that re-enters the horizon at the end of reheating
$f_{\rm re}(k_{\rm re}/2\pi)$	Comoving frequency corresponding to $k_{\rm re}$
Magnetogenesis Parameters	
Symbol	**Definition**
$B_0(k) = \sqrt{\mathcal{P}_{\rm B}(k,\eta_0)}$	Present-day magnetic field strength
$\mathcal{P}_{\rm B}(k,\eta) = \partial\rho_{\rm B}(k,\eta)/\partial\ln(k)$	Energy spectrum of magnetic field
$\mathcal{P}_{\rm E}(k,\eta) = \partial\rho_{\rm E}(k,\eta)/\partial\ln(k)$	Energy spectrum of electric field
$n_{\rm B}$	Magnetic spectral index
$n_{\rm E}$	Electric spectral index
Gravitational Wave Parameters	
Symbol	**Definition**
$h_{\mathbf{k}}$	Amplitude of tensor perturbation
$\rho_{\rm gw}$	Gravitational wave energy density
$\Omega_{\rm GW}h^2$	GW spectral energy density (dimensionless)
$n_{\rm gw}$	GW spectral index
$P_{\rm T}$	Tensor power spectrum
Primordial Black Hole Parameters	
Symbol	**Definition**
$M_{\rm pbh}$	Mass of the PBH
$\rho_{\rm pbh}$	Total energy density of PBHs
$T_{\rm BH}$	Black hole temperature
$\beta_{\rm pbh}(\rho_{\rm pbh}/\rho_c)$	Initial fractional energy density of PBHs
$f_{\rm PBH}$	Present-day PBH fraction as dark matter candidate

Table 2: List of reheating, magnetogenesis, gravitational wave, and PBH parameters.

Contents

List of Tables

Chapter 1

Introduction

The history of modern physics is shaped not only by its remarkable theoretical and experimental successes, but also by the recognition of the intrinsic limitations of its prevailing frameworks. Each major theoretical structure has achieved extraordinary explanatory power within a specific domain of validity, while simultaneously exposing conceptual or empirical inconsistencies that ultimately necessitated more fundamental descriptions. This dynamic interplay between success and failure has been central to the evolution of physical theory, guiding the transition from classical mechanics to quantum field theory and modern particle physics.

The foundations of modern science were laid during the scientific revolution of the sixteenth and seventeenth centuries. A decisive departure from the Aristotelian–Ptolemaic worldview was initiated by Nicolaus Copernicus (1473–1543), who, in *De revolutionibus orbium coelestium* (1543), proposed the heliocentric model of the solar system. This radical idea challenged the long-standing geocentric paradigm and redefined humanity's understanding of cosmic order. Subsequent advances were enabled by Tycho Brahe (1546–1601), whose unprecedentedly precise astronomical observations provided the empirical foundation for Johannes Kepler (1571–1630). Between 1609 and 1619, Kepler formulated his three laws of planetary motion, establishing that planetary orbits are elliptical and governed by precise mathematical relations.

The emergence of modern observational science was further advanced by Galileo Galilei (1564–1642), who, beginning in 1609, systematically applied the telescope to astronomical observations. His discoveries—including the moons of Jupiter, the phases of Venus, sunspots, and the rugged surface of the Moon—provided decisive empirical support for heliocentrism and marked the birth of modern observational astrophysics. Equally important was Galileo's emphasis on experiment and mathematical description, which became central methodological pillars of modern physics.

These developments culminated in the synthesis achieved by Isaac Newton (1643–1727). In his *Philosophi Naturalis Principia Mathematica* (1687), Newton formulated the laws of motion and the law of universal gravitation, unifying terrestrial and celestial dynamics within a single deterministic framework. Classical mechanics successfully described a vast range of phenomena, from planetary motion to everyday mechanics, and remained the dominant paradigm for more than two centuries. However, by the late nineteenth century, its failures at relativistic velocities, in strong gravitational fields, and at microscopic scales revealed the limits of its applicability. These shortcomings were not merely technical; they signaled the need for fundamentally new concepts of space, time, and matter.

Parallel to these developments, the early twentieth century witnessed a profound transformation in our understanding of space and time. In 1905, Albert Einstein introduced the theory of special relativity, which resolved inconsistencies between classical mechanics and the behavior of light, fundamentally redefining the concepts of space and time. This was followed in 1915 by the theory of general relativity, which provided a geometric description of gravitation as the curvature of spacetime. General relativity has been confirmed by numerous experimental tests, ranging from the perihelion precession of Mercury to the direct detection of gravitational waves in 2015 [1–6]. Nonetheless, its breakdown at spacetime singularities and its non-renormalizable character when treated as a quantum theory reveal its limitations as a fundamental description of nature.

In parallel, cosmology underwent a profound transformation into a precision science. The discovery of the expansion of the Universe by Edwin Hubble provided the first observational evidence for a dynamical cosmos, while subsequent theoretical developments based on Einstein's general relativity led to the formulation of the Big Bang model. Key observational pillars—including the successful predictions of primordial nucleosynthesis and the discovery of the cosmic microwave background (CMB)—firmly established the hot Big Bang scenario and its deep connection to high-energy particle physics in the early Universe.

The decisive breakthrough came with increasingly precise observations of the CMB. The COBE satellite first detected the near-perfect blackbody spectrum and primordial anisotropies, providing direct evidence for early-Universe fluctuations [7,8]. These results were dramatically refined by WMAP [9,10], which measured the temperature anisotropies with high precision and confirmed the consistency of the standard cosmological model. Most recently, the Planck mission delivered high-resolution measurements of both temperature and polarization anisotropies, revealing remarkable agreement with inflationary predictions and constraining cosmological parameters at the percent level [11,12].

Motivated by both conceptual shortcomings of the standard Big Bang model and its striking observational successes, Alan Guth [13] and others [14–17] proposed the paradigm of cosmic inflation to address fundamental issues such as the horizon and flatness problems. Inflation provides a natural mechanism for generating primordial density perturbations from quantum fluctuations, which subsequently seed the observed large-scale structure of the Universe [18,19]. The remarkable agreement between inflationary predictions and precision measurements of the cosmic microwave background (CMB) has elevated early-Universe cosmology to a central position in modern high-energy physics.

Despite this progress, several fundamental questions remain unresolved:

- **Nature of dark matter:** A wide range of astrophysical and cosmological observations—including galactic rotation curves [20–22], gravitational lensing [23,24], microlensing surveys [25,26], and precision CMB measurements [11]—provide compelling evidence for the existence of non-luminous, non-baryonic matter beyond the Standard Model of particle physics. However, despite extensive experimental and theoretical efforts, the fundamental nature and microphysical properties of dark matter remain unknown [11,27,28].

- **Dark energy and the cosmological constant problem:** Over the past few decades, multiple independent observations, such as high-redshift Type-Ia supernovae [29, 30], CMB-anisotropies [11], baryon acoustic oscillations (BAO) [31], large-scale structure surveys [24, 32], and weak gravitational lensing, have established that the Universe is currently undergoing accelerated expansion. Within the framework of general relativity and a homogeneous and isotropic Friedmann–Lemaître–Robertson–Walker (FLRW) spacetime, accelerated expansion requires a dominant energy component with negative pressure, characterized by an equation of state $w = p/\rho < -1/3$ [33, 34]. The simplest realization of this component is the cosmological constant Λ_g, corresponding to $w = -1$, which accounts for approximately 70% of the present energy density of the Universe [11, 34]. Nevertheless, understanding the physical origin of dark energy and resolving the cosmological constant problem [35, 36]—namely, the enormous discrepancy between the observed value of vacuum energy and theoretical expectations from quantum field theory—remain profound open challenge at the interface of cosmology, particle physics, and gravity.

- **Origin and microphysics of inflation:** Inflation [13–15] provides a compelling resolution to the horizon and flatness problems and successfully explains the origin of the nearly scale-invariant primordial fluctuations observed today [18, 19]. In particular, it predicts the amplitude of scalar perturbations on large scales, $A_s \simeq 2.1 \times 10^{-9}$, with a slightly red-tilted spectral index, in excellent agreement with observations [12]. While inflation is well described as an effective theory, the fundamental degrees of freedom responsible for driving inflation, its embedding in a more complete microscopic theory, and its precise energy scale remain unknown [37, 38]. Moreover, the lack of observational access to small scales limits our ability to discriminate among competing inflationary scenarios [38, 39].

- **Primordial relics:** Despite significant observational advances, the origin of several primordial relics observed in the present-day Universe remain unclear, signaling gaps in our understanding of early-Universe physics. These include the origin of the dark matter abundance [27, 40], a stochastic gravitational-wave background potentially probed by pulsar timing arrays [41–45], large-scale cosmic magnetic fields, often hypothesized to have a primordial origin [46, 47], and the observed matter–antimatter asymmetry [48, 49].

The Standard Model of particle physics and quantum field theory (QFT) have achieved remarkable success in describing fundamental interactions. However, several present-day relics observed in the Universe—such as the dark matter abundance, primordial magnetic fields, and the baryon asymmetry—cannot be explained within this framework alone. If these relics were produced during the very early stages of cosmic evolution, for instance during inflation or the pre-reheating epoch, then the post-inflationary dynamics, particularly the reheating era, play a crucial role in determining their present-day properties.

Despite its importance, the reheating phase remains poorly constrained observationally, primarily due to the lack of direct probes of small-scale dynamics [50–56]. Late-time processes such as structure formation and nonlinear gravitational evolution tend to erase or obscure most of the imprints of reheating, making it challenging to reconstruct this epoch using conventional cosmological observables. Nevertheless, a precise understanding of the reheating era is essential for establishing a complete and consistent picture of the thermal history of the Universe [50, 57–63].

In this context, direct or indirect observational signatures of reheating are of paramount importance. Motivated by this, the central goal of this thesis is to constrain the dynamics of the reheating phase using gravitational-wave observations, in the presence of primordial sources such as magnetic fields or scalar fields that originate at very early times. Gravitational waves, due to their weak interactions and ability to propagate largely unimpeded through cosmic history, provide a unique window into otherwise inaccessible epochs of the early Universe.

Throughout this thesis, we investigate how gravitational-wave experiments can be used to probe both the nature of primordial magnetic fields and the imprints of the reheating era. In particular, we explore theoretical frameworks and observational signatures that allow us to connect early-Universe magnetogenesis and scalar-field dynamics with present and future gravitational-wave observations, thereby shedding light on the physics of reheating and the origin of primordial relics.

This thesis is organized into seven chapters. It begins with an introductory chapter that outlines the motivation for this work and provides a brief overview of the historical development of modern cosmology. This is followed by a discussion of standard and non-standard cosmological models, highlighting their key successes as well as their limitations. We then review the origin of primordial magnetic fields and the challenges associated with their generation. Subsequently, the main results of the thesis are presented in a chapter-wise manner, detailing each of the studies carried out in this work. Finally, the concluding chapter summarizes the principal outcomes of the thesis and discusses possible directions for future research.

Chapter 2

Standard and Non-Standard Cosmology

2.1 Introduction

The standard Big Bang cosmology, together with its modern extension in the form of the ΛCDM model, provides a highly successful framework for describing the origin and evolution of the Universe. Based on general relativity and the assumption of large-scale homogeneity and isotropy, it is formulated within the Friedmann–Lemaître–Robertson–Walker (FLRW) spacetime and is capable of explaining a wide range of cosmological observations.

The concept of an expanding Universe, first proposed by Lemaître, was observationally confirmed by Hubble in 1929 through the discovery that galaxies recede with velocities proportional to their distances. This established the empirical foundation of the Big Bang framework. In the late 1940s, the theory of Big Bang nucleosynthesis (BBN) successfully predicted the primordial abundances of light elements, which are in good agreement with observations when the baryon density is fixed.

A major milestone in cosmology was the discovery of the cosmic microwave background (CMB) radiation in 1965, interpreted as relic radiation from the early hot Universe. Its blackbody spectrum and temperature anisotropies have been measured with high precision by missions such as COBE [7,8], WMAP [9,10], and Planck [11,12,64,65]. These anisotropies reveal acoustic peaks that provide a standard ruler for cosmology and are independently confirmed through baryon acoustic oscillations (BAO) in large-scale structure surveys [66,67].

The ΛCDM model also gives a consistent description of the thermal history of the Universe, from the radiation-dominated era to matter domination and the present phase of accelerated expansion, discovered through Type Ia supernova observations. This late-time acceleration is naturally explained by the cosmological constant Λ_g. Furthermore, the model successfully accounts for the formation and evolution of cosmic structures from nearly scale-invariant primordial perturbations with scalar spectral index $n_s \simeq 0.965$, consistent with both CMB measurements and large-scale structure observations [12,64,65,68].

One of the most remarkable features of the ΛCDM model is its predictive power: a small set of cosmological parameters suffices to explain diverse observations across widely separated epochs, establishing cosmology as a precision science with parameters such as the Hubble constant and matter density determined to percent-level accuracy. Table 2.1 summarizes some of the key predictions and their observational confirmations.

Table 2.1: Key observational successes of the standard ΛCDM cosmology. The parameter values are mainly inferred from the Planck 2018 results [11,69], with independent observational checks where available.

Quantity	**ΛCDM (Planck)**	**Observation / Check**
H_0	67.4 ± 0.5 km s^{-1} Mpc^{-1}	Local distance ladder ~ 73 km s^{-1} Mpc^{-1} [70]
Ω_m	0.315 ± 0.007	Galaxy surveys, BAO [71]
$\Omega_b h^2$	0.0224 ± 0.0001	Verified by BBN light-element abundances [72]
$\Omega_c h^2$	0.120 ± 0.001	Large-scale structure growth [71]
t_0	13.80 ± 0.02 Gyr	Oldest globular clusters ~ 13 Gyr [73]
$T_{\rm CMB}$	2.7255 K	COBE/FIRAS blackbody spectrum [74]
$z_{\rm rec}$	~ 1100	CMB acoustic peaks [11]
n_s	0.965 ± 0.004	Consistent with inflationary predictions [11]
σ_8	0.811 ± 0.006	Galaxy clustering, weak lensing [75]
(D/H)	2.5×10^{-5}	$(2.53 \pm 0.02) \times 10^{-5}$ from quasar absorbers [76]
Y_P	~ 0.2467	Metal-poor HII region measurements [77]
$N_{\rm eff}$	2.99 ± 0.17	Standard Model value 3.046 [11,78]
$\sum m_\nu$	< 0.12 eV (95% CL)	Consistent with oscillation limits [79]

Despite its success, the standard Big Bang model faces several conceptual challenges, including the flatness, horizon, and monopole problems. These issues indicate that, while the model accurately describes the evolution of the Universe after its earliest moments, it does not provide a natural explanation for the initial conditions.

To address these shortcomings, the idea of cosmic inflation—a brief period of accelerated expansion in the early Universe—was introduced. Inflation not only resolves these fundamental problems but also provides a mechanism for generating the primordial perturbations that seed large-scale structure.

Before discussing inflation in detail, it is essential to first understand the FLRW cosmology, which forms the foundation of the ΛCDM model.

2.2 FLRW Cosmology

The study of the universe at its largest scales begins with the assumption that the cosmos is homogeneous and isotropic on sufficiently large scales, an idea strongly supported by observations and forming the basis of modern cosmology [80–82]. These symmetries uniquely lead to the Friedmann–Lemaître–Robertson–Walker (FLRW) description of spacetime. Within this framework, the dynamics of the cosmic expansion are described by the scale factor and governed by the Friedmann equations derived from Einstein's field equations.

Observations of the cosmic microwave background further confirm the high degree of isotropy of the universe [11], while large-scale galaxy surveys demonstrate homogeneity on sufficiently large scales [83]. These symmetries strongly constrain the form of the spacetime metric, leading uniquely to the FLRW metric, given by [38, 84]

$$ds^2 = -\mathrm{dt}^2 + \mathrm{a}^2(\mathrm{t})\left[\frac{\mathrm{dr}^2}{1-\mathrm{kr}^2} + \mathrm{r}^2(\mathrm{d}\theta^2 + \sin^2(\theta)\mathrm{d}\phi^2)\right], \tag{2.1}$$

where $a(t)$ is the scale factor and $k = 0, +1, -1$, corresponds to a spatially flat, closed, or open universe, respectively. Here, we confine a fundamental quantity to the Hubble rate

$$H = \frac{\dot{a}}{a} \propto \frac{1}{t}. \tag{2.2}$$

Here $\dot{a} = \mathrm{da}/\mathrm{dt}$ is the derivative of the scale factor with respect to the cosmic time t. It is useful to rewrite the metric in the following form [38, 84]

$$ds^2 = -\mathrm{dt}^2 + \mathrm{a}^2(\mathrm{t})\left[\mathrm{dX}^2 + \mathrm{S_k}(\mathrm{X}^2)(\mathrm{d}\theta^2 + \sin^2(\theta)\mathrm{d}\phi^2)\right]. \tag{2.3}$$

where [38, 84]

$$r^2 = S_k(X^2) = \begin{cases} \sinh^2(X) & \text{if } k = -1 \\ X^2 & \text{if } k = 0 \\ \sin^2(X) & \text{if } k = +1 \end{cases} \tag{2.4}$$

Here, X plays the role of a radius. We now redefine the time coordinate as

$$\eta = \int^{\eta} \frac{dt}{a(t)}, \tag{2.5}$$

where η is known as the conformal time. In terms of this conformal time coordinate, the FLRW metric takes the form [38, 84]

$$ds^2 = a^2(\eta)\left[-\mathrm{d}\eta^2 + \mathrm{dX}^2 + \mathrm{S_k}(\mathrm{X}^2)(\mathrm{d}\theta^2 + \sin^2(\theta)\,\mathrm{d}\phi^2)\right]. \tag{2.6}$$

This coordinate system is particularly useful for studying the causal structure of an expanding spacetime. Light rays follow null paths, $ds^2 = 0$. Since the universe is isotropic, geodesic solutions correspond to constant θ and ϕ. For a radial light ray (with $\mathrm{d}\theta = \mathrm{d}\phi = 0$), the metric reduces to

$$ds^2 = 0 \quad \Rightarrow \quad a^2(\eta)\left[-\mathrm{d}\eta^2 + \mathrm{dX}^2\right] \quad \Rightarrow \quad \mathrm{dX} = \pm\mathrm{d}\eta. \tag{2.7}$$

Thus, in conformal coordinates, the null geodesic satisfies

$$X(\eta) = X_0 \pm (\eta - \eta_0). \tag{2.8}$$

This shows that in the η–X plane, light always propagates at 45°, just as it does in Minkowski space. In this coordinate system, the comoving distance between two comoving points is simply the coordinate difference ΔX, while the corresponding physical distance at time t is given by $d_p(t) = a(\eta)\,\Delta X$.

Particle Horizon:

The particle horizon represents the maximum comoving distance that light could have traveled since the beginning of the universe up to some later time η. If we assume that the universe starts at time η_i, then the comoving distance covered by light is

$$X_{ph} = \int_{\eta_i}^{\eta} d\eta' = \eta - \eta_i. \tag{2.9}$$

The corresponding proper distance is $d_{ph}(\eta) = a(\eta)(\eta - \eta_i)$, which describes the largest region that could have been in causal contact with an observer at time η. If η_i is finite, then the particle horizon is also finite. As a result, different regions of the CMB sky may appear to have never been in causal contact.

Friedmann Equations

To describe the dynamical evolution of an isotropic universe, we must relate the spacetime geometry to its matter-energy content. This relation is provided by Einstein's field equations in the background of the FLRW metric. In this framework, the matter content of the Universe is modeled as a homogeneous and isotropic perfect fluid. The corresponding energy-momentum tensor is given by [33, 81, 82]

$$T_{\mu\nu} = (\rho + P)u_\mu u_\nu + P g_{\mu\nu}, \tag{2.10}$$

where ρ denotes the energy density of the fluid and $P = w\rho$ represents its pressure, with w being the equation of state parameter.

For a comoving observer, the four-velocity is $u^\mu = (1, 0, 0, 0)$. This implies the non-vanishing components of the energy-momentum tensor to be $T^0_0 = \rho, \qquad T^j_i = P\delta^j_i$.

Einstein's field equations are given by ,

$$G_{\mu\nu} + \Lambda_g g_{\mu\nu} = 8\pi \mathrm{G_N} T_{\mu\nu}. \tag{2.11}$$

Here $G_{\mu\nu}$ denotes the Einstein tensor describing the curvature of spacetime, while $T_{\mu\nu}$ represents the energy–momentum tensor of matter and radiation. The constant $\mathrm{G_N}$ is Newton's gravitational constant. The parameter Λ_g is the cosmological constant, which can be interpreted as a uniform energy density associated with the vacuum and contributes to the large-scale dynamics of the Universe [34, 35].

For the FLRW metric, the nonzero components of the Einstein tensor are [81, 82]

$$G^0_0 = -\frac{3}{a^2}(\dot{a}^2 + k); \;\; G^j_i = -\frac{1}{a^2}(2a\ddot{a} + \dot{a}^2 + k)\delta^j_i \tag{2.12}$$

where the dot denotes derivative with respect to cosmic time t.

- The 00 component of Einstein's equations is

$$G^0_0 + \Lambda_g g^0_0 = 8\pi \mathrm{G_N} T^0_0 \Rightarrow \boxed{H^2 = \left(\frac{\dot{a}}{a}\right)^2 = \frac{8\pi \mathrm{G_N}}{3}\rho - \frac{k}{a^2} + \frac{\Lambda_g}{3}} \tag{2.13}$$

  where we have used $g^0_0 = -1$.

- Using the spatial components, we obtain

$$G^i_j + \Lambda_g g^j_i = 8\pi \mathrm{G_N} T^j_i \implies \boxed{\frac{\ddot{a}}{a} = -\frac{4\pi \mathrm{G_N}}{3}(\rho + 3P) + \frac{\Lambda_g}{3}} \tag{2.14}$$

Continuity Equation and its solution:

Combining Eq. (2.13) with Eq. (2.14), we can easily obtain the continuity equation (see Appendix A.1)

$$\dot{\rho} + 3H(\rho + P) = 0. \tag{2.15}$$

To solve this equation, we assume a constant equation of state $w = P/\rho$, which allows us to rewrite it as

$$\frac{\partial \rho}{\partial t} + 3(1+w)H\rho = 0. \tag{2.16}$$

The general solution of this equation is

$$\rho(a) = \rho_* \left(\frac{a}{a_*}\right)^{-3(1+w)}, \tag{2.17}$$

where ρ_* is the energy density at a reference scale factor a_*.

Thus, for a radiation-like fluid, the energy density scales as $\rho(a) \propto a^{-4}$, while for a matter-like fluid it scales as $\rho(a) \propto a^{-3}$. In the special case of $w = -1$, the energy density remains constant in time.

To study the behaviour of the scale factor, we first assume $k = 0$ and $\Lambda_g = 0$. From the first Friedmann equation, we obtain

$$\frac{\dot{a}}{a} = \pm C_N^{1/2} a^{-\frac{3(1+w)}{2}}, \tag{2.18}$$

where we define $C_N = \frac{\pi \mathrm{G_N}}{3}\rho_* a_*^{3(1+w)}$. Since our universe is expanding, we consider the positive branch. After integration, this gives

$$a(t) = a_* \left[\frac{3(1+w)}{2} H_*(t - t_*) + 1\right]^{\frac{2}{3(1+w)}}, \tag{2.19}$$

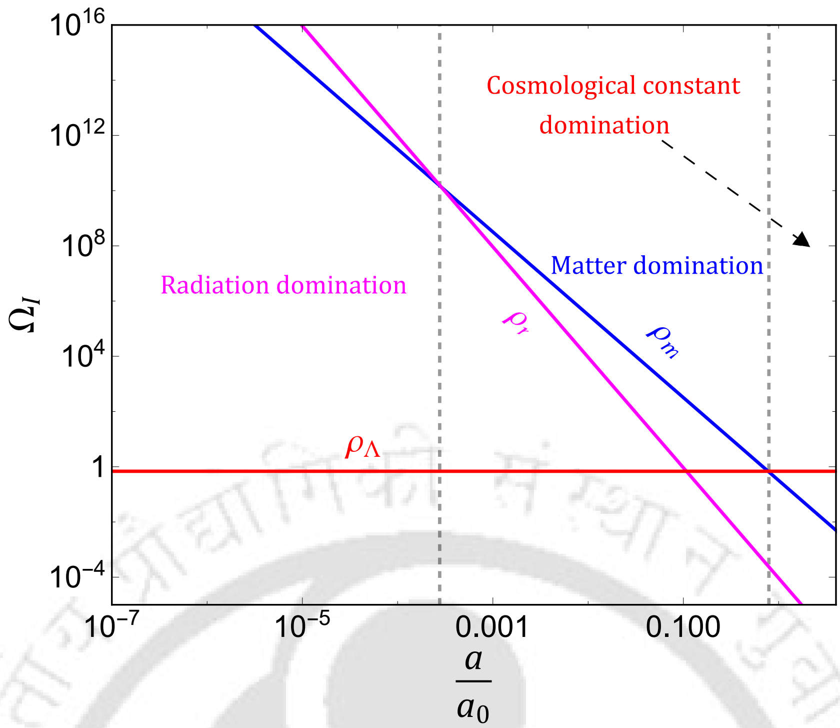

Figure 2.1: In the above figures, we have plotted the evolution of the different energy components like matter(blue), radiation(magenta), and dark energy(red) as a function of normalized scale factor (a/a_0).

where $H_* = \left(\frac{8\pi G_N \rho_*}{3}\right)^{1/2}$ and t_* is a reference time.

A special case arises for $w = -1$, for which the Friedmann equation admits an exponential expansion of the scale factor, $a(t) \propto e^{Ht}$. In this scenario, the energy density remains constant, $\rho = \text{const}$, and consequently the Hubble parameter H is also time-independent.

In Fig. 2.1, we illustrate the evolution of the fractional energy densities of the various components, defined as $\Omega_i \equiv \rho_i/\rho_{\text{crit}}$, as a function of the normalized scale factor a/a_0. a_0 is the scale factor today. Here, ρ_i denotes the energy density of the i-th component of the Universe, while $\rho_{\text{crit}} = 3H_0^2 M_{\text{P}}^2$ is the present-day critical energy density. This representation allows us to track the relative evolution of each component throughout cosmic history. As evident from the figure, the universe successively evolves from the radiation domination in very early times to matter domination, and finally to cosmological domination.

In the standard Big Bang picture, the universe is assumed to have always been dominated by normal matter with $w > 0$. The total energy density and pressure can then be expressed as

$$\rho = \sum_i \rho_i, \qquad P = \sum_i P_i, \tag{2.20}$$

with the equation of state for each component defined as $w_i = P_i/\rho_i$. The present-day fractional energy density of each component is $\Omega_{i,0} = \rho_{i,0}/\rho_{cr,0}$, where $\rho_{cr,0} = 3H_0^2 M_{\text{P}}^2$ is the *critical density* at present, and H_0 is the current Hubble parameter. Observational measurements give $H_0 \simeq 67.4\,\text{km}\,\text{s}^{-1}\,\text{Mpc}^{-1}$ [11].

The relative curvature contribution at present is given by

$$\Omega_{k,0} = -\frac{k}{a^2(t_0)H_0^2}, \tag{2.21}$$

with $a(t_0) = a_0 = 1$ denoting the present-day scale factor. Observations indicate that the Universe is very close to spatially flat, with $\Omega_{k,0} = 0.001 \pm 0.002$ from cosmological measurements [11].

Using these definitions, the Friedmann equation can be written in terms of the fractional densities as

$$\left(\frac{H^2}{H_0^2}\right) = \sum_i \Omega_{i,0} a^{-3(1+w_i)} + \Omega_{k,0} a^{-2}. \tag{2.22}$$

At the present time, this implies the relation

$$\sum_i \Omega_{i,0} + \Omega_{k,0} = 1. \tag{2.23}$$

Observationally, the present-day energy content of the Universe is dominated by dark energy and dark matter. In particular, measurements of the cosmic microwave background, together with other cosmological probes, indicate $\Omega_{\Lambda,0} \simeq 0.685$, $\Omega_{m,0} \simeq 0.315$, and $\Omega_{b,0} \simeq 0.049$, while the curvature contribution remains consistent with zero within observational uncertainties [11].

2.3 Standard Big Bang Cosmology

2.3.1 Flatness Problem

Within the framework of the standard Big Bang cosmology, dominated by ordinary matter or radiation, the expansion of the universe is always decelerating, i.e., $\ddot{a} < 0$. Consequently, the quantity a^2H^2 decreases with time, and the deviation from spatial flatness evolves as

$$\Omega - 1 \propto \frac{1}{a^2H^2}. \tag{2.24}$$

In such a decelerating background, the comoving Hubble radius $(aH)^{-1}$ grows with time, implying that any small departure from flatness ($|\Omega - 1|$) inevitably increases as the universe expands.

In contrast, present-day observations indicate that the universe is remarkably close to spatial flatness, with $\Omega \simeq 1$ to within a few percent [11]. Extrapolating this condition backwards in time imposes increasingly severe constraints on the initial deviation from flatness [18, 40, 85]. At the epoch of recombination ($z \sim 1100$), one requires $|\Omega - 1| < 10^{-3}$; during nucleosynthesis ($t \simeq 1$ sec), this bound tightens to $|\Omega - 1| \lesssim 10^{-16}$. Pushing further to the Planck epoch ($t \sim 10^{-43}$ sec), the initial deviation must have been tuned to an extraordinary precision,

$|\Omega - 1| < 10^{-60}$.

Such extreme sensitivity to initial conditions highlights the profound fine-tuning necessary in the standard Big Bang framework to account for the nearly flat universe observed today. This conundrum is referred to as the *flatness problem*.

2.3.2 Horizon Problem

Consider a comoving wavelength λ with its corresponding physical scale $d_{\rm ph} = a\lambda$, which at some epoch lies within the Hubble radius H^{-1}. In the standard Big Bang scenario, the expansion is always decelerating. As a result, at later times, the physical wavelength becomes much smaller than the Hubble radius, implying that a causally connected region can only encompass a fraction of the Hubble volume.

The maximum comoving distance a photon can travel from an initial time t_i to a later time t is given by

$$X_{\rm ph} = \int_{\eta_i}^{\eta} \frac{dt}{a(t)} = \int_{a_i}^{a} \frac{da}{a^2 H(a)} \sim a^{(1+3w)/2} - a_i^{(1+3w)/2}, \tag{2.25}$$

where $X_{\rm ph}$ denotes the particle horizon. For an equation-of-state parameter $w > -1/3$, the particle horizon grows monotonically with time, implying that regions previously outside each other's causal domain gradually come into contact.

To quantify this more precisely, the proper particle horizon distance is defined as

$$d_H = a \int_0^a \frac{da'}{H(a')\, a'^2}. \tag{2.26}$$

Assuming the universe is dominated by matter and radiation, the Hubble parameter can be written as

$$H(a) = H_0 \sqrt{\Omega_{m,0} a^{-3} + \Omega_{r,0} a^{-4}}, \tag{2.27}$$

where H_0 is the present-day Hubble parameter. The parameters $\Omega_{m,0}$ and $\Omega_{r,0}$ denote the present fractional energy densities of matter and radiation, respectively. The matter density parameter $\Omega_{m,0}$ includes both baryonic and cold dark matter components, while $\Omega_{r,0}$ accounts for relativistic species such as photons and neutrinos.

Using this expression for $H(a)$, the particle horizon becomes

$$d_H = a \int_0^a \frac{da'}{H_0 \sqrt{\Omega_{m,0} a' + \Omega_{r,0}}} = \frac{2a}{H_0 \Omega_{m,0}} \left(\sqrt{\Omega_{m,0} a + \Omega_{r,0}} - \sqrt{\Omega_{r,0}} \right). \tag{2.28}$$

The angular diameter distance is given by

$$d_A = a \int_a^1 \frac{da'}{H(a')\, a'^2} = \frac{2a}{H_0 \Omega_{m,0}} \left(\sqrt{\Omega_{m,0} + \Omega_{r,0}} - \sqrt{\Omega_{m,0} a + \Omega_{r,0}} \right). \tag{2.29}$$

The ratio of these two quantities, d_H/d_A, represents the angular radius of the particle horizon at a given scale factor:

$$\frac{d_H}{d_A} = \frac{\sqrt{\Omega_{m,0}a + \Omega_{r,0}} - \sqrt{\Omega_{r,0}}}{\sqrt{\Omega_{m,0} + \Omega_{r,0}} - \sqrt{\Omega_{m,0}a + \Omega_{r,0}}}. \tag{2.30}$$

The parameters entering this expression are well constrained by cosmological observations. In particular, measurements of the cosmic microwave background and other probes give $H_0 \simeq 67.4\,\mathrm{km\,s^{-1}\,Mpc^{-1}}$, $\Omega_{m,0} \simeq 0.315$, and $\Omega_{r,0} \simeq 9 \times 10^{-5}$ [11]. The radiation density parameter $\Omega_{r,0}$ is dominated by photons and relativistic neutrinos.

This ratio tends to zero as $a \to 0$. At the epoch of recombination, corresponding to a scale factor $a_{\rm rec} \simeq 10^{-3}$ (or redshift $z_{\rm rec} \simeq 1100$), substituting the above numerical values gives

$$\frac{d_H}{d_A}(a_{\rm rec}) \simeq 0.018. \tag{2.31}$$

This corresponds to an angular scale of roughly 1° on the CMB sky. Thus, the observable universe at recombination contains on the order of $\left(\frac{4\pi}{0.018}\right)^2 \sim 10^4$ connected regions.

Nevertheless, observations show that the CMB is highly homogeneous across the entire sky. The near-uniformity of widely separated regions, which could not have exchanged information within the standard Big Bang framework, implies a level of fine-tuned initial correlations that is both unnatural and theoretically unsatisfactory.

This fundamental inconsistency between causal structure and observational evidence constitutes the *horizon problem* of the standard Big Bang cosmology.

2.3.3 The Origin of Large-Scale Structure in the Universe

The galaxies, galaxy clusters, and the cosmic web observed today are understood as the result of the gravitational growth of small primordial fluctuations in the early Universe. These initial perturbations are imprinted in the cosmic microwave background (CMB) as tiny temperature anisotropies and subsequently evolve under gravitational instability to form the large-scale structures observed today.

A convenient way to characterize these primordial fluctuations is through the power spectrum of the comoving curvature perturbation, denoted by $P_{\mathcal{R}}(k)$. This quantity measures the variance of curvature perturbations per logarithmic interval in wavenumber k, and therefore encodes the statistical properties and scale dependence of the primordial fluctuations generated in the early Universe. Observations of temperature anisotropies in the CMB indicate that these primordial fluctuations had very small amplitudes and were nearly scale invariant. The corresponding power spectrum is commonly parameterized as

$$P_{\mathcal{R}}(k) \propto k^{n_s - 1}, \quad n_s \simeq 1, \tag{2.32}$$

where k is the comoving wavenumber and n_s denotes the scalar spectral index. A value $n_s = 1$ corresponds to a perfectly scale-invariant spectrum, known as the Harrison–Zel'dovich spectrum, while current observations indicate a slightly red-tilted spectrum with $n_s \approx 0.965$ [11] or recently obsered suggest that the spectrum should more scale invaraint nature near CMB scale where it predict the scalar spectral index $n_s \simeq 0.974 \pm 0.003$ [86].

Within the framework of the standard Big Bang cosmology, however, there is no causal mechanism between the initial singularity and the epoch of last scattering capable of generating correlations on super-horizon scales. Consequently, this scenario cannot account for the origin of the nearly scale-invariant primordial fluctuations that seeded the large-scale structure of the universe.

2.3.4 Relic Density Problem

In the earliest stages of the universe, at temperatures of order $T \sim 10^{15} - 10^{16}\,\text{GeV}$ near the grand unified theory (GUT) scale, the gauge symmetries of particle physics are expected to undergo spontaneous breaking. Such phase transitions naturally give rise to a variety of heavy relics, including magnetic monopoles, superheavy stable particles (such as gravitinos and moduli), and other states predicted in extensions of the Standard Model.

These relics are typically very massive and behave as non-relativistic matter once the background temperature falls below their rest mass. Their energy density then scales as a^{-3}, whereas the energy density of radiation redshifts more rapidly as a^{-4}. Consequently, even if these relics constitute only a tiny fraction of the total energy budget initially, their slower dilution ensures that they eventually dominate over the radiation component. This would drive the universe into a relic-dominated phase well before the epoch of Big Bang nucleosynthesis (BBN).

Such an early matter-dominated epoch would strongly disrupt the successful predictions of BBN, leading to light-element abundances incompatible with observations. Hence, the so-called *relic density problem* arises: GUT-scale phase transitions generically predict an overproduction of exotic relics whose energy density would come to dominate the universe, in stark contradiction with cosmological data.

2.3.5 Conditions for solving these problems

The standard Big Bang cosmology predicts a decelerating universe with $\ddot{a} < 0$, and for a simple matter or radiation-dominated era, the EoS of our universe is $w > -1/3$, which means the standard Big Bang has always had flatness and horizon problems. All these problems can be resolved if there exists a phase in the early universe satisfying the following conditions:

i) During this phase, the universe undergoes an accelerating expansion of the scale factor ($\ddot{a} > 0$) such that the comoving Hubble radius $(aH)^{-1}$ decreases with time.

ii) The phase should last long enough so that all the initial relics of unwanted long-lived particles are sufficiently diluted and cannot affect the late-time evolution.

iii) The post-phase thermal history should not reintroduce unwanted relics.

- From the Friedmann equation, we have seen that the deviation from spatial flatness evolves as $|\Omega - 1| \propto (aH)^{-2}$. If, in the early universe, the quantity (aH) grows substantially with time, then $|\Omega - 1|$ will be driven toward zero. Let us assume that at some initial time the value of this quantity is $|\Omega - 1|_i$ and at a later time it evolves to $|\Omega - 1|_e$. Then we can write the ratio of the final to the initial values as

$$\frac{|\Omega - 1|_e}{|\Omega - 1|_i} = \left(\frac{a_i H_i}{a_e H_e}\right)^2 = e^{-2\Delta \ln(aH)}. \tag{2.33}$$

  For many models of accelerated expansion, H changes slowly, so $\Delta \ln(aH) \simeq N$, where $N = \ln(a_e/a_i)$ is the e-folding number of the phase. To be consistent with observations, at the Planck time the deviation from flatness must satisfy $|\Omega - 1|_{\rm Plank} \leq 10^{-60}$. This means that if we start with some initial value, for example $|\Omega - 1|_i \simeq 1$ or 10^{-1}, and require it to decrease to about 10^{-60} by the end of the phase, then a simple calculation shows that the duration of this initial phase must be around $N > 60$, during which the universe undergoes accelerated expansion of the scale factor.

- The horizon problem can be addressed in much the same way as the flatness problem. If the universe undergoes a phase with equation-of-state parameter $w < -1/3$, the quantity (aH) increases with time and the comoving horizon shrinks. In this case, the proper particle horizon at the beginning of this phase can be large enough that the scales we observe today were once in causal contact.

  In the special case of $w = -1$, corresponding to a phase of accelerated expansion with constant Hubble rate $H_{\rm e}$, the scale factor evolves as

$$a(t) = a_i\, e^{H_{\rm e}(t-t_i)} = a_{\rm e}\, e^{-H_{\rm e}(t_{\rm e}-t)}, \tag{2.34}$$

  where a_i and $a_{\rm e}$ denote the scale factor at the onset and at the end of this rapid expansion phase, respectively.

  Including this phase prior to the standard Big Bang evolution, the proper particle horizon acquires an additional contribution from the interval $[t_i, t_{\rm e}]$,

$$d_H \simeq a \int_{t_i}^{t_{\rm e}} dt\, \frac{e^{H_{\rm e}(t_{\rm e}-t)}}{a_{\rm e}} = \frac{a}{a_{\rm e} H_{\rm e}} \left(e^N - 1\right), \tag{2.35}$$

  where $N = H_{\rm e}(t_{\rm e} - t_i)$ is the number of e-folds during the accelerated phase.

  In this framework, the ratio of the particle horizon to the angular diameter distance becomes

$$\frac{d_H}{d_A} \simeq \frac{H_0}{a_{\rm e} H_{\rm e}}\, e^N. \tag{2.36}$$

Requiring that $d_H > d_A$ leads to the condition

$$e^N > \frac{a_e H_e}{a_0 H_0}. \tag{2.37}$$

Thus, the horizon problem is solved provided that the accelerated expansion phase lasts sufficiently long so that the comoving scale corresponding to the present Hubble radius $(a_0 H_0)^{-1}$ was once inside the causal horizon before inflation began.

- As we have discussed for the GUT phase transition, there is a possibility of producing magnetic monopoles or some long-lived moduli fields. In the standard Big Bang cosmology, the universe is dominated either by radiation or by matter, treated as a fluid. For a long period, the universe was radiation dominated. When the background temperature drops below the rest mass of these unwanted massive particles, their relic abundance evolves as $\Omega_{\rm relic} \propto a$, which implies that over time the relic density grows. Thus, even a small initial fraction of such relics could eventually dominate the universe, disrupting the BBN process and conflicting with current observations. We can express the relic abundance of these massive particles as

$$\Omega_{\rm relic}(t) \propto \frac{n_i}{\rho_i}\left(\frac{a_i}{a(t)}\right)^3\left(\frac{H_i}{H(t)}\right)^2, \tag{2.38}$$

where n_i is the initial number density of the particles. Since the number density dilutes as $n(t) \propto a^{-3}$, if these unwanted particles are produced before a special phase in which the universe evolves exponentially with an equation of state $w = -1$, then the ratio of the final to the initial number density is $(n_e/n_i) \propto e^{-3N}$. Here $N = \ln(a_e/a_i)$ is the e-folding number of this special phase. For $w = -1$, the Hubble parameter remains nearly constant in time, i.e., $H_e \simeq H_i$, so the relic abundance at the end of this phase is $\Omega_{\rm relic} \propto e^{-3N}$. This means that if the duration of this phase lasts about $N \simeq 50$ e-folds, the final relic abundance of produced monopoles is suppressed by a factor of e^{-150}, which is sufficient to solve the relic problem of magnetic monopoles or other long-lived moduli fields.

2.4 The theory of Inflation

The theory of cosmic inflation, first proposed by Alan Guth in 1979–1980 [13], was introduced to resolve several fundamental shortcomings of the standard Big Bang cosmology described in the section above. Inflation is a brief epoch, beginning around 10^{-36} seconds and ending near 10^{-32} seconds after the Big Bang, during which the universe underwent an exponential expansion driven by the potential energy of a scalar field, the inflaton [13–16, 58, 84, 87–96]. While the inflaton slowly rolls along a flat region of its potential, the rapid expansion simultaneously addresses the flatness, horizon, and relic-density problems. The exponential growth of the scale factor dilutes any initial spatial curvature and suppresses relics such as magnetic monopoles or moduli fields produced at GUT scales, leaving the universe radiation dominated without excess relic contamination. Moreover, inflation provides a natural mechanism for generating nearly scale-invariant primordial fluctuations, a prediction that has been confirmed by observations of the CMB.

The action for a single canonical scalar field $\varphi(t, \mathbf{x})$ minimally coupled to gravity with potential $V(\varphi)$ is

$$\mathcal{S}_\varphi = \int d^4x\sqrt{-g}\mathcal{L}_\varphi = \int d^4x\sqrt{-g}\left[\frac{M_{\rm pl}^2}{2}R - \frac{1}{2}(\partial\varphi)^2 - V(\varphi)\right], \tag{2.39}$$

where $M_{\rm pl} = \sqrt{8\pi \mathrm{G_N}} = 2.18\times 10^{18}$ GeV is the reduced Planck mass. In cosmic time coordinates, we have $\sqrt{-g} = a^3$ for the FLRW metric. From the Euler–Lagrange equations,

$$\partial^\mu \frac{\delta(\sqrt{-g}\mathcal{L}_\varphi)}{\delta\partial^\mu\varphi} - \frac{\delta(\sqrt{-g}\mathcal{L}_\varphi)}{\delta\varphi} = 0, \tag{2.40}$$

we can obtain the equation of motion of the inflaton field ϕ as

$$\ddot{\varphi} + 3H\dot{\varphi} - \frac{\nabla^2\varphi}{a^2} + \frac{\partial V(\varphi)}{\partial\varphi} = 0. \tag{2.41}$$

Now, the energy-momentum tensor of a canonical scalar field has the following form:

$$T^\varphi_{\mu\nu} = -\frac{2}{\sqrt{-g}}\frac{\delta\mathcal{S}_\varphi}{\delta g^{\mu\nu}} = \partial_\mu\varphi\partial_\nu\varphi - g_{\mu\nu}\left(\frac{1}{2}\partial_\alpha\varphi\partial^\alpha\varphi + V(\varphi)\right) \tag{2.42}$$

In the FLRW background metric with $ds^2 = -dt^2 - a^2(t)\delta_{ij}dx^i dx^j$, the scalar field depends only on t, and the energy density and pressure are defined as [17, 58, 84, 87, 91, 93, 95]

$$\rho_\varphi = \frac{1}{2}\dot{\varphi}^2 + V(\varphi) + \frac{(\nabla\varphi)^2}{2a^2}; \qquad P_\varphi = \frac{1}{2}\dot{\varphi}^2 - V(\varphi) - \frac{(\nabla\varphi)^2}{6a^2}. \tag{2.43}$$

From the above two equations, we can conclude that if the gradient term $(\nabla\varphi)^2$ dominates over the other two terms, then we obtain $\omega_\varphi = P_\varphi/\rho_\varphi \simeq -1/3$. However, to solve the horizon and flatness problems, we require $w_\varphi < -1/3$. This means that during inflation, the gradient of the inflaton field, which is associated with its fluctuations, must remain small compared with the other two terms in order to sustain a successful inflationary era.

We can write the inflaton field as a sum of two parts as $\varphi(\mathbf{x}, t) = \varphi_0(t) + \delta\varphi(\mathbf{x}, t)$, where one is the homogeneous background field denoted as $\varphi_0(t)$, which only depends on time, and the other is the fluctuations of the inflaton field denoted as $\delta\varphi(\mathbf{x}, t)$, which depends on both time and space. The equation of state during inflation due to a single scalar field $\varphi(\mathbf{x}, t)$ is defined as

$$w_\varphi = \frac{P_\varphi}{\rho_\varphi} = \frac{\frac{1}{2}\dot{\varphi}^2 - V(\varphi) - \frac{(\nabla\varphi)^2}{6a^2}}{\frac{1}{2}\dot{\varphi}^2 + V(\varphi) + \frac{(\nabla\varphi)^2}{2a^2}}. \tag{2.44}$$

As inflation is driven by the homogeneous background field φ_0 and if the potential energy dominates over the kinetic energy, i.e., $\dot{\varphi}^2 \ll V(\varphi)$, then the EoS during inflation is $w_\varphi \simeq -1 < -1/3$, which means during this time, the scale factor evolves exponentially, i.e., $a(t) \propto e^{Ht}$.

The Friedmann equations for the canonical single scalar field are

$$H^2 = \frac{8\pi \mathrm{G_N}}{3}\left[\frac{1}{2}\dot{\varphi}^2 + V(\varphi)\right]; \qquad \frac{\ddot{a}}{a} = -\frac{8\pi \mathrm{G_N}}{3}\left[\dot{\varphi}^2 - V(\varphi)\right] \tag{2.45}$$

Combining these two, we can get the acceleration equation as $\dot{H} = -4\pi \mathrm{G_N}\dot{\varphi}^2$. To achieve an accelerated expansion phase, we require that $H(t)$ varies slowly, i.e., $\dot{H} \sim 0$. Note that to have a successful inflationary phase, the inflaton potential doesn't need to be flat; the only condition we have to satisfy is that the potential energy is dominant over the kinetic energy, i.e., $V(\varphi) >> \dot{\varphi}^2$.

The equation of motion of the background scalar field $\varphi_0(t)$ is given by

$$\ddot{\varphi}_0 + 3H\dot{\varphi}_0 + V_{,\varphi_0}(\varphi_0) = 0, \tag{2.46}$$

where $V_{,\varphi_0}(\varphi_0) = \partial V/\partial\varphi_0$. This equation is analogous to that of a particle rolling down a potential, subject to a friction term proportional to $3H\dot{\varphi}_0$.

In the regime where the friction term dominates, the system admits an attractor solution, known as the *slow-roll* solution, given by $\dot{\varphi}_0 \simeq -V_{,\varphi_0}(\varphi_0)/(3H)$. This approximation is valid when the acceleration term is negligible compared to the friction term, i.e., when $-\ddot{\varphi}_0/(H\dot{\varphi}_0) << 1$.

To characterize the inflationary dynamics, we introduce a set of dimensionless slow-roll parameters [17, 58, 84, 87, 91, 93, 95]

$$\epsilon_H = 2M_\mathrm{P}^2\left(\frac{H'(\varphi)}{H(\varphi)}\right)^2; \qquad \eta_H = 2M_\mathrm{P}^2\frac{H''(\varphi)}{H(\varphi)} \tag{2.47}$$

where ϵ_H and η_H denote the first and second Hubble slow-roll parameters, respectively. For a successful inflationary phase consistent with observations, the condition $\epsilon_H << 1$ must be satisfied initially. In a typical slow-roll scenario, ϵ_H gradually increases with time and eventually reaches unity, at which point inflation ends.

For convenience, these parameters can also be expressed in terms of the inflaton field and its potential as [17, 58, 84, 87, 91, 93, 95]

$$\epsilon_\varphi \simeq \frac{M_\mathrm{P}^2}{2}\left(\frac{V_{,\varphi}(\varphi)}{V(\varphi)}\right)^2 \simeq \frac{3}{2}\left(\frac{\dot{\varphi}_0^2}{V(\varphi)}\right); \qquad \eta_\varphi \simeq \frac{M_\mathrm{P}^2}{2}\left(\frac{2V_{,\varphi\varphi}}{V} - \left(\frac{V_{,\varphi}}{V}\right)^2\right) \tag{2.48}$$

Inflation naturally ends when the condition $\epsilon_\varphi \simeq 1$ is satisfied. At this stage, the kinetic energy of the inflaton field becomes comparable to its potential energy, and the accelerated expansion ($\ddot{a} > 0$) ceases. Subsequently, the inflaton field decays into Standard Model particles or beyond Standard Model components (e.g., dark matter), initiating the reheating phase.

The duration of inflation is typically quantified in terms of the number of e-folds,

$$N_{\rm end} = \ln\left(\frac{a_{\rm e}}{a_i}\right) \simeq \int_{t_i}^{t_{\rm e}} H(t){\rm d}t \simeq \int_{\varphi_{\rm end}}^{\varphi_{\rm i}} \frac{{\rm V}(\varphi_0)}{{\rm V}_{,\varphi_0}}\,{\rm d}\varphi_0. \tag{2.49}$$

To successfully address the horizon and flatness problems, the duration of inflation is required to be approximately $N_{\rm end} \simeq 50 - 70$.

2.4.1 $\alpha-$Attractor-E Inflation model

Among the various models to realize inflation, the class of $\alpha-$attractor models has received particular attention due to their theoretical robustness and observational viability. These models naturally arise in the framework of supergravity and conformal field theory, where the scalar field dynamics are governed by a non-trivial kinetic term characterized by a parameter α. The parameter α controls the curvature of the scalar field manifold and plays an essential role in predicting the inflationary parameters like the scalar spectral index n_s and tensor-to-scalar ratio r. Here we mainly discuss a very specific model known as the $\alpha-$attractor-E model, where the potential of the inflaton field is [97]

$$V(\varphi) = \Lambda^2\left(1 - \exp\left[-\sqrt{\frac{2}{3\alpha}}\frac{\varphi}{M_{\rm P}}\right]\right)^{2p} \tag{2.50}$$

Here, Λ sets the overall energy scale of inflation, α determines the curvature of the field space, and p is a positive integer that controls the steepness of the potential near its minimum. The parameter Λ can be fixed using CMB observations, while the remaining parameters p and α determine the spectral behavior of the perturbations at large scales.

For the specific choice $\alpha = 1$ and $n = 1$, the potential reduces to the Starobinsky model of inflation [19], which is one of the most successful models consistent with Planck CMB data. After the end of inflation, the inflaton field oscillates about the minimum of its potential. Depending on the stiffness of the potential, the effective equation of state of the inflaton field is modified and can be approximated as $w_\varphi \simeq (p-1)/(p+1)$.

To constrain the model parameters using CMB observations, an important observable is the scalar spectral index n_s, which is directly measured from large-scale fluctuations in the CMB anisotropies. Therefore, we treat n_s as a free parameter and use it, together with the potential parameters α and p, to constrain the remaining quantities in the model.

Assuming that the tensor fluctuations observed today originate entirely from quantum fluctuations produced during inflation, the tensor-to-scalar ratio can be related to the inflationary Hubble scale as $H_{k_*} \simeq \pi M_{\rm P}(rA_{\rm s}/2)^{1/2}$, where $A_{\rm s}$ is the amplitude of the scalar power spectrum at the CMB pivot scale $k_* \simeq 0.05\,{\rm Mpc}^{-1}$ [11]. The scalar spectral index (n_s), the amplitude of scalar perturbations ($A_{\rm s}$), and the tensor-to-scalar ratio (r) are all determined by the curvature and tensor perturbations; their detailed derivation is presented in Section 2.7.1.

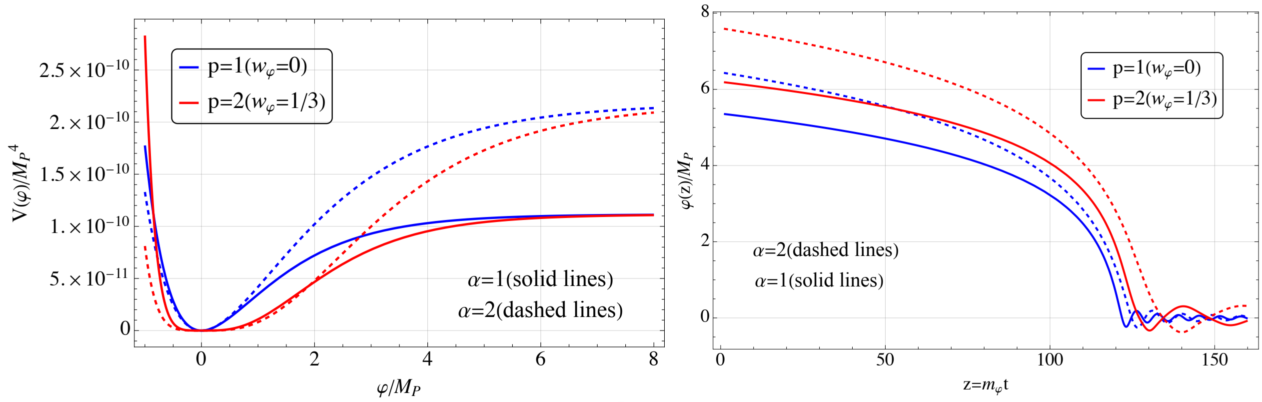

Figure 2.2: **Left** figure shows, how the inflaton potential ($\alpha-$attractor-E model) depend on the two inflationary parameters p and α. **Right** figure, we have plotted the evolution of the inflaton field as a function of cosmic time dimensionless via the inflaton mass m_φ. In both panels, the blue color corresponds to $p = 1(w_\varphi = 0)$ and red colors correspond to $p = 2(w_\varphi = 1/3$. Here, the solid lines correspond to $\alpha = 1$ and the dashed line corresponds to $\alpha = 2$.

Using these relations, the parameter Λ can be expressed as

$$\Lambda = M_\mathrm{P}\left(\frac{3\pi^2 r A_\mathrm{s}}{2}\right)^{1/4}\left(1+\frac{3\alpha(1-n_s)}{4p+2\sqrt{4p^2+6p\alpha(1+p)(1-n_s)}}\right)^{p/2}. \tag{2.51}$$

Now, to set the initial value of the inflaton field value from the observations, we can use the well-known relation between the slow-roll parameters with the scalar spectral index n_s, which is $n_s = 1 - 6\epsilon_\varphi + 2\eta_\varphi$. Now, utilizing this expression, we can write the initial field value of the inflaton field φ_{k_*} as

$$\varphi_{k_*} = \sqrt{\frac{3\alpha}{2}} M_\mathrm{P} \ln\left[1+\frac{4p+2\sqrt{4p^2+6p\alpha(1+p)(1-n_s)}}{3\alpha(1-n_s)}\right] \tag{2.52}$$

Whereas we can also identify the value of the tensor-to-scalar ratio at the CMB scale via the model parameters p and α along with the n_s as

$$r_{k_*} = \frac{192\alpha p^2(1-n_s)^2}{\left[4p+\sqrt{16p^2+24\alpha p(1-n_s)(1+p)}\right]^2} \tag{2.53}$$

Now for the intial velocity of the inflaton field, we used the Eq.(2.48), and we have define it via $\dot\varphi \simeq \sqrt{2\epsilon_\varphi} H_{k_*} M_\mathrm{P} \simeq H_{k_*}^2/(2\pi\sqrt{A_\mathrm{s}})$, where we H_{k_*} is the value of the Hubble constant at the time when the pivot scale left the horizon. Although for a perfect de-sitter inflationary background, the value of the Hubble constant remains unchanged, for a realistic inflationary model, there have been slight changes in the Hubble constant as inflation goes on. Once inflation ends the reheating follows.

2.5 Dynamics of Reheating

Inflation offers a natural framework to explain the large-scale uniformity of the Universe, including its near-perfect isotropy, homogeneity, and spatial flatness, as well as the origin of primordial perturbations. Yet, the inflationary expansion, occurring over an extremely short interval, leaves the Universe in a cold, dilute, and highly non-thermal state governed by oscillations of the inflaton field. Such a post-inflationary state is incompatible with the hot, dense plasma required for the onset of Big Bang Nucleosynthesis (BBN). To reconcile this, the Universe must undergo a transition phase in which the inflaton's energy is converted into ordinary matter and radiation, thereby producing a thermal bath of relativistic particles. This stage, known as reheating, is indispensable: it initiates the radiation-dominated epoch, setting the thermal history that enables both BBN and the formation of the Cosmic Microwave Background (CMB). Without reheating, the standard hot Big Bang picture could not be realized.

Reheating mechanisms can be perturbative, non-perturbative or combination of the both. In our work we mostly considered perturbative scenario

2.5.1 Perturbative Reheating Scenarios

Perturbative reheating represents one of the simplest mechanisms through which the inflaton transfers its energy into radiation. In this scenario, the inflaton field decays gradually while oscillating around the minimum of its potential. To illustrate, consider the inflaton field φ coupled to a light scalar field χ through the standard interaction term

$$\mathcal{L}_{\text{int}} \supset -\tfrac{1}{2}g^2\varphi^2\chi^2, \tag{2.54}$$

where g is a dimensionless coupling constant and χ is treated as a light radiation-like field. The corresponding equation of motion for the inflaton is

$$\ddot{\varphi} + 3H\dot{\varphi} + V_{,\varphi}(\varphi) + g^2\varphi\chi^2 = 0. \tag{2.55}$$

Here, χ is a quantum field. Since we are primarily interested in the evolution of the inflaton's energy density, it is useful to take the expectation value of χ^2 in either the vacuum or thermal state. The quantity $\langle\chi^2\rangle$ then acts effectively as a damping term. In the perturbative regime ($g \ll 1$) and at sufficiently late times, this backreaction can be modeled as an additional friction term proportional to $\dot{\varphi}$. Accordingly, the replacement $g^2\varphi\langle\chi^2\rangle \longrightarrow \Gamma_\varphi\dot{\varphi}$ can be made, where Γ_φ denotes the perturbative decay rate of the inflaton. The effective equation of motion then becomes

$$\ddot{\varphi} + 3H\dot{\varphi} + V_{,\varphi}(\varphi) = -\Gamma_\varphi\dot{\varphi}, \tag{2.56}$$

which explicitly demonstrates how the inflaton condensate dissipates its energy into radiation.

Multiplying Eq. (2.56) by $\dot{\varphi}$ and using the relation $\dot{\varphi}^2 = \rho_\varphi + P_\varphi$, we obtain

$$\frac{d\rho_\varphi}{dt} + 3H(1+w_\varphi)\rho_\varphi = -(1+w_\varphi)\Gamma_\varphi \rho_\varphi, \tag{2.57}$$

where we have used $P_\varphi = w_\varphi \rho_\varphi$, with w_φ denoting the average EoS of the inflaton field. The value of w_φ can be directly inferred from the form of the inflaton potential near its minimum. In particular, when the inflaton oscillates around the minimum, the α-attractor-E model reduces effectively to a power-law potential of the form $V(\varphi) \propto \varphi^{2p}$. For a general power-law potential, the average EoS of the inflaton field can be expressed as

$$w_\varphi = \frac{P_\varphi}{\rho_\varphi} = \frac{\frac{1}{2}\langle \dot{\varphi}^2 \rangle - \langle V(\varphi) \rangle}{\frac{1}{2}\langle \dot{\varphi}^2 \rangle + \langle V(\varphi) \rangle} \simeq \frac{p-1}{p+1} \tag{2.58}$$

To obtain the final expression in Eq. (2.58), we have used the relation $\langle \dot{\varphi}^2 \rangle = 2\langle V(\varphi) \rangle$. It should be noted that, in deriving the EoS, we neglected the spatial gradient term of the inflaton field, i.e., $(\nabla\varphi)^2$, under the assumption that inflaton fluctuations are negligible compared to its kinetic energy. This approximation is well justified during the later stages of the reheating era. However, immediately after inflation, in the preheating stage, this expression is not strictly valid [98–104]. Similarly, the evolution equation for the radiation energy density can be written as

$$\frac{d\rho_r}{dt} + 4H\rho_r = (1+w_\varphi)\Gamma_\varphi \rho_\varphi \tag{2.59}$$

Here we add the term $(1+w_\varphi)\Gamma_\varphi\rho_\varphi$, which represents the transfer of inflaton energy into the radiation energy density. The term $4H\rho_r$ denotes the Hubble friction, describing how the radiation energy density evolves due to the background expansion. Since radiation is sourced by the inflaton through $(1+w_\varphi)\Gamma_\varphi\rho_\varphi$, its energy density grows with time until the stage when $\rho_\varphi \simeq \rho_r$.

If we assume that during the reheating phase the Universe is dominated by two components, namely the inflaton field and the radiation field, then the system is governed by the following set of coupled equations:

$$\rho'_\varphi + \frac{3(1+w_\varphi)}{a}\rho_\varphi = -\frac{(1+w_\varphi)\Gamma_\varphi}{aH}\rho_\varphi, \tag{2.60a}$$

$$\rho'_r + \frac{4}{a}\rho_r = \frac{(1+w_\varphi)\Gamma_\varphi}{aH}\rho_\varphi, \tag{2.60b}$$

where the prime ($'$) denotes the derivative with respect to the scale factor, i.e., $\rho' = d\rho/da$. We rescale the scale factor at the beginning of the reheating as $a = a_{\rm e} = 1$. along with this we have the 1st Friedmann equation $H^2 = \frac{1}{3M_{\rm P}^2}(\rho_\varphi + \rho_r)$.

Initially, the Universe is dominated by the oscillating inflaton field ($\rho_\varphi \gg \rho_r$). As the inflaton decays, its energy density ρ_φ is converted into radiation, and the radiation energy density gradually increases with time. The efficiency of this energy transfer depends on the

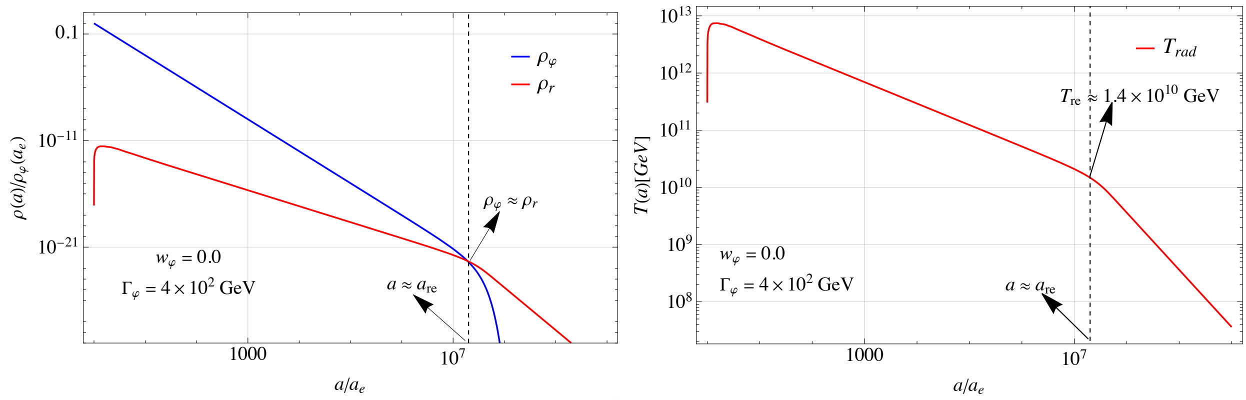

Figure 2.3: In the left panel, we plot the evolution of the inflaton energy density ρ_φ (blue) and the radiation energy density ρ_r (red) as functions of the normalized scale factor $a/a_{\rm e}$. The evolution is shown for a fixed value of the inflaton decay constant $\Gamma_\varphi = 4\times10^2$, GeV and assuming a constant equation of state $w_{\rm re} = 0$, corresponding to a matter-like expansion. In the right panel, we present the evolution of the background temperature for the same set of parameters.

decay width of the inflaton Γ_φ and on the inflaton EoS during reheating. In general, the decay rate of the inflaton is time-dependent, since it depends on both the EoS and the interaction between the inflaton and the radiation fields. However, in our analysis, we assume a constant decay rate for simplicity.

As we know, inflation ends when the slow-roll parameter $\epsilon_\varphi \simeq 1$. At this stage, the scale factor is denoted by $a_{\rm e}$, and the Hubble constant at the end of inflation is $H_{\rm e}$. We can therefore set the initial energy density of the inflaton field at $a_{\rm e} = 1$, where the reheating dynamics begin, as $\rho_\varphi^{\rm end} \simeq 3H_{\rm e}^2 M_{\rm P}^2$. For computational purposes, we normalize all energy densities by $\rho_\varphi^{\rm end}$ such that $\rho_\varphi(a_{\rm e}) = 1$.

For simplicity, we further assume that at the end of inflation the Universe contains only the inflaton energy density. Although there could be small radiation fluctuations, their initial energy density is negligible compared to that of the inflaton. Therefore, for numerical computations, we set the initial conditions as $\rho_\varphi(a_{\rm e} = 1) = 1$, and $\rho_r(a_{\rm e} = 1) = 10^{-20}$.

Since radiation is produced from the inflaton, the initial energy density of the radiation field is negligible. Assuming during the reheating era $H >> \Gamma_\varphi$ and $\rho_\varphi >> \rho_r$, the analytical solution of Eq.(2.60) during reheating can be approximately estimate as

$$\rho_\varphi(a) \simeq \rho_\varphi^{\rm end}\left(\frac{a_{\rm e}}{a}\right)^{3(1+w_\varphi)} \tag{2.61a}$$

$$\rho_r(a) \simeq \frac{2(1+w_\varphi)\Gamma_\varphi\rho_\varphi^{\rm end}}{(5-3w_\varphi)H_{\rm e}}\left(\left(\frac{a_{\rm e}}{a}\right)^{\frac{3(1+w_\varphi)}{2}} - \left(\frac{a_{\rm e}}{a}\right)^4\right) \tag{2.61b}$$

$$H(a) \simeq H_{\rm e}\left(\frac{a_{\rm e}}{a}\right)^{\frac{3(1+w_\varphi)}{2}} \tag{2.61c}$$

We recall that $H_{\rm e}$ is the Hubble constant defined at the end of inflation. The above solutions are only valid during the reheating era where $\rho_\varphi >> \rho_r$ [105]. From the above, we can see that if we consider $w_\varphi = 0$ (matter like evolution), then the inflaton field energy density goes as $\rho_\varphi(a) \propto a^{-3}$, as the radiation energy density goes as $\rho_r(a) \propto a^{-3/2}$. Generally, we know that radiation energy density goes as $\rho_r(a) \propto a^{-4}$, but during reheating, as the inflaton energy density directly sources radiation, there is continuous production of the radiation energy up to the point $\rho_\varphi \simeq \rho_r$. Here it is clear that both the inflaton energy density (ρ_φ) and radiation energy density (ρ_r) depend on the EoS of the inflaton field, i.e., w_φ. We recall that the EoS of the inflaton field for perturbative reheating scenarios depends on the shape of the potential near its minima. So the post-inflationary era will significantly impact the reheating dynamics, although it also depends on the decay width Γ_φ. Here, both w_φ and Γ_φ are the key parameters that determine how long the reheating era will sustain. Now, to define the bath temperature, we assume that the radiation produced by the inflaton decay and thermalizes instantaneously, thereby creating a background thermal bath. The temperature of the thermal bath is mainly related to the amount of radiation energy produced at a particular time, so we can use the Stefan-Boltzmann relation to determine the thermal bath temperature via the following equation

$$\rho_r(a) = \frac{\pi^2 g_*(T_{\rm rad})}{30} T^4_{\rm rad}(a) \tag{2.62}$$

where $g_*(T_{\rm rad})$ is the effective number of relativistic degrees of freedom associated with the thermal bath. Now the reheating temperature is defined at the point where both the inflaton field energy density and radiation energy density get equal, i.e., $\rho_\varphi(a_{\rm re}) \simeq \rho_r(a_{\rm re})$, here $a_{\rm re}$ is the normalised scale factor where reheating is completed.

In Fig.2.3, we have plotted the evolution of the energy density $\rho_\varphi(a)$ and $\rho_r(a)$ as functions of normalised scale factor a for $w_\varphi = 0.0$ and $\Gamma_\varphi = 4 \times 10^2\,\text{GeV}$. Here we have found that reheating completes near $a \simeq 2 \times 10^7$, where $\rho_\varphi \simeq \rho_r$. Here we also have noticed that during the reheating era, the inflaton energy density goes as $\rho_\varphi(a) \propto a^{-3(1+w_\varphi)}$ and $\rho_r(a) \propto a^{-3(1+w_\varphi)/2}$. After the completion of reheating, the radiation energy flows its usual scaling behaviour, i.e., $\rho_r(a > a_{\rm re}) \propto a^{-4}$, where $a_{\rm re}$ represent the value of the normalized scale factor where the reheating is complete. To get a standard radiation-dominated universe, the reheating phase must end, and reheating ends when the energy density of the radiation overtake the inflaton energy density, which happens when the following condition is satisfied, i.e., $\rho_\varphi(a_{\rm re}) \simeq \rho_r(a_{\rm re})$. From the left Fig.2.3, we have seen that when $a > a_{\rm re}$, the inflaton field decays exponentially and our universe is entirely dominated by the radiation field. Now one can determine the reheating temperature $T_{\rm re}$ as

$$T_{\rm re} = \left(\frac{30}{\pi^2 g_*^{\rm re}(T_{\rm re})}\right)^{1/4} \rho_r^{1/4}(a_{\rm re}) \tag{2.63}$$

In the right panel of Fig.2.3, we have shown the evolution of the radiation temperature $T_{\rm rad}(a)$ as a function of normalised scale factor a. From this figure, we have found that the reheating temperature for $w_\varphi = 0.0$ and $\Gamma_\varphi = 4 \times 10^2\,\text{GeV}$ is $T_{\rm rad}(a \simeq a_{\rm re}) = T_{\rm re} \simeq 1.4 \times$

10^{10} GeV. Although there is no direct experimental evidence for the reheating phase, the reheating temperature remains largely unconstrained. However, a conservative range often quoted in the literature is [59, 106–109]

$$T_{\rm BBN} \simeq 4 \text{ MeV} \leq T_{\rm re} \leq 10^{15}\,\text{GeV} \tag{2.64}$$

where the lower bound is imposed to ensure that the reheating phase completes before the onset of BBN, thereby preserving the successful prediction of primordial element abundances, whereas the upper limit is determined from the inflationary energy scale.

Recasting Cosmological Parameters in Terms of Reheating Equation of State and Temperature

After reheating, it is typically assumed that there is no significant injection of entropy that could alter the cosmic microwave background (CMB) or the neutrino background. This assumption of entropy conservation from the end of reheating to the present epoch implies $a^3(t)s = \text{const.}$, which leads to

$$g_{*,\rm re}\, T_{\rm re}^3 = \left(\frac{a_0}{a_{\rm re}}\right)^3 \left(2T_0^3 + 6 \times \frac{7}{8} T_{\nu,0}^3\right), \tag{2.65}$$

where s is the entropy density, $T_0 = 2.725$ K is the present CMB temperature, and $g_{*,\rm re}$ denotes the effective number of relativistic degrees of freedom at the end of reheating.

The present-day neutrino temperature is related to the CMB temperature as $T_{\nu,0} = \left(\frac{4}{11}\right)^{1/3} T_0$. Substituting this expression into Eq. (2.65), we obtain the following relation between the reheating temperature and the present-day CMB temperature:

$$T_{\rm re} = \left(\frac{43\, g_{*,\rm re}}{11}\right)^{1/3} \left(\frac{a_0}{a_{\rm re}}\right) T_0. \tag{2.66}$$

This relation connects the temperature at the end of reheating with today's CMB temperature, under the assumption that the universe evolved through a purely radiation-dominated phase between reheating and photon decoupling.

Defining the Reheating Temperature $T_{\rm re}$: Assuming a single-field inflaton scenario, after the end of inflation the inflaton field decays into both Standard Model and non-Standard Model particles. During the early stage of reheating, the inflaton field constitutes the dominant component of the energy density. Under this assumption, the effective equation of state during reheating can be approximated as $w_{\rm re} \simeq w_\varphi$. However, this approximation is not strictly valid near the completion of reheating, when the energy densities of the inflaton and radiation become comparable. For simplicity, we assume that the dynamics remain predominantly governed by w_φ.

Several studies have explored the impact of a time-dependent equation of state and found that it introduces only minimal corrections to the final results [99, 110–112]. Therefore, during reheating, the evolution of the background energy density is largely dictated by the inflaton component. Consequently, the evolution of the inflaton energy density during this phase can be expressed as $\rho_\varphi = \rho_\varphi^{\rm end}\,(a/a_{\rm e})^{-3(1+w_{\rm re})}$ [113–116]. Accordingly, the Hubble parameter evolves $H = H_{\rm e}\,(a/a_{\rm e})^{-3(1+w_{\rm re})/2}$ as [113]. Typically, the reheating temperature is defined at the point where the inflaton energy density equals the radiation energy density, i.e., $\rho_\varphi = \rho_r$. If we treat the radiation component as a bosonic species, its energy density can be written as $\rho_r = \frac{\pi^2 g(T)}{30}T^4$. Using this relation, the reheating temperature can be expressed as [113]

$$T_{\rm re} = \left(\frac{90 H_{\rm e}^2 M_{\rm P}^2}{\pi^2 g_{*,\rm re}}\right)^{1/4} {\rm Exp}\left[-\frac{3}{4}N_{\rm re}(1+w_{\rm re})\right]. \tag{2.67}$$

Alternatively, the duration of the reheating phase can be written as [113]

$$N_{\rm re} = \frac{1}{3(1+w_{\rm re})}\ln\left(\frac{90 H_{\rm e}^2 M_{\rm P}^2}{\pi^2 g_{*,\rm re} T_{\rm re}^4}\right). \tag{2.68}$$

Computing $k_{\rm e}$ and $k_{\rm re}$: In the previous paragraph, we discussed the reheating parameters, which primarily depend on the inflationary quantities such as the tensor-to-scalar ratio r, the amplitude of the scalar power spectrum $A_{\rm s}$, and the average equation of state $w_{\rm re}$. Although the duration of reheating is also related to the decay rate of the inflaton field, denoted by Γ_φ, for our purposes we define two relevant scales that will be used throughout our analysis. In this approach, the reheating parameters are treated as free parameters.

The first scale corresponds to the horizon size at the end of inflation, denoted by $k_{\rm e}$, and is defined as [117–119]

$$\frac{k_{\rm e}}{a_0} = \left(\frac{43\, g_{*,\rm re}}{11}\right)^{1/3}\left(\frac{\pi^2 g_{*,\rm re}}{90}\right)^{1/\alpha}\frac{H_{\rm e}^{1-2/\alpha}T_{\rm re}^{4/\alpha-1}T_0}{M_{\rm P}^{2/\alpha}}, \tag{2.69}$$

where $\alpha = 3(1+w_{\rm re})$.

Similarly, the comoving wavenumber associated with the horizon size at the end of reheating is given by [117–119]

$$\frac{k_{\rm re}}{a_0} = \left(\frac{43\, g_{*,\rm re}}{11}\right)^{1/3}\left(\frac{\pi^2 g_{*,\rm re}}{90}\right)^{1/2}\frac{T_0 T_{\rm re}}{M_{\rm P}}. \tag{2.70}$$

From Eq. (2.69), it is evident that the value of $k_{\rm e}$ depends primarily on the inflationary energy scale $H_{\rm e}$, the reheating temperature $T_{\rm re}$, and the equation of state parameter $w_{\rm re}$. Once the inflationary energy scale $H_{\rm e}$ is fixed, $k_{\rm e}$ is mainly determined by $T_{\rm re}$ and $w_{\rm re}$.

So to make our analysis model-independent, we treat the inflationary energy scale ($H_{\rm e}$) as a free parameter, but it should always satisfy the upper limit by the CMB observations [11]. Once we know the value of the inflationary scale, then the duration of the inflationary era, which is related to $k_{\rm e}$ is mainly depends on the reheating temperature $T_{\rm re}$ and the EoS $w_{\rm re}$. If the reheating is completed before the electroweak scale, then the value of the relativistic degree of freedom remains constant, i.e., $g_{*,\mathrm{re}}(T_{\mathrm{re}} > 300\,\mathrm{GeV}) = 106.75$.

2.6 Cosmological Perturbation theory

On large scales, the Universe is well described as *homogeneous and isotropic* by the FLRW metric, where all physical quantities depend only on time. This background explains the cosmic expansion, redshift, and the thermal origin of the CMB.

However, observations reveal small deviations from perfect homogeneity: the CMB shows anisotropies at the level of $\Delta T/T \sim 10^{-5}$, and matter forms galaxies and large-scale structures. To describe these features, we introduce *small perturbations* around the homogeneous background,

$$g_{\mu\nu} = \bar{g}_{\mu\nu} + \delta g_{\mu\nu}, \qquad \rho = \bar{\rho} + \delta\rho, \qquad \varphi = \bar{\varphi} + \delta\varphi. \tag{2.71}$$

Here, barred quantities denote background values, while δ terms represent small spatial fluctuations that seed structure formation via gravitational instability.

These perturbations originate from *quantum fluctuations* during inflation, stretched to cosmological scales and frozen as classical perturbations. Their evolution is studied using cosmological perturbation theory, leading to observable quantities such as the curvature perturbation $\mathcal{R}$ and tensor perturbations h_{ij}, whose statistical properties are described by their *power spectra*.

2.7 Metric Perturbations and Their Decomposition

Once the need for perturbations on top of the homogeneous FLRW background is established, the next step is to describe how small perturbations in the spacetime geometry can be mathematically formulated. In general relativity, the dynamics of spacetime are encoded in the metric tensor $g_{\mu\nu}$, and therefore any deviation from perfect homogeneity and isotropy can be represented as small perturbations to the background metric.

Starting from the background FLRW metric in conformal time η,

$$ds^2 = a^2(\eta)\left[-d\eta^2 + \delta_{ij}\,dx^i dx^j\right], \tag{2.72}$$

we introduce small perturbations $\delta g_{\mu\nu}$ such that $g_{\mu\nu} = \bar{g}_{\mu\nu} + \delta g_{\mu\nu}$.

The most general perturbed metric in conformal coordinates can then be written as

$$ds^2 = a^2(\eta)\Big[-(1+2\Phi)\,d\eta^2 + 2(B_{,i} + S_i)\,d\eta\,dx^i + \Big((1-2\Psi)\delta_{ij} + 2E_{,ij} + F_{(i,j)} + h_{ij}\Big)dx^i dx^j\Big], \tag{2.73}$$

where the perturbation quantities Φ, Ψ, B, E, S_i, F_i, and h_{ij} depend on both space and time. The physical interpretation of each term becomes transparent once we decompose the perturbations into scalar, vector, and tensor parts.

Decomposition into Scalar, Vector, and Tensor Modes

Due to the spatial flatness, the FLRW background enjoys SO(3) symmetry. Under this symmetry all the perturbation variables can be decomposed into irreducible scalar, vector, and tensor representation, which evolve independently at linear order.

Scalar modes are described by (Φ, Ψ, B, E), with

$$B_i = \partial_i B, \qquad E_{ij} = \left(\partial_i \partial_j - \frac{1}{3}\delta_{ij}\nabla^2\right) E. \tag{2.74}$$

They encode density and curvature perturbations.

Vector modes satisfy

$$\partial^i S_i = 0, \qquad \partial^i F_i = 0, \tag{2.75}$$

and represent transverse rotational perturbations, which typically decay in an expanding universe.

Tensor modes correspond to gravitational waves and obey

$$\partial^i h_{ij} = 0, \qquad h^i{}_i = 0. \tag{2.76}$$

They describe the two polarization states of primordial gravitational waves.

Gauge Transformations and Gauge-Invariant Variables

Under an infinitesimal coordinate transformation

$$x^\mu \to \tilde{x}^\mu = x^\mu + \xi^\mu, \tag{2.77}$$

the metric perturbations transform as

$$\delta g_{\mu\nu} \to \delta g_{\mu\nu} - \bar{\nabla}_\mu \xi_\nu - \bar{\nabla}_\nu \xi_\mu. \tag{2.78}$$

Considering the following scalar perturbing variable, $\xi^\mu = (\xi^0, \partial^i \xi)$, the scalar perturbations transform as

$$\tilde{\Phi} = \Phi - \dot{\xi}^0 - H\xi^0; \; \tilde{\Psi} = \Psi + H\xi^0; \; \tilde{B} = B + \frac{1}{a}\xi^0 - a\dot{\xi}; \; \tilde{E} = E - \xi. \tag{2.79}$$

For any scalar field (let say inflaton field) $\varphi(t, \mathbf{x}) = \bar{\varphi}(t) + \delta\varphi(t, \mathbf{x})$, the perturbation transforms as

$$\tilde{\delta\varphi} = \delta\varphi - \dot{\bar{\varphi}}\,\xi^0. \tag{2.80}$$

Similarly, the energy density can be decomposed as $\rho(t, \mathbf{x}) = \bar{\rho}(t) + \delta\rho(t, \mathbf{x})$. Since ρ is also a scalar quantity, its perturbation transforms under the gauge transformation as

$$\tilde{\delta\rho} = \delta\rho - \dot{\bar{\rho}}\,\xi^0. \tag{2.81}$$

Here an overbar denotes the homogeneous background quantity, while δ represents the corresponding perturbation.

The Bardeen potentials: Utilizing all the above transformations, one defines the gauge-invariant quantities in the scalar sector,

$$\Phi_B = \Phi - \frac{d}{dt}\left[a^2\left(\dot{E} - \frac{B}{a}\right)\right]; \;\; \Psi_B = \Psi + aH\left(\dot{E} - \frac{B}{a}\right). \tag{2.82}$$

Furthermore, if matter perturbations are included, a particularly important gauge-invariant quantity is the curvature perturbation on uniform-field (or uniform-density) hypersurfaces, which plays a central role in cosmological observables.

Curvature perturbation on uniform field hypersurfaces:

To understand the physical meaning of curvature perturbations, it is useful to consider the intrinsic curvature of spatial hypersurfaces. In the presence of scalar metric perturbations, the perturbed three-dimensional Ricci scalar of constant-time hypersurfaces is given by

$${}^{(3)}R = -\frac{4}{a^2}\nabla^2\Psi, \tag{2.83}$$

which shows that the metric perturbation Ψ directly characterizes the spatial curvature perturbation.

Given a single scalar field $\phi(t, \mathbf{x}) = \bar{\varphi}(t) + \delta\varphi(t, \mathbf{x})$, it is often convenient to evaluate the curvature perturbation on hypersurfaces where the scalar field is spatially uniform, i.e., $\delta\varphi = 0$. The curvature perturbation on such hypersurfaces is defined as

$$\mathcal{R} \equiv \Psi - \frac{H}{\dot{\bar{\varphi}}}\,\delta\varphi. \tag{2.84}$$

Here, $\bar{\varphi}$ denotes the background inflaton field, while $\delta\varphi$ represents its fluctuations. However, the above relation is generally valid for any scalar field.

This quantity represents the perturbation in the intrinsic spatial curvature on hypersurfaces of uniform scalar field. The combination is manifestly gauge-invariant because both Ψ and $\delta\varphi$ transform under a gauge transformation in such a way that their combination remains invariant.

Alternatively, one can define the curvature perturbation on hypersurfaces of uniform energy density. In this case the spatial hypersurfaces are chosen such that the total energy density is homogeneous, i.e. $\delta\rho = 0$. The curvature perturbation on these hypersurfaces characterizes the intrinsic spatial curvature associated with the metric perturbation Ψ.

Since the energy density can be decomposed as $\rho(t, \mathbf{x}) = \bar{\rho}(t) + \delta\rho(t, \mathbf{x})$, the curvature perturbation on uniform energy density hypersurfaces is defined as

$$\zeta \equiv -\Psi - \frac{H}{\dot{\bar{\rho}}}\,\delta\rho, \tag{2.85}$$

where $\bar{\rho}(t)$ denotes the homogeneous background energy density and $\delta\rho(t, \mathbf{x})$ represents its perturbation. The second term accounts for the shift between constant-time hypersurfaces and hypersurfaces of uniform energy density.

The quantity ζ therefore represents the perturbation in the intrinsic spatial curvature evaluated on slices where the energy density is spatially uniform. This combination is gauge-invariant, since the gauge transformations of Ψ and $\delta\rho$ cancel each other.

For adiabatic perturbations and on superhorizon scales, the curvature perturbations defined on uniform-field and uniform-density hypersurfaces coincide, giving $\zeta \simeq -\mathcal{R}$.

Physical interpretation

The quantity $\mathcal{R}$ (or equivalently ζ) represents the spatial curvature perturbation on hypersurfaces where the scalar field or total energy density is uniform. It measures the intrinsic curvature of constant-time hypersurfaces and thus encodes information about the spatial geometry of the perturbed universe.

Importantly, on superhorizon scales ($k \ll aH$), $\mathcal{R}$ remains nearly constant in time for adiabatic perturbations, making it a powerful tool to connect the physics of the early universe to late-time observables. Its power spectrum, $P_{\mathcal{R}}(k)$, determines the statistical distribution of primordial fluctuations and provides the initial conditions for the formation of cosmic structure and for the anisotropies in the cosmic microwave background (CMB).

Defining the Power Spectrum:

In quantum field theory, the expectation value of a randomly fluctuating scalar field vanishes, $\langle\hat{\varphi}(\mathbf{x}, t)\rangle = 0$, while its variance is non-zero$\langle\hat{\varphi}(\mathbf{x}, t)\hat{\varphi}(\mathbf{x}, t)\rangle \neq 0$. Fluctuations are therefore characterized by correlation functions, the simplest of which is the two-point correlation function whose Fourier representation defines the power spectrum.

The Fourier transform of the scalar field $\varphi(\mathbf{x}, t)$ is defined as

$$\varphi(\mathbf{x}, t) = \int \frac{d^3\mathbf{k}}{(2\pi)^{3/2}}\, e^{i\mathbf{k}\cdot\mathbf{x}}\, \varphi_{\mathbf{k}}(t). \tag{2.86}$$

The ensemble average of the field variance becomes

$$\langle\varphi(\mathbf{x}, t)\varphi(\mathbf{x}, t)\rangle = \int \frac{d^3\mathbf{k}}{(2\pi)^{3/2}} \int \frac{d^3\mathbf{k}'}{(2\pi)^{3/2}} e^{i\mathbf{x}\cdot(\mathbf{k}-\mathbf{k}')}\langle\varphi_{\mathbf{k}}(t)\varphi^*_{\mathbf{k}'}(t)\rangle. \tag{2.87}$$

The power spectrum $P_\varphi(k)$ is defined through

$$\langle \varphi_{\mathbf{k}}(t)\varphi^*_{\mathbf{k}'}(t)\rangle = \frac{2\pi^2}{k^3} P_\varphi(k)\, \delta^{(3)}(\mathbf{k}-\mathbf{k}'). \tag{2.88}$$

Substituting Eq. (2.88) into Eq. (2.87), we obtain

$$\langle \varphi(\mathbf{x},t)\varphi(\mathbf{x},t)\rangle = \int \frac{dk}{k} P_\varphi(k), \tag{2.89}$$

showing that $P_\varphi(k)$ gives the contribution to the variance per logarithmic interval in k.

The spectral index is defined as

$$n_\varphi = \frac{d\,\ln P_\varphi(k)}{d\,\ln k}, \tag{2.90}$$

and if n_φ depends on k, it is referred to as a running spectral index.

Quantization of the Scalar Field To compute the power spectrum from quantum fluctuations of the inflaton field, but this is true for any scalar field, so we can define it as an operator and expanded in Fourier modes,

$$\hat{\varphi}(\mathbf{x},t) = \int \frac{d^3\mathbf{k}}{(2\pi)^{3/2}} \left[u_{\mathbf{k}}(t)a_{\mathbf{k}}e^{i\mathbf{k}\cdot\mathbf{x}} + u^*_{\mathbf{k}}(t)a^\dagger_{\mathbf{k}}e^{-i\mathbf{k}\cdot\mathbf{x}}\right], \tag{2.91}$$

where $u_{\mathbf{k}}(t)$ are the mode functions and $a_{\mathbf{k}}$, $a^\dagger_{\mathbf{k}}$ are annihilation and creation operators satisfying the commutation relations

$$[a_{\mathbf{k}}, a_{\mathbf{k}'}] = 0, \qquad [a^\dagger_{\mathbf{k}}, a^\dagger_{\mathbf{k}'}] = 0, \qquad [a_{\mathbf{k}}, a^\dagger_{\mathbf{k}'}] = \delta^{(3)}(\mathbf{k}-\mathbf{k}'). \tag{2.92}$$

Canonical quantization implies the normalization condition $u^*_{\mathbf{k}}\dot{u}_{\mathbf{k}} - u_{\mathbf{k}}\dot{u}^*_{\mathbf{k}} = i$. Using this expansion, the vacuum expectation value of the Fourier modes becomes

$$\langle 0|\hat{\varphi}_{\mathbf{k}}\hat{\varphi}^\dagger_{\mathbf{k}'}|0\rangle = |u_{\mathbf{k}}(t)|^2\, \delta^{(3)}(\mathbf{k}-\mathbf{k}'). \tag{2.93}$$

Comparing this expression with Eq. (2.88), we obtain

$$P_\varphi(k) = \frac{k^3}{2\pi^2}|u_{\mathbf{k}}(t)|^2. \tag{2.94}$$

Thus, once the mode function $u_{\mathbf{k}}(t)$ is determined from the equation of motion of the scalar field, the power spectrum of quantum fluctuations follows directly.

Connection to observations

In inflationary cosmology, $\mathcal{R}$ originates from the quantum fluctuations of the inflaton field stretched to cosmological scales. Its two-point correlation function defines the scalar power spectrum

$$\langle \mathcal{R}_{\mathbf{k}} \mathcal{R}_{\mathbf{k}'} \rangle = (2\pi)^3 \delta^{(3)}(\mathbf{k} + \mathbf{k}') \frac{2\pi^2}{k^3} P_{\mathcal{R}}(k), \tag{2.95}$$

which can be related to the temperature anisotropies in the CMB and to the large-scale matter distribution. Therefore, $\mathcal{R}$ serves as a direct bridge between the microscopic dynamics of the early universe and macroscopic cosmological observables.

2.7.1 Equation of motion for the curvature perturbation in slow-roll inflation

The dynamical variable that governs scalar (curvature) perturbations during single-field inflation is most conveniently written in terms of the Mukhanov–Sasaki variable $v(\eta, \mathbf{x})$, which is related to the comoving curvature perturbation $\mathcal{R}(\eta, \mathbf{x})$ by [18]

$$v \equiv z\,\mathcal{R}, \qquad z(\eta) \equiv a(\eta)\,\frac{\dot{\varphi}_0}{H} = a(\eta)\sqrt{2\epsilon_\varphi}\,M_{\rm P}, \tag{2.96}$$

where $a(\eta)$ is the scale factor, η is conformal time, an overdot denotes derivative with respect to cosmic time t, $H = \dot{a}/a$ is the Hubble rate, $M_{\rm P} = (8\pi \mathrm{G_N})^{-1/2}$ is the reduced Planck mass and $\epsilon_\varphi \equiv \frac{3}{2}\left(\frac{\dot{\varphi}_0^2}{V(\varphi)}\right)$ is the first Hubble slow-roll parameter. The relation $\dot{\varphi}_0^2 = 2\epsilon M_{\rm P}^2 H^2$ was used to express z in terms of ϵ_φ.

Starting from the action for scalar perturbations to second order, one obtains the Mukhanov action [18, 82]

$$S^{(2)} = \frac{1}{2}\int d\eta\, d^3x \left[(v')^2 - (\nabla v)^2 + \frac{z''}{z}\,v^2\right], \tag{2.97}$$

where a prime denotes derivative with respect to conformal time η. Variation of this action yields the Mukhanov–Sasaki equation for each Fourier mode $v_k(\eta)$:

$$v_k'' + \left(k^2 - \frac{z''}{z}\right) v_k = 0. \tag{2.98}$$

In a quasi–de Sitter (slow-roll) background, the effective potential z''/z can be written as

$$\frac{z''}{z} = \frac{\nu_\varphi^2 - \frac{1}{4}}{\eta^2}, \tag{2.99}$$

where ν_φ is close to $3/2$ (more precisely $\nu_\varphi = \frac{3}{2} + \epsilon_\varphi + \frac{\eta_\varphi}{2}$ and the corrections are slow-roll suppressed). With this approximation Eq. (2.98) becomes the Bessel (Hankel) equation whose general solution is

$$v_k(\eta) = \sqrt{-\eta}\left[A_k\, H^{(1)}_{\nu_\varphi}(-k\eta) + B_k\, H^{(2)}_{\nu_\varphi}(-k\eta)\right]. \tag{2.100}$$

Choosing the Bunch–Davies vacuum selects the positive-frequency solution in the short-wavelength limit, which fixes $B_k = 0$ and

$$v_k(\eta) = \frac{\sqrt{\pi}}{2}\sqrt{-\eta}\, H^{(1)}_{\nu_\varphi}(-k\eta). \tag{2.101}$$

The comoving curvature perturbation for each mode is then $\mathcal{R}_k(\eta) = v_k(\eta)/z(\eta)$. In the long-wavelength (superhorizon) limit $|k\eta| \ll 1$ the Hankel function exhibits a power-law behavior and $\mathcal{R}_k$ approaches a constant (i.e. it "freezes out"):

$$\mathcal{R}_k(\eta) \xrightarrow{|k\eta|\ll 1} \frac{v_k(\eta)}{z(\eta)} \propto \frac{(-k\eta)^{\frac{1}{2}-\nu_\varphi}}{z(\eta)} \quad \Rightarrow \quad \mathcal{R}_k(\eta) \simeq \text{const.} \tag{2.102}$$

Evaluating the power spectrum of $\mathcal{R}$ at horizon exit $k = aH$ (or equivalently $-k\eta \sim 1$) gives, to leading order in slow-roll,

$$P_{\mathcal{R}}(k) \equiv \frac{k^3}{2\pi^2}\,|\mathcal{R}_k|^2 \simeq \frac{1}{8\pi^2\epsilon}\frac{H^2}{M_{\rm P}^2}\left(\frac{k}{aH}\right)^{3-2\nu_\varphi}. \tag{2.103}$$

Hence, the amplitude of scalar perturbations is determined by the Hubble rate during inflation and the slow-roll parameter ϵ_φ. Here, H and ϵ_φ are evaluated at the time when the corresponding mode exits the horizon. In practice, observables are defined at a specific pivot scale, denoted by k_*.

To compare theoretical predictions with observational data, it is useful to introduce a phenomenological parameterization of the curvature power spectrum. We parameterize it as

$$P_{\mathcal{R}} = A_{\rm s}(k_*)\left(\frac{k}{k_*}\right)^{n_s - 1 + \frac{1}{2}\frac{dn_s}{d\ln k}\ln(k/k_*)+\ldots}. \tag{2.104}$$

By comparing Eq. (2.103) and Eq. (2.104), we can identify the amplitude of the curvature perturbations as $A_{\rm s} \simeq H_*^2/8\pi^2\epsilon_\varphi M_{\rm P}^2$, and the spectral index as $n_s - 1 = 2\epsilon_\varphi + \eta_\varphi$. Furthermore, the tensor-to-scalar ratio can be related to the slow-roll parameters as $r_{k_*} \simeq 16\epsilon_\varphi$.

From CMB observations [11], both the amplitude $A_{\rm s}$ and the scalar spectral index n_s are tightly constrained. In particular, the curvature power spectrum at the pivot scale satisfies $P_{\mathcal{R}}(k_*) \simeq 10^{-9}$ [11]. However, at smaller scales, there are currently no strong observational constraints on $P_{\mathcal{R}}(k)$.

As a result, primordial black hole (PBH) formation is expected to be significant only at small scales, where a substantial enhancement of the curvature power spectrum is required. Specifically, PBH formation typically demands a peak amplitude of the order $P_{\mathcal{R}}(k >> k_*) \sim \mathcal{O}(0.01)$.

2.8 Primordial Black Holes: Motivation and Formation Mechanisms

Primordial Black Holes (PBHs) are hypothetical compact objects that may have formed in the very early Universe from the gravitational collapse of large overdense regions shortly after these fluctuations re-entered the Hubble horizon following the end of inflation [120–123]. Unlike astrophysical black holes, PBHs do not require stellar evolution or baryonic processes for their formation; instead, they originate purely from gravitational collapse. This fundamental distinction makes PBHs a unique probe of early-Universe physics.

One of the primary motivations for studying PBHs is their intimate connection with primordial curvature perturbations generated during or immediately after inflation. Since PBH formation requires large-amplitude density fluctuations, their abundance and mass spectrum provide a powerful probe of the primordial power spectrum on small scales, which is otherwise inaccessible to conventional cosmological observations such as the cosmic microwave background (CMB) and large-scale structure surveys. Furthermore, PBHs are compelling candidates for cold dark matter. Over a wide range of masses, PBHs could constitute a significant fraction, or even the entirety, of the observed dark matter abundance while remaining consistent with current observational constraints [124]. This possibility offers an attractive alternative to particle dark matter scenarios and establishes a direct link between early-Universe cosmology and gravitational physics.

Beyond their role as dark matter candidates, PBHs can also influence the thermal history of the Universe. Ultra-light PBHs, which evaporate via Hawking radiation before the epoch of Big Bang Nucleosynthesis (BBN), may contribute to the reheating of the Universe [125]. Moreover, Hawking evaporation naturally violates all three Sakharov conditions, allowing PBHs to play a potential role in explaining the observed matter–antimatter asymmetry of the Universe [126, 127].

An important consequence of PBH formation is the generation of secondary gravitational waves. The large density perturbations required for PBH production correspond to enhanced curvature perturbations on small scales, which inevitably source second-order gravitational waves. These induced gravitational waves form a primordial background that carries information about small-scale dynamics of the early Universe, which cannot be easily probed through large-scale observations such as the CMB or structure formation [128–141].

Several mechanisms have been proposed for PBH formation in the early Universe. These include: (i) inflationary scenarios that generate enhanced curvature perturbations, such as ultra-slow-roll inflation or multi-field inflationary models [142–156]; (ii) the collapse of overdense regions formed during first-order phase transitions, for example through bubble collisions [157, 158]; (iii) the collapse of topological defects, such as cosmic string loops, leading to PBH formation [159–161]. In addition, primordial magnetic fields can induce curvature perturbations that may also result in PBH production [162–164].

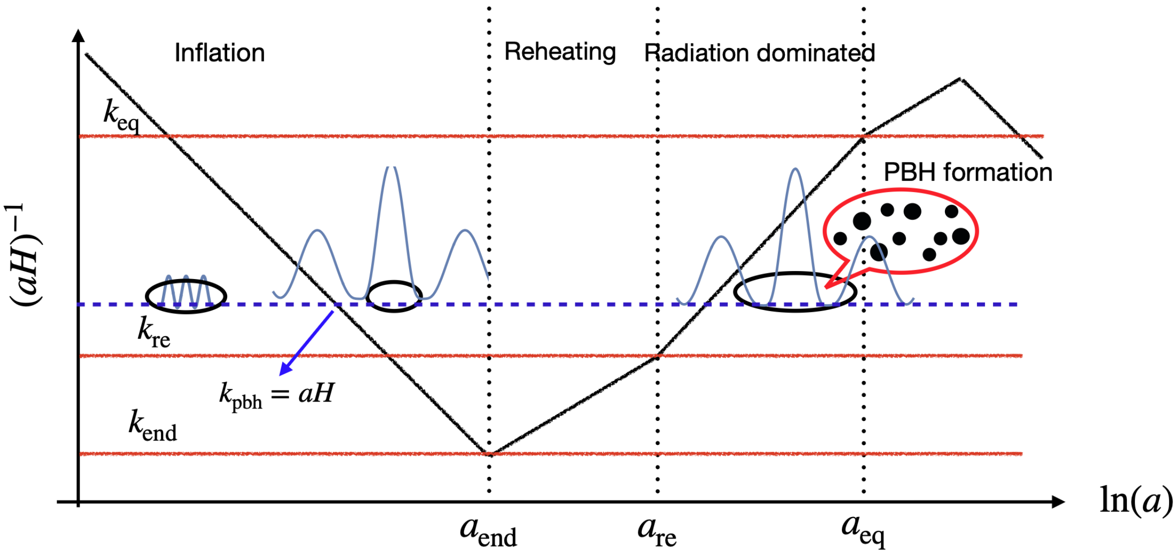

Figure 2.4: Evolution of the Hubble horizon as a function of the scale factor, $\ln(a)$, shown together with the evolution of the curvature perturbations. The horizontal lines indicate different comoving wavenumbers, while the blue dashed line marks the comoving wavenumber corresponding to the enhanced curvature perturbations responsible for primordial black hole (PBH) formation.

In summary, the study of primordial black holes is motivated by their ability to probe small-scale primordial perturbations, test inflationary models, constrain early-Universe dynamics, and provide viable explanations for dark matter and primordial gravitational-wave signals. With continued progress in both theoretical modeling and observational sensitivity, PBHs remain a key target for understanding the physics of the early Universe and its observational imprints.

In this section, we focus primarily on PBH formation mechanisms arising from enhanced curvature perturbations generated during inflation. To keep the analysis as model-independent as possible, we assume a log-normal form for the curvature power spectrum and consider Gaussian statistics for the curvature perturbations [165]. However, in more realistic scenarios, non-Gaussian effects can significantly influence the PBH formation process and the resulting abundance, particularly the initial fractional energy density of PBHs [166–169].

2.8.1 Curvature perturbations generated during inflation

Inflation is a phase of accelerated expansion that resolves the horizon and flatness problems. Quantum fluctuations generated during this epoch are stretched beyond the Hubble horizon and later become classical, providing the primordial seeds of large-scale structure. In addition to scalar (curvature) perturbations, inflation also produces tensor modes, whose CMB imprints probe the inflationary energy scale.

CMB observations tightly constrain the curvature power spectrum at the pivot scale k_*, yielding $A_s \simeq 2.1 \times 10^{-9}$ [12]. However, much weaker constraints exist at smaller scales

($k \gg k_*$), allowing for the possibility of significant small-scale enhancement, particularly in non-standard inflationary scenarios.

Primordial black holes (PBHs) can form from the gravitational collapse of sufficiently large overdensities in the early Universe. Since density perturbations are sourced by curvature perturbations, an enhanced small-scale curvature power spectrum can trigger PBH formation. During inflation, the comoving Hubble radius shrinks ($w < -1/3$), causing perturbation modes to exit the horizon. After inflation, during radiation or matter domination ($0 \leq w_{\text{eff}} \leq 1$), the comoving Hubble radius grows, and previously generated super-horizon modes re-enter the horizon.

Upon horizon re-entry, these modes induce density perturbations. If the overdensity is large enough that gravity overcomes pressure forces, gravitational collapse can occur, forming a PBH. Denoting the characteristic PBH scale by $k_{\text{pbh}} \gg k_{\text{cmb}}$, PBH formation requires a significant enhancement,

$$P_{\mathcal{R}}(k_{\text{pbh}}) \gg P_{\mathcal{R}}(k_{\text{cmb}}) \sim 10^{-9}, \tag{2.105}$$

with density perturbations approximately related by

$$P_{\mathcal{R}}(k_{\text{pbh}}) \sim \left(\frac{\delta\rho}{\rho}\right)^2. \tag{2.106}$$

Modes relevant for PBH formation typically re-enter the horizon during the radiation-dominated era. If their amplitude exceeds a critical threshold, gravitational collapse can occur. Numerical simulations indicate that in a radiation-dominated Universe, roughly $\mathcal{O}(0.1)$ of the horizon mass may collapse into a PBH [122, 123].

Threshold for collapse: The formation of a primordial black hole requires that the density contrast in an overdense region exceeds a critical threshold value, $\delta > \delta_c$, such that gravitational attraction can overcome the pressure support of the surrounding fluid. The criterion for PBH formation was first discussed by Carr [123], who showed that collapse occurs when the density contrast becomes larger than the effective pressure support characterized by the sound speed squared, c_s^2. Physically, the sound speed determines how efficiently pressure waves can propagate from the center to the boundary of an overdense region and counteract gravitational collapse.

According to the original argument by Carr (1975) [123], the critical density contrast is given by $\delta_c \simeq w$, where $w = p/\rho$ denotes the equation of state (EoS) of the background fluid. Modern numerical simulations, however, find $\delta_c \simeq 0.43$–0.47, with the exact value depending on the density profile and collapse dynamics [170–173].

Primordial black holes (PBHs) are expected to form after inflation when enhanced curvature perturbations re-enter the horizon. The post-inflationary evolution is uncertain, as the inflaton field dominates the energy density, allowing for an effective EoS that may deviate from radiation domination and even correspond to a stiff-like fluid, $w_{\rm re} > 1/3$.

Since δ_c depends on the EoS, it can be expressed as a function of $w_{\rm re}$ [174–176]

$$\delta_c \simeq \frac{3(1+w_{\rm re})}{5+3w_{\rm re}} \sin^2\left(\frac{\pi\sqrt{w_{\rm re}}}{1+3w_{\rm re}}\right), \tag{2.107}$$

which agrees well with numerical results, although it is not valid in the matter-like limit.

In a radiation-dominated era ($w = 1/3$), analytic estimates give $\delta_c \sim 0.4$, consistent with simulations [170–175]. More generally, numerical studies find $\delta_c \simeq 0.4$–$2/3$, demonstrating its sensitivity to the shape of the density profile [174–176].

PBH formation is characterized using the compaction function $\mathcal{C}(r)$, defined as [177–181]

$$\mathcal{C}(r) = \frac{2\,\delta M(r)}{R(r)}, \tag{2.108}$$

where $\delta M(r)$ is the mass excess and $R(r)$ is the areal radius. Collapse occurs when the peak value satisfies $\mathcal{C}_{\rm max} > \delta_c$.

Importantly, δ_c depends not only on the amplitude but also on the shape of the density profile. Broader overdensities lead to slower collapse due to distributed gravitational forces, requiring a larger threshold compared to sharper peaks [171].

Finally, the threshold δ_c also depends on the origin of perturbations [170–175]. In particular, curvature perturbations sourced by primordial magnetic fields generate anisotropic stresses that oppose collapse, leading to a higher δ_c even in a radiation-dominated background [163].

The mass of PBHs: In general, PBHs form through the gravitational collapse of primordial density fluctuations shortly after the corresponding modes re-enter the horizon. Since the physical size of an overdense region at horizon re-entry is comparable to the Hubble radius, the mass enclosed within the horizon can participate in the collapse and lead to PBH formation. This implies that the PBH mass is closely related to the horizon mass at the time of formation.

The fraction of the total horizon mass that collapses to form a PBH depends on the detailed collapse dynamics. However, several numerical simulations have shown that only a few percent of the horizon mass typically contributes to PBH formation. Therefore, we first compute the total mass enclosed within the horizon at the time of horizon crossing, $t \simeq t_{\rm h}$,

$$M_{\rm H}(t_{\rm h}) = \frac{4\pi}{3}\rho(t_{\rm h})H^{-3}\,. \tag{2.109}$$

Here, $\rho(t_{\rm h}) = 3M_{\rm P}^2 H^2(t_{\rm h})$ denotes the total background energy density at the time of horizon crossing. Substituting this expression into Eq. (2.109), the horizon mass can be written as $M_{\rm H} = 4\pi M_{\rm P}^2 H^{-1}$.

Typically, the PBH mass is related to the horizon mass through $M_{\rm pbh} = \gamma_c M_{\rm H}$, where $\gamma_c \sim 0.2$ is the collapse efficiency factor [124, 174]. Accordingly, for a given comoving wavenumber k, the PBH mass at horizon crossing can be expressed as $M_{\rm pbh}(t_{\rm h}) \simeq 4\pi\gamma_c M_{\rm P}^2 H^{-1}$. Since a comoving mode re-enters the horizon when $k = aH$, this relation can be rewritten as

$$M_{\rm pbh}(t_{\rm h}) = 4\pi\gamma_c M_{\rm P}^2 H^{-1} = 4\pi\gamma_c M_{\rm P}^2 \frac{a}{k}\,. \tag{2.110}$$

To estimate the PBH mass explicitly, we must determine the value of the scale factor at the time of PBH formation. For this purpose, we invoke entropy conservation. For completeness, let us consider a non-instantaneous reheating scenario characterized by an average equation of state $w_{\rm re} = p/\rho$. In this case, the evolution of the Hubble parameter and the scale factor is given by

$$\frac{a}{a_{\rm re}} = \left(\frac{H}{H_{\rm re}}\right)^{-2/3(1+w_{\rm re})}, \tag{2.111}$$

where $H_{\rm re}$ and $a_{\rm re}$ denote the Hubble parameter and the scale factor at the end of reheating, respectively.

In most scenarios, it is assumed that following inflation, the Universe enters a standard radiation-dominated era during which PBHs are formed. However, the duration of the reheating phase is uncertain. Here, we consider the possibility that PBHs are formed during the reheating era, where the background energy density evolves as $\rho(a) \propto a^{-3(1+w_{\rm re})}$. As discussed previously, the PBH mass is related to the horizon size and is typically inversely proportional to the Hubble parameter, i.e., $M_{\rm pbh} \propto H^{-1}$. In a non-instantaneous reheating scenario, the PBH mass depends not only on the position of the overdensity peak but also on the reheating parameters, $w_{\rm re}$ (average EoS during reheating phase) and $T_{\rm re}$ [182].

Assuming a single-stage reheating phase followed by a standard radiation-dominated era, with total entropy conserved after reheating, the Hubble parameter during reheating can be related as follows (for detailed calculations, see Appendix A.3)

$$H^{-1} = \frac{1}{M_{\rm P}}\left(\frac{\pi^2 g_{*,\rm eq}}{90}\right)^{\frac{1}{1+3w_{\rm re}}}\left(\frac{T_0}{k}\right)^{\frac{3(1+w_{\rm re})}{1+3w_{\rm re}}}\left(\frac{g_{*,\rm eq}}{g_{*,\rm re}}\right)^{\frac{w_{\rm re}}{1+3w_{\rm re}}}\left(\frac{T_{\rm re}}{M_{\rm P}}\right)^{\frac{1-3w_{\rm re}}{1+3w_{\rm re}}} \tag{2.112}$$

Substituting Eqs. (2.112) and (2.110) into the definition of the PBH mass, we obtain

$$M_{\rm pbh} \simeq 5.486\times10^{-39} M_\odot \left(\frac{\gamma_c}{0.2}\right)\left(\frac{\pi^2 g_{*,\rm re}}{90}\right)^{\frac{1}{1+3w_{\rm re}}}\left(\frac{T_0}{k}\right)^{\frac{3(1+w_{\rm re})}{1+3w_{\rm re}}}\left(\frac{g_{*,\rm eq}}{g_{*,\rm re}}\right)^{\frac{w_{\rm re}}{1+3w_{\rm re}}}\left(\frac{T_{\rm re}}{M_{\rm P}}\right)^{\frac{1-3w_{\rm re}}{1+3w_{\rm re}}}. \tag{2.113}$$

In our calculations, we adopt the reduced Planck mass, $M_{\rm P} = 1/\sqrt{8\pi G_{\rm N}} \simeq 4.31\times10^{-9}$, kg $\simeq 2.183\times10^{-39}, M_\odot$, where $1, M_\odot \simeq 1.9985\times10^{30}$, kg denotes the solar mass. If we further assume that the post-inflationary Universe is immediately dominated by radiation, the above expression simplifies to [154, 164, 183, 184]

$$M_{\rm pbh} \simeq 1.57 \times 10^{12}\, M_\odot \left(\frac{\gamma_c}{0.2}\right)\left(\frac{106.75}{g_{*,\rm re}(T)}\right)^{1/6}\left(\frac{g_{*,\rm eq}(T_0)}{3.81}\right)^{2/3}\left(\frac{1{\rm Mpc}^{-1}}{k}\right)^2. \tag{2.114}$$

From this expression, it is clear that PBHs formed at earlier times correspond to smaller masses, reflecting the smaller horizon size at earlier epochs. Conversely, PBHs formed at later times are expected to be more massive, since the horizon size increases with cosmic time during the post-inflationary evolution.

For example, let us consider a scenario in which the peak of the overdense region is located at $k \simeq 10^{15}\,{\rm Mpc}^{-1}$. If the Universe enters a radiation-dominated era immediately after inflation and PBHs form during this radiation-dominated phase, the corresponding PBH mass is $M_{\rm pbh} \simeq 1.57\times10^{-18} M_\odot$. However, if the post-inflationary evolution proceeds through a matter-like phase ($w_{\rm re} = 0$) during reheating, the PBH mass becomes dependent on the reheating temperature $T_{\rm re}$. For instance, if reheating ends at $T_{\rm re} = 10^6$ GeV, then for the same peak position the corresponding PBH mass is $M_{\rm pbh} \simeq 1.36 \times 10^{-18}\, M_\odot$. On the other hand, if reheating ends at $T_{\rm re} = 10^2$ GeV, the corresponding PBH mass decreases to $M_{\rm pbh} \simeq 1.36 \times 10^{-22}\, M_\odot$.

PBH abundance: Depending on the amplitude and scale of the primordial curvature perturbations, PBHs can form over a wide range of masses. Although PBHs are classical objects from which nothing can escape, quantum effects modify this picture. It was first shown by Hawking that black holes emit thermal radiation due to quantum field effects in curved spacetime [185]. This phenomenon is known as Hawking radiation and arises from particle creation near the event horizon. An observer located far from the black hole perceives it as blackbody radiation with temperature $T_{\rm BH} = \frac{\hbar c^2}{8\pi {\rm G_N} k_{\rm B} {\rm M}}$ [122, 185, 186], where $k_{\rm B}$ is the Boltzmann constant $\rm G_N$ is the Gravitational constant and M is the mass of the black-hole.

Due to this particle emission, black holes are not completely black but continuously lose mass over time. For a Schwarzschild black hole, the mass loss equation

$$\frac{\rm dM}{\rm dt} = -\frac{\hbar c^4}{15360\pi {\rm G_N^2}}\frac{1}{\rm M^2} = -\frac{\alpha_{BH}}{\rm M^2}, \tag{2.115}$$

where $\alpha_{\rm BH} = \hbar c^4/15360\pi{\rm G_N^2}$.

Solving Eq. (2.115), we obtain

$$\tau = t - t_{\rm f} = \frac{{\rm M_0^3} - {\rm M}^3(t)}{3\alpha_{\rm BH}}. \tag{2.116}$$

Here, $t_{\rm f}$ denotes the time at which the PBH is formed. The lifetime of a PBH is defined as the time required for complete evaporation after its formation. Taking the limit $M \to 0$, we obtain [187, 188]

$$\tau_{\rm ev} \simeq \frac{5120\pi G_{\rm N}^2}{\hbar c^4} {\rm M}_0^3 \simeq 407 \times \left(\frac{M_{\rm pbh}}{10^{10}\,{\rm gm}}\right) {\rm sec}\,. \tag{2.117}$$

A PBH with mass 5×10^{14} gm has a lifetime comparable to the age of the Universe, whereas a PBH with mass $M_{\rm pbh} = 10^9$ gm evaporates well before the onset of BBN. This implies that low-mass PBHs ($M_{\rm pbh} \leq 10^{15}$ gm), which would have evaporated by the present epoch, cannot serve as viable dark matter candidates.

PBHs with masses $M_{\rm pbh} \gtrsim 10^{15}$ gm can therefore be treated as cold dark matter. For this reason, it is common practice to quantify the PBH abundance by relating it to the present-day dark matter density. This is achieved by introducing the parameter [189]

$$f_{\rm PBH} \equiv \frac{\Omega_{\rm pbh}}{\Omega_{\rm c}}\,, \tag{2.118}$$

where $\Omega_i \equiv \rho_{i,0}/\rho_{c,0}$ denotes the present-day fractional energy density of the species i. Here, $\rho_{c,0} \simeq 3H_0^2 M_{\rm P}^2$ is the present-day critical energy density. According to recent observations, the present-day dark matter abundance is $\Omega_{\rm c}h^2 \simeq 0.120 \pm 0.001$ [71], with $h \simeq 0.6736 \pm 0.0054$ parameterizing the Hubble rate H_0 in units of $100\,{\rm km\,s^{-1}\,Mpc^{-1}}$ [70].

PBHs behave as non-relativistic matter, and hence their energy density scales as a^{-3} after formation. In contrast, the background energy density dilutes differently during different cosmological epochs. Let us assume that PBHs form during the reheating phase, when the background energy density evolves as $\rho \propto a^{-3(1+w_{\rm re})}$, and that reheating ends at a scale factor $a_{\rm re}$. In this case, the present-day PBH abundance $f_{\rm PBH}$ can be related to the initial fractional energy density at formation, $\beta_{\rm pbh} = \rho_{\rm pbh}/\rho|_{t=t_{\rm f}}$, where $t_{\rm f}$ is the time when the PBH was formed. One can then write [182]

$$f_{\rm PBH} = \beta_{\rm pbh}(M_{\rm pbh})\frac{\Omega_m h^2}{\Omega_{\rm c}h^2}\left(\frac{g_{*,\rm eq}}{g_{*,\rm re}}\right)\left(\frac{g_{*,\rm re}}{g_{*,\rm eq}}\right)^{\frac{1}{1+w_{\rm re}}}\left(\frac{T_{\rm re}}{T_{\rm eq}}\right)^{\frac{1-3w_{\rm re}}{1+w_{\rm re}}}\left(\frac{M_{\rm pbh}}{\gamma_c M_{\rm eq}}\right)^{-\frac{2w_{\rm re}}{1+w_{\rm re}}}\,, \tag{2.119}$$

where $\Omega_m h^2 \simeq 0.1424$ [69] represents the present-day total matter density of the Universe.

If we further assume a standard reheating scenario after inflation, corresponding to $w_{\rm re} = 1/3$, we recover the well-known functional form of $f_{\rm PBH}$ [146, 147, 154],

$$f_{\rm PBH} = \beta_{\rm pbh}\frac{\Omega_m h^2}{\Omega_{\rm c}h^2}\left(\frac{g_{*,\rm eq}}{g_{*,\rm re}}\right)^{1/4}\left(\frac{M_{\rm pbh}}{\gamma_{\rm c} M_{\rm eq}}\right)^{-1/2}\,. \tag{2.120}$$

From the above expression, it is clear that even if PBHs constitute the entirety of dark matter today, i.e., $f_{\rm PBH} \simeq 1$, the corresponding fractional energy density at the time of formation must be extremely small. This enhancement of the PBH fraction arises due to the relative dilution of the background energy density compared to the PBH energy density as the Universe expands.

Fractional energy density of PBHs at formation: The initial fractional energy density of PBHs at the time of formation is defined as $\beta_{\rm pbh} = \rho_{\rm pbh}(t_{\rm f})/\rho(t_{\rm f})$, where $\rho_{\rm pbh}(t_{\rm f})$ denotes the total energy density of PBHs at the formation time $t_{\rm f}$. This quantity depends on the total number density of PBHs, which in turn is determined by how the primordial density fluctuations are distributed over space.

Let us assume that the density contrast δ follows a probability distribution function $P(\delta)$, which can in principle be either Gaussian or non-Gaussian in nature. If PBH formation occurs only when the density contrast exceeds a critical threshold, $\delta > \delta_c$, the initial fractional energy density of PBHs at formation can be written as [142–149, 167, 183, 189–197]

$$\beta_{\rm pbh} = \int_{\delta_c}^{\infty} P(\delta)\,{\rm d}\delta\,. \tag{2.121}$$

The initial PBH fraction is extremely sensitive to the nature of the underlying distribution of δ. In particular, for non-Gaussian distributions, the resulting fractional energy density can be significantly larger compared to the case of a simple Gaussian distribution [166–169]. For general studies, we consider two different types of distribution functions,

$$P(\delta) = \begin{cases} \frac{1}{\sqrt{2\pi}\sigma}\, e^{-(\delta-\mu)^2/2\sigma^2} & \text{Gaussian} \\ {\rm C_N}\ \exp\left[-\frac{3}{2}\sqrt{1+\frac{x^2}{b^2}}\right] & \text{Non-gaussian} \end{cases} \tag{2.122}$$

where ${\rm C_N} = 2.13\sigma^{-1}$ and $b = 0.84\sigma$ [163, 164], and μ denotes the mean of the distribution. For computational convenience, we set $\mu = 0$ when considering a Gaussian distribution. Here, σ represents the variance of the smoothed density contrast at the mass scale $M_{\rm pbh}$, evaluated at the time when the corresponding scale re-enters the horizon.

For the Gaussian type distribution, we can compute the initial fractional energy density of the $\beta_{\rm pbh}$ as a function of the critical density contrast δ_c and the variance of the distribution σ as [142]

$$\beta_{\rm pbh} = \int_{\delta_c}^{\infty} \frac{1}{\sqrt{2\pi}\sigma} e^{-\frac{\delta^2}{2\sigma^2}}{\rm d}\delta \simeq \frac{1}{2}{\rm Erfc}\left[\frac{\delta_c}{\sqrt{2}\sigma}\right] \tag{2.123}$$

That means, the initial fractional energy density is very sensitive to the variance of the distribution, which is mainly dependent on the nature of the curvature power spectrum as well as the value of the critical threshold. When we consider a fully non-Gaussian type distribution, then to compute the fractional energy density, we have to solve the above integral numerically.

In Fig. 2.5, we show the behavior of the two distribution functions defined in Eq. (2.121), for a fixed value of the variance $\sigma = 0.1$, as a function of the density contrast δ. In the right panel of Fig. 2.5, we illustrate how the initial fractional energy density of PBHs varies over a wide range of the variance σ, for a fixed critical density contrast $\delta_c = 0.4$. It is evident that when a non-Gaussian distribution is considered, the resulting PBH spectrum becomes significantly broader, as PBHs can be efficiently produced even for smaller values of the variance.

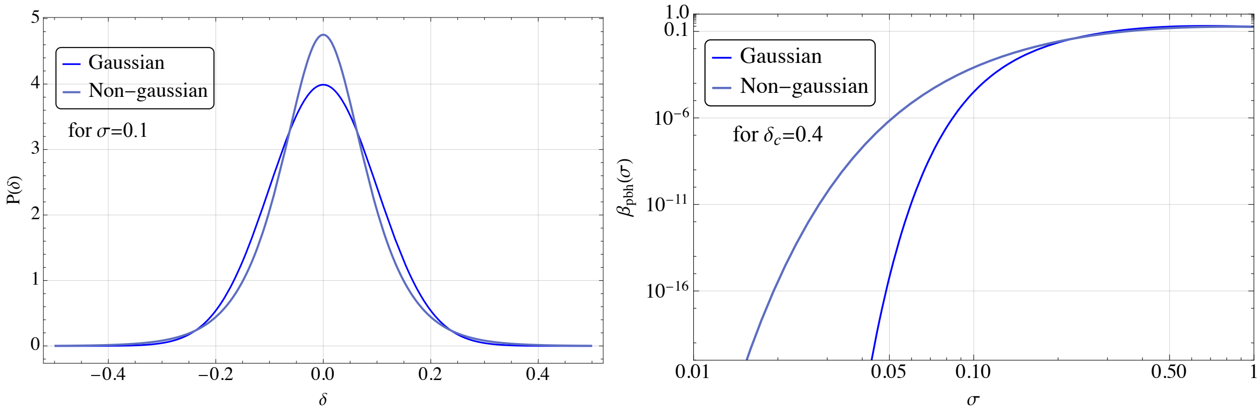

Figure 2.5: In the left panel, we have plotted the behaviour of the Gaussian and non-Gaussian distribution function for a fixed value of variance $\sigma = 0.1$ as a function of density contrast δ. In the right panel, we have plotted the $\beta_{\rm pbh}$ as a function of variance for a fixed value of $\delta_c \simeq 0.4$ for these two specific Gaussian and non-Gaussian distribution functions.

This clearly demonstrates that the initial fractional energy density of PBHs is highly sensitive to the choice of the distribution function. In the following subsection, we present a concrete example to explicitly illustrate how PBH formation depends on both the critical threshold δ_c and the assumed distribution function for a specific class of inflationary curvature perturbations.

PBH from primordial fluctuations

Now we are going to discuss how the inflationary curvature perturbation and its properties are related to the initial fractional abundance of the PBH. The comvoing curvature perturbations are excited when they leave the horizon during inflation, and it is quantified as the comoving curvature perturbation $\mathcal{R}$. Generally, these comoving curvature perturbations $\mathcal{R}$ are conserved on super-horizon for an adiabatic evolution during the post-inflationary evolution. When these enhanced super-horizon modes are re-entered into the horizon, they source the density fluctuations δ. Working in Fourier space, Taylor expanding at leading order in a gradient expansion of at linear order in $\mathcal{R}$, we can write the density contrast as [198]

$$\delta(\mathbf{x},t) \simeq \frac{2(1+w)}{5+3w}\frac{\nabla^2\mathcal{R}(\mathbf{x})}{(aH)^2} + \mathcal{O}(\mathcal{R}^2) \to \delta_{\mathbf{k}} \simeq -\frac{2(1+w)}{5+3w}\left(\frac{k}{aH}\right)^2\mathcal{R}_{\mathbf{k}} \tag{2.124}$$

If we consider that after inflation we have a simple radiation-dominated universe, then we can replace the value of $w = 1/3$ and get the density contrast as [142–149, 170, 198]

$$\delta_{\mathbf{k}} \simeq -\frac{4}{9}\left(\frac{k}{aH}\right)^2\mathcal{R}_{\mathbf{k}}. \tag{2.125}$$

The power spectrum associated with the density contrast δ in Fourier space as [142–149]

$$P_\delta(k) = \frac{16}{81}\left(\frac{k}{aH}\right)^4 P_{\mathcal{R}}(k) \tag{2.126}$$

where $P_{\mathcal{R}}(k)$ is the primordial curvature perturbation originated during inflation.

The initial fraction $\beta_{\rm pbh}$ depends on the form of the distribution function $P(\delta)$, which is primarily determined by the variance of the density contrast. To compute this variance, we introduce a window function $\mathcal{W}$ to smooth the density contrast $\delta(\mathbf{x}, t)$ over a scale $\mathrm{R_l} \simeq k^{-1} \simeq (aH)^{-1}$, corresponding to the scale at which PBHs predominantly form, i.e. $k \simeq k_{\rm pbh}$. The main purpose of introducing the window function is to eliminate unnecessary contributions from scales that do not participate in the collapse process. In other words, when computing the collapse mechanism, we are interested only in those physical scales that are directly involved in PBH formation.

Accordingly, the variance of the density contrast associated with the primordial power spectrum is given by [170, 189]

$$\sigma_{\mathrm{R_l}} \equiv \langle\delta^2\rangle_{\mathrm{R_l}} = \int_0^\infty \mathrm{d}\ln q\, \mathcal{W}^2(q, \mathrm{R_l})\, P_\delta(q) = \frac{16}{81}\int_0^\infty \mathrm{d}\ln q\, \mathcal{W}^2(q, \mathrm{R_l}) P_{\mathcal{R}}(q) \tag{2.127}$$

where $\mathcal{W}$ is the Fourier transform of a real-space window function. In most studies, either a volume-normalized Gaussian window function or a top-hat window function is employed, which can be written, as [199]

$$\mathcal{W}(k, \mathrm{R_l}) = \exp\left(-\frac{k^2\mathrm{R_l^2}}{2}\right); \qquad \mathcal{W}(k, \mathrm{R_l}) = \frac{3\sin(k\mathrm{R_l}) - 3k\mathrm{R_l}\cos(k\mathrm{R_l})}{(k\mathrm{R_l})^3}. \tag{2.128}$$

In the remainder of this work, we consistently adopt the Gaussian-type window function.

For computational purposes, we consider a general form of the enhanced inflationary curvature power spectrum, parameterized as [165]

$$P_{\mathcal{R}}(k) = A_{\rm s}\left(\frac{k}{k_*}\right)^{n_s-1} + A_0 \exp\left[-\frac{(k-k_{\rm p})^2}{\Delta_c\, k_{\rm p}^2}\right]. \tag{2.129}$$

The first part of the above spectrum satisfies the current CMB observational constraints [11], with the scalar spectral index n_s. Typically, such a spectrum arises from a simple slow-roll inflationary model, as discussed earlier in Sec. 2.7.1. In contrast, the second part corresponds to the enhanced curvature power spectrum, which originates from an ultra-slow-roll type inflationary model. Since our goal is not to study the detailed features of the ultra-slow-roll inflationary dynamics, we instead consider a general form of the enhanced curvature power spectrum, where A_0 denotes the amplitude of the peak and $k_{\rm p}$ specifies the position of the peak. The parameter Δ_c controls the shape of the enhanced curvature power spectrum.

In Fig.2.6, we plot the comoving curvature power spectrum $P_{\mathcal{R}}(k)$ as a function of the

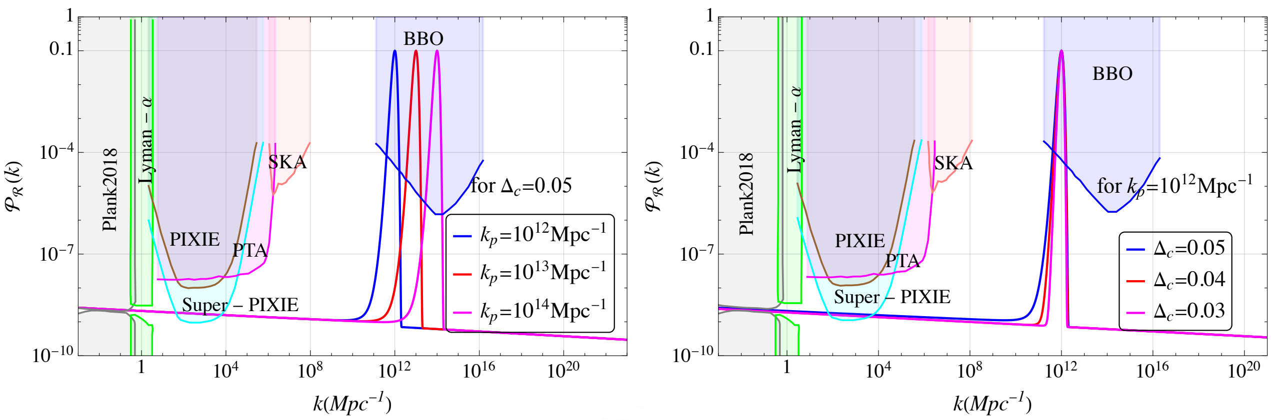

Figure 2.6: In the left panel, we plot the comoving curvature power spectrum $P_{\mathcal{R}}$ as a function of the comoving wavenumber k for a fixed value of $\Delta_c = 0.05$, where three different colors correspond to three different values of the peak wavenumber, $k_{\mathrm{p}} = 10^{12}, , 10^{13}$, and $10^{14}\mathrm{Mpc}^{-1}$. In the right panel, the comoving curvature power spectrum $P_{\mathcal{R}}$ is shown as a function of the comoving wavenumber for three different values of $\Delta_c = 0.05, 0.04$, and 0.03, while keeping the peak wavenumber fixed at $k_{\mathrm{p}} = 10^{12}\mathrm{Mpc}^{-1}$. In both panels, the peak amplitude is taken to be $A_0 = 0.1$, and the scalar spectral index is fixed at $n_s = 0.965$. The shaded regions indicate the current and future observational bounds on the curvature perturbation, which may be exceeded by different experiments operating in different frequency windows.

comoving wavenumber k, expressed in units of Mpc^{-1}. In the left panel of Fig.2.6, we consider three different peak positions, $k_{\mathrm{p}} = 10^{12}, , 10^{13}$, and 10^{14} Mpc^{-1}, for a fixed value of $\Delta_c = 0.05$. In the right panel, we illustrate the dependence of the curvature perturbation on Δ_c by choosing three different values, $\Delta_c = 0.05, , 0.04$, and 0.03, while fixing the peak position at $k_{\mathrm{p}} = 10^{12}, \mathrm{Mpc}^{-1}$. In both panels, we take $A_0 = 0.1$ as the amplitude of the peak frequency and normalize the scalar spectral index to $n_s = 0.965$ with $A_{\mathrm{s}} \simeq 2.1 \times 10^{-9}$, consistent with CMB-scale observations.

As can be seen, at CMB scales the dominant contribution arises from the first term of Eq. (2.129), while the contribution from the second term depends on the value of k_{p}. Using this general form of the curvature power spectrum, we now proceed to compute the initial fractional energy density of PBHs and their contribution to dark matter for both Gaussian and non-Gaussian type distributions.

Now our goal is to compute the fractional energy density of PBHs at the time of their formation due to the specific type of curvature perturbation defined in Eq. (2.129). As discussed earlier, for a Gaussian-type distribution, the initial PBH fraction, i.e., β_{pbh}, mainly depends on two quantities: the variance associated with the enhanced curvature power spectrum, and the threshold density contrast δ_c, above which PBH formation takes place.

Thus, for a generic enhanced curvature power spectrum, the variance σ can be defined as in Eq. (2.127). For a Gaussian-type window function, the variance can be written as

$$\sigma^2(M_{\mathrm{pbh}}) = \frac{16}{81}\int_0^\infty \frac{\mathrm{dq}}{q}(q\mathrm{R_l})^4 e^{-q^2\mathrm{R_l^2}} P_{\mathcal{R}}(q), \tag{2.130}$$

where $\mathrm{R_l}$ is the smoothing scale mainly responsible for PBH formation, and $M_{\rm pbh}$ denotes the PBH mass.

Since no other scale is present, it is reasonable to set $k = \mathrm{R_l}^{-1}$ and use the relation $k = aH$, where the perturbation with wavenumber k re-enters the Hubble radius. This allows us to obtain a relation between $\mathrm{R_l}$ and $M_{\rm pbh}$. It can be shown [147,200] that $\mathrm{R_l}$ and $M_{\rm pbh}$ are related as

$$\mathrm{R_l} = \frac{1}{k} = \left(\frac{2}{\gamma_c}\right)^{1/2} \left(\frac{g_{*,\rm re}}{g_{*,\rm eq}}\right)^{1/12} \left(\frac{1}{k_{\rm eq}}\right) \left(\frac{M_{\rm pbh}}{M_{\rm eq}}\right)^{1/2} . \tag{2.131}$$

Here, $k_{\rm eq}$ denotes the wavenumber that re-enters the Hubble radius at the time of matter–radiation equality, and $M_{\rm eq}$ represents the mass within the Hubble radius at equality. The quantities $g_{*,\rm re}$ and $g_{*,\rm eq}$ denote the effective number of relativistic degrees of freedom at the times of PBH formation and matter–radiation equality, respectively. One finds that $M_{\rm eq} = 5.83 \times 10^{50}$ gm. Using this result, the above relation between $\mathrm{R_l}$ and $M_{\rm pbh}$ can be expressed in terms of the solar mass $M_\odot$ as [147,200]

$$\left(\frac{\mathrm{R_l}}{\mathrm{Mpc}}\right) = \left(\frac{\mathrm{Mpc}^{-1}}{k}\right) = 4.72 \times 10^{-7} \left(\frac{\gamma_c}{0.2}\right)^{-1/2} \left(\frac{g_{*,\rm re}}{g_{*,\rm eq}}\right)^{1/12} \left(\frac{M_{\rm pbh}}{M_\odot}\right)^{1/2} . \tag{2.132}$$

Once the inflationary power spectrum is known, Eq.(2.132) can be substituted into Eq.(2.130) to compute the variance $\sigma^2(M_{\rm pbh})$. Using this result, the initial fractional energy density of PBHs with mass $M_{\rm pbh}$ can then be obtained. To compute the initial fractional energy density of PBHs arising from the inflationary curvature power spectrum defined in Eq. (2.129), we first evaluate the variance of the distribution associated with the curvature power spectrum using Eq. (2.130). For a Gaussian-type distribution, the initial PBH fraction $\beta_{\rm pbh}$ can then be obtained directly from Eq. (2.123). In contrast, for a non-Gaussian-type distribution, the corresponding integral defined in Eq. (2.121) is evaluated numerically.

We choose the position of the peak such that the resulting PBH mass satisfies $M_{\rm pbh} > 10^{15}$ gm, ensuring that the PBHs can survive until the present epoch and thus be treated as cold dark matter candidates. After computing the initial fractional energy density, the present-day PBH fraction as a dark-matter candidate, denoted by $f_{\rm PBH}$, is obtained using Eq. (2.120).

In Fig. 2.7, we plot the present-day PBH abundance as a dark-matter candidate, i.e., $f_{\rm PBH}$, as a function of the PBH mass $M_{\rm pbh}$ expressed in units of solar mass. In the left panel, we consider three different values of the peak wavenumber, $k_{\rm p} = 10^{12}$, 10^{13}, and 10^{14} Mpc^{-1}, while fixing the parameter $\Delta_c = 0.05$, which controls the width of the enhanced spectrum. The solid lines correspond to the Gaussian-type distribution, whereas the dashed lines represent the non-Gaussian-type distribution for the same set of parameters.

As shown in Eq. (2.132), the PBH mass is directly related to the position of the peak wavenumber. Consequently, changing the value of $k_{\rm p}$ shifts the PBH mass window accordingly. In particular, decreasing the value of $k_{\rm p}$ leads to the formation of more massive PBHs.

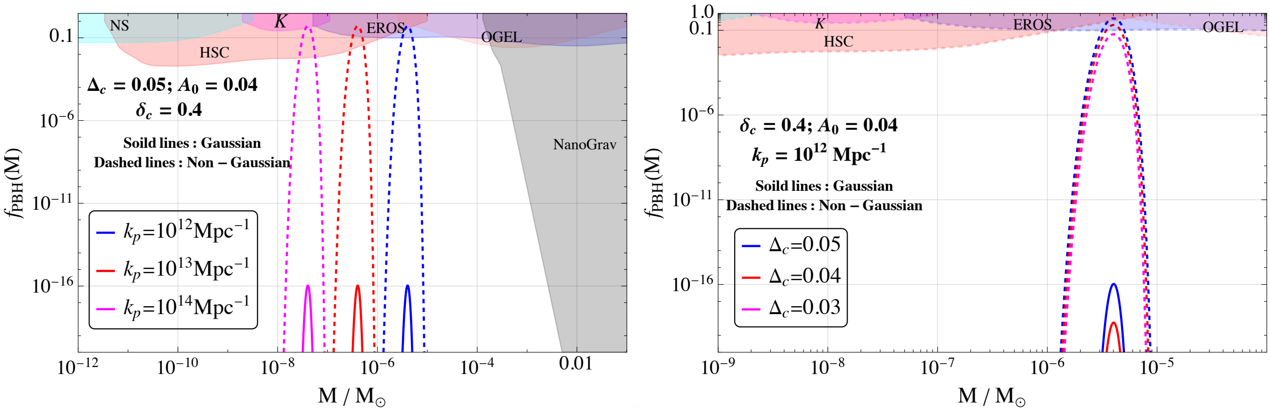

Figure 2.7: In this figure, we show the present-day PBH fraction contributing to the dark-matter abundance, f_{PBH}, as a function of the PBH mass (in units of solar mass). In the left panel, three different peak positions of the enhanced curvature power spectrum are considered for a fixed value of $\Delta_c = 0.05$. In the right panel, three different values of Δ_c are shown, indicated by different colors, while the peak position is fixed at $k_{\mathrm{p}} = 10^{12}, \mathrm{Mpc}^{-1}$. In both panels, the maximum amplitude is set to $A_0 = 0.04$, and the threshold value of the density contrast is taken to be $\delta_c = 0.4$. Solid lines correspond to the Gaussian distribution, whereas dashed lines represent the non-Gaussian distribution.

This behavior can be understood from Eq. (2.131), or intuitively from the fact that smaller wavenumbers re-enter the horizon at later times, when the horizon size is larger. Since the PBH mass is typically a fraction of the horizon mass at re-entry, this results in the formation of heavier PBHs.

In the left panel, we further observe that, for a fixed type of distribution, the value of f_{PBH} remains the same when other parameters such as the critical density contrast $\delta_c = 0.4$ [174,175] and the peak amplitude are held fixed. However, the initial fractional abundance and the present-day value of f_{PBH} depend significantly on the nature of the distribution, i.e., whether it is Gaussian or non-Gaussian.

Similarly, in the right panel of Fig. 2.7, we plot f_{PBH} as a function of the PBH mass M_{pbh} for a fixed peak wavenumber $k_{\mathrm{p}} = 10^{12}\ \mathrm{Mpc}^{-1}$, where three different colors correspond to three different values of Δ_c. This panel illustrates that both the shape of the PBH mass spectrum and the resulting abundance are sensitive to the value of Δ_c. As before, the solid lines denote the Gaussian-type distribution, while the dashed lines correspond to the non-Gaussian-type distribution. In both cases, the peak amplitude of the curvature power spectrum is fixed at $A_0 = 0.04$, and the critical density contrast is set to $\delta_c = 0.4$. The shaded regions indicate the observational bounds on f_{PBH} from various experiments.

2.9 Tensor Fluctuations: Quantum and Classical Origin

In this section, we develop the formal framework to describe the evolution of tensor perturbations of the metric, commonly referred to as gravitational waves (GWs). These tensor fluctuations can arise from two distinct origins. First, they may be generated during inflation when the corresponding modes exit the horizon, representing quantum fluctuations of the spacetime metric. Second, they can also be produced classically by anisotropic components of the energy-momentum tensor. In what follows, we establish the equations of motion governing these tensor modes and discuss the quantization procedure for their dynamical degrees of freedom in a cosmological background.

Since our primary interest lies in the evolution of tensor modes, we note that vector perturbations generally decay with time and therefore do not contribute significantly to the evolution of tensor perturbations, except in the presence of non-trivial sources that can sustain them [201]. In the absence of such sources, it is therefore consistent to neglect vector modes.

Accordingly, the perturbed FLRW metric, including only scalar and tensor perturbations, can be written as [202, 203]

$$ds^2 = a^2(\eta)\left[-(1+2\Phi)d\eta^2 + \{(1-2\Psi)\delta_{ij} + h_{ij}\}\, dx^i dx^j\right]. \tag{2.133}$$

where $h_{ij} = h^{(1)}_{ij} + h^{(2)}_{ij}$. Here $h^{(1)}_{ij}$ denotes the linear-order tensor modes, whose primary source is the vacuum fluctuations generated during inflation [204–207].

Even if we ignore the first-order tensor modes, non-trivial contributions can still arise from the second-order tensor modes. These are typically sourced by combinations of the first-order scalar perturbations, or they may arise directly from the anisotropic component of the energy-momentum tensor. The second-order Einstein equations are therefore governed by

$$G^{(2)}_{\mu\nu} = \kappa^2 T^{(2)}_{\mu\nu}. \tag{2.134}$$

Where $\kappa = 8\pi \mathrm{G_N}$. For the above metric, the spatial component of the second-order Einstein tensor $G^{(2)}_{ij}$ is given by [202, 203]

$$\begin{aligned} G^{(2)i}{}_j = a^{-2}\Big[\frac{1}{4}(h^{i\prime\prime}_j + 2\mathcal{H}h^{i\prime}_j - \nabla^2 h^i_j) + 2\Phi\partial^i\partial_j\Phi - 2\Psi\partial^i\partial_j\Phi + 4\Psi\partial^i\partial_j\Psi \\ +\partial^i\Phi\partial_j\Phi - \partial^i\Phi\partial_j\Psi - \partial^i\Psi\partial_j\Phi + 3\partial^i\Psi\partial_j\Psi \\ +\Big(2\Phi\nabla^2\Phi - 2\Psi\nabla^2\Phi + 4\Psi\nabla^2\Psi + (\nabla\Phi)^2 - (\nabla\Phi\cdot\nabla\Psi) + 3(\nabla\Psi)^2 \\ +2\Phi''\Phi + 4\mathcal{H}\Phi'\Phi - 2\Psi''\Psi - 4\mathcal{H}\Psi'\Psi\Big)\delta^i_j + (\text{higher order terms})\Big]. \end{aligned} \tag{2.135}$$

The second-order energy-momentum tensor is given by [202, 203]

$$T^{(2)i}{}_j = (\rho^{(0)} + P^{(0)})v^{(1)i}v^{(1)j} + P^{(0)}\Pi^{(2)i}{}_j + P^{(1)}\Pi^{(1)i}{}_j + P^{(2)}\delta^i_j, \tag{2.136}$$

where ρ, P, v, and Π denote the energy density, pressure, velocity, and anisotropic stress, respectively.

Tensor perturbations describe the transverse and traceless fluctuations of the spacetime metric and correspond to gravitational waves. They are represented by a symmetric, transverse, and traceless rank-2 tensor h_{ij} that perturbs the spatial part of the background metric. The transverse and traceless conditions ensure that h_{ij} contains only two physical degrees of freedom, corresponding to the two polarization states of gravitational waves, commonly denoted as h_+ and $h_\times$. Each polarization evolves as an independent massless field in an expanding Universe.

To isolate these tensor modes, we act on the spatial components of the Einstein equations with the projection tensor $\mathrm{P}_{ij}^{mn}(\mathbf{k})$, yielding [202, 203]

$$\mathrm{P}_{ij}^{mn}(\mathbf{k})G_{mn}^{(2)} = \kappa^2 \mathrm{P}_{ij}^{mn}(\mathbf{k})T_{mn}^{(2)}, \tag{2.137}$$

where the projection operator $\mathrm{P}_{ij}^{mn}(\mathbf{k})$ extracts the transverse-traceless component of the energy-momentum tensor and is defined as

$$\mathrm{P}_{ij}^{mn}(k) = \mathrm{P}_i^m(k)\mathrm{P}_j^n(k) - \frac{1}{2}\mathrm{P}^{mn}(k)\mathrm{P}_{ij}(k), \tag{2.138}$$

with $\mathrm{P}_{ij} = \delta_{ij} - \partial_i\partial_j/\Delta$ [202, 203].

Since only the transverse-traceless component of the energy-momentum tensor can source the tensor modes $h_{ij}(\mathbf{x}, \eta)$, after applying the projection operator P_{ij}^{mn} the left-hand side of Eq. (2.137) becomes

$$\begin{aligned}\mathrm{P}_{ij}^{mn}G_{mn}^{(2)} = &\frac{1}{4}(h_j^{i''} + 2\mathcal{H}h_j^{i'} - \nabla^2 h_j^i)\\ &+ \mathrm{P}_{ij}^{mn}\Big[2\Phi^{(1)}\partial^i\partial_j\Phi^{(1)} - 2\Psi^{(1)}\partial^i\partial_j\Phi^{(1)} + 4\Psi^{(1)}\partial^i\partial_j\Psi^{(1)}\\ &+ \partial^i\Phi^{(1)}\partial_j\Phi^{(1)} - \partial^i\Phi^{(1)}\partial_j\Psi^{(1)} - \partial^i\Psi^{(1)}\partial_j\Phi^{(1)} + 3\partial^i\Psi^{(1)}\partial_j\Psi^{(1)}\Big].\end{aligned} \tag{2.139}$$

Substituting this expression into Eq. (2.137), the evolution equation for the tensor mode $h_{ij}(\mathbf{x}, \eta)$ can be written as

$$h_{ij}^{''}(\mathbf{x}, \eta) + 2\mathcal{H}h_{ij}^{'}(\mathbf{x}, \eta) - \nabla^2 h_{ij}(\mathbf{x}, \eta) = \mathrm{P}_{ij}^{mn}\Big[\mathcal{S}_{mn} + \frac{2}{M_\mathrm{P}^2}T_{mn}^{(2)}\Big], \tag{2.140}$$

where the source term associated with the scalar perturbations is defined as [147, 183, 184, 194–196, 208–219]

$$\begin{aligned}\mathcal{S}_{mn}(\mathbf{x}, \eta) =&2\Phi\partial^i\partial_j\Phi - 2\Psi\partial^i\partial_j\Phi + 4\Psi\partial^i\partial_j\Psi\\ &+ \partial^i\Phi\partial_j\Phi - \partial^i\Phi\partial_j\Psi - \partial^i\Psi\partial_j\Phi + 3\partial^i\Psi\partial_j\Psi.\end{aligned} \tag{2.141}$$

Equation (2.140) shows that second-order gravitational waves can be generated by two distinct sources. The first arises from quadratic combinations of scalar perturbations contained in the Einstein tensor, represented by $\mathcal{S}_{mn}(\mathbf{x}, \eta)$. The second originates from the anisotropic components of the energy-momentum tensor, represented by $T_{mn}^{(2)}$. In the present work, we focus on the latter contribution from electromagnetic fields.

To solve Eq. (2.140), it is convenient to work in Fourier space. We therefore define the Fourier decomposition of the tensor perturbation as

$$h_{ij}(\mathbf{x},\eta) = \int \frac{d^3\mathbf{k}}{(2\pi)^{3/2}} e^{i\mathbf{k}\cdot\mathbf{x}} \Big[h^+_{\mathbf{k}}(\eta) e^+_{ij}(\mathbf{k}) + h^\times_{\mathbf{k}}(\eta) e^\times_{ij}(\mathbf{k}) \Big]. \tag{2.142}$$

The two time-independent polarization tensors e_{ij} and $\bar{e}_{ij}$ can be expressed in terms of two orthonormal basis vectors that are orthogonal to $\mathbf{k}$,

$$e^+_{ij}(\mathbf{k}) = \frac{1}{\sqrt{2}} \left(e^+_i(\mathbf{k}) e^+_j(\mathbf{k}) - e^\times_i(\mathbf{k}) e^\times_j(\mathbf{k}) \right), \tag{2.143a}$$

$$e^\times_{ij}(\mathbf{k}) = \frac{1}{\sqrt{2}} \left(e^+_i(\mathbf{k}) e^\times_j(\mathbf{k}) + e^\times_i(\mathbf{k}) e^+_j(\mathbf{k}) \right). \tag{2.143b}$$

Similarly, the energy-momentum tensor can be decomposed as

$$\frac{2}{M_{\mathrm{P}}^2} \mathrm{P}^{mn}_{ij} T^{(2)}_{mn} = \frac{2}{M_{\mathrm{P}}^2} \int \frac{d^3\mathbf{k}}{(2\pi)^{3/2}} e^{i\mathbf{k}\cdot\mathbf{x}} \Big[e^{(+)}_{ij}(\mathbf{k}) e^{(+)mn}(\mathbf{k}) + e^{(\times)}_{ij}(\mathbf{k}) e^{(\times)lm}(\mathbf{k}) \Big] T_{mn}(\mathbf{k},\eta), \tag{2.144}$$

where

$$T_{mn}(\mathbf{k},\eta) = \int \frac{d^3\mathbf{x}'}{(2\pi)^{3/2}} e^{-i\mathbf{k}\cdot\mathbf{x}'} T_{mn}(\mathbf{x}',\eta). \tag{2.145}$$

When solving Eq. (2.140), we consider one polarization state at a time. For each polarization mode λ, the equation of motion becomes [220–222]

$$h''^{(\lambda)}_{\mathbf{k}} + 2\mathcal{H} h'^{(\lambda)}_{\mathbf{k}} + k^2 h^{(\lambda)}_{\mathbf{k}} = \frac{2}{M_{\mathrm{P}}^2} e^{(\lambda)lm}(\mathbf{k}) T^{(2)}_{lm}(\mathbf{k},\eta). \tag{2.146}$$

This equation can be solved using the Green's function method. The full solution can be written as

$$h^{(\lambda)}_{\mathbf{k}}(\eta) = h^{\mathrm{vac}(\lambda)}_{\mathbf{k}}(\eta) + \frac{2}{M_{\mathrm{P}}^2} \int_{\eta_i}^{\eta} d\tilde{\eta}\, \mathcal{G}_k(\eta,\tilde{\eta}) \mathcal{T}^{(\lambda)}_{\mathbf{k}}(\tilde{\eta}), \tag{2.147}$$

where $\mathcal{T}^{(\lambda)}_{\mathbf{k}}(\eta) = e^{(\lambda)lm} T^{(2)}_{lm}(\mathbf{k},\eta)$.

Here $h^{\mathrm{vac}(\lambda)}_{\mathbf{k}}(\eta)$ represents the homogeneous solution corresponding to vacuum fluctuations of spacetime, while the second term describes the sourced contribution arising from the energy-momentum tensor. In our case, this sourced contribution originates from the electromagnetic field.

The function $\mathcal{G}_k(\eta,\eta_1)$ is the retarded Green's function associated with the tensor perturbation equation of motion in Eq. (2.146), satisfying

$$\left[\frac{\partial^2}{\partial\eta^2} + 2\mathcal{H}\frac{\partial}{\partial\eta} + k^2 \right] \mathcal{G}_k(\eta,\eta_1) = \delta(\eta-\eta_1), \qquad \mathcal{G}_k(\eta,\eta_1) = 0 \text{ for } \eta < \eta_1. \tag{2.148}$$

In general, the two polarization states of tensor perturbations are statistically independent. Therefore, the two-point correlation function of the tensor modes can be written as [202, 203, 220–222]

$$\langle h_{\mathbf{k}}^{(\lambda)}(\eta)\, h_{\mathbf{k}'}^{*(\lambda')}(\eta)\rangle = \delta^{(3)}(\mathbf{k}-\mathbf{k}')\,\delta_{\lambda\lambda'}\,\frac{2\pi^2}{k^3}\,P_{\mathrm{T}}^{\lambda}(k,\eta), \tag{2.149}$$

where $P_{\mathrm{T}}^{\lambda}(k,\eta)$ denotes the tensor power spectrum for the polarization mode λ.

From Eq. (2.147), the tensor mode consists of two distinct contributions: the vacuum component $h_{\mathbf{k}}^{\mathrm{vac}(\lambda)}$, arising from quantum fluctuations of spacetime, and the sourced component generated by the energy-momentum tensor. Since these two contributions originate from independent physical processes, they do not mix. Consequently, the total tensor power spectrum can be written as the sum of two independent components,

$$P_{\mathrm{T}}^{(\lambda)}(k) = P_{\mathrm{T}}^{\mathrm{vac}(\lambda)}(k) + P_{\mathrm{T}}^{\mathrm{sec}(\lambda)}(k), \tag{2.150}$$

where $P_{\mathrm{T}}^{\mathrm{vac}(\lambda)}(k)$ corresponds to the vacuum tensor power spectrum and $P_{\mathrm{T}}^{\mathrm{sec}(\lambda)}(k)$ represents the contribution generated by the source terms.

In the following subsection, we discuss these two contributions separately within a simplified scenario in which the Universe enters a radiation-dominated era immediately after inflation.

2.9.1 Quantum Production of Tensor Perturbations during Inflation

During inflation, the rapid accelerated expansion of the Universe amplifies not only scalar perturbations but also generates primordial tensor fluctuations, i.e., gravitational waves, originating from the quantum vacuum fluctuations of the metric. These tensor modes arise generically in inflationary scenarios and carry direct information about the energy scale and dynamics of inflation. In particular, their spectrum is determined by the Hubble parameter during inflation and the evolution of the background spacetime, providing a unique observational probe of the earliest stages of the Universe.

For the moment, we assume that no anisotropic stress is present. In this case, the first-order Einstein equations lead to the following equation of motion for the tensor perturbations $h_{ij}(\mathbf{x},\eta)$

$$h_{ij}''(\mathbf{x},\eta) + 2\frac{a'}{a}h_{ij}'(\mathbf{x},\eta) - \nabla^2 h_{ij}(\mathbf{x},\eta) = 0. \tag{2.151}$$

Upon quantization, the tensor perturbations can be decomposed in terms of Fourier modes $h_{\mathbf{k}}(\eta)$ as follows [202, 203, 207]

$$h_{ij}(\mathbf{x},\eta) = \int \frac{d^3\mathbf{k}}{(2\pi)^{3/2}}\left[a_{\mathbf{k}}^{\lambda}\epsilon_{ij}^{\lambda}(\mathbf{k})h_{\mathbf{k}}(\eta)e^{i\mathbf{k}\cdot\mathbf{x}} + a_{\mathbf{k}}^{\lambda\dagger}\epsilon_{ij}^{\lambda *}(\mathbf{k})h_{\mathbf{k}}^{*}(\eta)e^{-i\mathbf{k}\cdot\mathbf{x}}\right]. \tag{2.152}$$

Here $\epsilon_{ij}^{\lambda}(\mathbf{k})$ denotes the polarization tensor, where the index λ corresponds to the two polarization states $+$ and $\times$ of gravitational waves. The polarization tensors satisfy the conditions $\delta^{ij}\epsilon^{\lambda}_{ij}(\mathbf{k}) = k^i\epsilon^{\lambda}_{ij}(\mathbf{k}) = 0$, and we adopt the normalization $\epsilon^{ij\lambda}(\mathbf{k})\epsilon^{\lambda'*}_{ij}(\mathbf{k}) = 2\delta^{\lambda\lambda'}$. In the above decomposition, the ladder operators obey the standard quantization relations discussed in Eq.(2.92). In the absence of anisotropic stress, the Fourier mode $h_{\mathbf{k}}$ satisfies the differential equation

$$h''_{\mathbf{k}} + 2\frac{a'}{a}h'_{\mathbf{k}} + k^2 h_{\mathbf{k}} = 0. \tag{2.153}$$

In the above equation, the polarization index has been suppressed since, in this case, the tensor modes are linearly polarized and both polarization states evolve identically.

To solve this equation, it is convenient to introduce the Mukhanov-Sasaki variable $v_{\mathbf{k}}$ defined by $h_{\mathbf{k}} = (\sqrt{2}/M_{\rm P})(v_{\mathbf{k}}/a)$ [223]. Rewriting Eq.(2.153) in terms of $v_{\mathbf{k}}$, we obtain the equation [38, 223–228]

$$v''_{\mathbf{k}} + \left(k^2 - \frac{a''}{a}\right)v_{\mathbf{k}} = 0, \tag{2.154}$$

which corresponds to the equation of motion of a harmonic oscillator with time-dependent frequency $\omega_k^2(\eta) = k^2 - a''/a$.

In the sub-horizon limit, where $\omega_k^2(\eta) \simeq k^2$, the solution of the mode function reduces to a simple plane wave,

$$v_{\mathbf{k}} = \frac{e^{-ik\eta}}{\sqrt{2k}}, \tag{2.155}$$

which corresponds to the Bunch-Davies vacuum state for a quantum field in an expanding spacetime.

In contrast, on super-horizon scales the mode function admits two independent solutions,

$$v_{\mathbf{k}}(\eta) \propto a \qquad \text{and} \qquad v_{\mathbf{k}}(\eta) \propto 1/a^2. \tag{2.156}$$

These correspond respectively to a constant solution $h \propto$ const and a decaying solution. Consequently, in the super-horizon regime the amplitude of the tensor fluctuation $h_{\mathbf{k}}(\eta)$ remains approximately constant in time.

For a quasi-de Sitter spacetime, the quantity a''/a can be expressed in terms of the slow-roll parameter ϵ as

$$\frac{a''}{a} \simeq \frac{2+3\epsilon}{\eta^2}. \tag{2.157}$$

Defining a new parameter $\nu = \epsilon + 3/2$, Eq.(2.154) can be rewritten as

$$v''_{\mathbf{k}} + \left[k^2 - \frac{1}{\eta^2}\left(\nu^2 - \frac{1}{4}\right)\right] v_{\mathbf{k}} = 0. \tag{2.158}$$

The exact solution of this equation can be expressed in terms of Hankel functions,

$$v_{\mathbf{k}}(\eta) = \sqrt{-\eta}\left[C_1 H_\nu^{(1)}(-k\eta) + C_2 H_\nu^{(2)}(-k\eta)\right], \tag{2.159}$$

where C_1 and C_2 are integration constants and $H_\nu^{(1)}$, $H_\nu^{(2)}$ denote the Hankel functions of the first and second kind.

To determine the constants C_1 and C_2, we impose the condition that at the beginning of inflation all modes are well inside the horizon, so that the solution matches the Bunch-Davies vacuum. The asymptotic forms of the Hankel functions for $x \gg 1$ are

$$H_\nu^{(1)}(x >> 1) \simeq \sqrt{\frac{2}{\pi x}} e^{i(x - \frac{\pi}{2}\nu - \frac{\pi}{4})}; \qquad H_\nu^{(2)}(x >> 1) \simeq \sqrt{\frac{2}{\pi x}} e^{-i(x - \frac{\pi}{2}\nu - \frac{\pi}{4})}. \tag{2.160}$$

Matching with the plane-wave solution implies $C_2 = 0$, while the normalization condition leads to $C_1 = \frac{\sqrt{\pi}}{2} e^{i(\nu + \frac{1}{2})\frac{\pi}{2}}$. Substituting these constants gives

$$v_{\mathbf{k}}(\eta) = \frac{\sqrt{2}}{2} e^{i(\nu + \frac{1}{2})\frac{\pi}{2}} \sqrt{-\eta} H_\nu^{(1)}(-k\eta). \tag{2.161}$$

Using the generic definition, the tensor power spectrum can be written as

$$P_{\mathrm{T}}(k) = \frac{k^3}{2\pi^2} \sum_\lambda \left|h_{\mathbf{k}}^{(\lambda)}\right|^2. \tag{2.162}$$

At the end of inflation, all relevant modes lie outside the horizon, and the tensor power spectrum on super-horizon scales can be written as [117–119, 207, 229, 230]

$$P^{\mathrm{vac}}_{\mathrm{T,inf}}(k) = \frac{8}{M_{\mathrm{P}}^2}\left(\frac{H_{\mathrm{e}}}{2\pi}\right)^2 \left(\frac{k}{aH}\right)^{-2\epsilon} \simeq \frac{2}{\pi^2}\left(\frac{H_{\mathrm{e}}}{M_{\mathrm{P}}}\right)^2. \tag{2.163}$$

From the above expression, it is evident that in a slow-roll inflationary background ($\epsilon \ll 1$), the tensor power spectrum is nearly scale-invariant on large scales. Analogous to the curvature perturbation spectrum, one can define the tensor spectral index as $n_{\mathrm{T}} \simeq -2\epsilon$. Therefore, in simple slow-roll inflationary models, the tensor power spectrum exhibits a slight red tilt.

2.9.2 Inflationary observables and CMB constraints

Having derived the scalar and tensor primordial power spectra in the previous subsections, we now relate them to the inflationary observables constrained by Cosmic Microwave Background (CMB) measurements. Around a reference (pivot) scale k_{piv}, the scalar and tensor power spectra are conventionally parameterized as

$$\mathcal{P}_{\mathcal{R}}(k) = A_s(k_{\rm piv}) \left(\frac{k}{k_{\rm piv}}\right)^{n_s-1+\frac{1}{2}\alpha_s \ln(k/k_{\rm piv})+\cdots},$$
$$\mathcal{P}_T(k) = A_T(k_{\rm piv}) \left(\frac{k}{k_{\rm piv}}\right)^{n_T+\frac{1}{2}\alpha_T \ln(k/k_{\rm piv})+\cdots}, \tag{2.164}$$

where A_s (A_T) denotes the scalar (tensor) amplitude, n_s (n_T) is the corresponding spectral index, and $\alpha_s = dn_s/d\ln k$ ($\alpha_T = dn_T/d\ln k$) represents its running. An additional observable of particular importance is the tensor-to-scalar ratio,

$$r \equiv \frac{\mathcal{P}_T(k_{\rm piv})}{\mathcal{P}_{\mathcal{R}}(k_{\rm piv})}. \tag{2.165}$$

Using the scalar and tensor spectra obtained in Secs. 2.7.1 and 2.9.1, these observables can be expressed in terms of the slow-roll parameters. To leading order, one obtains

$$A_s \simeq \frac{H_*^2}{8\pi^2\epsilon_\varphi M_{\rm Pl}^2},\ A_T \simeq \frac{2H_*^2}{\pi^2 M_{\rm Pl}^2},\ r \simeq 16\epsilon_\varphi,$$
$$n_s - 1 \simeq -6\epsilon_\varphi + 2\eta_\varphi,\ n_T \simeq -2\epsilon_\varphi \tag{2.166}$$

which satisfy the well-known consistency relation $n_T = -r/8$ for canonical single-field slow-roll inflation.

The tensor-to-scalar ratio is particularly significant because it determines the energy scale of inflation. Combining the expressions for A_s and r yields

$$H_* = \pi M_{\rm Pl}\sqrt{\frac{rA_s}{2}}, \tag{2.167}$$

which relates the Hubble scale during inflation directly to the CMB observables.

The latest CMB observations provide stringent constraints on these parameters. At the pivot scale $k_{\rm piv} = 0.05\,{\rm Mpc}^{-1}$, the *Planck* 2018 analysis finds [11]

$$A_s = (2.10 \pm 0.03) \times 10^{-9}, \qquad n_s = 0.9649 \pm 0.0042, \tag{2.168}$$

while the combined *Planck* 2018 and BICEP/Keck analysis constrains the tensor-to-scalar ratio to [11]

$$r_{0.05} < 0.035 \qquad (95\%\ \text{C.L.}). \tag{2.169}$$

The observed value $n_s < 1$ indicates that the primordial scalar spectrum is slightly red-tilted, in excellent agreement with the predictions of slow-roll inflation. Furthermore, the current upper bound on r implies [11,12]

$$H_* \lesssim 5 \times 10^{13}\ \text{GeV}, \tag{2.170}$$

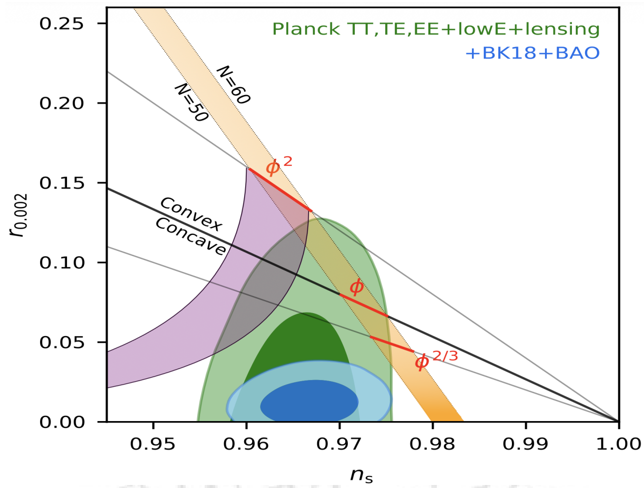

Figure 2.8: Constraints on the spectral index n_s and the tensor-to-scalar ratio r in the $r - n_s$ plane are shown from Planck 2018 data alone (green), and from the combined analysis including Planck, BICEP/Keck 2018 (BK18), and Baryon Acoustic Oscillation (BAO) data (cyan). The inclusion of BK18 and BAO significantly tightens the bounds on both n_s and r. [Source figure BICEP/Keck website].

placing a stringent upper limit on the inflationary energy scale. In the remainder of this work, the predictions of our model will be confronted with these observational constraints, particularly in the (n_s, r) plane.

Figure 2.8 shows the latest constraints in the (n_s, r) plane from the Planck Collaboration together with the predictions of representative inflationary models. Throughout this thesis, we will compare the predictions of our model against these observational bounds.

Post-Inflationary evolution of the tensor power spectrum:

Evolution during Reheating Era: Subsequent to inflation, reheating begins with the inflaton's energy transforming progressively into radiation, leading to a universe dominated by radiation. This phase can be characterized by intrinsic inflation parameters encompassing mass, self-coupling, and interactions with the radiation field. Within the perturbative framework, these parameters find effective representation through two fundamental quantities namely the reheating equation of state ($w_{\rm re}$) and the reheating temperature (T_{re}). During this epoch, the evolution of inflation's energy density is described by $\rho_\varphi = \rho_{\rm cri}(a/a_{\rm e})^{-3(1+w_{\rm re})}$, where $\rho_{\rm cri} = 3H_{\rm e}^2 M_{\rm P}^2$. Consequently, the Hubble parameter evolves as $H^2 = H_{\rm e}^2(a/a_{\rm e})^{-3(1+w_{\rm re})}$.

By incorporating these into Eq. 2.153, we obtain the solution for the tensor perturbation h_k during the reheating epoch

$$h_k^{\rm re}(x) = C_1 x^{l(w_{\rm re})} J_{l(w_{\rm re})}(x) + C_2 x^{l(w_{\rm re})} J_{-l(w_{\rm re})}(x) \tag{2.171}$$

Where $l(w_{\rm re}) = 3(w_{\rm re} - 1)/2(1 + 3w_{\rm re})$, and $x = k\eta$. The integration constants C_1 and C_2 are derived from the inflationary contribution at the end of inflation $\eta = \eta_{\rm e}$ through the continuity relation of the tensor fluctuations and their first-order derivatives. As our focus rests upon modes situated beyond the Hubble radius at the end of the inflationary epoch, we take the super-horizon limit, characterized by $x_e = k\eta_e << 1$, and obtain [117, 118]

$$C_1 = \frac{(3-2l)\Gamma(l)}{(1-l)} 2^{l-2} \left(\frac{k}{k_e}\right)^{2(1-l)} h_{\mathbf{k}}^{\rm inf}(k,\eta_e) \tag{2.172}$$

$$C_2 = 2^{-l}\Gamma(1-l) h_{\mathbf{k}}^{\rm inf}(k,\eta_e) \tag{2.173}$$

In the general scenario, the parameter $w_{\rm re}$ ranges within the interval $0 \leq w_{\rm re} \leq 1$. Under this constraint, the function $l(w_{\rm re})$ consistently assumes negative values. Given our specific interest in scales that reside beyond the horizon (i.e., $k < k_e$, which in turn implies $k/k_e < 1$), we note that $C_2 \ll C_1$. Exploiting these considerations tensor power spectrum at the end of reheating assumes the following form,

$$P_{\rm T,re}^{\rm vac}(k,\eta_{\rm re}) \simeq \frac{k^3}{2\pi^2}|C_2|^2 \left(\frac{k}{k_{\rm re}}\right)^{2l(w_{\rm re})} J_{-l(w_{\rm re})}(k/k_{\rm re}) J^*_{-l(w_{\rm re})}(k/k_{\rm re}) \tag{2.174}$$

The spectral behavior inherent in $P_{\rm T,re}^{\rm vac}$ assumes two distinct form for two distinct realms: $k_* < k < k_{\rm re}$ and $k_{\rm re} < k < k_e$. Now, utilizing Eq.(2.173) and the form of the Bessel function in these two limits, the tensor power spectrum defined at the end of reheating as

$$P_{\rm T,re}^{\rm vac}(k,\eta_{\rm re}) \simeq P_{\rm T,inf}^{\rm vac} \times \begin{cases} 1 & \text{for } k << k_{\rm re} \\ \mathcal{D}\left(\frac{k}{k_{\rm re}}\right)^{2l-1} & \text{for } k_{\rm re} < k < k_e \end{cases} \tag{2.175}$$

where we define $\mathcal{D}$ as

$$\mathcal{D} = \frac{2^{1-2l}\Gamma^2(1-l)}{\pi} \cos^2\left[-\frac{k}{k_{\rm re}} + \frac{1}{4}(1-2l)\pi\right] \tag{2.176}$$

From the above, we have seen that reheating dynamics are only effective for those modes that can re-enter the Hubble radius at the end of reheating; otherwise, the spectrum is unaffected by the reheating dynamics.

Evolution during Radiation Era: After the reheating epoch, the subsequent era is predominantly characterized by radiation, where the background energy density scales as a^{-4}, and consequently the Hubble parameter behaves as $H^2 = H_{\rm re}^2(a_{\rm re}/a)^4$, with $H_{\rm re}$ representing the Hubble parameter defined at the end of reheating. Within this context, the solution to the homogeneous component of the tensor evolution, as defined in Eq.2.153, is governed by the following expression:

$$h_{\mathbf{k}}^{\rm ra}(x) = \frac{1}{x}\left\{D_1 e^{-ix} + D_2 e^{ix}\right\} \tag{2.177}$$

The integration constants (D_1, D_2) encapsulate the imprint of the inflationary dynamics and reheating again through the continuity of tensor fluctuations and their first derivatives at the end of reheating $\eta = \eta_{\rm re}$. Through the application of these conditions, we arrive at the expression elucidated in

$$D_1(k) = \frac{h^\lambda_{k,\rm re}(i(k/k_{\rm re}) - 1) - (k/k_{\rm re}) {h^\lambda_{k,\rm re}}'}{2i} e^{i(k/k_{\rm re})} \tag{2.178a}$$

$$D_2(k) = \frac{(k/k_{\rm re}){h^\lambda_{k,\rm re}}' + h^\lambda_{k,\rm re}\,(i(k/k_{\rm re}) + 1)}{2i} e^{-i(k/k_{\rm re})} \tag{2.178b}$$

It is crucial to emphasize that the characteristics of these coefficients, denoted as D_1 and D_2, strongly depend on the inflationary and reheating dynamics. By using Eqs.(2.178) in Eq.(2.149), we can define the tensor power spectrum during the radiation-dominated era as:

$$P^{\rm vac}_{\rm T,ra}(k,\eta) = \frac{k^3}{2\pi^2}\frac{1}{x^2}\left\{|D_1(k)|^2 + |D_2(k)|^2\right\}. \tag{2.179}$$

The contribution from the earlier phase will enter though the integration constant (D_1, D_2) In the two extreme limit, the GW spectrum assumes the following simple forms in the super-horizon limit $(k < k_{\rm re})$,

$$\lim_{k<k_{\rm re}} P^{\rm vac}_{\rm T,ra}(k,\eta) = \frac{1}{2k^2\eta^2} P^{\rm vac}_{\rm T,re}(k,\eta_{\rm re}), \tag{2.180}$$

and in the sub-horizon limit $(k > k_{\rm re})$,

$$\lim_{k>k_{\rm re}} P^{\rm vac}_{\rm T,ra}(k,\eta) = \frac{1}{2k^2\eta^2}\left(\frac{k}{k_{\rm re}}\right)^2 P^{\rm vac}_{\rm T,re}(k,\eta_{\rm re}) \tag{2.181}$$

Here, $P_{\rm T,re}(k,\eta_{\rm re})$ represents the total tensor power spectrum produced from both quantum fluctuations during inflation and the secondary production from electromagnetic fields up to the end of reheating.

2.9.3 Computing the Dimensionless GWs energy density at *today:*

Gravity exhibits weak interactions with matter, ensuring that gravitational waves (GWs) are effectively decoupled from the rest of the universe on Planck scales. This allows us to neglect interactions with ordinary matter and self-interactions, assuming that sub-Hubble GWs propagate freely through space after their production (or re-entry into the Hubble radius in the case of inflationary signals). As the universe expands, the GW energy density decreases similarly to radiation, i.e., $\rho_{\rm gw} \propto a^{-4}$. Meanwhile, the physical wave number of GWs evolves as k/a.

We normalize the GW energy density at the time of neutrino decoupling as follows:

$$\Omega_{\rm GW}(k,\eta_\nu) = \frac{\rho_{\rm gw}(k,\eta_\nu)}{\rho_c(\eta_\nu)} \tag{2.182}$$

Here, $\Omega_{\rm GW}(k,\eta_\nu)$ represents the spectral energy density of GWs per logarithmic comoving wavenumber, defined at neutrino decoupling. The GW energy density at this time is given by [202, 215, 231]

$$\rho_{\rm gw}(k,\eta_\nu) = \frac{M_{\rm P}^2 k^2}{4a^2(\eta_\nu)} P_{\rm T}(k,\eta_\nu) \tag{2.183}$$

Where $P_{\rm T}(k,\eta_\nu)$ is the tensor power spectrum defined at neutrino decoupling. The spectrum of GW energy density per logarithmic frequency interval can be conveniently normalized by the critical energy density, denoted as $\rho_c(\eta_\nu)$, as expressed in Eq. (2.184):

$$\Omega_{\rm GW}(k,\eta_\nu) = \frac{\rho_{\rm gw}(k,\eta_\nu)}{\rho_c(\eta_\nu)} = \frac{1}{12}\frac{k^2 P_{\rm T}(k,\eta_\nu)}{a^2(\eta_\nu)H^2(\eta_\nu)} \tag{2.184}$$

Where $\rho_c(\eta_\nu) = 3H^2(\eta_\nu)M_{\rm P}^2$, and $M_{\rm P} \simeq 2.43 * 10^{18}$GeV represents the reduced Planck mass.

As we know, the energy density of GWs behaves as $\rho_{\rm gw} \propto a^{-4}$, exactly like the radiation energy density. We are interested in those modes that are well inside the Hubble radius at a later time (say, close to the epoch during radiation-matter equality) during radiation domination. On utilizing this property, the dimensionless energy density parameter $\Omega_{\rm GW}(k)$ today can be expressed in terms of $\Omega_{\rm GW}(k,\eta)$ as follows [202, 207, 215, 231]

$$\Omega_{\rm GW}(k)h^2 \simeq \left(\frac{g_{*,0}}{g_{*,\rm eq}}\right)^{1/3} \Omega_R h^2 \Omega_{\rm GW}(k,\eta) \tag{2.185}$$

Here, $\Omega_R h^2 \simeq 4.3\times 10^{-5}$ represents the present-day dimensionless energy density of the radiation component. Where $g_{*,\rm eq} \simeq g_{*,0} \simeq 3.35$ are the relativistic degrees of freedom defined at the matter-radiation equality and present-day, respectively.

Spectrum of Primary Gravitational Waves $\Omega_{\rm GW}^{\rm pri}(k)$

As we have seen, the tensor power spectrum associated with vacuum fluctuation during inflation in de-sitter inflationary background is scale invariant in nature. But in the presence of the non-instantaneous reheating scenarios, the present-day GW spectrum originating from the quantum fluctuation is modified depending on whether the wavenumber is inside the horizon or outside the horizon during the reheating era. So, for non-instantaneous reheating scenarios, the spectral energy density (SED) of the GW produced from the quantum fluctuations is [117–119, 207, 229]

$$\Omega_{\rm GW}^{\rm pri}(f)h^2 \simeq \frac{\Omega_{\rm r}h^2}{6}\left(\frac{g_{*,0}}{g_{*,\rm eq}}\right)^{1/3}\left(\frac{H_{\rm e}}{M_{\rm P}}\right)^2 \times \begin{cases} 1 & f < f_{\rm re}, \\ \mathcal{D}\left(\frac{f}{f_{\rm re}}\right)^{-n_w} & f > f_{\rm re}, \end{cases} \tag{2.186}$$

where $\mathcal{D} \simeq 2^{1-2l}\Gamma^2(1-l)/2\pi \simeq \mathcal{O}(1)$ and $n_w = 2(1-3w_{\rm re})/(1+3w_{\rm re})$ [117, 229] and $f = k/2\pi$ is the comoving frequency. It has been clear from the above that the super-horizon modes remain scale invariant, whereas the sub-horizon modes get modified depending on the EoS

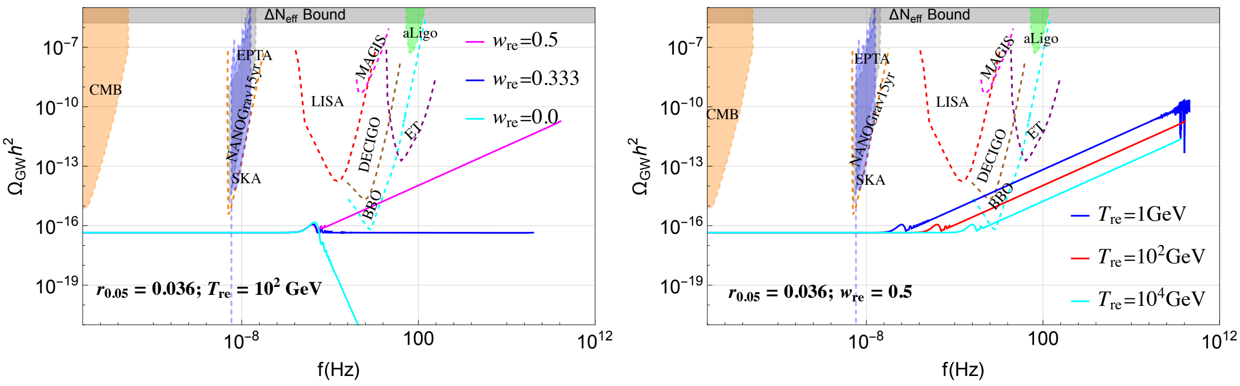

Figure 2.9: In the above figures, we show the spectral energy density of gravitational waves, $\Omega_{\rm GW}h^2$, as a function of the present-day observable frequency f (Hz) for two different scenarios. In the left panel, we fix the reheating temperature at $T_{\rm re} = 10^2\,$GeV, where the three different colors represent three distinct values of the average equation-of-state parameter: $w_{\rm re} = 0.0$ (cyan), 0.333 (blue), and 0.5 (magenta). In the right panel, we fix the equation-of-state parameter at $w_{\rm re} = 0.5$ and vary the reheating temperature $T_{\rm re}$ (in GeV), as indicated by the three different colors. In both cases, we consider the tensor-to-scalar ratio to be $r_{0.05} = 0.036$, which determines the corresponding inflationary energy scale. The dashed lines represent the projected sensitivity curves of various proposed GW detection experiments, while the shaded region denotes the observational bounds obtained from existing measurements.

$w_{\rm re}$. For $w_{\rm re} = 0$, the spectra become red tilted, i.e., $\Omega^{\rm pri}_{\rm GW}(f > f_{\rm re}) \propto f^{-2}$, whereas for radiation-like evolution, the spectrum remains scale invariant and we get a blue tilted GW spectrum for $w_{\rm re} > 1/3$ reheating scenarios. In Fig. 2.9, we have shown the present-day GW spectral energy density, $\Omega_{\rm GW}h^2$, as a function of the present-day observable frequency f (Hz) for two different reheating scenarios. In the left panel of Fig. 2.9, we consider a fixed reheating temperature $T_{\rm re} = 10^2\,$GeV but explore three different possible equations of state: $w_{\rm re} = 0$ (matter-like evolution), $w_{\rm re} = 1/3$ (radiation-like evolution), and $w_{\rm re} = 0.5$ (kination-like evolution). As discussed in Eq. (2.186), the modes that remain inside the horizon during reheating are affected by changes in the post-inflationary expansion history, and their GW spectral index is determined by the average equation of state as $\Omega^{\rm pri}_{\rm GW}(f) \propto f^{-n_w}$. For instance, when $w_{\rm re} = 0$, the spectrum for $f > f_{\rm re}$ behaves as $\Omega^{\rm pri}_{\rm GW}(f > f_{\rm re}) \propto f^{-2}$, whereas for a radiation-like evolution, it follows $\Omega^{\rm pri}_{\rm GW}(f) \propto f^{0}$. On the other hand, for $w_{\rm re} = 0.5$, the GW spectrum exhibits a blue tilt, scaling as $\Omega^{\rm pri}_{\rm GW}(f > f_{\rm re}) \propto f^{0.2}$.

Of particular interest are the modes that remain outside the horizon at the completion of reheating. Their spectral behaviour remains unchanged and continues to be scale-invariant in nature, i.e., $\Omega^{\rm pri}_{\rm GW}(f < f_{\rm re}) \propto f^{0}$. In the right panel of Fig. 2.9, we illustrate the dependence of the spectrum on the duration of the reheating phase. Here, we fix the equation of state at $w_{\rm re} = 0.5$ and vary the reheating temperature as $T_{\rm re} = 1$, 10^2, and $10^4\,$GeV, represented by three different colors. Since the equation of state is fixed at $w_{\rm re} = 0.5$, the spectral slope for the sub-horizon modes remains the same for all reheating temperatures, but the position of the spectral break shifts accordingly. A lower reheating temperature corresponds to a longer reheating duration, leading the spectral break to appear at smaller values of k, as clearly seen in the right panel of Fig. 2.9. In both panels, we have taken a fixed value of the tensor-to-scalar ratio, which determines the inflationary energy scale as $H_{\rm e} \simeq 10^{-5} M_{\rm P}$.

In conclusion, we have clearly seen that non-instantaneous reheating scenarios leave a significant imprint on the present-day GW spectrum. The spectral behaviour and the position of the spectral breaks in the GW spectrum provide valuable information about the reheating dynamics—specifically, how the background evolution proceeded during this phase and how long the reheating period extended after the end of inflation.

2.9.4 Secondary production of the Tensor perturbations due to Electromagentic fields

In the previous subsection, we computed the tensor power spectrum associated with vacuum fluctuations. In this subsection, we evaluate the tensor power spectrum sourced by electromagnetic fields. The two-point correlation function of the tensor modes sourced by the electromagnetic field can be written as

$$\langle h_{\mathbf{k}}^{(\lambda)}(\eta)\, h_{\mathbf{k}'}^{*(\lambda')}(\eta)\rangle = \frac{4}{M_{\rm P}^4}\int_{\eta_i}^{\eta} {\rm d}\eta_1 \mathcal{G}_{\rm k}(\eta,\eta_1)\int_{\eta_{\rm i}}^{\eta}{\rm d}\eta_2 \mathcal{G}_{\rm k}(\eta,\eta_2)\langle \mathcal{T}_{\mathbf{k}}^{(\lambda)}\mathcal{T}_{\mathbf{k}'}^{(\lambda')}\rangle \tag{2.187}$$

where $\mathcal{T}_{\mathbf{k}}^{(\lambda)} = e^{ij(\lambda)}(\mathbf{k})P_{ij}^{lm}T_{lm}^{(\rm EM)}$. The energy-momentum tensor of the electromagnetic field in Fourier space is given by

$$\begin{aligned} T_{lm}^{(\rm EM)}(\mathbf{k},\eta) = \frac{1}{4\pi a^2(\eta)}\int \frac{d^3\mathbf{q}}{(2\pi)^{3/2}}\Big[&B_l(q,\eta)B_m^*(\mathbf{q}-\mathbf{k},\eta) + E_l(\mathbf{q},\eta)E_m^*(\mathbf{q}-\mathbf{k},\eta) \\ &-\frac{1}{2}g_{lm}\Big(B_a(\mathbf{q},\eta)B^{*a}(\mathbf{q}-\mathbf{k},\eta) + (E_a(\mathbf{q},\eta)E^{*a}(\mathbf{q}-\mathbf{k},\eta)\Big)\Big]. \end{aligned} \tag{2.188}$$

Since only the transverse and traceless components can source tensor perturbations, the application of the projection tensor P_{ij}^{lm} eliminates all diagonal contributions of the energy-momentum tensor, leaving only the first two terms as the relevant sources. The polarization tensor $e^{ij(\lambda)}(\mathbf{k})$ satisfies the normalization condition

$$e^{ij(\lambda)}(\mathbf{k})e_{ij}^{(\lambda')}(\mathbf{k}') = 2\delta^{\langle\lambda'}\delta^{(3)}(\mathbf{k}-\mathbf{k}'). \tag{2.189}$$

Using this relation, the two-point correlation function of the energy-momentum tensor can be expressed as follows. Under the assumption of statistical homogeneity and isotropy, the correlator takes the standard form

$$\begin{aligned} \langle \mathcal{T}_{\mathbf{k}}^{(\lambda)}\mathcal{T}_{\mathbf{k}'}^{(\lambda')}\rangle = &\frac{1}{4\pi a^2(\eta_1)}\frac{1}{4\pi a^2(\eta_2)}\int\frac{d^3\mathbf{q}}{(2\pi)^3}\int\frac{d^3\mathbf{q}'}{(2\pi)^3}P_{ij}^{mn}(\mathbf{k})P_{ab}^{ij}(\mathbf{k}')\times \\ &\Big(\langle \tilde{B}_m(\mathbf{q},\eta)\tilde{B}_n^*(\mathbf{q}-\mathbf{k},\eta)\tilde{B}^{*a}(\mathbf{q}',\eta)\tilde{B}^b(\mathbf{q}'-\mathbf{k}',\eta')\rangle \\ &+\langle \tilde{E}_m(\mathbf{q},\eta)\tilde{E}_n^*(\mathbf{q}-\mathbf{k},\eta)\tilde{E}^a(\mathbf{q}',\eta')\tilde{E}^b(\mathbf{q}'-\mathbf{k}',\eta')\rangle\Big)\,. \end{aligned} \tag{2.190}$$

It is evident that the evaluation of $\langle \mathcal{T}_{\mathbf{k}}^{(\lambda)} \mathcal{T}_{\mathbf{k}'}^{(\lambda')} \rangle$ involves four-point correlation functions such as $\langle \tilde{B}_m \tilde{B}_n^* \tilde{B}^{*a} \tilde{B}^b \rangle$. These four-point functions can be expressed in terms of two-point correlation functions using Wick's theorem,

$$\begin{aligned}\langle \tilde{B}_m(\mathbf{q},\eta)\tilde{B}_m^*(\mathbf{q}-\mathbf{k},\eta)\tilde{B}_m^{*a}(\mathbf{q}',\eta')\tilde{B}_m^b(\mathbf{q}'-\mathbf{k}',\eta')\rangle = \\ \langle \tilde{B}_m(\mathbf{q},\eta)\tilde{B}_n^*(\mathbf{q}-\mathbf{k},\eta)\rangle\langle \tilde{B}^{*a}(\mathbf{q}',\eta')\tilde{B}^b(\mathbf{q}'-\mathbf{k}',\eta')\rangle \\ + \langle \tilde{B}_m(\mathbf{q},\eta)\tilde{B}^{*a}(\mathbf{q}',\eta')\rangle\langle \tilde{B}_n^*(\mathbf{q}-\mathbf{k},\eta)\tilde{B}^b(\mathbf{q}'-\mathbf{k}',\eta')\rangle \\ + \langle \tilde{B}_m(\mathbf{q},\eta)\tilde{B}^b(\mathbf{q}'-\mathbf{k}',\eta')\rangle\langle \tilde{B}_n^*(\mathbf{q}-\mathbf{k},\eta)\tilde{B}^{*a}(\mathbf{q}',\eta')\rangle. \end{aligned} \tag{2.191}$$

For convenience, we define the comoving electric and magnetic fields as

$$B_i = a^{-1}\tilde{B}_i; \quad B^i = a^{-3}\tilde{B}^i; \qquad E_i = a^{-1}\tilde{E}_i; \quad E^i = a^{-3}\tilde{E}^i. \tag{2.192}$$

In general, the tensor power spectrum sourced by the anisotropic stress of the electromagnetic field involves the unequal-time correlation function $\langle \mathcal{T}_{\mathbf{k}}^{(\lambda)}(\eta) \mathcal{T}_{\mathbf{k}'}^{(\lambda')}(\eta') \rangle$, which characterizes how the source at two different times contributes coherently to the production of tensor perturbations. However, retaining the full unequal-time structure makes the analysis analytically intractable. Therefore, it is common to assume equal-time correlations instead of unequal-time correlations, which significantly simplifies the calculations.

In most scenarios considered here, magnetic fields are generated during inflation or reheating and subsequently evolve adiabatically. Consequently, the physical processes responsible for gravitational-wave production are not significantly affected by the equal-time approximation. Physically, this assumption is justified when the coherence time of the anisotropic stress is much shorter than the typical timescale associated with gravitational-wave evolution. In this regime, the correlation between two different times can be approximated by a delta function in conformal time, effectively reducing the unequal-time correlation to an equal-time one. In the remainder of this work, we therefore assume that the source terms are equal-time correlated.

For a non-helical magnetic field, the two-point correlation functions can be expressed in terms of the corresponding power spectra as

$$\langle \tilde{B}_i(k,\eta)\tilde{B}_j^*(k',\eta)\rangle = \delta^{(3)}(k-k')(\delta_{ij}-\hat{k}_i\hat{k}_j)P_{\mathrm{B}}(k,\eta), \tag{2.193}$$

$$\langle \tilde{E}_i(k,\eta)\tilde{E}_j^*(k',\eta)\rangle = \delta^{(3)}(k-k')(\delta_{ij}-\hat{k}_i\hat{k}_j)P_{\mathrm{E}}(k,\eta). \tag{2.194}$$

Substituting these relations into Eq.(2.187), the tensor power spectrum sourced by electromagnetic fields can be written as [117, 118, 220–222, 229, 232–234]

$$
\begin{aligned}
P_{\mathrm{T}}^{\mathrm{sec}(\lambda)}(k,\eta) = {} & \frac{2}{M_{\mathrm{P}}^4}\int_{\eta_i}^{\eta} \mathrm{d}\eta_1\, \frac{\mathcal{G}_{\mathrm{k}}(\eta,\eta_1)}{\mathrm{a}^2(\eta_1)} \int_{\eta_i}^{\eta} \mathrm{d}\eta_1\, \frac{\mathcal{G}_{\mathrm{k}}(\eta,\eta_1)}{\mathrm{a}^2(\eta_1)} \\
& \times \int_0^{\infty} \frac{\mathrm{dq}}{q} \int_{-1}^{1} \mathrm{d}\mu\, \mathcal{F}(\mathrm{k},\mathrm{q},\mu) \frac{\mathcal{P}_{\mathrm{B}}(\mathrm{q},\eta_1 \mathcal{P}_{\mathrm{B}}(|\mathbf{k}-\mathbf{q}|,\eta_1) + \mathcal{P}_{\mathrm{E}}(\mathrm{q},\eta_1 \mathcal{P}_{\mathrm{E}}(|\mathbf{k}-\mathbf{q}|,\eta_1)}{[1+(\mathrm{q}/\mathrm{k})^2 - 2\mu(\mathrm{q}/\mathrm{k})]^{3/2}}.
\end{aligned}
\tag{2.195}
$$

In the non-helical case, both polarization states of the electromagnetic field contribute symmetrically. In contrast, for helical fields, the two circular polarization modes evolve differently due to the presence of parity-violating interactions. The scalar kernel can be expressed in a unified form as [220–222, 232, 234]

$$
\mathcal{F}(k,q,\mu) = \begin{cases} 2(1+\mu^2)(1+\beta^2), & \text{for non-helical fields,} \\ \dfrac{1}{16}(1+\lambda\mu)^2(1+\lambda\beta)^2, & \text{for helical fields,} \end{cases} \tag{2.196}
$$

where $\mu = \hat{\mathbf{k}}\cdot\hat{\mathbf{q}} = \cos\theta$ and $\beta = \widehat{\mathbf{k}-\mathbf{q}}\cdot\hat{\mathbf{k}}$. Here θ denotes the angle between $\mathbf{k}$ and $\mathbf{q}$, and $\lambda = \pm 1$ labels the helicity of the circular polarization states.

From the above expression, it is clear that once the time evolution of the electric and magnetic fields is known for a given cosmological epoch, and the corresponding Green's function is specified, the secondary contribution to the tensor power spectrum can be evaluated by substituting Eq. (2.196) into Eq. (2.195).

Production of secondary Tensor power spectrum during de-sitter inflationary background

In the previous subsection, we developed the general formalism for the tensor power spectrum sourced by the electromagnetic field. As an illustrative example, we now consider a simple single power-law type magnetic spectrum in order to study the secondary production of tensor perturbations. We assume that due to some non-trivial coupling during inflation, when the modes exit the horizon, they become excited and produce a significant amount of electromagnetic field. After the horizon crossing, the spectrum is assumed to follow a simple single power-law behaviour.

For simplicity, we consider only the magnetic field contribution in the calculation. In the final result, however, the tensor power spectrum can be written including contributions from both electric and magnetic fields. We parametrize the electromagnetic power spectrum as [117, 235–238]

$$
\mathcal{P}_{\mathrm{B}}^{\mathrm{inf}}(k,\eta) \simeq \begin{cases} H_{\mathrm{e}}^4 \mathcal{C}_{\mathrm{B}}(-k\eta)^{n_{\mathrm{B}}} & |-k\eta| \leq 1 \text{ (Super-horizon scales)} \\ 0 & |-k\eta| > 1 \text{ (sub-horizon scales)} \end{cases} \tag{2.197}
$$

We recall that here H_{e} denotes the Hubble constant during inflation, and we simply assume that it remains constant throughout the entire inflationary period.

In the above Eq.(2.198), we use a renormalised form of the power spectrum in which the k^4 contribution has been subtracted. This subtraction is necessary because these modes remain in the Bunch-Davies vacuum state, and the gauge field can only become excited when the modes leave the horizon. After horizon crossing, the fluctuations can be interpreted as a physical magnetic field. In practice, the energy density of the super-horizon modes is exponentially suppressed. For simplicity, we neglect their entire contribution by setting it to zero.

Similarly, the electric field spectrum can be parametrized in the same way. For a simple power-law behaviour of the electromagnetic field, one can write the above Eq.(2.195) as

$$P_{\mathrm{T}}^{\mathrm{sec}(\lambda)}(k,\eta) = \frac{2}{M_{\mathrm{P}}^4}\int_0^\infty \frac{\mathrm{dq}}{q}\int_{-1}^{1}\mathrm{d}\mu\,\frac{\mathcal{F}(\mathrm{k},\mathrm{q},\mu)}{[1+(\mathrm{q}/\mathrm{k})^2-2\mu(\mathrm{q}/\mathrm{k})]^{3/2}} \times\left(\int_{\eta_i}^{\eta_{\mathrm{e}}}\mathrm{d}\eta_1\,\frac{\mathcal{G}_{\mathrm{k}}(\eta_{\mathrm{e}},\eta_1)}{\mathrm{a}^2(\eta_1)}\tilde{\mathcal{P}}_{\mathrm{B}}^{1/2}(\mathrm{q},\eta_1)\tilde{\mathcal{P}}_{\mathrm{B}}^{1/2}(|\mathbf{k}-\mathbf{q}|,\eta_1)\right)^2 \tag{2.198}$$

In the above equation, $\mathcal{G}_k(\eta_{\mathrm{e}},\eta_1)$ represents the Green's function associated with Eq.(2.146). In a de-sitter inflationary background, the Green's function is well known and can be written as [239]

$$\mathcal{G}_k^{\mathrm{inf}}(\eta_{\mathrm{e}},\eta_1) = \frac{\Theta(\eta_{\mathrm{e}}-\eta_1)}{k^3\eta_1^2}\left[(1+k^2\eta_1\eta_{\mathrm{e}})\sin\Big(k(\eta_{\mathrm{e}}-\eta_1)\Big)+(\eta_1-\eta_{\mathrm{e}})\cos\Big(k(\eta_{\mathrm{e}}-\eta_1)\Big)\right]. \tag{2.199}$$

Before solving Eq.(2.198), we define two dimensionless parameters $x=-k\eta$ and $u=q/k$. Substituting Eq.(2.199) and Eq.(2.198) into the above expression, the tensor power spectrum sourced by the magnetic field in a de-sitter inflationary background can be written as

$$P_{\mathrm{T}}^{\mathrm{sec}(\lambda)}(k,\eta_{\mathrm{e}}) = 2\left(\frac{H_{\mathrm{e}}}{M_{\mathrm{P}}}\right)^4\mathcal{C}_{\mathrm{B}}^2\int_{u_{\min}}^{u_{\max}}\frac{du}{u}\int_{-1}^{1}\mathrm{d}\mu\frac{\mathcal{F}(\mathrm{u},\mu)}{[1+\mathrm{u}^2-2\mu\mathrm{u}]^{(3-\mathrm{n_B})/2}} \times\left(\int_{x_k}^{x_{\mathrm{e}}}\frac{\mathrm{d}x_1}{x_1}x_1^{n_{\mathrm{B}}-3}\left\{(1+x_1^2)\sin(x_e-x_1)+(x_1-x_e)\cos(x_e-x_1)\right\}\right)^2 \tag{2.200}$$

Here the lower limit of the integral is $x_k=-k\eta_k=1$. This lower limit of the time integration arises from the fact that the gauge field becomes excited only when the modes leave the horizon during inflation. When a particular mode is inside the horizon, it effectively remains in the ground state, and therefore it does not contribute to the production of tensor perturbations.

After evaluating the above integral, the tensor power spectrum at the end of the inflationary era can be written as [117, 118, 229]

$$P_{\mathrm{T}}^{\mathrm{sec}(\lambda)}(k,\eta_{\mathrm{e}}) \simeq 2\left(\frac{H_{\mathrm{e}}}{M_{\mathrm{P}}}\right)^4\mathcal{C}_{\mathrm{B}}^2\mathcal{F}_{n_{\mathrm{B}}}(k)\mathcal{I}_{\mathrm{inf}}^2(k) \tag{2.201}$$

where $\mathcal{F}_{n_{\rm B}}$ and $\mathcal{I}_{\rm inf}$ are defined as

$$\mathcal{F}_{n_{\rm B}} = \frac{16}{3n_B}\left[1-\left(\frac{k_*}{k}\right)^{n_{\rm B}}\right] + \frac{112}{15(2n_{\rm B}-3)}\left[\left(\frac{k_{\rm e}}{k}\right)^{2n_{\rm B}-3} - 1\right]. \tag{2.202}$$

$$\mathcal{I}_{\rm inf} \simeq \frac{1}{3n_{\rm B}}\left\{1-\left(\frac{k}{k_{\rm e}}\right)^{n_{\rm B}}\right\} \tag{2.203}$$

From Eq.(2.201), it follows that for a blue-tilted or nearly scale-invariant electromagnetic power spectrum, the resulting tensor power spectrum in a de-sitter inflationary background remains approximately scale-invariant. However, if the electric or magnetic field spectrum is red-tilted, the resulting tensor power spectrum is also red-tilted. In such a case, the tensor power spectrum typically behaves as $P_{\rm T}^{\rm sec(\lambda)}(k) \propto k^{-|n_{\rm B/E}|}$ [240].

Chapter 3

Birth of Cosmic Magnetic Fields

3.1 Introduction

The origin of cosmic magnetic fields remains one of the long-standing puzzles in modern cosmology. Observations across a wide range of astrophysical scales reveal the ubiquitous presence of magnetic fields in the Universe. In galaxies and galaxy clusters, magnetic field strengths are observed to be of the order of μ-Gauss [241–244], whereas the intergalactic medium exhibits much weaker fields with an average strength of order $10^{-9} - 10^{-16}$ Gauss [245–257]. While magnetic fields on galactic and cluster scales can be efficiently amplified through dynamo mechanisms, these processes require the presence of pre-existing seed fields. The origin of such seed fields is still unclear and may trace back to primordial processes in the early Universe. In particular, when considering large-scale magnetic fields with coherence lengths exceeding 1 Mpc across the sky, no known astrophysical mechanism is capable of generating magnetic fields of the observed strength.

Observations of cosmic microwave background (CMB) anisotropies provide the most stringent upper bounds on large-scale magnetic fields, yielding $B_0(1\text{ Mpc}) \leq 10^{-9}$ Gauss [245–247]. On the other hand, high-energy γ-ray observations of distant blazars place a lower bound on the strength of intergalactic magnetic fields, requiring $B_0(1\text{ Mpc}) \geq 10^{-17}$ Gauss [248–251]. Identifying viable mechanisms for the generation of these primordial magnetic seed fields is therefore crucial for understanding the origin of the magnetized Universe observed today.

Several mechanisms have been proposed for the generation of primordial magnetic fields, depending on the cosmological epoch and the underlying microphysics responsible for their origin. The properties of the generated magnetic fields, including their amplitude and spectral shape, depend sensitively on the background dynamics and the nature of the couplings involved. Below, we present a structured overview of the most widely studied magnetogenesis scenarios in the literature.

- **Inflationary Magnetogenesis:** Inflation provides a natural framework for generating magnetic fields on cosmological (super-horizon) scales. However, standard electromagnetism is conformally invariant, which prevents the amplification of magnetic fields in a conformally flat FRW background. To overcome this limitation, conformal invariance must be broken by introducing additional couplings to the gauge field. One commonly studied class of models involves **kinetic coupling**, where the interaction Lagrangian takes the form $\mathcal{L} = -\frac{1}{4}I^2(\phi)F_{\mu\nu}F^{\mu\nu}$ or $\mathcal{L} \propto \gamma I^2(\phi)F_{\mu\nu}\tilde{F}^{\mu\nu}$ [47,85,235,237,238,238,258–262,262–274], with $I(\phi)$ depending on the inflaton or a spectator scalar field. For simplicity, $I(\eta)$ is often parametrized as a time-dependent function of the form $I(\eta) \propto \eta^\alpha$, where α is a free parameter [235, 238]. Another well-studied scenario involves **axial (parity-violating) coupling**, $\mathcal{L} \propto -\frac{\alpha}{f_\phi}\phi F_{\mu\nu}\tilde{F}^{\mu\nu}$ [221,275–282], where ϕ is an axion-like inflaton field, leading to the generation of helical magnetic fields. Additionally, **curvature coupling** models, such as $\mathcal{L} \propto RF_{\mu\nu}F^{\mu\nu}$ or $R_{\mu\nu}A^\mu A^\nu$, have also been explored [85].

- **Magnetogenesis during Cosmological Phase Transitions:** Cosmological phase transitions in the early Universe, such as the electroweak and quantum chromodynamics (QCD) transitions, provide natural environments for the generation of primordial magnetic fields [47, 231, 283–295]. If a phase transition is of first order, the nucleation, expansion, and collision of true-vacuum bubbles drive strong out-of-equilibrium dynamics. These processes lead to charge separation, plasma turbulence, and the generation of electric currents, which can efficiently source magnetic fields through causal magnetohydrodynamic mechanisms [288, 292, 296]. The coherence length of the generated fields is limited by the horizon size at the time of the transition. In the presence of CP-violating interactions, the resulting magnetic fields may acquire non-zero helicity, triggering an inverse cascade that transfers magnetic power to larger scales [47, 297, 297–300]. The resulting magnetic field spectra are typically blue-tilted and depend on the transition temperature, latent heat, and duration of the phase transition. Such magnetic fields also act as sources of anisotropic stress, potentially leaving observable imprints in the stochastic gravitational wave background [231, 284–286, 301].

- **Topological Defects:** Topological defects [287, 302], such as cosmic strings [303–307], domain walls [308], and monopoles [309], can form during symmetry-breaking phase transitions in the early Universe and provide natural sites for magnetic field generation. The non-equilibrium dynamics associated with the formation, evolution, and decay of these defects can induce electric currents and vorticity in the surrounding primordial plasma, thereby sourcing magnetic fields through causal magnetohydrodynamic processes. In particular, superconducting cosmic strings can carry persistent currents along their cores, directly generating magnetic fields in the ambient medium. More generally, the motion and interaction of defect networks can stir the plasma, leading to turbulent flows that further amplify magnetic fields. Since these processes are causal, the resulting magnetic fields are correlated on sub-horizon scales determined by the defect dynamics and the symmetry-breaking scale, and typically exhibit blue-tilted spectra. These magnetic fields may also source anisotropic stress, leaving imprints on cosmological observables, including the stochastic gravitational wave background.

- **Higher-Order Cosmological Perturbations:** Higher-order cosmological perturbations naturally break the conformal invariance of the gauge field, leading to the excitation of gauge fields from the vacuum [233, 310]. In this context, velocity perturbations and relative velocities between oppositely charged particles can induce magnetic fields []. Although this mechanism can generate magnetic fields on all scales, the resulting field strengths are typically very weak. Nevertheless, such magnetic fields are unavoidable and can serve as a minimal primordial magnetic field background.

Among the proposed scenarios, inflationary magnetogenesis and the subsequent post-inflationary dynamics provide natural frameworks for generating magnetic fields on cosmological scales [311]. These mechanisms typically require the breaking of the conformal invariance of standard electromagnetism, which can be achieved through couplings to scalar fields, spacetime curvature, or higher-order operators. Depending on the specific model, the generated magnetic fields may exhibit distinctive spectral features and correlation properties, potentially leading to observable imprints such as a stochastic background of gravitational waves. Before discussing in detail the generation of large-scale magnetic fields during inflation, it is therefore useful to first provide an overview of how current observational data can be used to place constraints on the strength of primordial magnetic fields.

3.2 Observational Constraints on Large-Scale Magnetic Fields

A wide range of astrophysical and cosmological observations provide important constraints on the strength, coherence length, and origin of large-scale magnetic fields. Since magnetic fields can influence the dynamics of the Universe at different epochs, from the early radiation-dominated era to the present day, these observations probe magnetic fields across a broad range of length scales and cosmic times.

One of the most powerful probes of large-scale magnetic fields is the Cosmic Microwave Background (CMB). Primordial magnetic fields contribute to the energy–momentum tensor and act as a source of scalar, vector, and tensor perturbations. Consequently, they modify the temperature and polarization anisotropies of the CMB. In particular, magnetic fields can generate vector modes, which are otherwise absent in standard cosmology, and contribute to B-mode polarization. Measurements of the CMB angular power spectra therefore place stringent upper bounds on the amplitude of primordial magnetic fields, typically constraining the comoving field strength smoothed on megaparsec scales to be at most of order nanogauss. In addition, magnetic fields present during recombination induce Faraday rotation of the CMB polarization, leading to a frequency-dependent mixing of E- and B-modes, which provides an independent and complementary constraint.

Additional constraints arise from Big Bang Nucleosynthesis (BBN). Magnetic fields present in the early Universe contribute to the total energy density and can alter the expansion rate during the nucleosynthesis epoch. This affects the predicted abundances of light elements.

The agreement between theoretical predictions and observed primordial abundances therefore limits the magnetic energy density during BBN, providing indirect but robust constraints on primordial magnetic fields at very high redshifts.

Observations of Faraday rotation measures of distant extragalactic radio sources offer another important probe of large-scale magnetic fields, particularly in the intergalactic medium. As linearly polarized radiation propagates through a magnetized plasma, the plane of polarization is rotated by an amount proportional to the line-of-sight component of the magnetic field and the free-electron density. Statistical analyses of rotation measures, after accounting for Galactic and source contributions, constrain the amplitude and coherence length of magnetic fields on cosmological scales, typically yielding upper limits in the nanogauss range for megaparsec-scale fields.

Gamma-ray observations of distant blazars provide a unique and complementary method to probe extremely weak intergalactic magnetic fields. High-energy gamma rays emitted by blazars interact with the extragalactic background light, producing electron–positron pairs that subsequently upscatter Cosmic Microwave Background photons to GeV energies. The presence of intergalactic magnetic fields deflects these charged particles, suppressing or delaying the secondary gamma-ray signal. The non-observation of such cascade emission has been interpreted as evidence for a lower bound on the intergalactic magnetic field strength, typically in the range 10^{-17}–10^{-15} G, depending on the magnetic field coherence length.

Large-scale magnetic fields may also influence the formation and evolution of cosmic structures. Magnetic pressure and Lorentz forces can modify the growth of density perturbations, leaving imprints on large-scale structure observables such as the matter power spectrum, galaxy clustering, and the Lyman-α forest. While these constraints are generally more model-dependent, they provide additional upper limits on magnetic fields on megaparsec scales.

Taken together, these observational probes place strong and complementary constraints on large-scale magnetic fields over a wide range of epochs and length scales. While CMB and large-scale structure observations primarily provide upper limits on primordial magnetic fields, gamma-ray observations yield lower bounds on intergalactic fields in the late Universe. These constraints significantly restrict viable scenarios of cosmic magnetogenesis and motivate the study of additional observational signatures, such as gravitational waves sourced by magnetic fields, which will be discussed in subsequent sections.

3.3 Inflationary Magnetogenesis

Within the framework of inflationary cosmology, it is widely conjectured that the present-day large-scale magnetic fields, much like dark matter, may originate as cosmological relics from the early Universe. In particular, primordial magnetic fields can be generated through the inflationary dynamics of the electromagnetic (EM) field when its conformal invariance is broken via non-minimal couplings.

As a generic framework for inflationary magnetogenesis, we begin by considering the following Lagrangian [264, 312]:

$$\mathcal{L} = \mathcal{L}_g + \mathcal{L}_{gs} + \mathcal{L}_{gA}. \tag{3.1}$$

Here, $\mathcal{L}_g$ represents the purely gravitational sector, while $\mathcal{L}_{gs}$ describes the gravitational interactions of a massive scalar field. Since the standard electromagnetic action is conformally invariant, an additional interaction term is required to break this invariance and enable the generation of electric and magnetic fields during inflation. This is achieved by introducing a coupling function $f_{1,2}(\phi, R)$ in the electromagnetic sector $\mathcal{L}_{gA}$, which takes the form

$$\begin{aligned}\mathcal{L}_{gA} &= -\frac{1}{4}\sqrt{-g}g^{\mu\nu}g^{\alpha\beta}f_1^2(\varphi, R)F_{\mu\alpha}F_{\nu\beta} - \frac{1}{4}\sqrt{-g}g^{\mu\nu}g^{\alpha\beta}f_2^2(\varphi, R)F_{\mu\alpha}\tilde{F}_{\nu\beta} &(3.2)\\ &= -\frac{1}{4}\sqrt{-g}f_1^2(\varphi, R)F_{\mu\nu}F^{\mu\nu} - \frac{1}{4}\sqrt{-g}f_2^2(\varphi, R)F_{\mu\nu}\tilde{F}^{\mu\nu}. &(3.3)\end{aligned}$$

The total Lagrangian corresponding to Eq. (3.1) can then be written as [312]

$$\begin{aligned}\mathcal{L} = 2\kappa^{-2}\sqrt{-g}R + \sqrt{-g}\left[g^{\mu\nu}(D_\mu\varphi)^*(D_\nu\varphi) - V(\varphi)\right]\\ - \frac{1}{4}\sqrt{-g}f_1^2(\varphi, R)F_{\mu\nu}F^{\mu\nu} - \frac{1}{4}\sqrt{-g}f_2^2(\varphi, R)F_{\mu\nu}\tilde{F}^{\mu\nu}.\end{aligned} \tag{3.4}$$

Since all fundamental charged particles are produced after inflation during the reheating epoch, the covariant derivative can be simplified during inflation by replacing $D_\mu = \partial_\mu + ieA_\mu$ with $D_\mu = \partial_\mu$. Consequently, the Lagrangian reduces to

$$\begin{aligned}\mathcal{L} = 2\kappa^{-2}\sqrt{-g}R + \sqrt{-g}\left[g^{\mu\nu}(\partial_\mu\varphi)^*(\partial_\nu\varphi) - V(\varphi)\right]\\ - \frac{1}{4}\sqrt{-g}f_1^2(\varphi, R)F_{\mu\nu}F^{\mu\nu} - \frac{1}{4}\sqrt{-g}\gamma f_2^2(\varphi, R)F_{\mu\nu}\tilde{F}^{\mu\nu}.\end{aligned} \tag{3.5}$$

The total action of the system is therefore given by [221, 313]

$$\begin{aligned}\mathcal{S} &= \mathcal{S}_g + \mathcal{S}_{gs} + \mathcal{S}_{gA}\\ &= \int d^4x\sqrt{-g}\left(2\kappa^{-2}R + \left[g^{\mu\nu}(\partial_\mu\varphi)^*(\partial_\nu\varphi) - V(\varphi)\right] - \frac{1}{4}f_1^2(\varphi, R)F_{\mu\nu}F^{\mu\nu} - \frac{1}{4}\gamma f_2^2(\phi, R)F_{\mu\nu}\tilde{F}^{\mu\nu}\right).\end{aligned} \tag{3.6}$$

Here, φ is identified with the inflaton field, and R denotes the Ricci scalar. The electromagnetic field strength tensor is defined as $F_{\mu\nu} = \partial_\mu A_\nu - \partial_\nu A_\mu$, while its dual is given by $\tilde{F}^{\mu\nu} = \frac{1}{2}\epsilon^{\mu\nu\alpha\beta}F_{\alpha\beta}$, with $\epsilon^{\mu\nu\alpha\beta} = \frac{1}{\sqrt{-g}}\eta^{\mu\nu\alpha\beta}$. The functions f_1 and f_2 represent arbitrary conformal symmetry–breaking couplings. For simplicity, we assume $f_1(\varphi, R) = f_2(\varphi, R)$, and γ is introduced as a parity-violating parameter.

The four-vector potential can be decomposed as $A_\mu = (A_0, \partial_i S + V_i)$. Working in the Coulomb gauge, defined by $A_0 = 0$ and $\partial_i V^i = 0$, and adopting the spatially flat FLRW metric in conformal coordinates,

$$ds^2 = a(\eta)^2 \left(-d\eta^2 + dx^2 + dy^2 + dz^2\right), \tag{3.7}$$

The action takes the form

$$\begin{aligned}\mathcal{S} = \int d^4x\sqrt{-g}\,\Big(2\kappa^{-2}R + [g^{\mu\nu}(\partial_\mu\varphi)^*(\partial_\nu\varphi) - V(\varphi)] \\ + \frac{1}{a^4}\Big\{f_1^2(\varphi,R)\left(\frac{1}{2}A_i'A_i' - \frac{1}{2}\partial_iA_j\partial_iA_j\right) + \gamma f_1^2(\varphi,R)\eta^{ijk}A_i'\partial_jA_k\Big\}\Big).\end{aligned} \tag{3.8}$$

Owing to the conformal structure of the electromagnetic sector, the action in Eq. (3.8) becomes independent of the scale factor. Spatial indices are raised and lowered using the Kronecker delta. Expanding the vector potential in Fourier space,

$$A_i(\eta,x) = \sum_{\lambda=\pm}\int \frac{d^3k}{(2\pi)^3}\epsilon_i^\lambda(\mathbf{k})e^{i\mathbf{k}\cdot\mathbf{x}}u_k^\lambda(\eta), \tag{3.9}$$

with the reality condition $u_{-k}^\lambda = u_k^{\lambda *}$, the polarization vectors $\epsilon_i^\lambda(\mathbf{k})$ satisfy

$$\epsilon_i^\lambda(\mathbf{k})k^i = 0, \qquad \delta^{ij}\epsilon_i^\lambda(\mathbf{k})\epsilon_j^{\lambda'}(\mathbf{k}) = \delta^{\lambda\lambda'}.$$

The corresponding mode functions obey the equation of motion [221,235,238,264–266,314]

$$u_k^{(\lambda)''} + 2\frac{f_1'}{f_1}u_k^{(\lambda)'} + 2\gamma\lambda k\frac{f_1'}{f_1}u_k^{(\lambda)} + k^2u_k^{(\lambda)} = 0, \tag{3.10}$$

where the prime denotes differentiation with respect to conformal time η.

Defining the conjugate momentum $\pi_k^\lambda = f_1^2\left(u_k^{\lambda'} + \lambda\gamma k u_k^\lambda\right)$, the Hamiltonian can be written as

$$\mathcal{H} = \frac{f_1^2}{2}\sum_{\lambda=1,2}\int\frac{d^3k}{(2\pi)^3}\left(u_k^{\lambda *'}u_k^{\lambda'} + k^2u_k^{\lambda *}u_k^\lambda\right). \tag{3.11}$$

Upon quantization, the field variables are promoted to operators and expressed in terms of time-dependent creation and operators [262,311] as

$$\pi_k^\lambda = -if_1\sqrt{\frac{k}{2}}(a_k^\lambda - a_{-k}^{\lambda\dagger})\ ;\ u_k^\lambda = \frac{1}{f_1}\sqrt{\frac{1}{2k}}(a_k^\lambda + a_{-k}^{\lambda\dagger}), \tag{3.12}$$

with the canonical commutation relation

$$[a_k^{\lambda'}, a_{k'}^{\lambda\dagger}] = (2\pi)^3\delta^{\lambda\lambda'}\delta^{(3)}(\mathbf{k}-\mathbf{k}').$$

The Hamiltonian for each mode k then becomes [262, 311]

$$H_k = \frac{k}{4}\sum_{\lambda}\left(a_k^{\lambda\dagger}a_k^{\lambda} + a_{-k}^{\lambda}a_{-k}^{\lambda\dagger} + \mathrm{cc}\right) = \sum_{\lambda}\frac{k}{2}\left(a_k^{\lambda\dagger}a_k^{\lambda} + a_k^{\lambda}a_k^{\lambda\dagger}\right), \tag{3.13}$$

which is diagonal. The time evolution of the system can be described using Bogoliubov transformations,

$$a_k^{\lambda}(\tau) = \alpha_k^{\lambda}(\tau)a_k^{\lambda}(0) + \beta_k^{\lambda *}(\tau)a_{-k}^{\lambda\dagger}(0),$$

where the Bogoliubov coefficients satisfy $|\alpha_k^{\lambda}|^2 - |\beta_k^{\lambda}|^2 = 1$. The quantity $|\beta_k^{\lambda}|^2$ corresponds to the number density of photons produced from the vacuum. The explicit forms of the Bogoliubov coefficients are consistent with the normalization condition

$$f_1^2\left(u_k^{\lambda}u_k^{\prime *\lambda} - u_k^{*\lambda}u_k^{\prime\lambda}\right) = i,$$

are given by [237]

$$\alpha_k^{\lambda} = f_1\left(\sqrt{\frac{k}{2}}u_k^{\lambda} + \frac{i}{\sqrt{2k}}u_k^{\prime\lambda}\right), \qquad \beta_k^{\lambda} = f_1\left(\sqrt{\frac{k}{2}}u_k^{\lambda} - \frac{i}{\sqrt{2k}}u_k^{\prime\lambda}\right). \tag{3.14}$$

The electric and magnetic power spectra can be expressed in terms of the mode functions as [237]

$$\mathcal{P}_E = \frac{f_1^2 k^3}{4\pi^2 a^4}\sum_{\lambda=\pm}|u_k^{\lambda\prime}|^2, \qquad \mathcal{P}_B = \frac{f_1^2 k^5}{4\pi^2 a^4}\sum_{\lambda=\pm}|u_k^{\lambda}|^2. \tag{3.15}$$

To facilitate solving the mode equation, we introduce a new field variable $\mathcal{V}_k^{(\lambda)} = f_1 u_k^{(\lambda)}$, under which Eq. (3.10) transforms into [235, 238, 264–267, 314, 315]

$$\mathcal{V}_k^{(\lambda)\prime\prime} + \left(k^2 - \frac{f_1''}{f_1} + 2\gamma\lambda k\frac{f_1'}{f_1}\right)\mathcal{V}_k^{(\lambda)} = 0. \tag{3.16}$$

In terms of this transformed variable, the electric and magnetic power spectra become [235, 236, 238, 266]

$$\mathcal{P}_B(k) = \frac{k^5}{4\pi^2 a^4}\sum_{\lambda=\pm}|\mathcal{V}_k^{(\lambda)}|^2, \qquad \mathcal{P}_E(k) = \frac{k^3}{4\pi^2 a^4}\sum_{\lambda=\pm}\left|\mathcal{V}_k^{(\lambda)\prime} - \frac{f_1'}{f_1}\mathcal{V}_k^{(\lambda)}\right|^2. \tag{3.17}$$

Using these observables, we will first compute the electromagnetic spectra in a de Sitter inflationary background without specifying a particular inflationary model, and subsequently derive constraints on the magnetogenesis parameters from present-day large-scale magnetic field (LSMF) bounds.

3.3.1 Evolution of the Electromagnetic field during Inflation:

To solve the evolution of the gauge field during inflation, we have to know the exact nature of the coupling function. For simplicity, we conisder a simple power-law type behaviour of the coupling dunction which is defined as [235–238, 262, 266, 311]

$$f_1(\eta) = \begin{cases} (a/a_{\rm e})^n & \text{for } a \leq a_{\rm e} \\ 1 & \text{for } a > a_{\rm e} \end{cases} \tag{3.18}$$

where $a_{\rm e}$ is the scale factor defined at the end of inflation, i.e., $\eta = \eta_{\rm e}$, where $\eta_{\rm e}$ is the conformal time defined at the end of inflation. No,w depending on the nature of the coupling, which is mainly defined by the parameter n, the behavior of the magnetic field will get modified [222, 236, 238, 262]. Throughout our analysis, we simply consider de-sitter inflationary background where the evolution of the scale factor is governed by $a(\eta) \simeq -1/(H_{\rm e}\eta)$. So in the de-sitter inflationary background, we can express the function formed of the coupling function in terms of the conformal time η as [117, 235–238, 262, 266, 311, 316]

$$f_1(\eta) = \begin{cases} (\eta_{\rm e}/\eta)^n & \text{for } a \leq a_{\rm e} \\ 1 & \text{for } a > a_{\rm e} \end{cases} \tag{3.19}$$

Now, if we look into Eq.(3.16), depending on the γ parameter, either we get a non-helical magnetic field for $\gamma = 0$, or we get a helical magnetic field for a non-zero value of γ, i.e., $\gamma \neq 0$. We are going to discuss these two scenarios separately.

Non-helical magnetic field: To get a non-helical magnetic field, we consider $\gamma = 0$, and then the equation of motion of the modified mode function is [221, 235, 238, 264–266, 314]

$$\mathcal{V}_{\mathbf{k}}^{(\lambda)''} + \left(k^2 - \frac{f_1''}{f_1}\right)\mathcal{V}_{\mathbf{k}}^{(\lambda)} = 0. \tag{3.20}$$

Replacing $f_1''/f_1 = n(n+1)/\eta^2$ in the above Eq.(3.20), we obtain

$$\mathcal{V}_{\mathbf{k}}'' + \left(k^2 - \frac{n(n+1)}{\eta^2}\right)\mathcal{V}_{\mathbf{k}} = 0 \tag{3.21}$$

The general solution of the above equation can be written in term of Bessel function [235, 238, 266, 314]

$$\mathcal{V}_{\mathbf{k}}(\eta) = \sqrt{-\eta}\left\{c_1 \mathrm{J}_{n+\frac{1}{2}}(-k\eta) + c_2 \mathrm{Y}_{n+1/2}(-k\eta)\right\} \tag{3.22}$$

To determine the values of c_1 and c_2, we impose the Bunch-Davies initial condition, assuming that all observed modes today were deep inside the Hubble horizon at the beginning of inflation. In the sub-horizon limit $|-k\eta| \to \infty$, the solution of the gauge field reduces to a simple plane wave $\mathcal{V}_{\mathbf{k}}(-k\eta \to \infty) \simeq e^{-ik\eta}/\sqrt{2k}$. Using this as an initial condition, we obtain the integration constants c_1 and c_2 as [235]

$$c_1 = \sqrt{\frac{\pi}{4k}}\frac{\exp(i\pi n/2)}{\cos(-\pi n)}, \qquad c_2 = \sqrt{\frac{\pi}{4k}}\frac{\exp(i\pi(1-n)/2)}{\cos(-\pi n)}. \tag{3.23}$$

Combining these results, we express the solution of the gauge field during inflation in terms of the Hankel function as [117, 235, 236, 238]

$$\mathcal{V}_{\mathbf{k}}(\eta) = \sqrt{-\frac{\pi\eta}{4}}e^{i(n+1/2)\pi/2}\mathrm{H}^{(1)}_{n+\frac{1}{2}}(-k\eta). \tag{3.24}$$

Now replacing this value in the above Eq.(3.17), we can write the electric and magnetic power spectrum during inflation is [117, 235–238]

$$\mathcal{P}_{\mathrm{B}}^{\mathrm{inf}}(k,\eta) = \frac{k^4}{8\pi a^4(\eta)}(-k\eta)\left|\mathrm{H}^{(1)}_{n+\frac{1}{2}}(-k\eta)\right|^2 \tag{3.25a}$$
$$\mathcal{P}_{\mathrm{E}}^{\mathrm{inf}}(k,\eta) = \frac{k^4}{8\pi a^4(\eta)}(-k\eta)\left|\mathrm{H}^{(1)}_{n-\frac{1}{2}}(-k\eta)\right|^2 \tag{3.25b}$$

As we are mainly interested on the large scale modes which had exit the horizon during inflation, i.e., $k < k_{\mathrm{e}}$, so all the we are interested on, are outside the horizon at the end of inflation. So if we take the super-horizon limit $-k\eta < 1$, then at the end of inflation i.e., $\eta = \eta_{\mathrm{e}}$, we can approximate the magnetic and electric power spectrum as [117, 235–238]

$$\left.\begin{aligned}\mathcal{P}_{\mathrm{B}}^{\mathrm{inf}}(k,\eta) &= \frac{H_{\mathrm{e}}^4}{8\pi}\frac{2^{2|n|+1}\Gamma^2\left(|n|+\frac{1}{2}\right)}{\pi^2}(-k\eta)^{-2|n|+4}\\ \mathcal{P}_{\mathrm{E}}^{\mathrm{inf}}(k,\eta) &= \frac{H_{\mathrm{e}}^4}{8\pi}\frac{\Gamma^2\left(|n|-\frac{1}{2}\right)2^{2|n|-1}}{\pi^2}(-k\eta)^{-2|n|+6}\end{aligned}\right\} \text{ for } n > \frac{1}{2}, \tag{3.26}$$

$$\left.\begin{aligned}\mathcal{P}_{\mathrm{B}}^{\mathrm{inf}}(k,\eta) &= \frac{H_{\mathrm{e}}^4}{8\pi}\frac{\Gamma^2\left(|n|-\frac{1}{2}\right)2^{2|n|-1}}{\pi^2}(-k\eta)^{-2|n|+6}\\ \mathcal{P}_{\mathrm{E}}^{\mathrm{inf}}(k,\eta) &= \frac{H_{\mathrm{e}}^4}{8\pi}\frac{2^{2|n|+1}\Gamma^2\left(|n|+\frac{1}{2}\right)}{\pi^2}(-k\eta)^{-2|n|+4}\end{aligned}\right\} \text{ for } n < -\frac{1}{2}. \tag{3.27}$$

From the above, we have found that depending on the nature of the coupling parameter n, the nature of the magnetic field and electric field spectral behavior get modified.

Backreaction and Strong Coupling problem: In models featuring a coupling of the form $f_1^2 F_{\mu\nu}F^{\mu\nu}$, the effective electromagnetic gauge coupling is given by $\alpha_{\mathrm{em}} = e^2/f_1^2$. Consequently, if the coupling function satisfies $f_1 \ll 1$ at the beginning of inflation, the effective gauge coupling becomes very large. This places the system in the strong coupling regime, rendering the perturbative treatment of the gauge field unreliable. Conversely, if the scenario is initialized with $f_1 \gg 1$ and evolves toward $f_1 = 1$ by the end of inflation, thus restoring conformal symmetry, the effective gauge coupling remains small throughout, with $\alpha_{\mathrm{em}} \lesssim e^2$. In such cases, the model avoids the strong coupling problem.

For the specific choice of the coupling function discussed in Eq. (3.18), we find that for $n > 0$, the initial value of the function is very small, $f_1(\eta_i) \ll 1$, where η_i denotes the beginning of the inflationary era. This implies that models with $n > 0$ generally suffer from strong coupling issues at early times. In contrast, for $n < 0$, the coupling function starts with a large value, avoiding the strong coupling problem altogether. As discussed in Eq. (3.27), for the regime $n < -1/2$, the electric and magnetic power spectra exhibit the following behavior

$$\mathcal{P}_{\mathrm{B}}^{\mathrm{inf}}(k,\eta) = \frac{H_{\mathrm{e}}^4}{8\pi}\frac{\Gamma^2\left(|n|-\frac{1}{2}\right)2^{2|n|-1}}{\pi^2}(-k\eta)^{n_{\mathrm{E}}+2}, \tag{3.28}$$

$$\mathcal{P}_{\mathrm{E}}^{\mathrm{inf}}(k,\eta) = \frac{H_{\mathrm{e}}^4}{8\pi}\frac{2^{2|n|+1}\Gamma^2\left(|n|+\frac{1}{2}\right)}{\pi^2}(-k\eta)^{n_{\mathrm{E}}}, \tag{3.29}$$

where $n_{\mathrm{E}} = 4-2|n|$ denotes the spectral index of the electric field. From the above discussion, it is evident that a scale-invariant magnetic power spectrum requires $n = -3$. For this specific choice of the coupling parameter, the electric spectrum scales as $\mathcal{P}_E(k,\eta) \propto (-k\eta)^{-2}$, implying that in the limit $|-k\eta| \to 0$, the energy density of the electric field diverges. Consequently, the electric energy density may exceed the inflationary background energy density by the end of inflation. Therefore, the choice $n = -3$ leads to a significant backreaction problem.

This consideration imposes both upper and lower bounds on the coupling parameter n. Beyond a certain threshold, the backreaction becomes negligible and the model remains consistent. To determine the lower bound on n, one must compute the total energy density associated with the electromagnetic field at the end of inflation, i.e., at conformal time $\eta = \eta_{\mathrm{e}}$. For $n < 0$, the total energy density of the electromagnetic field is given by

$$\rho_{\mathrm{EM}}^{\mathrm{inf}} = \int_{k_*}^{k_{\mathrm{e}}} d\ln(k) \times \mathcal{P}_{\mathrm{B/E}}(k,\eta_{\mathrm{e}}) \simeq \frac{H_{\mathrm{e}}^4}{8\pi}\frac{2^{2|n|+1}\Gamma^2\left(|n|+\frac{1}{2}\right)}{\pi^2}\frac{(1-(k_*/k_{\mathrm{e}})^{n_{\mathrm{E}}})}{n_{\mathrm{E}}}. \tag{3.30}$$

To compute the total electromagnetic energy density, we integrate over the comoving wavenumber k in the range $k_* \le k \le k_{\mathrm{end}}$, where k_* is the pivot scale corresponding to large wavelengths observable in the CMB, and k_{end} is the smallest scale that exits the horizon at the end of inflation. We take the ultraviolet cutoff to be $k_{\mathrm{UV,c}} = k_{\mathrm{end}}$, as only those modes that exit the horizon during inflation are excited via the coupling; modes that remain subhorizon throughout inflation stay in the Bunch-Davies vacuum and do not contribute to the observable magnetic field strength.

By requiring that the total energy density of the electromagnetic field remains subdominant compared to the background inflationary energy density at the end of inflation, we find that the coupling parameter must satisfy $n \ge -2.2$, assuming an inflationary energy scale $H_{\mathrm{inf}} \simeq 10^{-5}M_{\mathrm{P}}$ and an inflationary duration of $N_{\mathrm{inf}} \simeq 55$, where N_{inf} denotes the number of e-folds between horizon exit of the pivot scale and the end of inflation. Thus, to simultaneously avoid both the backreaction and strong coupling problems, the allowed range for the coupling parameter is $-2.2 \le n < 0$. Within this range, the magnetic power spectrum is always blue-tilted. For instance, at $n = -2$, the electric power spectrum becomes scale-invariant, while the magnetic power spectrum scales as $\mathcal{P}_B(k, \eta_e) \propto k^2$, indicating that most of the magnetic energy is concentrated near the cutoff scale $k \simeq k_{\rm end}$. As a result, the amplitude of large-scale magnetic fields is suppressed at the end of inflation.

3.3.2 Effect of Schwinger Pair Production

One important effect that may influence the evolution of primordial electromagnetic fields is the Schwinger production of charged particle–antiparticle pairs. In inflationary magnetogenesis models based on a time-dependent gauge kinetic function, a sufficiently strong electric field can trigger non-perturbative pair production from the vacuum. The produced charged particles induce an electric current, which acts as an effective conductivity of the medium. As a result, the conductivity introduces an additional damping term in the gauge-field equation of motion and can suppress the further amplification of the electromagnetic field. Therefore, it is important to examine whether the Schwinger effect significantly modifies the magnetogenesis scenario considered in this thesis.

We begin with the gauge-field action

$$S_A = -\frac{1}{4}\int d^4x\, \sqrt{-g}\, I^2(\phi) F_{\mu\nu}F^{\mu\nu}, \tag{3.31}$$

where $I(\phi)$ is the gauge kinetic function. The time evolution of $I(\phi)$ breaks the conformal invariance of electromagnetism and leads to the amplification of gauge-field fluctuations during inflation and reheating.

Ignoring the induced conductivity, the Fourier modes of the gauge field satisfy

$$A_k'' + 2\frac{I'}{I}A_k' + k^2 A_k = 0. \tag{3.32}$$

When the generated electric field becomes sufficiently strong, charged particles are produced through the Schwinger mechanism. These particles generate an induced conductivity σ, and the gauge-field equation is modified to

$$A_k'' + \left(2\frac{I'}{I} + \frac{a\sigma}{I^2}\right)A_k' + k^2 A_k = 0. \tag{3.33}$$

The Schwinger effect becomes important when the conductivity term is comparable to or larger than the amplification term. Therefore, the gauge-field evolution remains essentially unaffected provided

$$2\frac{I'}{I} \gg \frac{a\sigma}{I^2}. \tag{3.34}$$

To estimate the induced conductivity, we follow Ref. [?]. In the relativistic regime, the conductivity can be approximated as

$$\sigma \simeq \frac{2en_e}{E}, \tag{3.35}$$

where n_e is the number density of the produced charged particles. The evolution of n is governed by

$$n_e' + 2\mathcal{H}n_e = 2a\Gamma, \tag{3.36}$$

where Γ denotes the Schwinger pair-production rate. For a nearly constant electric field,

$$\Gamma \simeq \frac{(eE)^2}{4\pi^3} \exp\left(-\frac{\pi m^2}{eE}\right), \tag{3.37}$$

with m being the fermion mass.

Assuming that the production process reaches a quasi-steady state, one may estimate $n_e \simeq \frac{\Gamma}{H}$, which gives

$$\sigma \simeq \frac{e^3 E}{2\pi^3 H} \exp\left(-\frac{\pi m^2}{eE}\right). \tag{3.38}$$

Since the gauge field is kinetically coupled through $I(\phi)$, the effective gauge coupling is given by $e_{\text{eff}} = \frac{e}{I}$. Consequently, the conductivity term entering Eq. (3.33) is suppressed by the coupling function. For the class of models considered in this thesis, where the coupling evolves as $I(\eta) \propto \eta^n$, the condition in Eq. (3.34) can be written approximately as

$$2n \gtrsim \frac{e^3}{2\pi^3 I^2} \exp\left(-\frac{\pi m^2}{eE}\right). \tag{3.39}$$

Equation (3.39) shows that the importance of the Schwinger effect depends on both the fermion mass and the coupling function. For heavy charged particles satisfying $m \gg H$, the exponential factor strongly suppresses pair production, making the induced conductivity negligible. On the other hand, light charged particles can produce a sizable conductivity, which may significantly affect the gauge-field evolution.

Throughout this thesis, we restrict our analysis to coupling functions satisfying $I(\eta) \geq 1$ in order to avoid the strong-coupling problem. Moreover, we consider magnetogenesis parameters $n > 1/2$, which are required to generate sufficiently strong magnetic fields. Within this parameter space, the effective gauge coupling remains sufficiently small, and the Schwinger effect is expected to have only a limited impact during most of the evolution. Nevertheless, as the coupling function approaches unity near the end of inflation or reheating, the induced conductivity can become important and partially suppress the amplification of the electromagnetic field. Therefore, the Schwinger effect is expected to mainly affect modes leaving the horizon close to the end of inflation, or equivalently, modes amplified near the end of reheating in the sawtooth coupling scenario.

A complete treatment of the Schwinger effect requires solving the coupled evolution of the gauge field, the induced current, and the produced charged particles self-consistently. Such an analysis is beyond the scope of the present thesis and is left for future investigation.

Results for Inflationary Magnetogenesis (Non-helical): As discussed earlier, in order to avoid the strong-coupling problem in this class of magnetogenesis scenarios, we restrict ourselves to the parameter range $-2.2 < n < 0$. For this choice of parameters, the magnetic power spectrum behaves as $\mathcal{P}_{\rm B}^{\rm inf}(k,\eta) \propto k^{6-2|n|}$, which implies that the resulting magnetic spectrum is always blue-tilted.

For simplicity, we consider an instantaneous reheating scenario. We assume that immediately after the end of inflation, the Universe becomes highly conductive, leading to a rapid suppression of the electric field, while the magnetic field is frozen on super-horizon scales. Under these assumptions, the present-day magnetic field strength evaluated at the 1 Mpc scale can be expressed as [117]

$$B_0(1\,{\rm Mpc}^{-1}) \simeq 6.74\times 10^{-10}\, 2^{|n|-\frac{1}{2}}\Gamma\left(|n|-\frac{1}{2}\right)\left(\frac{1\,{\rm Mpc}^{-1}}{k_{\rm e}}\right)^{3-|n|} {\rm Gauss}\,. \tag{3.40}$$

We find that both the spectral shape and the present-day amplitude of the generated magnetic field are highly sensitive to the choice of the coupling parameter n. In particular, variations in n affect not only the tilt of the magnetic power spectrum but also the overall normalization of the magnetic field strength today. A precise determination of the present-day magnetic field predicted by the model therefore requires a detailed understanding of the reheating dynamics and the subsequent evolution of the electrical conductivity. These aspects will be discussed in Chapter 3.

In this work, we focus on an instantaneous reheating scenario. Adopting the upper bound on the tensor-to-scalar ratio, $r_{0.05} \simeq 0.036$, together with the scalar amplitude at CMB scales, $A_s \simeq 2.1\times 10^{-9}$ [11], we infer a Hubble scale during inflation of $H_{\rm e} \simeq 10^{-5}\, M_{\rm P}$. Substituting these values into Eq. (2.69), we find that the total duration of inflation corresponds to $N_{\rm inf} \simeq 59$ e-folds.

As an illustrative example, using this value in Eq. (3.40), we obtain a present-day magnetic field strength at the 1 Mpc scale of $B_0(1\,{\rm Mpc}) \simeq 7.4\times 10^{-34}$ G for $n = -2$, where the magnetic spectrum is blue tilted. For $n = -1.9$, the predicted field strength is further suppressed, yielding $B_0(1\,{\rm Mpc}) \simeq 2.5\times 10^{-36}$ G. The corresponding results for other values of the coupling parameter n in the instantaneous reheating scenario are summarized in Table 3.1.

Helical-magnetic field:

For the helical magnetogenesis scenario, we consider the coupling function to be of the form $f_1(\varphi, R) = f_2(\varphi, R)$, where the behaviour of the coupling function $f_1(\varphi, R)$ is defined in

n	-2.1	-2.0	-1.9	-1.8	-1.7
$B_0(1\,\mathrm{Mpc})$ (in Gauss)	2.2×10^{-31}	7.4×10^{-34}	2.5×10^{-36}	8.7×10^{-39}	3.06×10^{-41}

Table 3.1: In this table, we list the present-day magnetic field strength evaluated at the 1 Mpc scale for different values of the coupling parameter n, assuming an instantaneous reheating scenario.

Eq. (3.19). Using this functional form of the coupling function, the equation of motion for the mode function $\mathcal{V}_{\mathbf{k}}^{(\lambda)} = f(\phi, R)u_{\mathbf{k}}^{(\lambda)}$ can be written as [235, 238, 266]

$$\ddot{\mathcal{V}}_k^{(\lambda)}(z) + \left[\frac{1}{z^2}\left(\frac{1}{4} - (n+1/2)^2\right) + \frac{\kappa}{z} - \frac{1}{4}\right]\mathcal{V}_k^{(\lambda)}(z) = 0. \tag{3.41}$$

Here, the new variables are defined as $z = 2ik\eta$ and $\kappa = in\gamma\lambda$, and the over-dot denotes differentiation with respect to the newly defined dimensionless variable z.

The solution of Eq. (3.41) is given by the well-known Whittaker function [266],

$$\mathcal{V}_{\mathbf{k}}^{(\lambda)} = C_1 W_{\kappa,(n+1/2)}(z) + C_2 W_{-\kappa,(n+1/2)}(-z). \tag{3.42}$$

To determine the constants C_1 and C_2, we impose the Bunch–Davies initial condition, which assumes that all modes observed today were deep inside the Hubble horizon during inflation. In the sub-horizon limit $|-k\eta| \to \infty$, the mode function reduces to a simple plane wave, $\mathcal{V}_{k,\mathrm{BD}}^{(\lambda)} = e^{-ik\eta}/\sqrt{2k}$. Using this as the initial condition in Eq. (3.42), we obtain [235, 238, 266]

$$\mathcal{V}_{\mathbf{k}}^{(\lambda)}(\eta) = \frac{1}{\sqrt{2k}} e^{i\pi\kappa} W_{\kappa,(n+1/2)}(2ik\eta). \tag{3.43}$$

To study the spectral behavior of the generated electric and magnetic fields in this magnetogenesis scenario, we simplify Eq. (3.43) in the super-horizon limit, i.e., $|-k\eta| \ll 1$. In this limit, the Whittaker function reduces to [238, 266]

$$\lim_{z\ll1} W_{\lambda,\mu}(z) \to \frac{\Gamma(-z\mu)}{\Gamma\left(\frac{1}{2} - \lambda - \mu\right)} z^{\frac{1}{2}+\mu} + \frac{\Gamma(z\mu)}{\Gamma\left(\frac{1}{2} - \lambda + \mu\right)} z^{\frac{1}{2}-\mu}. \tag{3.44}$$

Using this asymptotic form in the solution given in Eq. (3.43), one can derive the electric and magnetic power spectra at the end of inflation for super-horizon modes as [238]

$$\mathcal{P}_{\mathrm{E}}^{\mathrm{inf}}(k) = \frac{H_{\mathrm{e}}^4}{4\pi^2} \frac{\cosh(n\pi\gamma)}{(1+\gamma^2)2^{2|n|-2}} \frac{\Gamma^2(2|n|}{\Gamma^2(|n| - i|n|\gamma)} (k\eta_{\mathrm{e}})^{4-2|n|} \tag{3.45a}$$

$$\mathcal{P}_{\mathrm{B}}^{\mathrm{inf}}(k) = \frac{H_{\mathrm{e}}^4}{4\pi^2} \frac{\cosh(n\pi\gamma)}{(1+\gamma^2)2^{2|n|-2}} \frac{\Gamma^2(2|n|}{\Gamma^2(|n| - i|n|\gamma)} (k\eta_{\mathrm{e}})^{4-2|n|} \left\{\gamma^2 + \frac{(1+2n\gamma^2)^2}{(2n-1)^2}(k\eta_{\mathrm{e}})^2\right\} \tag{3.45b}$$

Here we find that both the electric field and the magnetic field exhibit the same spectral behavior, where the electric and magnetic spectral indices are governed by $n_{\mathrm{B}} = n_{\mathrm{E}} = 4 - 2|n|$. Most interestingly, we also observe that when we set $\gamma = 0$, the solution exactly matches the non-helical case derived in Eq. (3.28), in which the magnetic field spectrum is more blue tilted compared to the electric field spectrum.

To avoid the strong coupling problem, we restrict our analysis to the parameter range $-2.2 < n < 0$. Furthermore, in order to avoid the backreaction issue, the parameters γ and the coupling parameter n must be chosen in such a way that the energy density of the produced electromagnetic fields remains smaller than the background energy density, i.e., $\rho^{\rm inf}_{\rm EM}(\eta_{\rm e}) \leq \rho_\varphi(\eta_{\rm e})$. Here, $\rho_\varphi(\eta_{\rm e}) \simeq 3H_{\rm e}^2 M_{\rm P}^2$ denotes the inflaton energy density evaluated at the end of inflation.

Present-day magentic field strength: In this specific kind of inflationary magnetogenesis model, we have found that both the electric field and magentic field have same spectral behaviour as well as the amplitude of the electric field and magentic field expoentially depend on the helicity parameter $\gamma(\neq 0)$ and the coupling parameter n. If we simple assume instantineous reheating scenarios with $H_{\rm e} \simeq 10^{-5} M_{\rm P}$ then the effective duration of the inflationary era is $N_{\rm inf} \simeq 59$ (using Eq.(2.69)). Now utilizing this value in the above Eq.(3.45), we can write the present-day magnetic field strength at large scale as

$$B_0(1,\mathrm{Mpc}^{-1}) \simeq 1.6\times 10^{-9}\, \frac{\Gamma(2|n|)\cosh(n\pi\gamma/2)}{(1+\gamma^2)2^{|n|-1}\Gamma(|n|-i|n|\gamma)} \times \left\{\gamma^2 + \frac{(1+2n\gamma^2)^2}{(2n-1)^2}\left(\frac{1\mathrm{Mpc}^{-1}}{k_{\rm e}}\right)^2\right\}^{1/2}\left(\frac{1\mathrm{Mpc}^{-1}}{k_{\rm e}}\right)^{n_{\rm B}/2} \mathrm{Gauss} \tag{3.46}$$

For a quantitative analysis, we first consider $\gamma = 0$ with $n = -2.0$. In this case, the present-day magnetic-field strength at the $1\,\mathrm{Mpc}^{-1}$ scale is $B_0(1\,\mathrm{Mpc}^{-1}) \simeq 7.4\times 10^{-34}$ Gauss, which exactly matches the prediction of the non-helical magnetogenesis scenario. Next, for the same value of the coupling parameter $n = -2.0$ but with $\gamma = 0.1$, we find that the present-day magnetic-field strength at the $1\,\mathrm{Mpc}^{-1}$ scale is $B_0(1\,\mathrm{Mpc}^{-1}) \simeq 5.6\times 10^{-10}$ Gauss. As the value of γ is increased further, the magnetic-field strength grows exponentially.

Observations of the CMB temperature and polarization anisotropies impose stringent constraints on large-scale magnetic fields, requiring the present-day magnetic-field strength to satisfy $B_0(1\,\mathrm{Mpc}^{-1}) \leq 10^{-9}$ Gauss [245–247, 317, 318]. Using this bound, we find that for $n = -2.0$, corresponding to a scale-invariant magnetic field spectrum, the helicity parameter is constrained to be $\gamma \leq \gamma^{\rm max} \simeq 0.2$. If the magnetic spectral index is changed by varying the value of n, the corresponding upper bound on the helicity parameter is significantly modified. For instance, for a blue-tilted magnetic field with $n_{\rm B} = 0.2$, and assuming an instantaneous reheating scenario, the upper bound on the helicity parameter is relaxed to $\gamma^{\rm max} \simeq 1.2$.

In Fig. 3.1, we plot the present-day magnetic field strength $B_0(1\,\mathrm{Mpc}^{-1})$ as a function of the magnetogenesis coupling parameter n (see Eq. (3.19)). For comparison, we consider both types of magnetogenesis models: the solid curves correspond to the magnetic-field strength predicted in the helical magnetogenesis scenario, while the dashed curve represents the prediction from

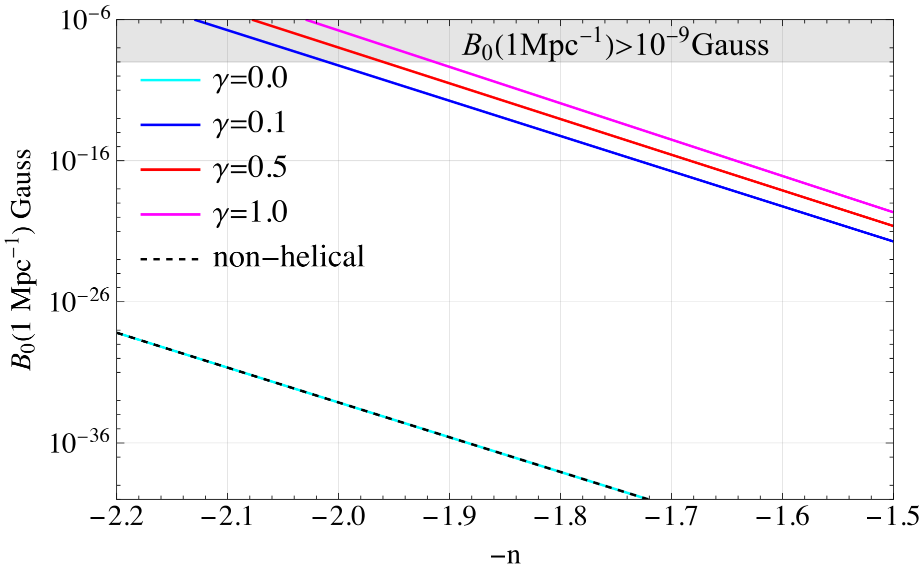

Figure 3.1: In this figure, we plot the present-day magnetic-field strength at the $1\,\mathrm{Mpc}^{-1}$ scale over a wide range of the magnetogenesis coupling parameter n, assuming an instantaneous reheating scenario. We consider two types of magnetogenesis models: the solid curves correspond to the helical magnetogenesis scenario, while the dashed curve represents the non-helical magnetogenesis scenario. In the helical case, we consider four distinct values of the helicity parameter, $\gamma = 0.0$, 0.1, 0.5, and 1.0, shown by four different colored solid curves. The black dashed curve denotes the magnetic-field strength predicted by the non-helical magnetogenesis model.

the non-helical magnetogenesis scenario. In the helical case, we consider four different values of the helicity parameter, $\gamma = 0.0$, 0.1, 0.5, and 1.0, shown by different colors, whereas the black dashed line denotes the non-helical magnetogenesis case.

We clearly observe that for $\gamma = 0.0$ both models yield identical results. This is expected, since in the limit $\gamma = 0.0$ the equation of motion of the helical magnetic field (see Eq. (3.46)) reduces to that of the non-helical magnetic field (see Eq. (3.40)). As the value of γ increases, the present-day magnetic-field strength also increases, reflecting its exponential dependence on γ. Moreover, increasing $|n|$ further enhances the generated magnetic-field strength due to its exponential dependence on $|n|$.

The key difference between these two magnetogenesis scenarios is that for non-zero $\gamma\,(\neq 0)$ the helical magnetogenesis mechanism produces a significantly stronger magnetic field, which can readily satisfy the observationally relevant present-day magnetic-field strength without requiring any additional post-inflationary enhancement [117, 237].

Chapter 4

Probing Reheating Phase via Inflationary Magnetogenesis Scenarios and Secondary Gravitational Waves

4.1 Introduction

In the previous chapter, we discussed the possible origin of large-scale magnetic fields. In particular, we focused on their generation during the inflationary epoch, when the mode functions exit the horizon. In the presence of a non-trivial coupling, the gauge field can become excited, leading to the production of a significant amount of magnetic field. Specifically, we considered a class of models in which the gauge field is kinetically coupled to the background through an interaction term of the form $f_1^2(\eta)F_{\mu\nu}F^{\mu\nu}$, or through an axial coupling of the form $\gamma f_1^2(\eta)F_{\mu\nu}\tilde{F}^{\mu\nu}$. These scenarios are commonly referred to as Ratra-type magnetogenesis models. In such models, it has been shown that explaining the observed large-scale magnetic fields with the coupling $f_1^2(\phi)F_{\mu\nu}F^{\mu\nu}$ typically leads to either the strong-coupling problem or the backreaction problem. In this chapter, we demonstrate that both of these issues can be alleviated by taking into account the post-inflationary evolution of the electromagnetic fields.

In this work, we show that large-scale magnetic fields can undergo a non-trivial evolution after inflation, primarily governed by the electrical conductivity of the plasma and the duration of the reheating phase. Since the thermal history of the Universe and the evolution of electrical conductivity during reheating remain uncertain, we consider two extreme limiting cases:

1. a highly conducting plasma throughout the reheating epoch, and
2. a reheating phase characterized by negligible electrical conductivity.

We find that the present-day magnetic field strength can be significantly modified in both scenarios, depending on the duration of reheating, which is controlled by the two parameters: one is the reheating temperature denoted as $T_{\rm re}$, and the other is the average EoS during reheating, i.e., $w_{\rm re}$. In particular, in the limit of vanishing conductivity, the energy transfer between electric and magnetic fields becomes efficient, especially on super-horizon scales. The efficiency of this conversion is determined by the energy gap between the electric and magnetic components. Remarkably, we identify a broad region of parameter space in which the observed large-scale magnetic fields can be explained without encountering either the strong-coupling or the backreaction problem.

We further investigate the observational imprints of inflationary magnetic fields on the stochastic gravitational-wave (GW) background. The anisotropic stress of the electromagnetic field acts as a source for tensor perturbations during the early stages of cosmic evolution [117, 118, 220–222, 229, 232–234], as we already have discussed in chapter 2. We find that a non-instantaneous reheating phase leaves distinctive signatures on the present-day GW spectrum [117]. In particular, the spectrum exhibits a characteristic break at a frequency $f_{\rm re}$, which is directly related to the reheating temperature. Moreover, the spectral shape of the GW background depends not only on the electromagnetic spectral index but also on the average equation of state $w_{\rm re}$ during reheating [117]. Notably, for stiff-like reheating equations of state ($w_{\rm re} > 1/3$), the GW spectrum develops multi-spectral features that could be probed by future GW observatories such as LISA, DECIGO, and BBO.

This paper is organized as follows. First, we analyze the inflationary and post-inflationary evolution of electric and magnetic fields in the limiting cases of vanishing and infinite electrical conductivity, and identify the conditions under which large-scale magnetic fields can be generated without strong-coupling or backreaction problems. We then study how the electromagnetic-field–sourced GW spectrum is modified by reheating dynamics. Finally, we demonstrate how spectral features of the GW background can be used to extract information about the reheating history, including the average equation of state $w_{\rm re}$ and the duration of reheating, parameterized by the reheating temperature $T_{\rm re}$.

4.2 Magnetogenesis: quantizing the gauge field and evolution of its power spectrum

As we mentioned in this chapter, we consider a simple Ratra-type magnetogenesis model, in which we can generate a non-helical magnetic field during inflation by introducing a time-dependent coupling function. So the effective action for the electromagnetic field is [47, 85, 235, 237, 238, 238, 258, 259, 262–268]

$$\mathcal{S}_{\rm EM} = -\frac{1}{4}\int d^4x\sqrt{-g}g^{\alpha\beta}g^{\mu\nu}f_1^2(\eta)F_{\mu\alpha}F_{\nu\beta}. \tag{4.1}$$

we recall that here $F_{\mu\nu} = \partial_\mu A_\nu - \partial_\nu A_\mu$ is the electromagnetic field tensor and A_μ is the vector potnetial. To solve the gauge field, we simply assume a spatially flat FLRW metric, and we are working on the Coulomb gauge. We can decompose the vector potential as

$$A_i(\eta,\mathbf{x}) = \sum_{\lambda=1,2}\int \frac{d^3k}{(2\pi)^3}\epsilon_i^\lambda(\mathbf{k})e^{i\mathbf{k}.\mathbf{x}}u_{\mathbf{k}}^\lambda(\tau), \tag{4.2}$$

with the reality condition $u^\lambda_{-\mathbf{k}} = u^{\lambda*}_{\mathbf{k}}$, the polarization vector $\epsilon_i^\lambda(\mathbf{k})$ corresponding to two modes $\lambda = 1, 2$, and satisfies $\epsilon_i^\lambda(\mathbf{k})k_i = 0$ and $\epsilon_i^\lambda(\mathbf{k})\epsilon_i^{\lambda'}(\mathbf{k}) = \delta_{\lambda\lambda'}$. Whereas the electric and magnetic power spectrum in term of mode function $u^\lambda_{\mathbf{k}}$ is defined in Eq.(3.15).

Power spectrum can now be computed once we know the mode function $u^\lambda_{\mathbf{k}}$ for a given inflationary and magnetogenesis model. Since, $(\mathcal{P}_E, \mathcal{P}_B)$ are connected to the direct physically measurable quantities, we chose to take a slightly different but transparent approach by directly solving the equations for comoving power spectrum ($\mathcal{P}^c_E = (a^4/f_1^2)\mathcal{P}_E, \mathcal{P}^c_B = (a^4/f_1^2)\mathcal{P}_B$) as

$$\mathcal{P}^{c'}_E + 4\frac{f_1'}{f_1}\mathcal{P}^c_E = -\mathcal{P}^{c'}_B \tag{4.3a}$$

$$\mathcal{P}^{c''}_B + 2\frac{f_1'}{f_1}\mathcal{P}^{c'}_B + 2k^2\mathcal{P}^c_B = 2k^2\mathcal{P}^c_E. \tag{4.3b}$$

The above equations clearly state that once the comoving magnetic power spectrum $\mathcal{P}^c_B$ is known, $\mathcal{P}^c_E$ can be automatically obtained from the second equation, and vice versa. Hence, it is sufficient to set the initial condition for the comoving magnetic spectrum, $\mathcal{P}^c_B|_{-k\tau\to\infty} = k^4/4\pi^2 f_1^2$, which can be obtained by explicitly solving for the electromagnetic mode function, (Eq.3.10) for $u^\lambda_{\mathbf{k}}$, and applying both the Bunch-Davis (BD) vacuum and normalization conditions, namely $u^\lambda_{\mathbf{k}}\big|_{\rm BD} = 1/(\sqrt{2kf_1^2})e^{-ik\eta}$.

4.2.1 Evolution of electromagnetic power spectrum through different phases

Our main objective is to trace the evolution of the electromagnetic power spectrum from the inflationary period to the current era and then compare it with the observed limit on the magnetic power spectrum. To this end, we will examine the gravitational wave power spectrum's development in the presence of this electromagnetic source.

Evolution During inflation:

During Inflation, we assume the ansatz for the gauge coupling function as [237, 238, 262]

$$f_1(\eta) = \begin{cases} \left(\frac{a}{a_{\rm e}}\right)^n & \text{for } a \le a_{\rm e} \\ 1 & \text{for } a > a_{\rm e} \end{cases}. \tag{4.4}$$

Note that after the end of inflation set at $a_{\rm e}$, the coupling function becomes unity, which restores the usual conformal symmetry of the electromagnetic field.

To solve for the spectrum analytically, we further assumed inflation to be approximately de Sitter type, and with this assumption, the scale factor behaves as $a = -1/H_{\rm e}\eta$, where $H_{\rm e}$ is the Hubble constant. With the above choice of gauge coupling function, one can easily obtain the analytic solution for the magnetic power spectrum as

$$\mathcal{P}^c_B = (a^4/f_1^2)\mathcal{P}_B = (-k\eta)^{1+2n}(c_1 H_{n+\frac{1}{2}}(k\eta)^2 + c_2|H_{n+\frac{1}{2}}(k\eta)|^2 + c_3 H^*_{n+\frac{1}{2}}(k\eta)^2). \tag{4.5}$$

Where c_1, c_2, c_3 are the integration constants, and $(H_{n+1/2}, H^*_{n+1/2})$ are the Hankel functions of the first kind and their complex conjugate. The electric power spectrum can be easily computed from Eq.(4.3). Since, in the asymptotic past limit, $a^4\mathcal{P}^c_B|_{-k\eta\to\infty} = k^4/4\pi^2 f_1^2$, one obtains the integration constants to be

$$c_1 = c_3 = 0 \ ; \ c_2 = \frac{k^4}{8\pi}\left(\frac{1}{-k\eta_{\rm e}}\right)^{2n}. \tag{4.6}$$

Once we obtain the expression for $\mathcal{P}_B^c$, the corresponding electric counterpart can be obtained from Eq.(4.3), and using Eq. (4.6), we get the final expressions for the electromagnetic power spectrum [237] as,

$$\mathcal{P}_{\rm B}^{\rm inf}(k,\eta) = \frac{d\rho_B}{dln(k)} = \frac{k^4}{8\pi a^4(\eta)}(-k\eta)\left|H^{(1)}_{n+\frac{1}{2}}(-k\eta)\right|^2, \tag{4.7}$$

$$\mathcal{P}_{\rm E}^{\rm inf}(k,\eta) = \frac{d\rho_E}{dln(k)} = \frac{k^4}{8\pi a^4(\eta)}(-k\eta)\left|H^{(1)}_{n-\frac{1}{2}}(-k\eta)\right|^2. \tag{4.8}$$

To analyse the power spectrum's characteristics at the super-horizon scale, where all the relevant modes are well outside the Hubble radius at the end of inflation, we consider the limit where $k/aH_{\rm e} << 1$. Depending on the sign of n, we can express the electric and magnetic power spectrum in a simpler form, as explained in [235, 237, 238]

$$\left.\begin{aligned} \mathcal{P}_{\rm B}^{\rm inf}(k,\eta) &= \frac{H_{\rm e}^4}{8\pi}\frac{2^{2|n|+1}\Gamma^2\left(|n|+\frac{1}{2}\right)}{\pi^2}(-k\eta)^{-2|n|+4} \\ \mathcal{P}_{\rm E}^{\rm inf}(k,\eta) &= \frac{H_{\rm e}^4}{8\pi}\frac{\Gamma^2\left(|n|-\frac{1}{2}\right)2^{2|n|-1}}{\pi^2}(-k\eta)^{-2|n|+6} \end{aligned}\right\} \text{for } n > \tfrac{1}{2}, \tag{4.9}$$

$$\left.\begin{aligned} \mathcal{P}_{\rm B}^{\rm inf}(k,\eta) &= \frac{H_{\rm e}^4}{8\pi}\frac{\Gamma^2\left(|n|-\frac{1}{2}\right)2^{2|n|-1}}{\pi^2}(-k\eta)^{-2|n|+6} \\ \mathcal{P}_{\rm E}^{\rm inf}(k,\eta) &= \frac{H_{\rm e}^4}{8\pi}\frac{2^{2|n|+1}\Gamma^2\left(|n|+\frac{1}{2}\right)}{\pi^2}(-k\eta)^{-2|n|+4} \end{aligned}\right\} \text{for } n < -\tfrac{1}{2}. \tag{4.10}$$

After obtaining the power spectrum during inflation, we can use it as a boundary condition to solve for the power spectrum during reheating. It is important to note that for $n > 1/2$, the ratio of the two field strengths turns out to be $\mathcal{P}_{\rm B}^{\rm inf}(k)/\mathcal{P}_{\rm E}^{\rm inf}(k) \propto (k\eta)^{-2} \gg 0$. This immediately suggests that, at the end of inflation, the magnetic field strength dominates over the electric field strength for $n > 1/2$. However, it should be emphasized that the case $n > 0$ suffers from a strong coupling problem. On the other hand, for $n < 0$, the situation is reversed: the electric field strength dominates over the magnetic field strength, i.e. $\mathcal{P}_{\rm E}^{\rm inf}(k)/\mathcal{P}_{\rm B}^{\rm inf}(k) \propto (k\eta)^{-2} \gg 0$ and in this case there is no strong coupling issue. To estimate the magnetic field strength at the end of inflation for a specific set of parameters, we consider an inflationary energy scale of $H_{\rm e} \simeq 10^{-5}M_{\rm P}$ and an inflationary duration corresponding to $N_{\rm inf} = 55$ e-folds.Now we can define the magnetic field strength at the end of inflation as $B(k,\eta_{\rm e}) = \sqrt{\mathcal{P}_{\rm B}^{\rm inf}(k,\eta_{\rm e})}$. For $n = 2$, which corresponds to a scale-invariant magnetic spectrum, the field strength at a comoving scale of $k = 1\ {\rm Mpc}^{-1}$ is found to be $B_{n=2}(1\ {\rm Mpc}^{-1}) \simeq 10^{46}$ G. In contrast, for $n = -2$, where the magnetic spectrum exhibits a scale-dependent behavior with $B_{n=-2} \propto k$, the field strength at the same scale is estimated as $B_{n=-2}(1\ \mathrm{Mpc}^{-1}) \simeq 10^{23}$ G. Notably, for scale-dependent spectra, the field strength is influenced by the duration of inflation due to the factor $(k/k_{\rm e})^{n_B}$, whereas for scale-invariant spectra, it remains independent of the inflationary duration.

Results for Inflationary Magnetogenesis: The strength of the electromagnetic power spectrum at the end of inflation is governed by equations (3.26),(3.27). Assuming an instantaneous reheating scenario, and the inflationary Hubble parameter $H_{\rm e} \simeq 10^{-5} M_{\rm P}$, we can determine the present-day magnetic field strength as follows:

$$B_0(k) \simeq 1.84 \times 10^{-12}\ \mathrm{G} \left(\frac{k}{k_{\rm e}}\right)^{2-|n|} \times \begin{cases} 2^{n+\frac{1}{2}}\Gamma(n+\frac{1}{2}) & \text{for } n > 1/2 \\ 2^{n-\frac{1}{2}}\Gamma(n-\frac{1}{2})\frac{k}{k_{\rm e}} & \text{for } n < -1/2 \end{cases}. \tag{4.11}$$

Notably, the case of $n = 2$ yields a scale-invariant magnetic field. Despite the scale-invariance, it faces the challenge of the strong coupling problem due to the large effective electromagnetic gauge coupling $\propto 1/f^2$, at the onset of inflation. However, it can generate a magnetic field strength of around $\sim 10^{-11}$ G. Note that such a strong magnetic field can have a sizable impact on the tensor-to-scalar ratio, which we will discuss in the GW section. On the other hand, the $n = -2$ coupling leads to a scale-dependent magnetic field strength is $B_0(1\,\mathrm{Mpc}^{-1}) \simeq 1.45 \times 10^{-36}$ G, which is very small compared with the current observational bound on the 1 Mpc scale [319–321].

As we already have discussed the backreaction and strong coupling issue, for this kind of model in 3, where we have found that $n > 0$ have issue with storng coupling, but they effectively produced sontroger magnetic field at large scale, where as $-2.2 < n < 0$ brnace has not issue with strong coupling and backreaction issue, but the produced magnetic field strength is quite low, as with in this range, the produced magnetic field strongly blue tilted, so most of the magnetic energy density store in the high frequency. So to avoid the strong coupling and backreaction issue, we restated our analysis within the limit $-2.2 < n < 0$.

In the following section, we explore how reheating scenarios involving negligible or low electrical conductivity (EC) can enhance the magnetic field through induction effects (see, for instance, [311]).

4.2.2 Evolution During reheating phase:

During reheating, we now consider two extreme cases with regard to the electrical conductivity of the background medium.

1. **High-Conductivity approximation:** This is the conventional and well-studied scenario where all fundamental charged particles are efficiently produced immediately after inflation and get instantaneously thermalised, and the high-temperature background results in a very large electrical conductivity of the universe. In this high-conductivity limit, the rapid response of the charged particles causes the electric field to decay almost

instantaneously, effectively removing it from the post-inflationary dynamics. As a result, during reheating, only the magnetic field survives. This can be easily understood from the dynamical equation

$$\mathcal{P}_E^{c'} + 2\sigma\mathcal{P}_E^c = -\mathcal{P}_B^{c'} \tag{4.12a}$$

$$\mathcal{P}_B^{c''} + \sigma\mathcal{P}_B^{c'} + 2k^2\mathcal{P}_B^c = 2k^2\mathcal{P}_E^c. \tag{4.12b}$$

We assume the background conductivity σ to be constant. Before we embark, on few points are in order. In the above evolution equation for the comoving electromagnetic power spectrum during reheating, we assume the gauge coupling function $f_1(\eta) = 1$ (see Eq.(4.4)) after the end of inflation $a > a_\mathrm{e}$. Further, the equations do not explicitly depend on the scale factor, and that is due to the underlying conformal invariance of the gauge fields. During reheating, there is no coupling term to break the invariance like the one in Eq.(4.1). Our goal is to work in the large conductivity limit. It can be seen that in the limit $\sigma \to \infty$, and large scale $k \to 0$, the consistent solution of the above set of equations would be

$$\mathcal{P}_E^c(\eta) \approx 0 \implies |E|^2 \approx 0,$$
$$\mathcal{P}_B^c(\eta) \approx \mathcal{B} \implies |B|^2 \approx \tfrac{\mathcal{B}}{a(\eta)^4}.$$

Where the integration constant $\mathcal{B} = a_\mathrm{e}^4\mathcal{P}_B^c(\eta_\mathrm{e})$ is calculated at the time of inflation end. The present-day magnetic field spectrum $\mathcal{P}_B^0$ with the field strength B_0 can therefore be calculated as

$$a_0^4\mathcal{P}_B^0(k) \simeq a_\mathrm{re}^4\mathcal{B} \implies B_0 \simeq \frac{\sqrt{\mathcal{B}}a_\mathrm{e}^2}{a_0^2}. \tag{4.13}$$

We restrict our analysis to parameter regimes that avoid both strong coupling and back-reaction issues. Since the electric field is no longer present in this case, there is no energy transfer from the electric field to the magnetic field via the Faraday induction mechanism. Therefore, the magnetic field evolves adiabatically for those modes that remain super-horizon during reheating. Therefore, the magnetic energy density redshifts as a^{-4} due to the expansion of the universe. Consequently, the comoving magnetic field power spectrum at the end of reheating is given approximately by $\tilde{\mathcal{P}}_B(k,\eta_\mathrm{reh}) \simeq \tilde{\mathcal{P}}_B(k,\eta_\mathrm{e})$. The present-day magnetic field strength at $1\,\mathrm{Mpc}$ scales for a coupling parameter $n = -2$ is calculated as $B_0(1\,\mathrm{Mpc}^{-1}) \simeq 1.45 \times 10^{-36}\,\mathrm{G}$. In contrast, for the lower bound of the coupling parameter, $n \simeq -2.2$, the present-day magnetic field strength is enhanced to $B_0(1\,\mathrm{Mpc}^{-1}) \simeq 1.3 \times 10^{-31}\,\mathrm{G}$. These estimates suggest that for the coupling parameter $-2.2 < n < 0$, it cannot produce sufficient strength of the magnetic field at 1 Mpc scale. However, for the case of vanishingly small conductivity, we indeed show that sufficient magnetic field strength can be obtained

2. **Low Conductivity approximation:** In this case, we assume that the electrical conductivity of the universe remains small during reheating. This assumption is strongly motivated by the fact that, during reheating, the electrically neutral inflaton field is the dominant energy density until the end of reheating. In such a scenario, we are going to discuss how reheating helps us to explain the current observational limit. They have the same evolution equation defined in Eq.(4.12). As stated earlier, we assume $\sigma \to 0$ limit. So, we can identify the solutions of Eqs(4.12) as comoving electric and magnetic power spectrum defined as $\mathcal{P}_B^c = a^4\mathcal{P}_B$ and $\mathcal{P}_E^c = a^4\mathcal{P}_E$. And the solution of the Eqs(4.12) is governed by

$$a^4\mathcal{P}_B = \frac{\mathcal{B}+\mathcal{E}}{2} + \frac{\mathcal{B}-\mathcal{E}}{2}\cos(2k(\eta-\eta_{\rm e})), \tag{4.14a}$$

$$a^4\mathcal{P}_E = \frac{\mathcal{B}+\mathcal{E}}{2} - \frac{\mathcal{B}-\mathcal{E}}{2}\cos(2k(\eta-\eta_{\rm e})), \tag{4.14b}$$

where $(\mathcal{B},\mathcal{E})$ are the appropriate initial conditions,

$$\mathcal{E} = \frac{a_{\rm e}^4\mathcal{P}_{\rm E}^{\rm inf}(\eta_{\rm e})}{f^2(\eta_{\rm e})} = \frac{k^4}{8\pi}\frac{2^{2n+1}\Gamma^2\left(n+\frac{1}{2}\right)}{\pi^2}\left(\frac{k}{k_{\rm e}}\right)^{-2n}, \tag{4.15}$$

$$\mathcal{B} = \frac{a_{\rm e}^4\mathcal{P}_{\rm B}^{\rm inf}(\eta_{\rm e})}{f^2(\eta_{\rm e})} = \frac{k^4}{8\pi}\frac{\Gamma^2\left(n-\frac{1}{2}\right)2^{2n-1}}{\pi^2}\left(\frac{k}{k_{\rm e}}\right)^{2-2n} \tag{4.16}$$

In de Sitter space, we can identify it through $|-\eta_{\rm e}| = 1/k_{\rm e}$ where $k_{\rm e}$ is the highest wavenumber that crossed the horizon at the end of inflation. The above two Eqs. (4.15),(4.16) are evaluated at the end of inflation for the super-horizon modes approximation.

During the post-inflationary phase, if there is no further gauge field production, the electromagnetic energy density scales as $\rho_{\rm em} \propto a^{-4}$ [238, 263–265, 275, 314]. However, it is important to note that the individual evolution of the electric and magnetic field components, E^2 and B^2, may deviate from each other, as their behavior depends sensitively on the electrical conductivity of the universe during reheating [237,270,311]. This nontrivial evolution can be attributed to Faraday induction, through which electric energy can be converted into magnetic energy, and vice versa, depending on the field strengths [237,311]. For example, the case we just discussed in the above Eq.4.14a, where the Faraday effect is evident. However, it would be pronounced in large-scale limit $k\eta \to 0$, when the above equations are approximated as,

$$\mathcal{P}_B = \frac{1}{a^4}(\mathcal{B}+(\mathcal{B}-\mathcal{E})k^2(\eta-\eta_{\rm e})^2) \simeq \frac{\mathcal{B}}{a^4} + \frac{\mathcal{B}-\mathcal{E}}{H^2a^6}k^2, \tag{4.17}$$

$$\mathcal{P}_E = \frac{1}{a^4}(\mathcal{E}-(\mathcal{B}-\mathcal{E})k^2(\eta-\eta_{\rm e})^2) \simeq \frac{\mathcal{E}}{a^4} - \frac{\mathcal{B}-\mathcal{E}}{H^2a^6}k^2, \tag{4.18}$$

Where, we utilize the relation $\eta - \eta_e \sim 1/(aH)$. The above equation clearly indicates how the Faraday effect transfers energy from electric to magnetic modes and vice versa with time behavior $\mathcal{P}_B \propto 1/a^6H^2$, which has been discussed earlier in the literature [237,262].

In what follows, we focus on the intermediate regime $-2.2 < n < 0$, corresponding to $-0.4 < n_{\rm E} < 4$, where both strong coupling and backreaction problems are absent. In this case, as stated earlier electric field is stronger than the magnetic field at the end of inflation, $\mathcal{E} \gg \mathcal{B}$. The Faraday effect, therefore, leads to an additional enhancement of the magnetic field, and at the end of reheating, one obtains,

$$\mathcal{P}_E(k,\eta_{\rm re}) \simeq \frac{1}{a_{\rm re}^4}(\mathcal{E} + (\mathcal{B}-\mathcal{E})k^2\eta_{\rm re}^2) \simeq \frac{\mathcal{E}}{a_{\rm re}^4} \tag{4.19}$$

$$\mathcal{P}_B(k,\eta_{\rm re}) \simeq \mathcal{B} - (\mathcal{B}-\mathcal{E})k^2\eta_{\rm re}^2 \simeq \frac{\mathcal{E}k^2}{a_{\rm re}^6 H_{\rm re}^2}. \tag{4.20}$$

After the end of reheating, assuming the universe is dominated by the relativistic plasma with infinite conductivity, the electric field quickly decays, and the magnetic field evolves adiabatically till the present day. The present-day magnetic field B_0 can be calculated as

$$a_0^4\mathcal{P}_B^0(k,\eta_{\rm re}) \simeq \frac{\mathcal{E}k^2}{a_{\rm re}^2 H_{\rm re}^2} \implies B_0 \simeq \frac{\sqrt{\mathcal{E}}k}{a_{\rm re}H_{\rm re}a_0^2} \tag{4.21}$$

Here, we have observed that due to the Faraday induction effect, there is significant conversion of electric field energy into magnetic field energy. To highlight this effect, we present some numerical comparisons for two extreme cases of electrical conductivity. For the zero electrical conductivity (EC) case with coupling parameter $n = -2.0\,(n_{\rm E} = 0)$, where the magnetic field energy density scales as k^2, we find that for a reheating temperature $T_{\rm re} = 10^{-2}\,$GeV and equation of state $w_{\rm re} = 0$, the present-day magnetic field strength is $B_0(1\,{\rm Mpc}^{-1}) \simeq 1.86 \times 10^{-27}\,$G. In contrast, for the same parameters but assuming infinite EC, the strength drops to $B_0(1\,{\rm Mpc}^{-1}) \simeq 8.85 \times 10^{-40}\,$G. Similarly, for the same reheating temperature with $w_{\rm re} = 1/3$, we find that the present-day magnetic field strength in the zero EC case is $B_0(1\,{\rm Mpc}^{-1}) \simeq 1.27 \times 10^{-15}\,$G, while the infinite EC case yields $B_0(1\,{\rm Mpc}^{-1}) \simeq 7.3 \times 10^{-34}\,$G. Therefore, it is evident that for a fixed reheating temperature, the zero conductivity scenario leads to a significant enhancement in the magnetic field strength, up to a factor of $10^{14} - 10^{19}$ compared to the infinite conductivity case, due to efficient electric-to-magnetic energy conversion.

Constraining the Reheating parameter from the Backreaction at the end of Reheating: Before we embark on the production of gravitational waves, let us derive a generic constraints on the reheating parameter space due to additional production of gauge field. As we now consider a general reheating history, it is important to account for the possibility that the equation of state (EoS) parameter during reheating satisfies $w_{\rm re} > 1/3$. In such cases, the background energy density dilutes faster than the electromagnetic (EM) energy density.

Specifically, the inflationary energy density evolves as $\rho_\phi(\eta) \propto a^{-3(1+w_{\rm re})}$, whereas the electromagnetic energy density evolves as $\rho_{\rm em}(\eta) \propto a^{-4}$. This implies that the fractional energy density of the EM field increases during reheating according to $\delta\rho_{\rm em}(\eta) \equiv \frac{\rho_{\rm em}(\eta)}{\rho_\phi(\eta)} \propto a^{3w_{\rm re}-1}$. Therefore, depending on the reheating dynamics, there may arise a situation in which the EM energy density becomes comparable to or even exceeds the background energy density.

This scenario is particularly constrained by Big Bang Nucleosynthesis (BBN). If the universe is dominated by magnetic field energy at the onset of BBN, it might disrupt the formation of light elements. Since the predictions of BBN are in excellent agreement with observations, we must impose a consistency condition that the total EM energy density at the end of reheating remains subdominant to the background radiation energy density, $\rho_{\rm em}(\eta_{\rm reh}) < \rho_r(\eta_{\rm reh})$. Imposing this condition leads to nontrivial constraints on the reheating dynamics.

These constraints are further modified depending on the post-inflationary conductivity of the universe. Let us first consider the case of high electrical conductivity. In this limit, only the magnetic field survives during reheating. As discussed previously, and within the allowed parameter range $-2.2 < n < 0$, the magnetic power spectrum is blue-tilted and evolves adiabatically, as described by Eq. (3.27). In this high-conductivity regime, the fractional energy density of the magnetic field evolves as $\delta\rho_B(\eta) \equiv \frac{\rho_B(\eta)}{\rho_\varphi(\eta)} \propto a^{3w_{\rm re}-1}$, similar to the general EM case. Thus, for sufficiently large $w_{\rm re}$, the magnetic field can become dynamically significant and potentially dominate the energy budget, leading to tight constraints on the reheating duration and EoS.

$$\delta\rho_B(\eta_{\rm re}) \simeq \left(\frac{H_{\rm e}}{M_{\rm P}}\right)^2 \frac{2^{3-n_{\rm E}}\Gamma^2\left(\frac{3-n_{\rm E}}{2}\right)\left(1-(k_*/k_{\rm e})^{n_{\rm E}+2}\right)}{24\pi^3(n_{\rm E}+2)} \exp[N_{\rm re}(3w_{\rm re}-1)] \tag{4.22}$$

On the other hand, in the zero electrical conductivity limit, both electric and magnetic fields are present during the reheating era. We assume that the electric field decays only after reheating completes, when the universe becomes fully dominated by radiation. Therefore, before the end of reheating, both fields contribute to the total electromagnetic energy density. To consistently avoid backreaction in this regime, it is essential to account for the combined influence of both the electric and magnetic fields. Consequently, in the zero conductivity limit, the electromagnetic fractional energy density must be defined by including contributions from both components.

$$\begin{aligned}\delta\rho_{em}(\eta_{\rm re}) \simeq \left(\frac{H_{\rm e}}{M_{\rm P}}\right)^2 \frac{2^{5-n_{\rm E}}}{24\pi^3}\Bigg[&\frac{\Gamma^2\left(\frac{5-n_{\rm E}}{2}\right)\left(1-(k_*/k_{\rm e})^{n_{\rm E}}\right)}{n_{\rm E}} \\ &+\frac{\Gamma^2\left(\frac{3-n_{\rm E}}{2}\right)\left(1-(k_*/k_{\rm e})^{n_{\rm E}+2}\right)}{4(n_{\rm E}+2)}\Bigg] \exp[N_{\rm re}(3w_{\rm re}-1)]\end{aligned} \tag{4.23}$$

As seen from Eqs.(4.22) and (4.23), the fractional electromagnetic energy density increases with time only in reheating scenarios with $w_{\rm re} > 1/3$. For example, in the high-conductivity limit with $w_{\rm re} = 0.5$, the minimum reheating temperature required to prevent the magnetic

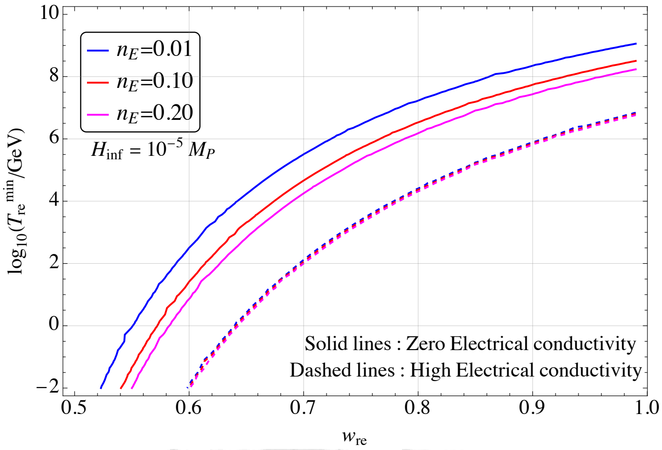

Figure 4.1: Lowest allowed reheating temperature (in GeV) as a function of the reheating equation-of-state parameter $w_{\rm re}$ over a wide parameter range. The three different colors correspond to distinct values of the electric spectral index: $n_{\rm E} = 0.01$ (**blue**), $n_{\rm E} = 0.1$ (**red**), and $n_{\rm E} = 0.2$ (**magenta**). Solid lines represent the case of vanishing electrical conductivity (EC), while dashed lines correspond to the high-conductivity limit. Throughout the analysis, the inflationary energy scale is fixed at $H_{\rm inf} \simeq 10^{-5} M_{\rm Pl}$.

field from dominating before the onset of the radiation-dominated era is $T_{\rm re}^{\rm min} \sim 10^{-2}\,{\rm GeV}$. In contrast, for the same equation of state but in the zero electrical conductivity limit, the corresponding minimum reheating temperature is significantly higher, $T_{\rm re}^{\rm min} \sim 3 \times 10^{2}\,{\rm GeV}$.

In Fig. 4.1, we present the lowest allowed reheating temperature, denoted by $T_{\rm re}^{\rm min}$ (in GeV), as a function of the reheating equation of state parameter $w_{\rm re}$, for three different values of the electric spectral index: $n_{\rm E} = 0.01$, 0.1, and 0.2. These parameter choices ensure that the model remains free from both backreaction and strong coupling problems during inflation as well as during reheating. As previously discussed, for $w_{\rm re} > 1/3$, the background energy density dilutes faster than the electromagnetic (EM) energy density, allowing the latter to potentially dominate at later stages of reheating. The curves in the figure indicate the threshold values of $T_{\rm re}$ below which the EM field would dominate over the background energy density before reheating completes.

In this plot, solid lines represent the zero electrical conductivity limit, while dashed lines correspond to the high conductivity limit. As observed, the constraints in the high conductivity scenario are less sensitive to the spectral index $n_{\rm E}$, since only the magnetic field contributes, and the total magnetic energy density, being strongly blue-tilted, is relatively insensitive to variations in $n_{\rm E}$. In contrast, in the zero conductivity case, the majority of the EM energy budget is due to the electric field, whose energy density is highly sensitive to $n_{\rm E}$ for the chosen parameter range.

In this work, we neglect the magnetohydrodynamic (MHD) evolution of sub-horizon modes, which are most susceptible to MHD effects. Consequently, for blue-tilted magnetic spectra, the estimates provided here are expected to be significantly altered in more realistic scenarios. However, since a full treatment of MHD dynamics lies beyond the scope of this study, we

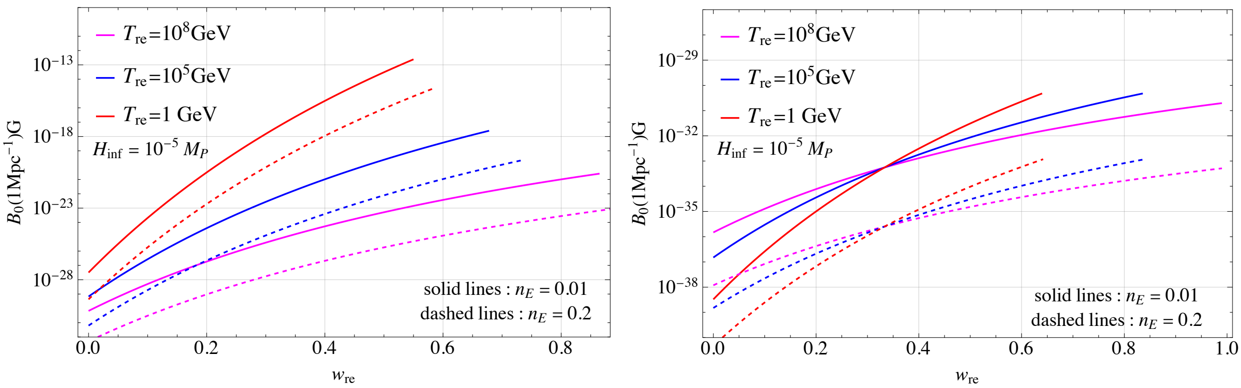

Figure 4.2: Present-day magnetic field strength evaluated at the scale $1\,\mathrm{Mpc}^{-1}$ as a function of the reheating equation-of-state parameter w_{re}. The three different colors represent three distinct values of the reheating temperature. Solid lines correspond to $n_{\mathrm{E}} = 0.01$, while dashed lines indicate $n_{\mathrm{E}} = 0.20$. The left panel shows the case of vanishing electrical conductivity during reheating, whereas the right panel corresponds to the limit of infinite conductivity. In both cases, we impose the condition that the total electromagnetic (EM) energy density remains subdominant to the background energy density throughout reheating, ensuring that the Universe does not enter a magnetic-field-dominated phase before the onset of Big Bang Nucleosynthesis (BBN).

present our results as indicative bounds.

Using these bounds, we analyze the behavior of the present-day magnetic field under two limiting cases, zero electrical conductivity and infinite electrical conductivity during reheating. In Fig. 4.2, we plot the present-day magnetic field strength as a function of the reheating equation of state w_{re}, for three different reheating temperatures: $T_{\mathrm{re}} = 1\,\mathrm{GeV}$, $10^5\,\mathrm{GeV}$, and $10^8\,\mathrm{GeV}$.

In the left panel of Fig. 4.2, corresponding to the zero conductivity limit, we observe that a significant portion of the electric field energy is converted into magnetic field energy during reheating. As a result, the present-day magnetic field amplitude is considerably enhanced. In contrast, the right panel corresponds to the infinite conductivity limit, where no such conversion takes place. Consequently, the magnetic field strength today is much smaller compared to the zero conductivity case.

We further observe that increasing the equation of state w_{re} and decreasing the reheating temperature T_{re} both tend to enhance the present-day magnetic field strength. This enhancement is driven by the dilution of magnetic energy due to cosmic expansion. For larger w_{re}, the background energy density redshifts more rapidly, allowing the Universe to reach lower reheating temperatures over a shorter timescale. As a result, magnetic fields experience less dilution from expansion, leading to a stronger residual amplitude today.

Moreover, we find that for more blue-tilted electric spectra, the magnetic field strength at large scales decreases. This is because the magnetic spectrum becomes increasingly blue-tilted with growing n_{E}, suppressing power on large scales. For instance, considering the zero conductivity case with $n_{\mathrm{E}} \simeq 0.01$, $T_{\mathrm{re}} \simeq 1\,\mathrm{GeV}$, and $w_{\mathrm{re}} \simeq 0.5$, the magnetic field today at $1\,\mathrm{Mpc}^{-1}$ is $B_0 \simeq 3.04 \times 10^{-14}\,\mathrm{G}$. In contrast, for the same reheating parameters but in the infinite conductivity case, the present-day magnetic field is significantly weaker, $B_0 \simeq 3.01 \times 10^{-32}\,\mathrm{G}$.

These results highlight the crucial role of post-inflationary gauge field evolution in determining the final amplitude of the magnetic field. In particular, the electrical conductivity of the Universe during reheating has a significant impact on the resulting magnetic field strength observable today.

4.3 Generation of Secondary Gravitational Waves from Electromagnetic field:

In this section, we focus on the secondary gravitational waves generated during the inflationary and post-inflationary eras due to the non-trivial production of the electromagnetic (EM) field. In the present magnetogenesis scenario, a non-helical magnetic field is produced. As discussed earlier, to avoid the strong coupling and backreaction problems, we restrict our analysis to the parameter range $-2.2 < n < 0$. Within this regime, the electric field constitutes the dominant component, and therefore it is expected to play the primary role in sourcing the tensor modes.

Interestingly, we find that in a de Sitter inflationary background, a scale-invariant or blue-tilted electric or magnetic spectrum leads to the same scale-invariant tensor power spectrum during inflation. The final amplitude of the tensor power spectrum depends on the strength of the electric and magnetic fields at the time of horizon crossing [240].

After the end of inflation, we consider a non-instantaneous reheating scenario. Consequently, the present-day GW spectrum is sensitive to the details of the reheating dynamics. There are three distinct epochs during which the electromagnetic field can source secondary GWs.

The first phase corresponds to inflation, when both the electric and magnetic fields are generated from vacuum fluctuations. This is followed by the reheating phase, during which the conductivity of the plasma plays a crucial role. If the electrical conductivity is negligible, both the electric and magnetic fields are present and contribute to GW production. In contrast, if the Universe becomes highly conducting immediately after inflation, the electric field rapidly decays, and only the magnetic field continues to source GWs.

Even after the completion of reheating, when the conductivity is very high, the magnetic field can continue to source GWs up to neutrino decoupling. After neutrino decoupling, free-streaming neutrinos generate anisotropic stress that compensates the anisotropic stress of the magnetic field in the plasma, thereby suppressing further GW sourcing.

It is convenient to decompose the tensor power spectrum into two components: one arising from vacuum fluctuations and the other from the source term. Since these two contributions are uncorrelated, we write

$$P_{\mathrm{T}}(k,\eta) = P_{\mathrm{T}}^{\mathrm{pri}}(k,\eta) + P_{\mathrm{T}}^{\mathrm{sec}}(k,\eta), \tag{4.24}$$

where $P_{\mathrm{T}}^{\mathrm{pri}}(k,\eta)$ denotes the vacuum contribution and $P_{\mathrm{T}}^{\mathrm{sec}}(k,\eta)$ represents the EM-sourced component.

For a general power-law electromagnetic spectrum of the form $\mathcal{P}_{\mathrm{B/E}}(k,\eta) \propto (k\eta)^{n_{\mathrm{B/E}}}$, the tensor power spectrum at time η can be expressed as [229]

$$P_{\mathrm{T}}^{\mathrm{sec}}(k,\eta) = \frac{2}{M_{\mathrm{P}}^4}\left[\int_{\eta_i}^{\eta} d\eta_1 a^2(\eta_1)\mathcal{G}_{\mathbf{k}}(\eta_f,\eta_1)\mathcal{P}_{\mathrm{B/E}}(k,\eta_1)\right]^2 \times \int_0^{\infty}\frac{dq}{q}\int_{-1}^{1} d\mu \frac{(q/k)^{n_{\mathrm{B/E}}} f(\mu,\beta,\lambda)}{\left[1+\left(\frac{q}{k}\right)^2 - 2\mu\frac{q}{k}\right]^{\frac{3-n_{\mathrm{B/E}}}{2}}}. \tag{4.25}$$

Here, $f(k,q,\lambda) = (1+\mu^2)(1+\beta^2)$, with $\mu = \hat{\mathbf{k}}\cdot\hat{\mathbf{q}}$ and $\beta = \widehat{\mathbf{k}-\mathbf{q}}\cdot\hat{\mathbf{k}}$ [222, 229, 246, 322]. The parameter $n_{\mathrm{B/E}}$ denotes the spectral index of the magnetic or electric field, depending on which component dominates during the time interval from η_i to η.

In the following subsection, we discuss separately the contributions to the secondary tensor fluctuations arising from each of these different cosmological epochs.

4.3.1 Tensor power spectrum during Inflation:

During inflation, both the electric field and magnetic field were present and continuously generated, so both fields will contribute to the tensor perturbations. Now to solve the above Eq.(4.25), we have to know the function behaviour of the Green's function associated with the tensor perturbation equation, and in the de Sitter inflationary background, the Green's function is well established, and it can be written as [220, 232]

$$\mathcal{G}_k^{\mathrm{inf}}(\eta,\eta') = \frac{1}{k^3\eta'^2}\Big[(1+k^2\eta\eta')\sin(k(\eta-\eta')) + k(\eta'-\eta)\cos(k(\eta'-\eta))\Big]\,\Theta(\eta-\eta'). \tag{4.26}$$

In general, magnetic fields are produced when they exit the horizon during inflation, and in the super-horizon approximation, we can write the magnetic and electric power spectrum as a simple power law type spectrum, which can be parameterized as

$$\mathcal{P}_{\mathrm{B}}^{\mathrm{inf}}(k,\eta) = H_{\mathrm{e}}^4\mathcal{C}_{\mathrm{B}}^2(n_{\mathrm{B}})(-k\eta)^{n_{\mathrm{B}}};\ \mathcal{P}_{\mathrm{E}}^{\mathrm{inf}}(k,\eta) = H_{\mathrm{e}}^4\mathcal{C}_{\mathrm{E}}^2(n_{\mathrm{E}})(-k\eta)^{n_{\mathrm{E}}} \tag{4.27}$$

where n_{B} and n_{E} are the magnetic and electric spectral indices, which mainly depend on the coupling parameter n. As we are working in the regime, where the model does not have any strong coupling issue and backreaction issue, i.e. $-2.2 < n < 0$, so where the electric field spectral index can be identified as $n_{\mathrm{E}} = 4-2|n|$, whereas the magnetic spectral index can be identified as $n_{\mathrm{B}} = n_{\mathrm{E}}+2$.

Now, for the computation purpose, we have considered the magnetic field part, and solved the tensor power spectrum defined in Eq.(2.146), only for the magnetic field, but when we compute the total power spectrum, we consider both the electric field and magnetic field. As we mentioned, the gauge field is only excited from the Bunch-Davies vacuum when the corresponding mode leaves the horizon, so to perform the above time integral, we have to be careful about it. Let's assume we are interested in a single wave number k, and its left the horizon at $\eta = \eta_k$, and we want to compute the tensor power spectrum at the end of inflation, i.e., $\eta = \eta_e$, then we can write it as

$$P_{\mathrm{T}}^{\mathrm{sec}}(k,\eta) = \frac{2}{M_{\mathrm{P}}^4}\left[\int_{\eta_k}^{\eta} d\eta_1 a^2(\eta_1)\mathcal{G}_{\mathbf{k}}(\eta_f,\eta_1)\mathcal{P}_{\mathrm{B}}(k,\eta_1)\right]^2 \times \int_0^\infty \frac{dq}{q}\int_{-1}^{1} d\mu \frac{(q/k)^{n_{\mathrm{B}}} f(\mu,\beta,\lambda)}{\left[1+\left(\frac{q}{k}\right)^2 - 2\mu\frac{q}{k}\right]^{\frac{3-n_{\mathrm{B}}}{2}}}. \tag{4.28}$$

To solve the above equation, we have conisder a de sitter inflationary background where the scale factor simple evolve as $a(\eta) \simeq -1/(H_e\eta)$ and now utilizing this in the above equation Eq.(4.28) and replacing the power-law formed of the magnetic power spectrum, we can write the tensor power spectrum at the end of inflation as

$$P_{\mathrm{T}}^{\mathrm{sec}}(k,\eta) = 2\left(\frac{H_e}{M_{\mathrm{P}}}\right)^4 \mathcal{C}_{\mathrm{B}}^2\mathcal{I}_{\mathrm{inf}}^2(k,\eta_e)\times\mathcal{F}_{n_{\mathrm{B}}}(k) \tag{4.29}$$

where we have defined

$$\mathcal{I}_{\mathrm{inf}}(k) = \int_{\eta_k}^{\eta_e}\frac{d\eta_1}{\eta_1}\frac{\mathcal{G}_k(\eta_e,\eta_1)}{\eta_1}(k\eta_1)^{n_{\mathrm{B}}} \tag{4.30}$$

and

$$\mathcal{F}_{n_{\mathrm{B}}}(k) = \int_0^\infty \frac{dq}{q}\int_{-1}^{1} d\mu \frac{(q/k)^{n_{\mathrm{B}}} f(\mu,\beta,\lambda)}{\left[1+\left(\frac{q}{k}\right)^2 - 2\mu\frac{q}{k}\right]^{\frac{3-n_{\mathrm{B}}}{2}}} \tag{4.31}$$

As we have seen that the magnetic field or the electric field can only grow after exiting the horizon, and for simplicity, we can assume that at the end of inflation $\eta \to 0$, then we can further simplify the Green's function as

$$\mathcal{G}_k^{\mathrm{inf}}(0,\eta') = \frac{1}{k^3\eta'^2}\left[-\sin(k\eta') + k\eta\cos(k\eta')\right]. \tag{4.32}$$

It is evident that the primary contribution to Green's function arises from the super-horizon scale, particularly in the limit $|k\eta'| \ll 1$. In this regime, we can approximate $\mathcal{G}_{\mathbf{k}}(\eta') \approx \eta'/3$. Utilizing these considerations and incorporating all assumptions, we proceed to derive the tensor power spectrum after inflation within the de Sitter inflationary background

$$\mathcal{I}_{\mathrm{inf}}(k,\eta_e) \simeq -\frac{1}{3}\int_1^{x_e}\frac{dx_1}{x_1}x_1^{n_{\mathrm{B}}} \simeq \frac{1}{3n_{\mathrm{B}}}\left\{1-\left(\frac{k}{k_e}\right)^{n_{\mathrm{B}}}\right\} \tag{4.33}$$

Similarly, to compute the $\mathcal{F}_{n_{\mathrm{B}}}(k)$, we have redefined our variable to a dimensionless variable

$u = q/k$ and rewritten the above quantity in terms of this new variable u

$$\mathcal{F}_{n_{\rm B}}(k) = \int_{u_{\rm min}}^{u_{\rm max}} \frac{du}{u} \frac{u^{n_{\rm B}} \mathcal{F}(\mu\,\beta)}{(1+u^2-2\mu u)^{(3-n_{\rm B})/2}} \tag{4.34}$$

As our sourced magnetic field is non-helical, for a non-helical magnetic field, the functional formed of $\mathcal{F}(\mu,\beta)$ is $\mathcal{F}(\mu,\beta) = 2(1+\mu^2)(1+\beta^2)$. Now we can see that this integral has a singularity at $u = \mu = 1$, so above this singularity, we break the integral into two parts

$$\mathcal{F}_{n_{\rm B}}(k) = \int_{u_{\rm min}}^{1} \frac{du}{u} \frac{u^{n_{\rm B}} \mathcal{F}(\mu\,\beta)}{(1+u^2-2\mu u)^{(3-n_{\rm B})/2}} + \int_{1}^{u_{\rm max}} \frac{du}{u} \frac{u^{n_{\rm B}} \mathcal{F}(\mu\,\beta)}{(1+u^2-2\mu u)^{(3-n_{\rm B})/2}} \tag{4.35}$$

In the approximation limit, if we compute the above integral, we have found that

$$\mathcal{F}_{n_{\rm B}}(k) \simeq \frac{8}{3n_{\rm B}}\left(1-\left(\frac{k_*}{k}\right)^{n_{\rm B}}\right) + \frac{56}{15(2n_{\rm B}-3)}\left(\left(\frac{k_{\rm e}}{k}\right)^{2n_{\rm B}-3} - 1\right). \tag{4.36}$$

Here, $\mathcal{C}_{\rm E}(n_{\rm E}) = \frac{2^{5-n_{\rm E}}\,\Gamma^2\left(\frac{5-n_{\rm E}}{2}\right)}{8\pi^3}$ determines the amplitude of the electric field.

Interestingly, for a de Sitter inflationary background, we find that when the electric or magnetic spectra are either blue-tilted or scale-invariant, both fields generate scale-invariant tensor perturbations [240]. In contrast, for red-tilted electric or magnetic spectra, the resulting tensor power spectrum becomes scale-dependent and typically follows $P^{\rm sec}_{\rm T,inf}(k,\eta_{\rm e}) \propto k^{-|n_{\rm B/E}|}$. In the present scenario, since the dominant contribution arises entirely from the electric field, the tensor power spectrum sourced by the electric field is expected to scale as $P^{\rm sec}_{\rm T,inf}(k) \propto \left(\frac{H_{\rm e}}{M_{\rm P}}\right)^4$, given that the electric field power spectrum behaves as $\mathcal{P}_E(k) \propto H_{\rm e}^4$. In contrast, the tensor power spectrum originating from vacuum quantum fluctuations of spacetime follows $P^{\rm vac}_{\rm T,inf}(k) \propto \left(\frac{H_{\rm e}}{M_{\rm P}}\right)^2$.

For blue-tilted electric spectra with $n_{\rm E} > 0$, the vacuum contribution typically dominates on large (CMB) scales, as the electric field power is concentrated at small scales. However, for $n_{\rm E} < 0$ (corresponding to $n < -2$), the electric field becomes red-tilted, with its energy concentrated on large scales. In this case, it becomes possible for the secondary tensor modes sourced by the electric field to dominate over the primary vacuum contribution at CMB scales.

4.3.2 Tensor power spectrum during reheating

After inflation, all fundamental particles are produced through the decay of the inflaton field. The nature of gravitational wave (GW) production in the subsequent reheating era depends sensitively on the electrical conductivity of the Universe. As previously discussed, in the limit of negligible conductivity, both electric and magnetic fields are present and evolve freely. In contrast, in the case of large or infinite conductivity, the electric field is quickly suppressed due to the high response of charged particles, leaving only the magnetic field. Additionally, in the zero-conductivity limit, energy transfer from the electric to the magnetic field via the

Faraday induction mechanism significantly enhances the magnetic field amplitude. However, such enhancement does not occur in the high-conductivity regime, resulting in much weaker magnetic fields.

Consequently, in the infinite conductivity limit, the secondary GW production sourced by the magnetic field is expected to be suppressed, particularly at large scales. Since we are interested in scenarios that lead to successful magnetogenesis without encountering strong coupling or backreaction issues, we focus on the case where conductivity during reheating is negligible, and the coupling parameter lies within the range $-2.2 < n < 0$. In this regime, the dominant post-inflationary contribution to the stochastic gravitational wave background (SGWB) arises from the electric field.

During the reheating phase, the corresponding Green's function can be expressed as [229]

$$\mathcal{G}_k(x, x_1) = \theta(x - x_1)\frac{\pi x^l x_1^{1-l}}{2k\sin(l\pi)}\left[J_l(x)J_{-l}(x_1) - J_{-l}(x)J_l(x_1)\right] \tag{4.37}$$

Since the tensor power spectrum is sourced by the electric field, the tensor spectrum generated during reheating due to the electromagnetic field, evaluated at the end of reheating, can be generally expressed as

$$P_{T,s}^{\rm re} = \frac{2H_{\rm e}^4}{M_{\rm P}^4}\left(\frac{k}{k_{\rm e}}\right)^{2(\delta-2)}\mathcal{C}_{\rm E}^2(n_{\rm E})\left(\frac{k}{k_{\rm e}}\right)^{2n_{\rm E}}\mathcal{C}_{\rm m,re}^2(x_{\rm re}, x_{\rm e})\mathcal{F}_{n_{\rm E}}(k), \tag{4.38}$$

where $\mathcal{F}_{n_{\rm E}}$ is defined in Eq. (4.36) and $\mathcal{C}_{\rm m,re}(x_{\rm re}, x_{\rm e})$ is defined as [229]

$$\mathcal{C}_{\rm m,re}(x_{\rm re}, x_{\rm e}) = \int_{x_{\rm e}}^{x_{\rm re}} dx_1\, x_1^{-\delta}\mathcal{G}_k(x_{\rm re}, x_1), \tag{4.39}$$

Upon analyzing the spectrum, we find that the presence of a non-instantaneous reheating phase introduces an overall factor of the form $(k_{\rm re}/\kappa_{\rm end})^{2(\delta-2)}$, where $\delta = 4/(1+3w_{\rm re})$. This indicates that the amplitude of the spectrum can either be enhanced or suppressed depending on the equation of state during reheating: it is enhanced for $w_{\rm re} > 1/3$ and suppressed for $w_{\rm re} < 1/3$.

Moreover, we observe that for modes that remain outside the horizon during reheating ($k < k_{\rm re}$), the secondary tensor spectrum behaves as $\mathcal{P}_{\rm s}^{\rm re}(k \ll k_{\rm re}, \eta_{\rm re}) \propto k^{2n_{\rm E}}$. In contrast, for modes that re-enter the horizon during reheating ($k \gg k_{\rm re}$), the spectrum scales as $\mathcal{P}_{\rm s}^{\rm re}(k \gg k_{\rm re}, \eta_{\rm re}) \propto k^{2n_{\rm E}-|n_w|-2}$, where $n_w = 2(1-3w_{\rm re})/(1+3w_{\rm re})$.

4.3.3 Tensor power spectrum during radiation dominted era

For this specific choice of coupling, there are no significant additional contributions to the gravitational wave spectrum from the radiation-dominated era. This is because, following reheating, it is generally assumed that all fundamental particles are produced and the Universe becomes thermalized, resulting in a highly conductive plasma. As a consequence, the electric field component is rapidly suppressed. However, the magnetic field survives and evolves adiabatically, with its energy density decreasing solely due to the expansion of the background.

Therefore, the tensor power spectrum sourced by the magnetic field after reheating, evaluated at the time of neutrino decoupling, is governed by the expression [229].

$$P^{\lambda}_{\mathrm{ra,SEC}}(k,\eta_\nu) = \frac{2H_\mathrm{e}^4}{k^2\eta_\nu^2 M_\mathrm{P}^4}\left(\frac{k_\mathrm{re}}{k_\mathrm{e}}\right)^{2(\delta-2)}\mathcal{C}_\mathrm{B}^2(n_\mathrm{B})\left(\frac{k}{k_\mathrm{e}}\right)^{2n_\mathrm{B}}\mathcal{I}_\mathrm{ra}{}^2(x_\nu,x_\mathrm{re})\mathcal{F}_{n_\mathrm{B}}(k) \tag{4.40}$$

We recall that $n_\mathrm{B} = n_\mathrm{E} + 2$ is the magnetic spectral index for $n < 0$ magnetogenesis scenarios. Here, $\mathcal{I}_\mathrm{ra}(x_\nu, x_\mathrm{re})$ is defined as [229]

$$\mathcal{I}_\mathrm{ra}(x_\nu,x_\mathrm{re}) = \int_{x_\mathrm{re}}^{x_\nu} dx_1 \frac{\sin(x_1 - x_\nu)}{x_1}. \tag{4.41}$$

As for the low-frequency regions, we found that $\mathcal{I}_\mathrm{ra} = \gamma_1$, where $\gamma_1 \sim 0.5$ at the epoch of neutrino decoupling.

In this context, we observe that the tensor power spectrum generated during this phase includes an overall enhancement factor. This enhancement originates from the dynamics of the reheating phase: while the background energy density dilutes as $a^{-3(1+w_\mathrm{re})}$, the magnetic field energy density redshifts as a^{-4}. As a result, depending on the equation of state (EoS), the gravitational wave contribution from magnetic fields can either be enhanced (for $w_\mathrm{re} > 1/3$) or suppressed (for $w_\mathrm{re} < 1/3$).

Specifically, within the framework of this magnetogenesis model, a significant contribution to the tensor spectrum in the frequency range $f_\nu < f < f_\mathrm{re}$ arises only when $w_\mathrm{re} > 1/3$ and the coupling parameter satisfies $n > 1/2$. Here, n refers to the coupling constant associated with the magnetogenesis scenario discussed in the above Eq.(4.4).

4.3.4 Spectral Analysis of Primary Gravitational Waves (PGWs)

For simplicity, we decompose the total dimensionless energy density associated with gravitational waves (GWs) into two distinct components, denoted as $\Omega_\mathrm{GW}(f) = \Omega_\mathrm{GW}^\mathrm{pri}(f) + \Omega_\mathrm{GW}^\mathrm{sec}(f)$. Specifically, $\Omega_\mathrm{GW}^\mathrm{pri}(f)$ represents contributions originating from quantum vacuum fluctuations, while $\Omega_\mathrm{GW}^\mathrm{sec}(f)$ encompasses the contributions attributed to electromagnetic fields. To comprehensively examine the spectral characteristics of GWs across the entire observable frequency spectrum, we separately discuss two distinct scenarios based on the reheating dynamics, namely, $w_\mathrm{re} < 1/3$ and $w_\mathrm{re} > 1/3$.

Primary Gravitational Waves (PGWs) refer exclusively to the contributions arising from quantum fluctuations during inflation. To analyze the effects of post-inflationary dynamics on the gravitational wave (GW) spectrum, we consider two distinct regimes: (a) super-horizon scales, $f < f_\mathrm{re}$, where modes remain outside the horizon before the end of reheating, and (b) sub-horizon scales, $f_\mathrm{re} < f < f_\mathrm{end}$, where modes re-enter the horizon before the end of reheating. While inflation alone typically generates a scale-invariant tensor power spectrum, these regimes reveal distinct spectral behaviors. The present-day GW spectrum, produced by inflation, can be expressed as [119, 229]

$$\Omega_{\rm GW}^{\rm pri}(f) \simeq 1.12 \cdot 10^{-17} \left(\frac{\Omega_R h^2}{4.3 \cdot 10^{-5}}\right) \left(\frac{H_{\rm e}}{10^{-5} M_{\rm P}}\right)^2 \times \begin{cases} 1 & f < f_{\rm re} \\ (f/f_{\rm re})^{-n_w} & f_{\rm re} < f < f_{\rm end}, \end{cases} \tag{4.42}$$

From this expression, we observe that, for super-horizon modes ($f < f_{\rm re}$), the spectrum remains scale-invariant, consistent with the inflationary tensor power spectrum. However, for modes that re-entered the horizon before reheating completed ($f > f_{\rm re}$), the spectrum is no longer scale-invariant. Specifically, for reheating scenarios with an equation of state $w_{\rm re} > 1/3$ (stiff-fluid-like), the spectrum has a blue tilt, while for $w_{\rm re} < 1/3$ it has a red tilt. This difference arises because, in $w_{\rm re} < 1/3$ scenarios, GW modes that remain inside the horizon for longer durations experience greater dilution, as the background energy density decays more slowly compared to the GW energy density. Conversely, for $w_{\rm re} > 1/3$ scenarios, modes are amplified by spending longer periods within the horizon, due to the faster decay of background energy density relative to GW energy density.

Spectral Analysis of Secondary Gravitational Waves (SGWs)

In analyzing the spectrum of secondary gravitational waves (SGWs) over a broad frequency range, we concentrate on contributions arising from inflationary magnetogenesis, while neglecting the primary gravitational waves sourced by vacuum fluctuations. Two limiting scenarios are considered based on the conductivity of the Universe during reheating. In the first case, we assume zero electrical conductivity, where both electric and magnetic fields are present throughout the reheating phase. In the second scenario, we consider infinite electrical conductivity, in which only the magnetic field survives and evolves adiabatically after inflation.

Zero Electrical Conductivity during the Reheating Era: Under the assumption of negligible electrical conductivity during reheating, both electric and magnetic fields persist during this epoch. In the parameter range that avoids both strong coupling and backreaction issues, namely $-0.4 < n_{\rm E} < 4$, the electric field typically dominates. Consequently, the SGW spectrum is predominantly sourced by the electric field during inflation and reheating. Although the magnetic field can contribute to SGW production in the subsequent radiation-dominated era (up to neutrino decoupling), the contribution from the reheating phase is generally dominant.

The shape of the resulting GW spectrum is sensitive to the background evolution during reheating. Specifically, for reheating scenarios with an equation of state parameter $w_{\rm re} < 1/3$, the present-day SGW spectrum sourced by the electromagnetic field is

$$\begin{aligned} \Omega_{\rm GW}^{\rm sec}(f)h^2 \simeq 2.26 \times 10^{-26} \left(\frac{\Omega_R h^2}{4.3 \times 10^{-5}}\right) \left(\frac{H_{\rm e}}{10^{-5} M_{\rm P}}\right)^4 \mathcal{I}_{\rm inf}^2 \mathcal{C}_\beta^2(n_{\rm E})\, \mathcal{F}_\beta(f) \\ \times \begin{cases} 1, & f_* < f < f_{\rm re}, \\ \left(\frac{f}{f_{\rm re}}\right)^{-|n_w|}, & f_{\rm re} < f < f_{\rm end}. \end{cases} \end{aligned} \tag{4.43}$$

whereas for the reheating scenarios with $w_{\rm re} > 1/3$, the spectral behaviour due to EM field is

$$\Omega^{\rm sec}_{\rm GW,pinf}(f)h^2 \simeq 2.26\times 10^{-26}\left(\frac{\Omega_R h^2}{4.3\times 10^{-5}}\right)\left(\frac{H_{\rm e}}{10^{-5}M_{\rm P}}\right)^4\left(\frac{f_{\rm re}}{f_{\rm end}}\right)^{2(n_w+n_{\rm E})}\mathcal{C}^2_\beta(n_{\rm E})\,\mathcal{F}_{n_{\rm E}}(f)$$
$$\times\begin{cases}\mathcal{A}_1\left(\frac{f}{f_{\rm re}}\right)^{2n_{\rm E}}, & f_* < f < f_{\rm re},\\ \mathcal{A}_2\left(\frac{f}{f_{\rm re}}\right)^{2n_{\rm E}-|n_w|}, & f > f_{\rm re}\end{cases} \tag{4.44}$$

Here, we clearly observe an additional enhancement factor associated with reheating scenarios where $w_{\rm re} > 1/3$, which arises from the specific evolution of the background dynamics during the reheating phase. This enhancement originates from the differential dilution rates between the background energy density and the electromagnetic (EM) field energy density. For $w_{\rm re} > 1/3$, the background energy density redshifts more rapidly than the EM field, leading to a relative amplification of the SGW signal. The coefficients $\mathcal{A}_1$ and $\mathcal{A}_2$, which characterize this enhancement, are provided in Appendix A.4.

Infinite Electrical Conductivity During the Reheating Era: In scenarios with infinite electrical conductivity during reheating, electric fields are rapidly dissipated, implying that any contributions from electric fields to the secondary gravitational wave (SGW) background arise solely from their inflationary production. In contrast, magnetic fields can persist and contribute during both the reheating and radiation-dominated eras. However, as demonstrated, even for reheating scenarios with $w_{\rm re} > 1/3$, the magnetic field amplitude remains relatively weak, rendering the induced SGW signal subdominant compared to the primary gravitational waves generated during inflation.

Therefore, for reheating scenarios with $w_{\rm re} < 1/3$, the SGW spectrum retains the same spectral behavior as described in Eq. (4.43). Conversely, for $w_{\rm re} > 1/3$, the SGW spectrum is no longer dominated by the magnetic field alone and may receive non-negligible contributions from the residual electric field produced during inflation.

$$\Omega^{\rm sec}_{\rm GW}(f)h^2 \simeq 2.26\times 10^{-26}\left(\frac{\Omega_R h^2}{4.3\times 10^{-5}}\right)\left(\frac{H_{\rm e}}{10^{-5}M_{\rm P}}\right)^4\left(\frac{f_{\rm re}}{f_{\rm end}}\right)^{2n_{\rm B/E}}\mathcal{I}^2_{\rm inf}\mathcal{C}^2_\beta(n_{\rm B/E})\,\mathcal{F}_\beta(k)$$
$$\times\begin{cases}\left(\frac{f}{f_{\rm re}}\right)^{2n_{\rm E}}, & f_* < f < f_{\rm re},\\ \left(\frac{f}{f_{\rm re}}\right)^{2n_{\rm E}+|n_w|}, & f_{\rm re} < f < f_{\rm end}.\end{cases} \tag{4.45}$$

To achieve a successful magnetogenesis scenario without encountering strong coupling or back-reaction issues, the zero electrical conductivity limit during reheating is particularly favorable within the coupling range $-2.2 < n < 0$ (equivalently, $-0.4 < n_{\rm E} < 4$). In particular, for the subclass with $n < -2.0$ (i.e., $n_{\rm E} < 0$), the electric field produced during inflation is red-tilted. This red tilt enhances the power at large scales and can significantly impact the tensor power spectrum, including at cosmic microwave background (CMB) scales, for both $w_{\rm re} < 1/3$ and $w_{\rm re} > 1/3$ reheating scenarios.

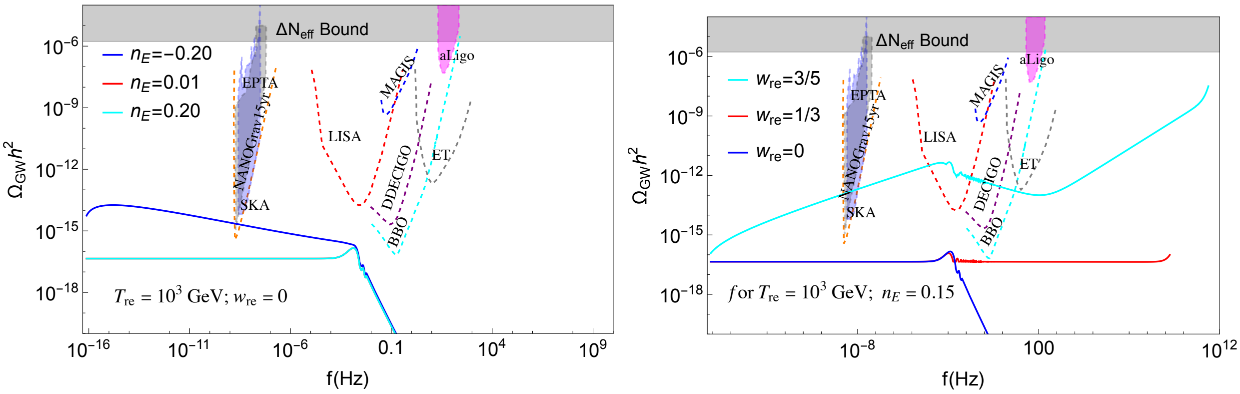

Figure 4.3: Present-day gravitational-wave energy density $\Omega_{\rm GW}h^2$ plotted as a function of frequency f (in Hz) for $w_{\rm re} = 0$, illustrating two different parameter dependencies. In the left panel, the variation of the GW amplitude with the magnetogenesis parameter $n_{\rm E}(= 4 - 2|n|)$ is shown for a fixed reheating temperature $T_{\rm re} = 10^3\,$GeV, where different colors represent four distinct values of the electric spectral index. In the right panel, we plotted for different equations of state $w_{\rm re} = 0,\ 1/3$ and $3/5$ for a fixed electric spectral index $n_{\rm E} = 0.15$ with a fixed value of reheating temperature $T_{\rm re} = 10^3\,$GeV.

Most notably, these scenarios can generate a sizable tensor-to-scalar ratio at CMB scales, potentially exceeding the current observational upper bound $r_{0.05} \leq 0.036$. In the following discussion, we explore how this observational constraint can be used to place stringent bounds on both the reheating dynamics and the magnetogenesis model parameter n.

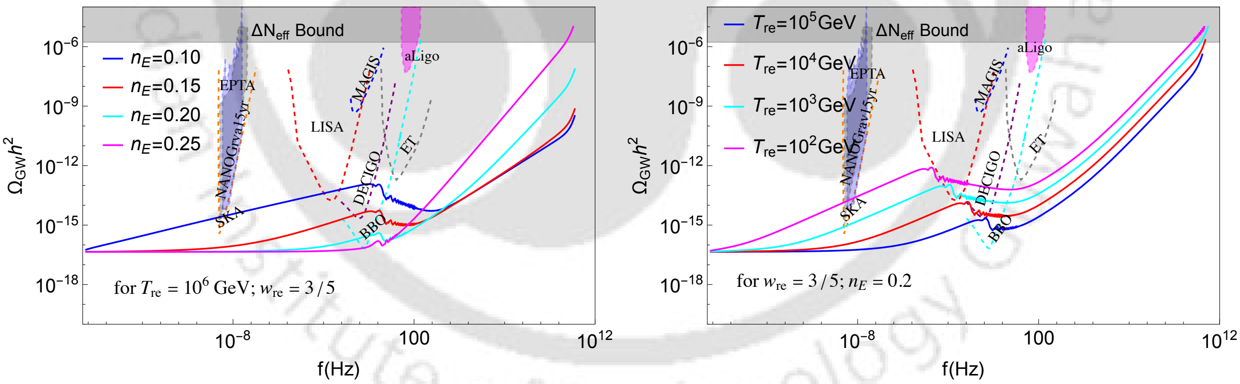

Figure 4.4: Present-day gravitational-wave energy density $\Omega_{\rm GW}h^2$ as a function of the comoving frequency f (Hz) for non-helical magnetogenesis with coupling $n < -1/2$, assuming negligible electrical conductivity during reheating and a stiff-like equation of state $w_{\rm re} = 3/5$. The left panel illustrates how the amplitude and spectral tilt of the GW background depend on the electric spectral index $n_{\rm E}$ (shown in different colors) for a fixed reheating temperature $T_{\rm re} = 10^6\,$GeV. The right panel highlights the impact of the reheating temperature on both the amplitude and the peak structure of the GW spectrum for a fixed spectral index $n_{\rm E} = 0.2$.

4.4 Results and Discussion:

In Fig. 4.3, we present the present-day gravitational wave (GW) energy spectrum, $\Omega_{\rm GW}h^2(f)$, as a function of the observed frequency f (Hz), for different values of the electric spectral index $n_{\rm E}$ and the reheating equation of state $w_{\rm re}$.

In the left panel, we plot the present-day GW spectrum for three different values of the electric spectral index, $n_{\rm E} = -0.20,\, 0.01$, and 0.20, assuming a fixed reheating dynamics. Specifically, we consider a matter-like evolution after inflation, i.e., $w_{\rm re} = 0$, and fix the reheating temperature to $T_{\rm re} = 10^3\,{\rm GeV}$.

Since we assume a matter-like evolution during reheating, the background energy density dilutes faster than the electromagnetic energy density. Moreover, in the absence of any coupling after inflation, the post-inflationary contribution from the electromagnetic field is expected to be subdominant compared to the inflationary contribution. For simplicity, we assume a de Sitter inflationary background.

For a blue-tilted electric spectrum ($n_{\rm E} \geq 0$), the produced secondary GW spectrum is scale-invariant at low frequencies, corresponding to modes that re-enter during the radiation-dominated era. In this regime, the spectral energy density behaves as $\Omega_{\rm GW}h^2(f < f_{\rm re}) \propto f^0$. However, modes that re-enter during the reheating phase experience additional dilution due to the matter-like background, leading to a red-tilted spectrum at higher frequencies, $\Omega_{\rm GW}h^2(f > f_{\rm re}) \propto f^{-2}$.

On the other hand, for a red-tilted electric spectrum ($n_{\rm E} < 0$), the GW spectrum exhibits a red tilt even at low frequencies. In this case, the spectral behavior is given by $\Omega_{\rm GW}h^2(f < f_{\rm re}) \propto f^{-|n_{\rm E}|}$, while for higher frequencies, $\Omega^{\rm sec}_{\rm GW}h^2(f > f_{\rm re}) \propto f^{-2-|n_{\rm E}|}$.

However, as shown in the left panel of Fig. 4.3, for all three values of $n_{\rm E}$ considered, the high-frequency GW spectrum behaves as $\Omega^{\rm sec}_{\rm GW}h^2(f > f_{\rm re}) \propto f^{-2}$. This behavior arises due to the dominant contribution from primary GWs. For the chosen parameter set, the primary GW component dominates over the secondary contribution at high frequencies. In particular, for $w_{\rm re} = 0$, the primary GW spectrum follows $\Omega^{\rm pri}_{\rm GW}h^2(f > f_{\rm re}) \propto f^{-2}$, as discussed in Eq. (4.42).

In the right panel of Fig. 4.3, we show the GW spectrum for different values of the reheating equation of state, $w_{\rm re} = 0,\, 1/3$, and $3/5$, while fixing $T_{\rm re} = 10^3\,{\rm GeV}$ and $n_{\rm E} = 0.15$. An interesting feature emerges when considering a stiff-like equation of state ($w_{\rm re} > 1/3$). In this case, the spectral behavior of the GW background is significantly modified. Notably, even for a simple single power-law electromagnetic spectrum, the resulting GW spectrum exhibits multiple spectral features. Depending on the choice of parameters, the resulting GW spectrum can fall within the sensitivity range of future GW detectors such as LISA, DECIGO, and BBO, making this scenario observationally testable.

In Fig. 4.4, we present the present-day gravitational wave (GW) spectrum $\Omega_{\rm GW}h^2(f)$ as a function of the observable frequency f (in Hz) for reheating scenarios with an equation of state $w_{\rm re} > 1/3$. For such scenarios, the spectrum typically exhibits more spectral features compared to the $w_{\rm re} < 1/3$ case, owing to the more complex interplay between primary and secondary

GW sources.

The left panel illustrates the dependence of the GW spectrum on the electric spectral index $n_{\rm E}$, fixing $w_{\rm re} = 3/5$ and the reheating temperature $T_{\rm re} = 10^6\,$GeV. Depending on the value of $n_{\rm E}$, we observe a variety of spectral structures: in some cases, the spectrum exhibits three distinct breaks, in others two, and occasionally only one. This rich spectral behavior arises from the varying dominance of the different contributions to the GW background.

For instance, considering $n_{\rm E} = 0.15$ with $w_{\rm re} = 3/5$ and $T_{\rm re} = 10^6\,$GeV, the spectrum near the CMB scale appears scale-invariant due to the dominance of primary GWs (PGWs) over secondary GWs (SGWs). At intermediate frequencies $f < f_{\rm re}$, the spectrum transitions to a blue-tilted behavior $\Omega_{\rm GW}h^2(f) \propto f^{2n_{\rm E}}$, as SGWs sourced by the blue-tilted electric field become dominant. In the range $f_{\rm re} \ll f \ll f_{\rm end}$, the spectrum shows a red-tilted behavior due to the suppression of SGWs by reheating dynamics. Finally, at high frequencies $f \gg f_{\rm re}$, the spectrum becomes blue-tilted again, following $\Omega_{\rm GW}h^2(f) \propto f^{|n_w|}$, where PGWs regain dominance.

The right panel of Fig. 4.4 shows the impact of the reheating duration on the present-day GW amplitude. For a fixed $w_{\rm re} = 3/5$, increasing the reheating temperature leads to a gradual suppression of the overall GW amplitude. This behavior is consistent with the scaling $(k_{\rm e}/k_{\rm re})^{2|n_w|}$, which parametrizes the enhancement due to electromagnetic field contributions during reheating for $w_{\rm re} > 1/3$.

Constraining model parameters through the Tensor-to-Scalar Ratio r: This magnetogenesis model generates significant electric and magnetic fields capable of producing gravitational waves (GWs) strong enough to pass various sensitivity thresholds and create notable tensor fluctuations at CMB scales. For $w_{\rm re} > 1/3$ reheating scenarios, the reheating dynamics introduce an overall enhancement factor, $(k_{\rm e}/k_{\rm re})^{|n_w|}$, related to the duration of the reheating phase. However, constraints on tensor fluctuations at CMB scales, quantified by the tensor-to-scalar ratio $r_{0.05}$, place a limit on GW strength at the pivot scale: $\Omega_{\rm GW}h^2 \leq 1.14\times10^{-7} r_{0.05}A_s$. Here, $A_s \simeq 2.1\times10^{-9}$ is the current bound on the scalar amplitude at the pivot scale.

Using the limit $r_{0.05} \leq 0.036$, we find that the coupling parameter n for magnetogenesis should satisfy $-2.1 \leq n \leq 0$. This bound holds universally, even for instantaneous reheating. For prolonged reheating scenarios with $w_{\rm re} > 1/3$, these constraints become more robust, limiting both the reheating dynamics and the magnetogenesis model. Thus, utilizing the upper bound $r_{0.05} \leq 0.036$ at the pivot scale, we derive the following constraint,

$$1 \geq \frac{182\, r A_s \mathcal{A}_1}{(3-2n_{\rm E})}\left(\frac{k_{\rm e}}{k_{\rm re}}\right)^{2|n_w|}\left(\frac{k_*}{k_{\rm e}}\right)^{2n_{\rm E}}\mathcal{C}_{\rm E}^2(n_{\rm E}). \tag{4.46}$$

Using this constraint, we set bounds on the reheating temperature for specific values of the equation of state (EoS) across five discrete values of the magnetic spectral index $n_{\rm E} = 0.01, 0.1, 0.2, 0.3,$ and 0.4, as shown in Table (4.1).

In our analysis, we treat the reheating equation-of-state parameter $w_{\rm re}$ as a free parameter, allowing it to take arbitrary values. However, in specific inflationary models—for example,

$w_{\rm re}$	$n_{\rm E} = 0.01$	$n_{\rm E} = 0.1$	$n_{\rm E} = 0.2$	$n_{\rm E} = 0.3$	$n_{\rm E} = 0.4$
	$T_{\rm re}$ (GeV)	$T_{\rm re}$ (Ge)V	$T_{\rm re}$ (GeV)	$T_{\rm re}$ (GeV)	$T_{\rm re}$ (GeV)
0.4	1.77×10^{9}	–	–	–	–
0.5	5.65×10^{12}	1.28×10^{7}	2.89	–	–
0.6	8.2×10^{13}	1.46×10^{10}	5.41×10^{5}	–	–
0.7	3.59×10^{14}	4.86×10^{11}	1.92×10^{8}	4.82×10^{4}	7.91

Table 4.1: Minimum reheating temperature corresponding to different values of the reheating equation-of-state parameter $w_{\rm re}$. The table presents the results for five distinct choices of the electric spectral index $n_{\rm E}$, illustrating how the lower bound on the reheating temperature varies with both $w_{\rm re}$ and $n_{\rm E}$.

those with power-law potentials of the form $V(\phi) \propto \phi^{2m}$, $w_{\rm re}$ can be uniquely determined based on the dynamics of the scalar field. In this work, we adopt a generalized approach by leaving $w_{\rm re}$ unconstrained. As an illustration, to avoid the overproduction of tensor perturbations at CMB scales, consider the case where the magnetic spectral index is $n_{\rm E} = 0.01$ (nearly scale-invariant). For a reheating equation-of-state $w_{\rm re} = 0.4$, the lower bound on the reheating temperature is found to be $T_{\rm re}^{\rm min} \simeq 1.77 \times 10^{9}\,{\rm GeV}$. If the reheating temperature falls below this value, electromagnetic fields generated via this mechanism can produce excessive tensor fluctuations at large scales, violating current observational constraints on the tensor-to-scalar ratio. We summarize the lower bounds on reheating temperatures for various parameter combinations in Table (4.1).

Constraining Reheating and Magnetogenesis Parameters through $\Delta N_{\rm eff}$ Bound:

During the epoch of decoupling, the CMB is influenced by the total radiation energy density. Any excess energy that behaves as radiation-like fields may impact the CMB [323]. In our case, the primordial GWs carry significant energy, and since GWs evolve as a^{-4} like radiation, frequencies $f > 10^{-15}$ Hz can be treated as extra radiation energy that may affect the CMB (see related discussions in [231, 324]). This excess radiation can be quantified by the additional relativistic degrees of freedom at decoupling, expressed as $\Delta N_{\rm eff}$, indicating the extra neutrino species predicted beyond the Standard Model. Using this, we derive the following constraint [229, 231],

$$\Delta N_{\rm eff} \geq \frac{1}{\Omega_\gamma h^2}\frac{8}{7}\left(\frac{11}{4}\right)^{4/3}\int_{f_*}^{f_{\rm end}}\frac{df}{f}\Omega_{\rm GW}h^2(f). \tag{4.47}$$

Assuming the present-day photon density parameter as $\Omega_\gamma h^2 \simeq 2.48 \times 10^{-5}$, the combined latest Planck-2018 and Baryon Acoustic Oscillation (BAO) data predict $\Delta N_{\rm eff} \simeq 0.284$ (within a 2σ range) [11], setting an upper bound on primordial GWs, $\Omega_{\rm GW}h^2 < 1.67 \times 10^{-6}$ [68].

At high frequencies, the GW spectrum behaves as $\Omega_{\rm GW}h^2 \propto f^{2n_{\rm E}}$ for $f < f_{\rm re}$, while for modes well within the horizon ($f \gg f_{\rm re}$), it follows $\Omega_{\rm GW}h^2 \propto f^{2n_{\rm E}-n_w}$. Therefore, if $2n_{\rm E} > n_w$, the spectrum has a red tilt for $f > f_{\rm re}$; otherwise, it has a blue tilt. Using this bound, we find that for reheating scenarios with $w_{\rm re} = 0$, the maximum allowed magnetic spectral index consistent with the $\Delta N_{\rm eff}$ bound is $n_{\rm E} \leq 1.0$. This constraint also restricts the reheating temperature for a fixed magnetic spectral index and equation of state (EoS). For instance, with $w_{\rm re} = 0$ and $n_{\rm E} = 1.0$, the reheating temperature should be below $T_{\rm re} < 10^3$ GeV. For $n_{\rm E} = 0.9$ and $w_{\rm re} = 0$, a more relaxed bound is obtained, $T_{\rm re} \leq 10^7$ GeV.

For higher EoS, $w_{\rm re} > 1/3$, at high frequencies with $n_{\rm E} > 0.3$, the GW spectrum follows $\Omega_{\rm GW}h^2 \propto f^{2n_{\rm E}+|n_w|}$. In this regime, secondary GW production during inflation is more substantial compared to late-time production, and since the background dilutes faster than the GW energy density (for $w_{\rm re} > 1/3$ scenarios), these frequency modes are more enhanced. Thus, for $w_{\rm re} > 1/3$, this bound imposes even stronger constraints on both the magnetic spectral index and reheating dynamics.

In our scenario, both the electric and magnetic fields are generated during inflation and evolve adiabatically after inflation. As a result, there are two stages during which the electromagnetic (EM) field can generate significant curvature perturbations: during inflation and during the reheating era.

On a uniform-density hypersurface, the comoving curvature perturbation is defined as

$$\zeta = -\Phi - \mathcal{H}\frac{\delta\rho}{\rho'}. \tag{4.48}$$

Since we are interested in the secondary curvature perturbation generated by the EM field, we neglect the primary contribution from vacuum fluctuations throughout this discussion. The EM field can source the curvature perturbation in two ways. First, it directly contributes through the energy-density perturbation, $\delta\rho/\rho'$. Second, it sources the metric perturbation Φ. The first contribution becomes important during inflation, when the gauge field is generated from quantum fluctuations. The second contribution can also be enhanced during reheating, particularly when the equation of state satisfies $w_{\rm re} > 1/3$.

Induced curvature perturbation during inflation:

We first consider the curvature perturbation generated during inflation, when the relevant modes are already outside the horizon. Our goal is to determine which contribution dominates the induced curvature perturbation on super-horizon scales.

The perturbed Einstein constraint equation in the Newtonian gauge is given by [33,226,227]

$$3\mathcal{H}(\mathcal{H}\Phi + \Psi') - \nabla^2\Psi = -\frac{a^2\delta\rho}{2M_{\rm P}^2}. \tag{4.49}$$

For super-horizon modes ($k \ll aH$), the gradient term satisfies $k^2\Psi \ll 1$ and can therefore be neglected. During inflation, this reduces to

$$\zeta_\Psi^{\rm inf} = \Psi \simeq -\frac{a^2\delta\rho}{6\mathcal{H}^2M_{\rm P}^2} = -\frac{1}{2}\frac{\delta\rho}{\rho}. \tag{4.50}$$

The contribution from the second term of Eq. (4.48) is

$$\zeta_{\delta\rho}^{\rm inf} \simeq -H\frac{\delta\rho}{\dot{\rho}} \simeq -\frac{1}{2\epsilon}\frac{\delta\rho}{\rho}, \tag{4.51}$$

where we have used $\dot{\rho} = -3H\dot{\phi}^2$ [38], with $\dot{\phi}$ denoting the inflaton velocity.

Comparing Eqs. (4.50) and (4.51), we obtain $\zeta_{\Psi}^{\rm inf}/\zeta_{\delta\rho}^{\rm inf} = \epsilon$. Since the slow-roll parameter satisfies $\epsilon \ll 1$, the metric contribution is strongly suppressed. Therefore, on super-horizon scales the induced curvature perturbation is dominated by the energy-density perturbation, corresponding to the second term in Eq. (4.48).

Induced curvature power spectrum from IMFs:

In our magnetogenesis scenario, the electric field dominates over the magnetic field during inflation. Consequently, the induced curvature perturbation is mainly sourced by the electric field.

The curvature power spectrum induced by the electromagnetic field at the end of inflation is given by [325, 326]

$$\mathcal{P}_\zeta^{\rm ind}(k,\eta_{\rm e}) = \frac{1}{8\epsilon^2\rho_c^2}\int\frac{dq}{q}\int_{-1}^{1}d\gamma\,\frac{(1-\gamma^2)\mathcal{P}_{\rm E}(q,\eta_{\rm e})\mathcal{P}_{\rm E}(|\mathbf{k}-\mathbf{q}|,\eta_{\rm e})}{|1-\mathbf{q}/\mathbf{k}|^5}, \tag{4.52}$$

where $\gamma = \hat{q}\cdot\hat{k} = \cos\theta$, and θ is the angle between the wave vectors $\mathbf{k}$ and $\mathbf{q}$.

Substituting the electric-field power spectrum from Eq. (??) into Eq. (4.52), we obtain

$$\mathcal{P}_\zeta^{\rm ind}(k) \simeq \frac{1}{72\epsilon^2}\left(\frac{H_{\rm e}}{M_{\rm P}}\right)^4\mathcal{C}_{\rm E}^2(n_{\rm E})\left(\frac{k}{k_{\rm e}}\right)^{2n_{\rm E}}\mathcal{F}_{n_{\rm E}}(k), \tag{4.53}$$

where

$$\mathcal{F}_{n_{\rm E}}(k) \simeq \frac{4}{3}\left[\frac{1}{n_{\rm E}}\left(1-\left(\frac{k_*}{k}\right)^{n_{\rm E}}\right)+\frac{1}{5-2n_{\rm E}}\left(1-\left(\frac{k}{k_{\rm e}}\right)^{5-2n_{\rm E}}\right)\right]. \tag{4.54}$$

In deriving Eq. (4.53), we have used $\rho_c = 3H_{\rm e}^2M_{\rm P}^2$, which is the background inflaton energy density at the end of inflation.

Equation (4.53) shows that the induced curvature power spectrum depends on both the amplitude of the electromagnetic field and the slow-roll parameter ϵ. Since ϵ varies only slowly during inflation, the large-scale behaviour of the spectrum is mainly determined by the factor $k^{2n_{\rm E}}$. Therefore, the spectral tilt of the induced curvature perturbation is directly controlled by the electric-field spectral index.

For the non-helical magnetogenesis scenario considered here, where $\mathcal{C}_{\rm E} = \mathcal{O}(1)$, the induced curvature perturbation remains much smaller than the primary curvature perturbation generated by vacuum fluctuations. The ratio between the induced and primary curvature power spectra is

$$\frac{\mathcal{P}_\zeta^{\rm ind}(k_*)}{P_\zeta^{\rm vac}(k_*)} \simeq \frac{\pi^2}{9\epsilon}\mathcal{C}_{\rm E}^2\left(\frac{H_{\rm e}}{M_{\rm P}}\right)^2\left(\frac{k_*}{k_{\rm e}}\right)^{2n_{\rm E}}. \tag{4.55}$$

Even for an almost scale-invariant electric-field spectrum, the induced contribution remains subdominant because $\mathcal{C}_{\rm E} = \mathcal{O}(1)$, while $\epsilon \sim 10^{-4}$ in the α-attractor E-model considered in this work.

Post-inflationary contribution for $w_{\rm re} > 1/3$ reheating:

The situation changes when reheating is characterized by a stiff equation of state, $w_{\rm re} > 1/3$. Although the electromagnetic energy density is subdominant during inflation, its fractional contribution grows during reheating because the background energy density redshifts faster, $\frac{\delta\rho_{\rm em}}{\rho} \propto a^{3w_{\rm re}-1}$. Consequently, the induced curvature perturbation can be significantly enhanced if the reheating period lasts sufficiently long.

For the blue-tilted spectra considered here ($n_{\rm E} > 0$), most of the electromagnetic energy is concentrated at small scales. During reheating, these short-wavelength modes enter the horizon and are efficiently damped by magnetohydrodynamic (MHD) effects. In contrast, the CMB modes remain outside the horizon throughout reheating and are therefore unaffected by this damping. Since the scalar amplitude at the CMB pivot scale is tightly constrained to be $A_s \simeq 2.1 \times 10^{-9}$, the induced curvature perturbation must satisfy this observational bound.

At super-horizon scales, the induced curvature power spectrum after inflation is

$$\mathcal{P}_\zeta^{\rm ind}(k, \eta > \eta_{\rm e}) \simeq \frac{1}{9(1+w_{\rm re})^2}\frac{1}{\rho^2(\eta)}P_{\delta\rho_{\rm em}}(k,\eta), \tag{4.56}$$

where $P_{\delta\rho_{\rm em}}(k,\eta)$ is the power spectrum of the electromagnetic energy-density perturbation,

$$P_{\delta\rho_{\rm em}}(k,\eta) = \int\frac{dq}{q}\int_{-1}^{1}d\gamma\frac{(1-\gamma^2)\mathcal{P}_{\rm E}(q,\eta)\mathcal{P}_{\rm E}(|\mathbf{k}-\mathbf{q}|,\eta)}{[1+q^2/k^2-2\gamma q/k]^{5/2}}. \tag{4.57}$$

Using the electric-field spectrum, we obtain

$$\mathcal{P}_\zeta^{\rm ind}(k,\eta) = \frac{1}{9(1+w_{\rm re})^2}\frac{H_{\rm e}^8\mathcal{C}_{\rm E}^2}{\rho^2(\eta_{\rm e})}\left(\frac{k}{k_{\rm e}}\right)^{2n_{\rm E}}\left(\frac{a}{a_{\rm e}}\right)^{2(3w_{\rm re}-1)}\mathcal{F}_{n_{\rm E}}(k). \tag{4.58}$$

After reheating, the electric field is rapidly dissipated because of the high conductivity of the primordial plasma. Therefore, it no longer contributes to the curvature perturbation. Although the magnetic field survives, its energy density on large scales is too small to produce any significant contribution. The induced curvature power spectrum at the end of reheating is therefore

$$\mathcal{P}_\zeta^{\rm ind}(k,\eta_{\rm re}) \simeq \frac{1}{81(1+w_{\rm re})^2}\left(\frac{H_{\rm e}}{M_{\rm P}}\right)^4\mathcal{C}_{\rm E}^2\left(\frac{k}{k_{\rm e}}\right)^{2n_{\rm E}}\left(\frac{k_{\rm e}}{k_{\rm re}}\right)^{2|n_w|}\mathcal{F}_{n_{\rm E}}(k). \tag{4.59}$$

Requiring this contribution to remain below the observed scalar amplitude gives

$$A_s \geq \frac{20\mathcal{C}_{\rm E}^2}{243 n_{\rm E}(5-2n_{\rm E})(1+w_{\rm re})^2}\left(\frac{H_{\rm e}}{M_{\rm P}}\right)^4\left(\frac{k_*}{k_{\rm e}}\right)^{2n_{\rm E}}\left(\frac{k_{\rm e}}{k_{\rm re}}\right)^{2|n_w|}. \tag{4.60}$$

Figure **??** shows the minimum reheating temperature as a function of the reheating equation of state for a fixed tensor-to-scalar ratio, $r_{0.05} = 0.036$. The four curves correspond to $n_{\rm E} = 0.01$, 0.1, 0.2, and 0.3.

For example, when $n_{\rm E} = 0.01$ and $w_{\rm re} = 0.5$, the minimum allowed reheating temperature is approximately $T_{\rm re} \simeq 5 \times 10^3$ GeV. Increasing the electric spectral index relaxes this bound because the induced curvature perturbation becomes smaller. Although the reheating temperature is more strongly constrained for larger values of $w_{\rm re}$, we find that the induced curvature perturbation always remains below the observed primordial spectrum for all the cases considered in this work. Therefore, the model is fully consistent with the CMB constraint on the scalar curvature perturbation.

4.5 Conclusions

In this chapter, we have investigated the generation of primordial magnetic fields through an inflationary coupling of the form $f_1^2(\phi)F_{\mu\nu}F^{\mu\nu}$, with a particular focus on the effects of non-instantaneous reheating. We explored how the electrical conductivity during the reheating phase influences the evolution of electromagnetic fields, analyzing two limiting cases: zero and infinite conductivity. Our analysis demonstrates that the reheating phase plays a critical role in determining the present-day strength of magnetic fields on large scales.

By varying the reheating parameters, namely the effective equation of state $w_{\rm re}$ and the reheating temperature $T_{\rm re}$, we showed that it is possible to satisfy current observational bounds on large-scale magnetic fields within the coupling range $-2.1 < n < 0$, provided the reheating scenario involves negligible electrical conductivity. This regime is also free from strong coupling and backreaction problems. For example, under matter-like reheating ($w_{\rm re} = 0$) with $T_{\rm re} \simeq 10^{-2}$ GeV and $n \simeq -2.1$ ($n_{\rm E} \simeq -0.2$), the present-day magnetic field strength at the 1 Mpc scale can reach $B_0(1\,{\rm Mpc}^{-1}) \simeq 4.26 \times 10^{-25}$ G. For a radiation-like evolution with the same parameters, the strength can be as high as $B_0(1\,{\rm Mpc}^{-1}) \simeq 3.99 \times 10^{-13}$ G. In the case of stiff-like evolution ($w_{\rm re} = 0.5$), the maximum field strength achievable for $n_{\rm E} \simeq 0.25$ and $T_{\rm re} \simeq 10^{-2}$ GeV is about $B_0(1\,{\rm Mpc}^{-1}) \simeq 4.97 \times 10^{-15}$ G. These results show that for $w_{\rm re} > 1/3$, slightly blue-tilted electric spectra can produce magnetic fields strong enough to be detectable in future gravitational wave experiments.

In the second part of this work, we explored the generation of secondary gravitational waves (SGWs) from these magnetogenesis scenarios. For $w_{\rm re} < 1/3$, the SGW spectrum peaks at high frequencies and could be detectable by future GW detectors. In contrast, for $w_{\rm re} > 1/3$, the gravitational wave spectrum undergoes non-trivial evolution and may be relevant even at

CMB scales, offering potential constraints via future B-mode polarization measurements. Most notably, higher $w_{\rm re}$ values lead to multiple spectral breaks in the present-day GW spectrum, which could be observed by experiments like LISA, BBO, DECIGO, or even SKA. While radiation-like reheating allows the largest magnetic field strengths, the resulting GW signals often fall below detector sensitivity. However, higher $w_{\rm re}$ scenarios are not only favorable for magnetogenesis but also offer greater promise for GW detection.

In summary, our results show that to successfully realize inflationary magnetogenesis in Ratra-type models, without encountering strong coupling or backreaction issues, one must consider non-trivial reheating scenarios with negligible electrical conductivity. Furthermore, some parameter ranges allow for the simultaneous generation of detectable gravitational wave signals. Our study, therefore, provides a crucial framework for connecting inflationary magnetogenesis with future GW observations and for constraining the physics of reheating.

Chapter 5

Magnetogenesis from Sawtooth Coupling: Gravitational Wave Probe of Reheating

5.1 Introduction

In the previous chapter, we demonstrated that the post-inflationary conversion of electric fields into magnetic fields can successfully explain the origin of large-scale cosmic magnetic fields without encountering the strong-coupling or backreaction problems. In that analysis, it was assumed that the electromagnetic (EM) field is generated only during inflation, and that after the end of inflation the conformal symmetry of the gauge field is automatically restored due to the nature of the coupling. Under this assumption, the subsequent conversion of electric energy density into magnetic energy density on super-horizon scales can enhance the magnetic field amplitude and potentially account for the magnetic fields observed in cosmic voids.

However, this scenario faces difficulties when the post-inflationary evolution of the Universe is taken into account. In particular, if the reheating phase lasts for a sufficiently long duration, the absence of further gauge field production leads to a significant dilution of the magnetic field. Although an efficient conversion of electric energy density to magnetic energy density can occur on super-horizon scales, the prolonged reheating period suppresses the final magnetic field amplitude, resulting in a present-day magnetic field strength that is too small to satisfy observational constraints. To address this issue, in this chapter we investigate a scenario in which the gauge field continues to be produced after inflation through a sawtooth-type coupling, allowing continuous magnetic field generation during both inflation and the reheating phase.

Inflation provides a compelling mechanism for generating large-scale magnetic fields from quantum fluctuations [13–17]. However, the standard electromagnetic action is conformally invariant, which implies that magnetic fields generated during inflation typically decay as $B \propto a^{-2}$ with the expansion of the Universe. Consequently, explicit breaking of conformal invariance is required to sustain significant magnetic field strengths. Various mechanisms have been proposed to achieve this, most commonly through couplings of the form $f_1^2(\varphi)F_{\mu\nu}F^{\mu\nu}$. Nevertheless, many of these models suffer from severe theoretical challenges, including strong coupling and backreaction problems [221, 237, 238, 259, 262–267, 270, 311, 326, 326–330].

A key requirement for successful inflationary magnetogenesis is the generation of a nearly scale-invariant magnetic spectrum on cosmological scales, particularly around 1 Mpc [221, 238]. Although some models produce scale-dependent magnetic spectra at large scales, achieving the required field strength often demands inflationary scenarios with a relatively low energy scale [236, 331]. Moreover, many existing studies include reheating effects only partially and often fail to reproduce the observed large-scale magnetic fields once realistic post-inflationary evolution is taken into account.

Importantly, the parameters describing reheating are not independent of inflation. In realistic cosmological scenarios, the dynamics of reheating are closely connected to the underlying inflationary model. Even within the simplest perturbative reheating framework, the inflationary parameters—such as the inflationary energy scale $H_{\rm e}$ and the number of e-folds $N_{\rm inf}$—can be expressed in terms of two reheating parameters: the effective equation of state $w_{\rm re}$ and the reheating temperature $T_{\rm re}$. Therefore, incorporating reheating consistently is essential for a realistic description of inflationary magnetogenesis.

In this chapter, we systematically incorporate reheating dynamics using a model-independent perturbative reheating framework described in [55]. Our analysis shows that reheating plays a crucial role in determining the evolution of the gauge field. In particular, we find that in many inflationary magnetogenesis scenarios, a reheating phase characterized by matter-like evolution and a low reheating temperature leads to an extremely weak present-day magnetic field, well below observational limits. This indicates that an additional mechanism is required to enhance the magnetic field amplitude after inflation [117, 237, 311]. We demonstrate that allowing the coupling responsible for magnetogenesis to remain active during reheating can significantly modify the magnetic field evolution. In this framework, even though the resulting magnetic spectrum may exhibit strong scale dependence, a prolonged reheating phase with a sufficiently low reheating temperature can still produce magnetic field strengths consistent with current observations.

Another important observational consequence of primordial magnetic fields arises from their ability to source gravitational waves (GWs). Although large-scale magnetic fields are primarily inferred through indirect astrophysical observations, their presence in the early Universe can generate a stochastic gravitational wave background (SGWB). Since gravitational waves interact very weakly with the cosmic plasma, they propagate almost freely through the Universe and therefore provide a clean probe of the physical processes occurring during and after inflation.

We analyze the gravitational wave signatures produced by inflationary electromagnetic fields and show that they can generate a potentially observable SGWB signal. Such signals may be detectable by current and upcoming gravitational wave experiments, including pulsar timing arrays (PTAs) [41–45, 332, 333] and the Square Kilometre Array (SKA) [334], as well as future space- and ground-based detectors such as LISA [335, 336], BBO [337–339], DECIGO [340–342], and the Einstein Telescope (ET) [343, 344], or detectors operating in the μHz frequency range [345, 346]. Our results highlight the potential of gravitational wave observations as a powerful probe of inflationary magnetogenesis and the post-inflationary evolution of the Universe.

This chapter is organized as follows. In Section 5.2, we introduce the magnetogenesis model based on the coupling $f_1^2(\varphi)F_{\mu\nu}F^{\mu\nu}$ and show how a modified coupling function can simultaneously alleviate the strong coupling and backreaction problems. We also discuss the role of perturbative reheating and analyze how the magnetic spectrum depends on reheating dynamics. In Section 5.4, we investigate the gravitational wave signatures of the model and demonstrate that it can generate strong GW signals in the nano-Hz frequency range, potentially observable by future GW experiments. Finally, in Section 5.5, we summarize our main results and discuss their implications for the origin of large-scale cosmic magnetic fields and their observational signatures.

5.2 Evolution of the Gauge Field

In a spatially flat Friedmann–Lemaître–Robertson–Walker (FLRW) background, the standard electromagnetic action is conformally invariant. As a consequence, the gauge field cannot be excited by the cosmological expansion alone. To generate non-trivial electromagnetic fields, it is therefore necessary to introduce a coupling that breaks this conformal symmetry. A commonly studied example is a time-dependent kinetic coupling of the form $f_1^2(\eta)F_{\mu\nu}F^{\mu\nu}$.

In the presence of such a coupling, the equation of motion for the gauge field mode function $\mathcal{A}_k^{(\lambda)}$ takes the form

$$\mathcal{A}_k^{(\lambda)\prime\prime} + \left(k^2 - \frac{f_1''}{f_1}\right)\mathcal{A}_k^{(\lambda)} = 0, \tag{5.1}$$

where primes denote derivatives with respect to conformal time η, and λ represents the polarization state. Once the functional form of the coupling function $f_1(\eta)$ is specified, the evolution of the gauge field can be determined during the period when the coupling remains active.

in this chapter, we consider a *sawtooth-type magnetogenesis scenario*, in which the coupling function remains active not only during inflation but also throughout the reheating phase. This allows continuous production and evolution of the gauge field during both epochs.

Functional behavior of the coupling function: We assume a broken power-law form for the coupling function. During inflation, the coupling function increases with the scale factor following a power-law behavior,

$$f_1(a) \propto a^n.$$

After the end of inflation, during the reheating phase, the coupling function decreases according to another power-law behavior,

$$f_1(a) \propto a^{-m}.$$

The full functional form of the coupling function can therefore be written as

$$f_1(a) = \begin{cases} \left(\dfrac{a}{a_i}\right)^n, & a_i \le a \le a_e \\ \left(\dfrac{a_e}{a_i}\right)^n \left(\dfrac{a_e}{a}\right)^m, & a_e \le a \le a_{re} \\ 1, & a > a_{re} \end{cases} \tag{5.2}$$

Here a_e and a_{re} denote the scale factors at the end of inflation and at the end of reheating, respectively.

For a de Sitter inflationary background, the scale factor evolves as $a(\eta) = -1/H_I\eta$. During

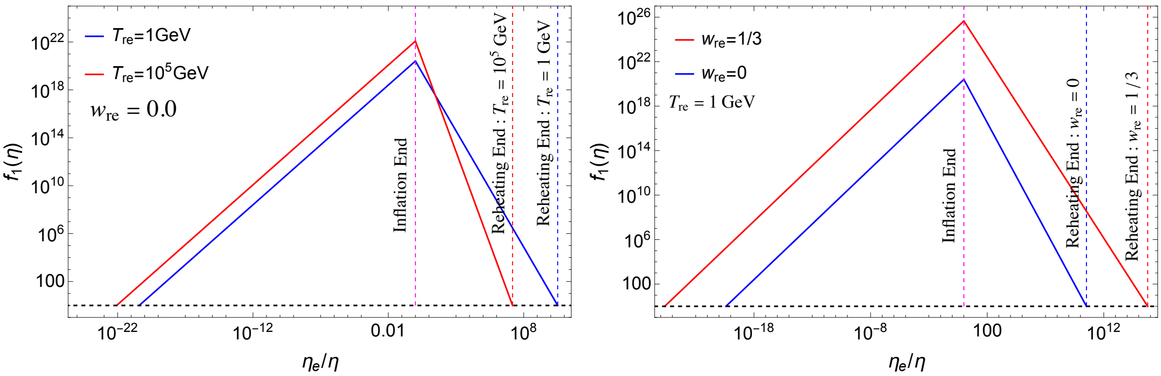

Figure 5.1: Evolution of the coupling function $f_1(\eta)$ in the early Universe, shown as a function of $\eta_{\rm e}/\eta$. In the left panel, a constant reheating equation of state $w_{\rm re} = 0$ is assumed, and the effect of two different reheating temperatures is illustrated: $T_{\rm re} = 1\,{\rm GeV}$ (blue) and $T_{\rm re} = 10^5\,{\rm GeV}$ (red). In the right panel, the reheating temperature is fixed at $T_{\rm re} = 1\,{\rm GeV}$, while two different equations of state are considered, $w_{\rm re} = 0$ (blue) and $w_{\rm re} = 1/3$ (red). In both panels, the black dashed horizontal line marks the reference value $f_1(\eta) = 1$.

reheating, the scale factor evolution depends on the effective equation of state parameter w_{re}. In terms of conformal time, the scale factor can be written as

$$a(\eta > \eta_e) = a_e \left(\frac{\eta}{\eta_e}\right)^{\delta}, \tag{5.3}$$

where the parameter δ is related to the reheating equation of state through $\delta(w_{re}) = 2/1 + 3w_{re}$.

Now, expressing the coupling function in terms of conformal time, we obtain

$$f_1(\eta) \propto \begin{cases} \left(\frac{\eta_i}{\eta}\right)^n & a_i \leq a \leq a_{\rm e}, \\ \left(\frac{\eta_e}{\eta}\right)^\alpha & a_{\rm e} \leq a \leq a_{\rm re}, \\ 1 & a > a_{\rm re} \end{cases} \tag{5.4}$$

where $\alpha = 2n\beta/(1 + 3w_{\rm re})$, and we define $\beta = N_{\rm inf}/N_{\rm re}$. Here, $N_{\rm inf}$ and $N_{\rm re}$ represent the e-folding numbers of the inflationary and reheating eras, respectively. This relation must hold to restore the conformal nature of the gauge field at the end of reheating. In Fig. 5.1, we show the evolution of the coupling function $f_1(\eta)$ during inflation and the subsequent reheating phase for two different scenarios. In the left panel, we fix the equation of state to $w_{\rm re} = 0$, and plot the behavior of $f_1(\eta)$ for two different reheating temperatures, $T_{\rm re} = 1\,{\rm GeV}$ (blue) and $T_{\rm re} = 10^5\,{\rm GeV}$ (red) as function of conformal time η. In the right panel, we fix the reheating temperature to $T_{\rm re} = 1\,{\rm GeV}$, and illustrate the effect of two different equations of state, $w_{\rm re} = 0$ (blue) and $w_{\rm re} = 1/3$ (red). In both panels, we set $n = 1.0$. Now, we consider this functional form of the coupling to solve both the strong coupling and backreaction issues. We will discuss how this type of coupling is free from both of these. Let us first address the backreaction issue. If we work in the regime where $0 < n \leq 2$, then both the electric and magnetic spectral energy densities, $\mathcal{P}_{\rm B}(k)$ and $\mathcal{P}_{\rm E}(k)$, are blue-tilted in nature. The maximum energy generated during inflation due to the coupling is proportional to the inflation energy scale, i.e. $\rho_{\rm EM} \propto H_I^4$ (for instance, see [117, 235, 237, 238]). We note that for $n = 2$, the spectrum of the magnetic field is scale-invariant, whereas for other values of n, it becomes scale-dependent [117].

Since we consider the coupling after inflation, there will be further production of the gauge field during the reheating era. Therefore, the reheating scenario must be constrained to prevent excessive production of the gauge field.

In models with a coupling of the form $f_1^2 F_{\mu\nu}F^{\mu\nu}$, the effective electromagnetic gauge coupling is defined as $\alpha_{\rm em} = e^2/f_1^2$. As shown in Refs. [117,236], generating (nearly) scale-invariant magnetic spectra typically requires the coupling function $f_1(\eta)$ to be small at the beginning of inflation and to grow toward unity by the end of inflation, thereby restoring the conformal symmetry of the gauge field action. This setup, however, implies a strong effective gauge coupling e^2/f_1^2 during the early stages of inflation, potentially leading to a strong coupling problem due to the large interaction strength with the background.

In contrast, in this chapter, we adopt a modified scenario where the coupling function begins with $f_1(\eta) = 1$, grows throughout inflation, and reaches a maximum at the end of inflation. To restore conformal symmetry, $f_1(\eta)$ then decreases during reheating and returns to unity by the end of the reheating phase [236,331]. Because $f_1(\eta) \geq 1$ throughout the entire evolution in our model, the effective coupling strength e^2/f_1^2 remains bounded above by its standard value, avoiding the strong coupling issue.

To prevent the backreaction problem, we choose model parameters such that the total energy density of the generated electromagnetic field remains smaller than the background (radiation) energy density at the end of reheating. This approach, based on the modified evolution of the coupling function, allows us to address both the strong coupling and backreaction issues, while still producing magnetic fields of sufficient strength to match current large-scale observational constraints.

In the following subsection, we will solve the gauge field equation within generalized reheating scenarios. Before proceeding, however, we must first discuss the inflationary and reheating parameters that will be used throughout the later parts of this paper.

5.3 Evolution of the gauge field during inflation and post-inflationary era

As this kind of coupling generates a non-helical magnetic field, where both the helicity modes '+' and '−' are equally enhanced from the vacuum, we can simplify our calculations by dropping the polarization index 'λ' from Eq. (3.10). We further define another variable $\mathcal{A}_{\mathbf{k}}(\eta) = f_1 A_\mu^{\mathbf{k},\lambda}(\eta)$. Since we have already dropped the polarization index in this definition, we can rewrite the equation of motion (EoM) of the gauge field in terms of $\mathcal{A}_{\mathbf{k}}$, leading to the following equation [347]

$$\mathcal{A}_{\mathbf{k}}''(\eta) + \left(k^2 - \frac{f_1''}{f_1}\right)\mathcal{A}_{\mathbf{k}}(\eta) = 0. \tag{5.5}$$

Replacing $f_1''/f_1 = n(n+1)/\eta^2$, we obtain [347]

$$\mathcal{A}_{\mathbf{k}}''(\eta) + \left(k^2 - \frac{n(n+1)}{\eta^2}\right)\mathcal{A}_{\mathbf{k}}(\eta) = 0. \tag{5.6}$$

The general solution of the above equation is given in terms of Bessel functions

$$\mathcal{A}_{\mathbf{k}}(\eta) = \sqrt{-\eta}\left\{c_1 \mathrm{J}_{n+\frac{1}{2}}(-k\eta) + c_2 \mathrm{Y}_{n+\frac{1}{2}}(-k\eta)\right\}. \tag{5.7}$$

To determine the values of c_1 and c_2, we impose the Bunch-Davies initial condition, assuming that all observed modes today were deep inside the Hubble horizon at the beginning of inflation. In the sub-horizon limit $|-k\eta| \to \infty$, the solution of the gauge field reduces to a simple plane wave $\mathcal{A}_{\mathbf{k}}(-k\eta \to \infty) \simeq e^{-ik\eta}/\sqrt{2k}$. Using this as an initial condition, we obtain the integration constants c_1 and c_2 as [235]

$$c_1 = \sqrt{\frac{\pi}{4k}}\frac{\exp(i\pi n/2)}{\cos(-\pi n)}, \qquad c_2 = \sqrt{\frac{\pi}{4k}}\frac{\exp(i\pi(1-n)/2)}{\cos(-\pi n)}. \tag{5.8}$$

Combining these results, we express the solution of the gauge field during inflation in terms of the Hankel function as [117, 235]

$$\mathcal{A}_{\mathbf{k}}(\eta) = \sqrt{-\frac{\pi\eta}{4}}e^{i(n+1/2)\pi/2}\mathrm{H}^{(1)}_{n+\frac{1}{2}}(-k\eta). \tag{5.9}$$

Defined the Electric and Magnetic Spectral Energy Density at the End of Inflation:

Once we obtain the solution of the gauge field, we can compute the magnetic and electric energy densities at the end of inflation, i.e., at $\eta = \eta_{\mathrm{e}}$. We find [117]

$$\mathcal{P}_{B,\mathrm{inf}}(k,\eta) = \frac{d\rho_B}{d\ln k} = \frac{k^4}{8\pi a^4(\eta)}(-k\eta)\left|H^{(1)}_{n+\frac{1}{2}}(-k\eta)\right|^2, \tag{5.10}$$

$$\mathcal{P}_{E,\mathrm{inf}}(k,\eta) = \frac{d\rho_E}{d\ln k} = \frac{k^4}{8\pi a^4(\eta)}(-k\eta)\left|H^{(1)}_{n-\frac{1}{2}}(-k\eta)\right|^2. \tag{5.11}$$

Here, the subscript 'inf' denotes quantities defined during inflation.

To analyze the spectral behavior of the magnetic and electric fields, we simplify the above equations. We are particularly interested in modes that are far outside the horizon before the end of inflation, i.e., $k < k_{\mathrm{e}}$. In this regime, we take the super-horizon approximation

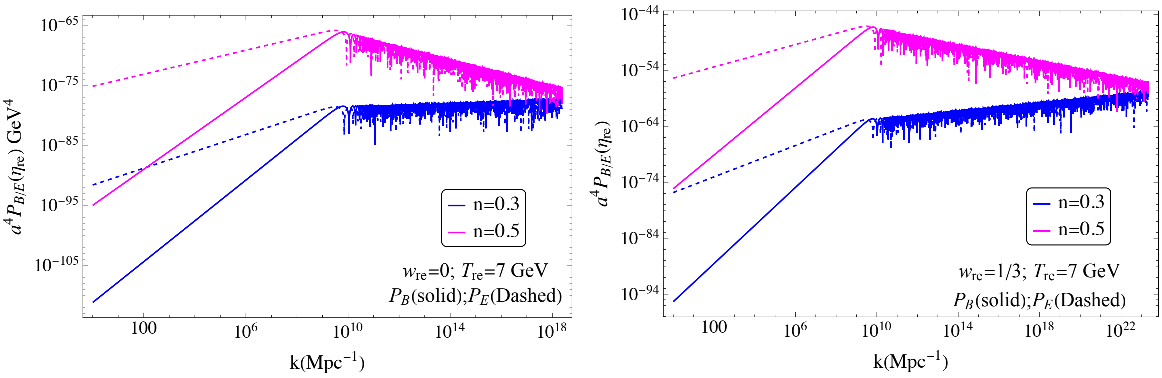

Figure 5.2: Comoving electric and magnetic power spectra, $a^4\mathcal{P}_{\rm B/E}(k)$, as a function of the comoving wavenumber k (in Mpc^{-1}). **Left panel:** Reheating scenario with equation of state $w_{\rm re} = 0$. **Right panel:** Reheating scenario with $w_{\rm re} = 1/3$. In both panels, the blue curves correspond to $n = 0.3$, while the magenta curves correspond to $n = 0.5$. The reheating temperature is fixed at $T_{\rm re} = 7\,$GeV. Solid lines represent the comoving magnetic spectral energy density, whereas dashed lines denote the comoving electric spectral energy density.

$|-k\eta_{\rm end}| \ll 1$, allowing us to express the above equations in the following form [235, 237, 238]

$$\left.\begin{aligned}\mathcal{P}_{B,\rm inf}(k,\eta) &= \frac{H_{\rm inf}^4}{8\pi}\frac{2^{2|n|+1}\Gamma^2\left(|n|+\frac{1}{2}\right)}{\pi^2}(-k\eta)^{-2|n|+4},\\ \mathcal{P}_{E,\rm inf}(k,\eta) &= \frac{H_{\rm inf}^4}{8\pi}\frac{\Gamma^2\left(|n|-\frac{1}{2}\right)2^{2|n|-1}}{\pi^2}(-k\eta)^{-2|n|+6}\end{aligned}\right\}\quad \text{for } n > \frac{1}{2}, \tag{5.12}$$

$$\left.\begin{aligned}\mathcal{P}_{B,\rm inf}(k,\eta) &= \frac{H_{\rm inf}^4}{8\pi}\frac{\Gamma^2\left(|n|-\frac{1}{2}\right)2^{2|n|-1}}{\pi^2}(-k\eta)^{-2|n|+6},\\ \mathcal{P}_{E,\rm inf}(k,\eta) &= \frac{H_{\rm inf}^4}{8\pi}\frac{2^{2|n|+1}\Gamma^2\left(|n|+\frac{1}{2}\right)}{\pi^2}(-k\eta)^{-2|n|+4}\end{aligned}\right\}\quad \text{for } n < -\frac{1}{2}. \tag{5.13}$$

From the above expressions, we see that for a coupling with $n > 0$, the magnetic field spectrum becomes scale-invariant for $n = 2$, while the electric field follows $\mathcal{P}_{E,\rm inf}(k) \propto k^2$. Since the electric field spectrum is blue-tilted, it avoids backreaction issues in this case. However, for $n > 2$, the magnetic spectrum becomes red-tilted, leading to an infrared (IR) divergence at large wavelengths. If we set the cutoff wavelength to the current CMB pivot scale, $k_{\rm cut} = k_* = 0.05$ Mpc^{-1}, we can impose a strong constraint on n such that the total energy density of the produced magnetic field remains below the total inflaton energy density. This gives an upper bound on the coupling parameter $n \leq 2.18$. This bound is derived assuming an inflationary duration corresponding to $N_{\rm inf} = 55$ e-folds, where $N_{\rm inf}$ represents the number of e-folds during inflation.

Additionally, a scale-invariant magnetic field is also possible for $n = -3$. However, as our analysis aims to simultaneously avoid both the backreaction and strong coupling problems, we discard the $n < 0$ cases due to their inherent strong coupling issues.

5.3.1 Production during Reheating

As discussed earlier, the coupling function $f_1(\eta)$ remains active during reheating, leading to additional magnetic field generation. Incorporating its functional form into the equation of motion (EoM) for $\mathcal{A}_{\mathbf{k}}$ during reheating, we obtain

$$\mathcal{A}_{\mathbf{k}}'' + \left(k^2 - \frac{\alpha(\alpha+1)}{\eta^2}\right)\mathcal{A}_{\mathbf{k}} = 0. \tag{5.14}$$

Here, α is defined as

$$\alpha = \frac{2m}{1+3w_{\mathrm{re}}} = \frac{2n\beta}{1+3w_{\mathrm{re}}}, \tag{5.15}$$

where β depends on the reheating dynamics, influencing the spectral behavior of the magnetic field.

The general solution to this equation is

$$\mathcal{A}_{\mathbf{k}}^{\mathrm{re}}(k, \eta > \eta_{\mathrm{e}}) = \sqrt{k\eta}\left\{d_1 J_{\alpha+1/2}(k\eta) + d_2 J_{-\alpha-1/2}(k\eta)\right\}, \tag{5.16}$$

where J_ν are Bessel functions, and d_1 and d_2 are integration constants. These constants are determined by enforcing the continuity of $\mathcal{A}_{\mathbf{k}}$ and its first derivative at the transition point $\eta = \eta_{\mathrm{e}}$.

Applying these conditions yields

$$d_1 = \frac{\pi x_{\mathrm{e}}^{1/2}}{2\cos(\pi\alpha)}\left[\mathcal{A}_{\mathbf{k}}^{\mathrm{inf}}(x_{\mathrm{e}})\tilde{\mathrm{J}}_{-\alpha-1/2}(x_{\mathrm{e}}) + \mathcal{A}_{\mathbf{k}}^{\mathrm{inf}\prime}(x_{\mathrm{e}})\mathrm{J}_{-\alpha-1/2}(x_{\mathrm{e}})\right], \tag{5.17a}$$

$$d_2 = \frac{\pi x_{\mathrm{e}}^{1/2}}{2\cos(\pi\alpha)}\left[\mathcal{A}_{\mathbf{k}}^{\mathrm{inf}}(x_{\mathrm{e}})\tilde{\mathrm{J}}_{\alpha+1/2}(x_{\mathrm{e}}) - \mathcal{A}_{\mathbf{k}}^{\mathrm{inf}\prime}(x_{\mathrm{e}})\mathrm{J}_{\alpha+1/2}(x_{\mathrm{e}})\right], \tag{5.17b}$$

where $x_{\mathrm{e}} = -k\eta_{\mathrm{e}} = k/k_{\mathrm{e}}$, and the auxiliary functions are

$$\tilde{\mathrm{J}}_{\alpha+1/2}(x_{\mathrm{e}}) = \frac{(1+\alpha)\mathrm{J}_{\alpha+1/2}(x_{\mathrm{e}}) - x_{\mathrm{e}}\mathrm{J}_{\alpha+3/2}(x_{\mathrm{e}})}{x_{\mathrm{e}}}, \tag{5.18a}$$

$$\tilde{\mathrm{J}}_{-\alpha-1/2}(x_{\mathrm{e}}) = \frac{\alpha\mathrm{J}_{-\alpha-1/2}(x_{\mathrm{e}}) + x_{\mathrm{e}}\mathrm{J}_{-\alpha+1/2}(x_{\mathrm{e}})}{x_{\mathrm{e}}}. \tag{5.18b}$$

Since we are primarily interested in modes that exited the horizon well before the end of inflation, i.e., $k < k_{\mathrm{e}}$, we focus on the regime where $x_{\mathrm{e}} \ll 1$.

Under the super-horizon approximation, the expressions for the coefficients d_1 and d_2 sim-

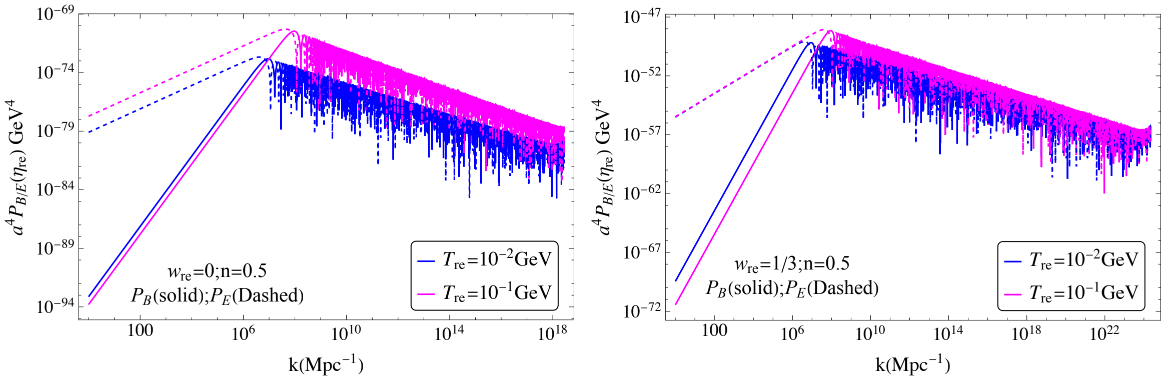

Figure 5.3: Comoving electric and magnetic spectral energy densities, $a^4\mathcal{P}_{\rm B/E}$, plotted as a function of the comoving wavenumber k for two representative reheating scenarios. The left panel corresponds to an equation of state $w_{\rm re} = 0.0$ with $n = 0.5$, while the right panel shows the case $w_{\rm re} = 1/3$ with the same value of n. In both panels, blue curves represent $T_{\rm re} = 10^{-2}\,$GeV and magenta curves correspond to $T_{\rm re} = 10^{-1}\,$GeV. Solid lines denote the magnetic contribution, whereas dashed lines indicate the electric component.

plify to

$$d_1 \simeq \sqrt{\frac{\pi}{4k}}\left(-x_{\rm e}^{-n-\alpha-1}\frac{i2^{n+\alpha}(\alpha-n)\Gamma(n+1/2)}{\cos(\pi\alpha)\Gamma(1/2-\alpha)}+\mathcal{O}(2)\right), \tag{5.19a}$$

$$d_2 \simeq \sqrt{\frac{\pi}{4k}}\left(-x_{\rm e}^{-n+\alpha}\frac{i2^{n-\alpha-1}(1+n+\alpha)\Gamma(n+1/2)}{\cos(\pi\alpha)\Gamma(\alpha+3/2)}+\mathcal{O}(2)\right). \tag{5.19b}$$

To determine the spectral energy densities of the magnetic and electric fields, we substitute the mode function $\mathcal{A}_{\mathbf{k}}$ into the relevant expressions. However, further simplifications are required to analyze the spectral behavior effectively.

Since we define the comoving spectrum at the end of reheating ($\eta = \eta_{\rm re}$), the spectrum can be categorized into two distinct regimes:

- **Super-horizon limit:** $k < k_{\rm re}$
- **Sub-horizon limit:** $k_{\rm re} < k < k_{\rm e}$

Super-Horizon Limit ($k_* < k < k_{\rm re}$)

For super-horizon modes, the spectral energy densities of the magnetic and electric fields are given by

$$\mathcal{P}_{\rm B}(k,\eta_{\rm re}) \simeq \frac{H_{\rm e}^4}{8\pi}\frac{2^{2n-1}(\alpha-n)^2\Gamma^2(n+1/2)}{\cos^2(\pi\alpha)\Gamma^2(1/2-\alpha)\Gamma^2(\alpha+3/2)}\left(\frac{x_{\rm re}}{x_{\rm e}}\right)^{2(\alpha+1)}\left(\frac{k}{k_{\rm e}}\right)^{4-2n}\left(\frac{a_{\rm e}}{a_{\rm re}}\right)^4, \tag{5.20a}$$

$$\mathcal{P}_{\rm E}(k,\eta_{\rm re}) \simeq \frac{H_{\rm e}^4}{8\pi}\frac{2^{2n+1}(\alpha-n)^2\Gamma^2(n+1/2)}{\cos^2(\pi\alpha)\Gamma^2(1/2-\alpha)\Gamma^2(\alpha+1/2)}\left(\frac{x_{\rm re}}{x_{\rm e}}\right)^{2\alpha}\left(\frac{k}{k_{\rm e}}\right)^{2-2n}\left(\frac{a_{\rm e}}{a_{\rm re}}\right)^4. \tag{5.20b}$$

The factor $(a_{\rm e}/a_{\rm re})^4$ arises due to the expansion of the universe from the end of inflation to the completion of reheating. Notably, the presence of the coupling function during reheating enhances the total energy density of super-horizon modes by a factor of $(x_{\rm re}/x_{\rm e})^{2(\alpha+1)}$. While the spectral indices of the magnetic and electric fields are determined by the parameter n, the post-inflationary coupling governs the amplification of these fields.

A particularly interesting case arises for $n=2$, where the magnetic field spectrum remains scale-invariant, while the electric field spectrum exhibits a red tilt. This red tilt leads to an ultraviolet (UV) divergence in the electric field spectrum. However, even in this case, a truly scale-invariant magnetic spectrum cannot be achieved due to backreaction issues, which will be discussed later.

Sub-Horizon Limit ($k_{\rm re} < k < k_{\rm e}$)

For sub-horizon modes, the spectral energy densities are given by

$$\mathcal{P}_{\rm B}(k,\eta_{\rm re}) \simeq \frac{H_{\rm e}^4}{8\pi}\frac{2}{\pi}\frac{2^{2(n+\alpha)}(\alpha-n)^2\Gamma^2(n+1/2)}{\cos^2(\pi\alpha)\Gamma^2(1/2-\alpha)}\left(\frac{k}{k_{\rm e}}\right)^{2-2(n+\alpha)}\left(\frac{a_{\rm e}}{a_{\rm re}}\right)^4, \tag{5.21a}$$

$$\mathcal{P}_{\rm E}(k,\eta_{\rm re}) \simeq \frac{H_{\rm e}^4}{4\pi}\frac{2^{2(n+\alpha)}(\alpha-n)^2\Gamma^2(n+1/2)}{\cos^2(\pi\alpha)\Gamma^2(1/2-\alpha)}\left(\frac{k}{k_{\rm e}}\right)^{2-2(n+\alpha)}\left(\frac{a_{\rm e}}{a_{\rm re}}\right)^4. \tag{5.21b}$$

In this regime, both the magnetic and electric field spectra share the same spectral index, which is consistently red-tilted. As a result, the total electromagnetic (EM) energy density attains its maximum at $k = k_{\rm re}$.

Generally, super-horizon modes exhibit a blue-tilted spectrum, whereas sub-horizon modes remain red-tilted. This spectral behavior arises from the specific form of the gauge field coupling function, which is chosen to address both the backreaction and strong coupling problems simultaneously. Moreover, the coupling function is designed to restore the conformal nature of the gauge field by reaching unity at the end of reheating.

To analyze the spectral behavior of the magnetic and electric spectral energy densities, denoted as $\mathcal{P}_{\rm B}$ and $\mathcal{P}_{\rm E}$, we have plotted the comoving magnetic and electric spectral energy densities, defined as $a^4\mathcal{P}_{\rm B/E}$, at the end of reheating as a function of the comoving wavenumber (in Mpc^{-1}).

In Fig. 5.2, we consider two different values of the coupling constant: $n=0.3$ (blue) and $n=0.5$ (red), for two different equations of state (EoS): $w_{\rm re}=0.0$ (left panel) and $w_{\rm re}=1/3$ (right panel). In both cases, the reheating temperature is fixed at $T_{\rm re} = 7\,\mathrm{GeV}$. The solid lines represent the magnetic spectral energy density ($\mathcal{P}_{\rm B}$), whereas the dashed lines correspond to the electric spectral energy density ($\mathcal{P}_{\rm E}$).

For super-horizon modes ($k < k_{\rm re}$), the spectral behavior of the electric and magnetic fields differs, as predicted earlier. However, for sub-horizon modes ($k > k_{\rm re}$), both spectral energy densities follow the same behavior, as discussed in Eqs. (5.21). Additionally, depending on the coupling nature, if we aim to generate a significant magnetic field on large scales, we find that in most cases, the maximum energy density is stored at $k \simeq k_{\rm re}$ for both magnetic and electric fields.

Similarly, in Fig. 5.3, we plot the comoving spectral energy density $a^4\mathcal{P}_{\mathrm{B/E}}$ as a function of the comoving wavenumber k for a fixed coupling parameter $n = 0.5$, considering two different EoS values: $w_{\mathrm{re}} = 0.0$ (left panel) and $w_{\mathrm{re}} = 1/3$ (right panel). In both figures, blue represents $T_{\mathrm{re}} = 10^2\,\mathrm{GeV}$, while red corresponds to $T_{\mathrm{re}} = 0.1\,\mathrm{GeV}$. Here, the dashed lines indicate the comoving spectral energy density of the electric field, whereas the solid lines correspond to the comoving spectral energy density of the magnetic field.

From Eqs. (5.20), we observe that the super-horizon scaling behavior of the magnetic and electric fields is dictated by the coupling parameter n. Since we consider a single value, $n = 0.5$, the spectral tilt remains the same in both panels, even for sub-horizon modes at a fixed reheating temperature.

Furthermore, in the case of $w_{\mathrm{re}} = 1/3$, the spectral energy density of the super-horizon electric field modes retains the same amplitude, irrespective of the reheating temperature. This seemingly counterintuitive behavior arises due to the factor $(x_{\mathrm{re}}/x_{\mathrm{e}})^{2\alpha}$. For $w_{\mathrm{re}} = 1/3$, the evolution of the relevant background quantities compensates in such a way that the electric field undergoes the same enhancement regardless of the reheating temperature.

However, for the magnetic field, we find that even in the $w_{\mathrm{re}} = 1/3$ reheating scenario, an additional enhancement factor, $(k_{\mathrm{e}}/k_{\mathrm{re}})^2$, exists. As a result, changing the reheating temperature alters the amplitude of the magnetic field due to this factor, while the spectral index remains unchanged.

Present-day Magnetic Field Strength In this type of magnetogenesis model, the electromagnetic fields restore their conformal symmetry after reheating as the coupling function becomes $f_1(\eta > \eta_{\mathrm{re}}) = 1$. Since there are no additional dynamics that break the conformal nature of the electromagnetic (EM) fields, the effective production of gauge fields ceases after reheating.

During reheating, all fundamental particles are already produced, and the universe reaches a high-temperature state, behaving as a highly dense conducting plasma. As a result, the electric field component rapidly decays and is washed out from the universe. Therefore, after reheating (during the radiation-dominated era), the only surviving component is the magnetic field.

Since we are not considering magnetohydrodynamics (MHD) effects and are interested in modes that remain far outside the horizon during the radiation-dominated era, we can safely ignore MHD effects for those modes. Typically, these large-scale modes evolve adiabatically after their production, with the energy density of the magnetic field scaling as $\rho_{\mathrm{B}} \propto a^{-4}$ due to the expansion of the universe.

Under this assumption, the present-day magnetic field strength can be expressed as

$$\mathbf{B}_0(k) \simeq \frac{k_{\mathrm{e}}^2}{(8\pi)^{1/2}} \frac{2^{n-1/2}(\alpha - n)\Gamma(n+1/2)}{\cos(\pi\alpha)\Gamma(1/2-\alpha)\Gamma(\alpha+3/2)} \left(\frac{k_{\mathrm{e}}}{k_{\mathrm{re}}}\right)^{\alpha+1} \left(\frac{k}{k_{\mathrm{e}}}\right)^{2-n}. \tag{5.22}$$

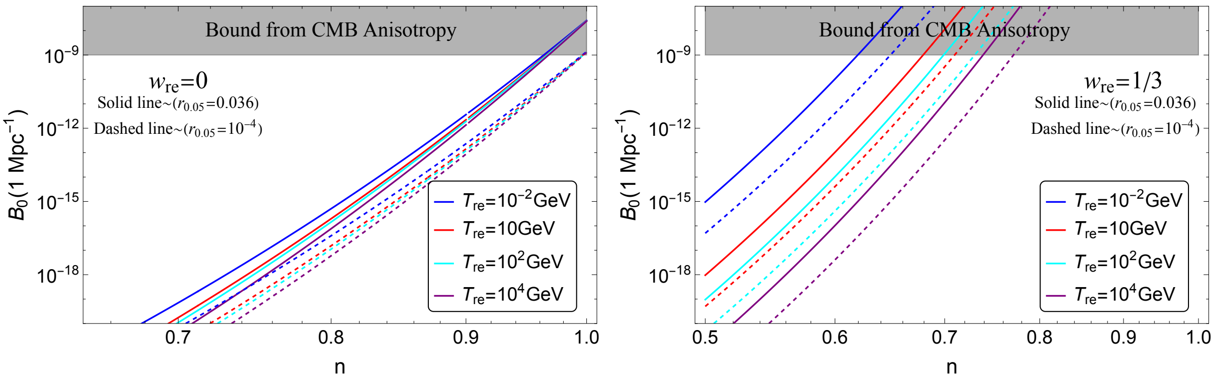

Figure 5.4: Present-day magnetic field strength B_0, evaluated at the scale 1 Mpc^{-1}, shown as a function of the coupling constant n for two reheating scenarios. The left panel corresponds to a reheating equation of state $w_{\rm re} = 0$, while the right panel shows the case $w_{\rm re} = 1/3$. In both panels, different colors denote different reheating temperatures $T_{\rm re}$. Solid lines correspond to a tensor-to-scalar ratio $r_{0.05} = 0.036$, whereas dashed lines represent $r_{0.05} = 10^{-4}$.

EoS	$w_{\rm re} = 0.0$			$w_{\rm re} = 1/3$		
n	0.7	0.8	0.9	0.45	0.5	0.55
$T_{\rm re}$(GeV)	10^4	24.5	0.043	1.02×10^5	58.4	10^{-2}
B_0 (G)	4.3×10^{-21}	1.7×10^{-16}	3.3×10^{-12}	2.9×10^{-25}	1.66×10^{-19}	3.2×10^{-13}

Table 5.1: Upper bounds on the reheating temperature obtained from the requirement that the gauge-field energy density remains subdominant to the background, thereby avoiding backreaction effects. The bounds are evaluated for selected values of the coupling constant n and for two reheating equations of state, $w_{\rm re} = 0$ and $w_{\rm re} = 1/3$. The table also lists the corresponding present-day magnetic field strength B_0 (in Gauss) associated with these parameter choices.

To analyze the dependency of the present-day magnetic field strength $B_0(k)$ on the magnetogenesis parameters (such as the initial coupling constant n) and the reheating dynamics (in terms of reheating temperature $T_{\rm re}$ and average equation of state $w_{\rm re}$), we have plotted $B_0(1\ {\rm Mpc}^{-1})$ as a function of the coupling parameter n in Fig. (5.4).

In the left panel of Fig. 5.4, we show the present-day magnetic field strength evaluated at the 1 Mpc scale for $w_{\rm re} = 0$, where different colors correspond to different values of the reheating temperature $T_{\rm re}$. In the right panel, we plot $B_0(1\ {\rm Mpc}^{-1})$ as a function of the coupling parameter n for radiation-like reheating scenarios with $w_{\rm re} = 1/3$.

In both figures, we consider two different values of the tensor-to-scalar ratio $r_{0.05}$: solid lines correspond to $r_{0.05} = 0.036$, while dashed lines represent $r_{0.05} = 10^{-4}$. Since we have fixed the Hubble parameter during inflation as $H_{\rm e} = \pi M_{\rm P}\sqrt{r_{0.05} A_s/2}$, changing the value of $r_{0.05}$ effectively modifies the inflationary energy scale.

From both figures, we observe that for a fixed equation of state $w_{\rm re}$ and reheating temperature $T_{\rm re}$, an increase in the coupling parameter n leads to a gradual increase in the present-day magnetic field strength. This behavior arises due to the initial value of the gauge field generated during inflation, which is governed by the factor $(k/k_{\rm e})^{-2|n|+4}$.

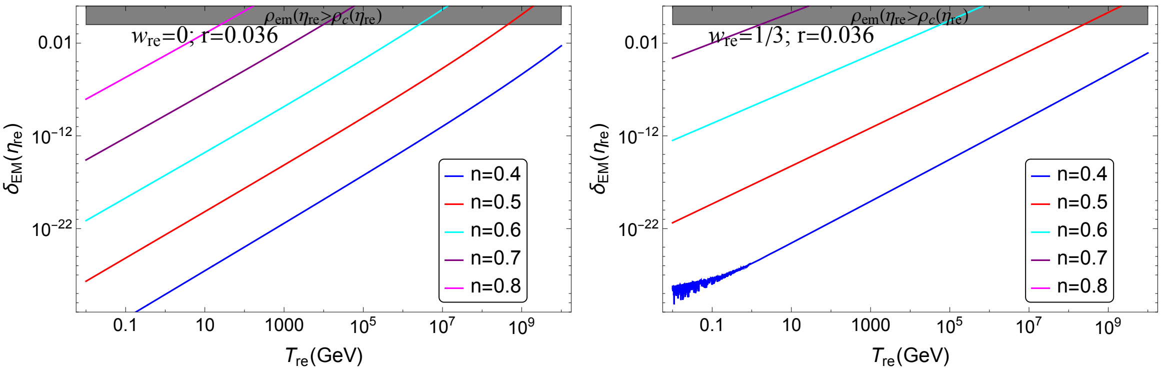

Figure 5.5: Fractional energy density of the electromagnetic field, $\delta_{\rm EM}$, shown as a function of the reheating temperature $T_{\rm re}$ (in GeV) for two different reheating equations of state. The left panel corresponds to $w_{\rm re} = 0.0$, while the right panel shows the case $w_{\rm re} = 1/3$. In both panels, different colored curves represent different values of the coupling parameter n. The dark gray shaded region indicates the part of the parameter space where the electromagnetic energy density becomes comparable to the background energy density, signaling the onset of significant backreaction effects.

Additionally, we find that lowering the reheating temperature enhances the overall strength of the gauge field. This effect is due to the prolonged duration of the reheating period, which allows for increased production of the gauge field during reheating.

Backreaction issue

Including the coupling function $f_1(\eta)$ in the action with the electromagnetic (EM) field breaks conformal symmetry, leading to significant EM field generation during both inflation and reheating. To avoid backreaction with the inflaton field at the end of reheating, we must compute the total energy density produced due to the coupling. The total EM energy density at the end of reheating is defined as

$$\rho_{\rm em}(\eta_{\rm re}) = \int_{k_{\rm re}}^{k_{\rm e}} d\ln(k) \left\{\mathcal{P}_{\rm B}(k,\eta_{\rm re}) + \mathcal{P}_{\rm E}(k,\eta_{\rm re})\right\}, \tag{5.23}$$

where the integration limits are chosen from $k_{\rm re}$ to $k_{\rm e}$, since $k_{\rm re}$ is the highest mode that can re-enter the horizon at the end of reheating. Notably, since the spectrum peaks at $k \simeq k_{\rm re}$, extending the lower limit to $k_{\rm cmb}$ does not significantly alter the result.

The fractional energy density of the EM field at the end of reheating is then defined as $\delta_{\rm EM} = \frac{\rho_{\rm em}(\eta_{\rm re})}{\rho_{\rm c}(\eta_{\rm re})}$, where $\rho_{\rm c}(\eta_{\rm re}) = 3H^2(\eta_{\rm re})M_{\rm P}^2$, and $H(\eta_{\rm re})$ is the Hubble parameter at the end of reheating. Utilizing Eq. (5.21) in Eq. (5.23), we obtain:

$$\begin{aligned}\delta_{\rm EM}(\eta_{\rm re}) = \frac{1}{24}\left(\frac{H_{\rm e}}{M_{\rm P}}\right)^2 \left(\frac{k_{\rm re}}{k_{\rm e}}\right)^{2-2(n+\alpha)} \frac{2^{2n+1}(\alpha-n)^2\Gamma^2(n+1/2)}{\cos^2(\alpha\pi)\Gamma^2(1/2-\alpha)} \\ \times\left\{\frac{1}{\Gamma^2(\alpha+1/2)} + \frac{2^{2\alpha}}{\pi}\right\}\left(\frac{a_{\rm e}}{a_{\rm re}}\right)^{1-3w_{\rm re}}.\end{aligned} \tag{5.24}$$

Here, the term $(a_{\rm e}/a_{\rm re})^{1-3w_{\rm re}}$ accounts for the relative dilution of the EM field energy density

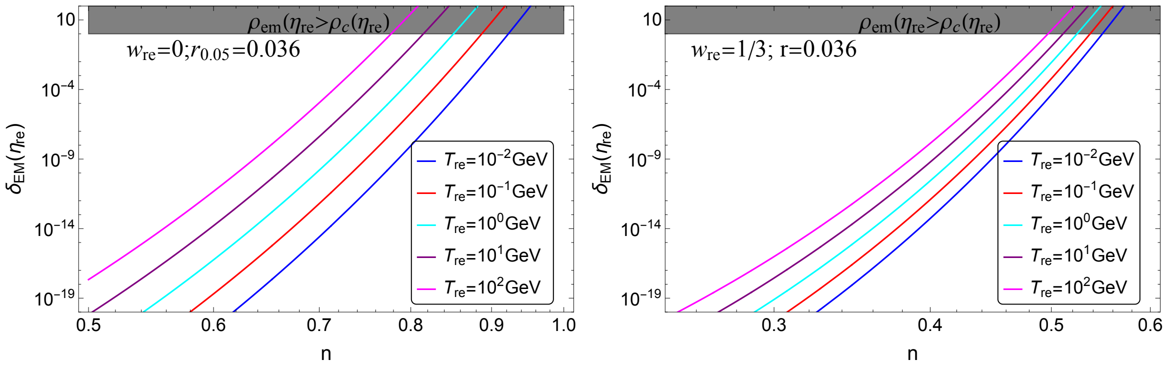

Figure 5.6: Fractional electromagnetic energy density δ_{EM} shown as a function of the coupling parameter n for two reheating scenarios. The left panel corresponds to an equation of state $w_{\mathrm{re}} = 0.0$, while the right panel shows the case $w_{\mathrm{re}} = 1/3$. In both panels, different colored curves represent different reheating temperatures T_{re} (in GeV). The dark gray shaded region marks the parameter space where the electromagnetic energy density becomes comparable to the background energy density, indicating the onset of significant backreaction effects.

compared to the background.

In Fig. 5.5, we illustrate how the fractional energy density of the produced EM field depends on reheating scenarios and coupling parameters. Specifically, in Fig. 5.5, we plot $\delta_{\mathrm{EM}}(\eta_{\mathrm{re}})$ as a function of reheating temperature T_{re} (in GeV) for two distinct equations of state: $w_{\mathrm{re}} = 0.0$ (left) and $w_{\mathrm{re}} = 1/3$ (right). Different colors represent different values of the coupling parameter n.

From the figure, we observe that for a fixed reheating temperature (e.g., $T_{\mathrm{re}} = 0.1\,\mathrm{GeV}$), increasing n leads to a gradual increase in the total energy density. This arises because the initial EM energy density produced during inflation depends on n. A larger n results in a less blue-tilted spectrum, leading to a comparatively higher energy density on larger scales.

Since the coupling function during reheating is no longer a free parameter, it strongly depends on reheating dynamics. This effect is evident in both figures: when the EoS changes, the EM field production rate is significantly affected due to background evolution. For a matter-like evolution ($\rho_\phi \propto a^{-3}$), the universe spends a longer duration in reheating compared to a radiation-like scenario ($\rho_\phi \propto a^{-4}$).

To satisfy the condition $f(\eta_{\mathrm{re}}) = 1$, for $w_{\mathrm{re}} = 0$ reheating, we must effectively choose a lower value of α for a fixed n, while for $w_{\mathrm{re}} = 1/3$, α is relatively larger. A higher α corresponds to stronger EM field production during reheating. Consequently, for a fixed n and T_{re}, radiation-like evolution results in greater EM field production.

Similarly, in Fig. 5.6, we plot $\delta_{\mathrm{EM}}(\eta_{\mathrm{re}})$ as a function of n for $w_{\mathrm{re}} = 0.0$ (left) and $w_{\mathrm{re}} = 1/3$ (right), where different colors indicate different reheating temperatures. We find that to avoid backreaction for $w_{\mathrm{re}} = 0.0$, the maximum allowed coupling parameter is $n < 1$ for a wide range of reheating temperatures. For example, for $T_{\mathrm{re}} = 1\,\mathrm{GeV}$ with $w_{\mathrm{re}} = 0.0$, the maximum allowed value is $n^{\max} \simeq 0.83$, while for $w_{\mathrm{re}} = 1/3$, it is $n^{\max} \simeq 0.53$.

Table 5.1 presents estimates of the lowest possible reheating temperature T_{re} (in GeV) for

$w_{\rm re} = 0.0$ and $w_{\rm re} = 1/3$, along with the corresponding present-day magnetic field strength at 1 Mpc. We find that: - For $w_{\rm re} = 0$, ensuring a backreaction-free scenario requires $0.75 \leq n \leq 0.92$, while the reheating temperature remains low: $10^{-2} \leq T_{\rm re} \leq 10^{2}$ GeV. - For $w_{\rm re} = 1/3$, the allowed n range is narrower: $0.5 \leq n \leq 0.55$, with a similar reheating temperature range.

Interestingly, a higher reheating temperature leads to stronger magnetic field generation on small scales. However, the present-day magnetic field strength at 1 Mpc remains relatively small.

5.4 Generation of Gravitational Waves

Gravitational waves (GWs) are among the most promising probes for investigating the early Universe. In the context of a de Sitter inflationary background, a primary, nearly scale-invariant GW spectrum is generically produced. However, the final observed spectrum depends sensitively on the post-inflationary dynamics of the Universe.

A detailed discussion of the primordial GW production from quantum vacuum fluctuations during inflation has already been presented in Chapter 2 (Section 2.9); therefore, it is not repeated here. Instead, we focus on the classical production of GWs sourced by electromagnetic fields.

Nevertheless, when evaluating the present-day GW spectrum, we incorporate contributions from both the primordial (vacuum) and the electromagnetic sources.

5.4.1 Production of Secondary GWs

In this subsection, we discuss the production mechanisms of secondary gravitational waves (SGW) sourced by the electromagnetic (EM) field generated during and after inflation. As analyzed in the earlier sections, for this type of coupling, where both the backreaction issue and the strong coupling problem are addressed simultaneously, the model parameters must be chosen such that the large-scale magnetic field generated during inflation remains subdominant compared to the background energy density.

However, since the coupling function remains active during reheating, we find a significant enhancement in both the magnetic and electric energy densities, even for modes that remain outside the horizon before the end of reheating. Notably, the production of the magnetic field reaches its maximum at the end of reheating, where the coupling function satisfies $f(\eta = \eta_{\rm re}) = 1$. This allows us to neglect the contribution of tensor perturbations sourced by the EM field during inflation.

Thus, the dominant production of secondary GWs occurs in two distinct phases:

- **During reheating**, when the amplified EM energy density acts as a source for tensor perturbations.

- **During the radiation-dominated era**, where any remaining sourced fields (magnetic field) continue to contribute to GW production.

Generation of Tensor Perturbations During Reheating

For super-horizon modes, the electric field energy density dominates over the magnetic field. Once the modes re-enter the horizon, both the electric and magnetic fields exhibit the same spectral behavior with equal amplitude (see Fig. 5.2). Since we are computing the tensor power spectrum generated during reheating, we can simplify our analysis by neglecting the magnetic field contribution for now.

The tensor power spectrum induced by the electric field during reheating, evaluated at $\eta = \eta_{\rm re}$, is given by

$$\begin{aligned} P_{\rm T}^{\rm sec}(k,\eta_{\rm re}) = &\frac{2}{M_{\rm P}^4 k^4}\int_{u_{\rm min}}^{u_{\rm max}}\frac{du}{u}\int_{-1}^{1}d\mu\frac{f(\mu,\gamma)}{[1+u^2-2\mu u]^{3/2}} \\ &\times\left[\int_{x_{\rm e}}^{x_{\rm re}}dx_1 a^2(x_1)\mathcal{G}_k(x_{\rm re},x_1)\mathcal{P}_{\rm E}^{1/2}(ux_1)\mathcal{P}_{\rm E}^{1/2}(|1-u|x_1)\right]^2 \end{aligned} \tag{5.25}$$

Here, we define the dimensionless variable $u = q/k$ and $x_{\rm re} = k\eta_{\rm re}$, where $\eta_{\rm re}$ is the conformal time at the end of reheating. The above integral does not admit an exact analytical solution, but we can rewrite it in the following approximate form

$$P_{\rm T}^{\rm sec}(k,\eta_{\rm re}) \simeq \frac{|\mathcal{B}|^4}{32}\left(\frac{H_{\rm e}}{M_{\rm P}}\right)^4\left(\frac{k}{k_{\rm e}}\right)^{2(\delta-2n-2\alpha)}\left\{\overline{\mathcal{I}_1(k,\eta_{\rm re})}+\overline{\mathcal{I}_2(k,\eta_{\rm re})}\right\}, \tag{5.26}$$

where the terms $\mathcal{I}_1$ and $\mathcal{I}_2$ are defined as

$$\mathcal{I}_1(k,\eta_{\rm re}) = \int_{u_{\rm min}}^{1}du\,u^2u^{-2(n+\alpha)}\int_{-1}^{1}d\gamma\, f(\gamma,\beta)\left[\int_{x_{\rm e}}^{x_{\rm re}}dx_1 x_1^{1-\delta}\mathcal{G}_k(x_{\rm re},x_1)J_{\alpha-\frac{1}{2}}(ux_1)J_{\alpha-\frac{1}{2}}(x_1)\right]^2, \tag{5.27a}$$

$$\mathcal{I}_2(k,\eta_{\rm re}) = \int_{1}^{u_{\rm max}}du\,u^2u^{-4(n+\alpha)}\int_{-1}^{1}d\gamma\, f(\gamma,\beta)\left[\int_{x_{\rm e}}^{x_{\rm re}}dx_1 x_1^{-1-\delta}\mathcal{G}_k(x_{\rm re},x_1)J^2_{\alpha-\frac{1}{2}}(ux_1)\right]^2. \tag{5.27b}$$

In these expressions, we have defined $u_{\rm max} = k_{\rm e}/k$ and $u_{\rm min} = k_*/k$, where k_* is the pivot scale observed the CMB, and $k_{\rm e}$ is the highest mode leaving the horizon at the end of inflation. The overline indicates the oscillation average of the corresponding quantity.

Since an exact analytical solution is not feasible, we evaluate the spectral behavior by considering specific limits. We are particularly interested in large-scale magnetic fields that could explain the presently observed cosmic magnetic field. For super-horizon scales ($k \ll k_{\rm re}$), we estimate the tensor power spectrum as

$$P_{\rm T}^{\rm sec}(k\ll k_{\rm re},\eta_{\rm re}) \simeq \frac{|\mathcal{B}|^4}{48}\frac{2^{2-4\alpha}\Gamma^2(l)}{\Gamma^4(\alpha+\frac{1}{2})\Gamma^2(1+l)}\left(\frac{H_{\rm e}}{M_{\rm P}}\right)^4\frac{1-\left(\frac{k_*}{k}\right)^{2-2n}}{(2-2n)(2\alpha-\delta+2)}\left(\frac{x_{\rm e}}{x_{\rm re}}\right)^{2(\delta-2\alpha)}\left(\frac{k}{k_{\rm e}}\right)^{4(1-n)}. \tag{5.28}$$

From Eq. (5.28), we observe that the tensor power spectrum due to the electric field follows $P_{\rm T}^{\rm sec}(k \ll k_{\rm re}, \eta_{\rm re}) \propto k^{4(1-n)}$, which is twice the spectral index of the electric field, i.e., $\mathcal{P}_{\rm E}(k) \propto k^{2(1-n)}$ (see Eq. (5.20b)). This result implies that for $n > 1$, the tensor power spectrum exhibits a red-tilted spectrum, leading to an overproduction of tensor fluctuations at large wavelengths. Consequently, this could violate the current observational bound on the tensor-to-scalar ratio, $r_{0.05} \leq 0.036$ [12, 64, 65, 348].

For instance, considering $w_{\rm re} = 0$ and a reheating temperature of $T_{\rm re} = 1$ GeV, we find that to satisfy the observational bound on r, the coupling parameter must be constrained as $n_{\rm max} \leq 1.07$. However, for the same set of parameters, we find that the produced electromagnetic fields can easily backreact with the background (see Fig. 5.6).

Generation of tensor perturbation during radiation-dominated era:

After reheating, there is no further production of the gauge field, but during the reheating era, the production of the gauge field is significant. During reheating, all fundamental particles are produced from the decay of the inflaton field, and the temperature of the universe was very high. Consequently, we can assume that the conductivity during the radiation-dominated era was also very high. In the presence of high conductivity, the electric field decays quickly due to the rapid response of charged particles (mainly electrons) in the plasma medium, while the magnetic field freezes (if we ignore magnetohydrodynamics). As we have seen, the magnetic field strength at the end of reheating is quite high at small scales near $k \simeq k_{\rm re}$ (see Fig. 5.3), and it can further produce tensor fluctuations. However, the source due to the magnetic field is only effective up to the neutrino decoupling era, i.e., $\eta = \eta_\nu$, because after neutrinos decouple from the thermal bath, they can balance the anisotropies induced by the magnetic field [349, 350]. Therefore, for the radiation-dominated era, the time range should be from $x_{\rm re}$ to $x_\nu = k\eta_\nu$.

$$P_{\rm T}^{\rm sec}(k, \eta_\nu) = \frac{2}{M_{\rm P}^4 k^4}\left(\int_{x_{\rm re}}^{x_\nu} dx_1 \frac{\mathcal{G}{\rm ra}(x_\nu, x_1)}{a^2(x_1)}\right)^2 \times \int_0^\infty \frac{dq}{q}\int_{-1}^{1} d\mu f(\mu,\beta)\frac{\tilde{\mathcal{P}}_{\rm B}(k,\eta_{\rm re})\tilde{\mathcal{P}}_{\rm B}(|\mathbf{k}-\mathbf{q}|\eta_{\rm re})}{[1+(q/k)^2-2\mu(q/k)]^{3/2}} \tag{5.29}$$

Here, the tilde denotes the comoving quantity, i.e., $\tilde{\mathcal{P}}_{\rm B}(k,\eta_{\rm re}) = a^4(\eta)\mathcal{P}_{\rm B}(k,\eta)$. This is convenient because, after reheating, there is no further production of the gauge field. Due to high conductivity and the absence of an electric field, the magnetic field evolves adiabatically and, due to background expansion, dilutes as a^{-4}. To facilitate the time integral separately, we express the transient power spectrum in terms of these comoving quantities.

Utilizing Eq. (5.21), we can define the comoving magnetic spectral energy density $\tilde{\mathcal{P}}_{\rm B}$ as

$$\tilde{\mathcal{P}}_{\rm B}(k, \eta > \eta_{\rm re}) = \frac{k^4|\mathcal{B}|^2}{8\pi}\left(\frac{k}{k_{\rm e}}\right)^{-2(n+\alpha+1)}\left(\frac{k}{k_{\rm re}}\right){\rm J}^2_{\alpha+\frac{1}{2}}(k/k_{\rm re}) \tag{5.30}$$

here we identify $\mathcal{B}$ as

$$\mathcal{B} = \frac{2^{n+\alpha}(\alpha - n)\Gamma\left(n + \frac{1}{2}\right)}{\cos(\pi\alpha)\Gamma\left(\frac{1}{2} - \alpha\right)} \tag{5.31}$$

Now, we can write the tensor power spectrum produced during the radiation-dominated era as

$$\begin{aligned} P_{\mathrm{T,ra}}^{\mathrm{sec}}(k,\eta) = {} & \frac{k^4|\mathcal{B}|^4}{32\pi^2 M_{\mathrm{P}}^4}\left(\frac{k}{k_{\mathrm{e}}}\right)^{-4(n+\alpha+1)} x_{\mathrm{re}}^2\left(\int_{x_{\mathrm{re}}}^{x_\nu} dx_1 \frac{\mathcal{G}_{\mathbf{k}}(x_\nu, x_1)}{a^2(x_1)}\right)^2 \\ & \times \int_{u_{\min}}^{u_{\max}} \frac{du}{u}\int_{-1}^{1} d\mu \frac{f(\mu,\gamma)}{[1+u^2-2u\mu]^{3/2}} u^{3-2(n+\alpha)}(|1-u|)^{3-2(n+\alpha)}\mathrm{J}_{\alpha+1/2}^2(ux_{\mathrm{re}})\mathrm{J}_{\alpha+1/2}^2(|1-u|x_{\mathrm{re}}) \end{aligned} \tag{5.32}$$

We can numerically solve the above integral by performing the time and momentum integrals separately. However, to analyze the spectral behavior of the tensor power spectrum, we can also evaluate it analytically by considering two different limits: (i) the spectral behavior of the tensor power spectrum for modes that remain outside the horizon before the end of reheating ($k < k_{\mathrm{re}}$), and (ii) the spectral behavior of modes that are inside the horizon before the end of reheating ($k > k_{\mathrm{re}}$).

Computing the Tensor Power Spectrum for $k < k_{\mathrm{re}}$: For modes that remain outside the horizon before the end of reheating ($k < k_{\mathrm{re}}$), we can take the limit $x_{\mathrm{re}} = k/k_{\mathrm{re}} < 1$ to simplify the integral. We also split the momentum integral into two parts, $k_{\mathrm{cmb}}/k < u < 1$ and $1 < u < k_{\mathrm{e}}/k$. Utilizing this, we can express the tensor power spectrum as

$$P_{\mathrm{T,ra}}^{\mathrm{sec}}(k,\eta_\nu) = \frac{k^4|\mathcal{B}|^4}{32\pi^2 M_{\mathrm{P}}^4}\left(\frac{k}{k_{\mathrm{e}}}\right)^{-4(n+\alpha+1)} x_{\mathrm{re}}^2\left(\int_{x_{\mathrm{re}}}^{x_\nu} dx_1 \frac{\mathcal{G}_{\mathbf{k}}(x_\nu, x_1)}{a^2(x_1)}\right)^2 \times \left\{F_{uu}^1(k,\eta_{\mathrm{re}}) + F_{uu}^2(k,\eta_{\mathrm{re}})\right\} \tag{5.33}$$

where we define

$$F_{uu}^1(k,\eta_{\mathrm{re}}) = \int_{u_{\min}}^{1}\frac{du}{u}\int_{-1}^{1} d\mu f(\mu,\gamma) u^{3-2(n+\alpha)}\mathrm{J}_{\alpha+1/2}^2(ux_{\mathrm{re}})\mathrm{J}_{\alpha+1/2}^2(x_{\mathrm{re}}) \tag{5.34}$$

$$F_{uu}^2(k,\eta_{\mathrm{re}}) = \int_{1}^{u_{\max}}\frac{du}{u^4}\int_{-1}^{1} d\mu f(\mu,\gamma) u^{6-4(n+\alpha)}\mathrm{J}_{\alpha+1/2}^4(ux_{\mathrm{re}}) \tag{5.35}$$

Numerical evaluation shows that $F_{uu}^1(k,\eta_{\mathrm{re}}) \gg F_{uu}^2(k,\eta_{\mathrm{re}})$ (see Appendix A.4). Focusing only on F_{uu}^1, in the limit $x_{\mathrm{re}} \ll 1$ with $k_{\mathrm{cmb}}/k < u < 1$, we find

$$F_{uu}^1(k,\eta_{\mathrm{re}}) \simeq \frac{8}{3}\frac{2^{-4(\alpha+1/2)}}{\Gamma^4(\alpha+1/2)} x_{\mathrm{re}}^{4(\alpha+3/2)}\frac{1}{4-2n}\left\{1 - \left(\frac{k_0}{k}\right)^{4-2n}\right\} \tag{5.36}$$

5.4.2 Defining the Present-Day Dimensionless Gravitational Wave Spectrum Energy Density $\Omega_{\rm GW}h^2$

Gravitational waves (GWs) weakly interact with matter and can freely propagate without losing their original nature after being produced during a radiation-dominated era. The GW energy density, which scales as $\rho_{\rm GW} \propto a^{-4}$, can be normalized by the total energy density at the production time, $\rho_c(\eta)$. Presently, this density parameter is given by

$$\Omega_{\rm GW}(k,\eta) = \frac{\rho_{\rm GW}(k,\eta)}{\rho_c(\eta)} = \frac{1}{12}\frac{k^2 P_{\rm T}(k,\eta)}{a^2(\eta)H^2(\eta)}, \tag{5.37}$$

where $\rho_c(\eta) = 3H^2(\eta)M_{\rm P}^2$, with the reduced Planck mass $M_{\rm P} \approx 2.43 \times 10^{18}$ GeV.

The GW energy density follows the radiation scaling behavior, making modes within the Hubble radius near radiation-matter equality particularly relevant. The present-day energy density parameter $\Omega_{\rm GW}(k)h^2$ is then given by

$$\Omega_{\rm GW}(k)h^2 \simeq \left(\frac{g_{*,0}}{g_{*,\rm eq}}\right)^{1/3} \Omega_R h^2 \Omega_{\rm GW}(k,\eta), \tag{5.38}$$

where $\Omega_R h^2 = 4.3 \times 10^{-5}$, $g_{*,\rm eq} \simeq g_{*,0} = 3.35$, and denote relativistic degrees of freedom at equality and today, respectively.

The spectral energy density (SED) of GWs helps us distinguish between different production mechanisms, such as vacuum fluctuations and sourced fields like the electromagnetic field.

Spectral Behavior of Primary GWs: Primordial gravitational waves (PGWs) originate from vacuum fluctuations during the inflationary era. As previously discussed, these tensor perturbations exhibit a nearly scale-invariant spectrum in a de Sitter inflationary background. However, the present-day amplitude and shape of the PGW spectrum are influenced by the post-inflationary evolution of the universe. In particular, non-standard reheating scenarios can significantly modify the spectral behavior of GWs, especially for modes that re-enter the horizon before the end of reheating. Consequently, the present-day spectrum of PGWs, depending on the comoving wavenumber, can be characterized by the following expression [117, 119, 229]

$$\Omega_{\rm GW}^{\rm pri}(f)h^2 \simeq \frac{\Omega_{\rm r}h^2\, g_{*,0}^{1/3}}{6\, g_{*,\rm eq}^{1/3}}\frac{H_{\rm e}^2}{M_{\rm P}^2} \times \begin{cases} 1 & f < f_{\rm re}, \\ \mathcal{D}_1\left(\frac{f}{f_{\rm re}}\right)^{-n_w} & f > f_{\rm re}, \end{cases} \tag{5.39}$$

where $\mathcal{D} \simeq 2^{1-2l}\Gamma^2(1-l)/2\pi \simeq \mathcal{O}(1)$ and $n_w = 2(1-3w_{\rm re})/(1+3w_{\rm re})$ [117, 229].

For GWs produced solely from vacuum fluctuations, modes remaining outside the horizon before reheating end are not affected by reheating dynamics and retain a scale-invariant spectrum regardless of the equation of state (EoS). However, for modes that re-enter the horizon before reheating ends, the spectrum depends on the reheating phase dynamics. Specifically, for $w_{\rm re} = 0$ (matter-like reheating), the spectrum follows f^{-2} for $f > f_{\rm re}$, whereas for $w_{\rm re} = 1/3$, it remains scale-invariant. For $w_{\rm re} > 1/3$, the spectrum transitions to a blue-tilted behavior, scaling as f^{-n_w}. For instance, with $w_{\rm re} = 0.5$, the spectrum scales as $f^{0.4}$.

Spectral Behavior of Secondary GWs: Similarly, for GWs sourced by electromagnetic fields, we approximate the SED of secondary GWs as

$$\Omega_{\rm GW}^{\rm sec}h^2 \simeq \frac{\Omega_{\rm r}h^2}{6}\left(\frac{g_{*,0}}{g_{*,\rm eq}}\right)^{1/3}\left(\frac{H_{\rm e}}{M_{\rm P}}\right)^4\left(\frac{a_{\rm e}}{a_{\rm re}}\right)^{2(1-3w_{\rm re})}\left(\frac{x_{\rm re}}{x_{\rm e}}\right)^{4(\alpha+1)}\overline{\mathcal{I}^2(f,\eta_{\rm re},\eta_\nu)}$$
$$\times\begin{cases}\mathcal{A}_1(f/f_{\rm end})^{2(4-2n)} & f_* < f < f_{\rm re}\\ \mathcal{A}_2(x_{\rm re}/x_{\rm e})^{4(n-2)}(f/f_{\rm end})^{4(1-n-\alpha)} & f_{\rm re} < f < f_{\rm end}\end{cases} \tag{5.40}$$

where we define $\mathcal{A}_1$ and $\mathcal{A}_2$ as

$$\mathcal{A}_1 = \frac{|\mathcal{B}|^4 2^{-4(n+1/2)}}{144\,\pi^2(4-2n)\Gamma^4(\alpha+1/2)}, \tag{5.41a}$$

$$\mathcal{A}_2 = \frac{|\mathcal{B}|^4}{360\,\pi^4}\frac{1}{2(n+\alpha)-2}, \tag{5.41b}$$

where $\mathcal{B}$ is defined in Eq. (5.31). Here, $\mathcal{I}_{\rm ra}(k,k_{\rm re},k_\nu)$ is defined as [229]

$$\mathcal{I}(k,\eta_{\rm re},\eta_\nu) = \int_{x_{\rm re}}^{x_\nu} dx_1\frac{\sin(x_1-x_\nu)}{x_1}. \tag{5.42}$$

As for the low-frequency regions, we found that $\mathcal{I}(k<k_\nu) = \gamma_1$, where $\gamma_1 \sim 0.5$ at the epoch of neutrino decoupling.

In the above expression, the factor $(a_{\rm e}/a_{\rm re})^{2(1-3w_{\rm re})}$ arises from the relative dilution of the magnetic field energy density and background energy density. The magnetic energy density scales as a^{-4}, whereas the background energy density scales as $a^{-3(1+w_{\rm re})}$. The factor $(x_{\rm re}/x_{\rm e})^{4(\alpha+1)}$ accounts for additional magnetic field production due to coupling during reheating.

For super-horizon modes, the spectral shape of secondary GWs is governed by the initial gauge field coupling during inflation via n, yielding a spectral index twice the magnetic spectral index for super-horizon modes (see Eq. (5.20)). For sub-horizon modes, the spectral tilt is also twice the magnetic spectral index, scaling as $4(1-n-\alpha)$ (see Eq. (5.21)). This follows naturally since the SED of secondary GWs is proportional to the square of the magnetic spectral energy density (see Eq. (5.29)), i.e., $\Omega_{\rm GW}(k,\eta) \propto \mathcal{P}_{\rm B}^2(k,\eta)$.

In Fig. 5.7, we present the spectral energy density (SED) of gravitational waves (GWs), $\Omega_{\rm GW}$, as a function of the comoving frequency f (Hz) for two different values of the equation of state (EoS) during reheating, $w_{\rm re} = 0.0$ (left) and $w_{\rm re} = 1/3$ (right). In both cases, we set the reheating temperature to $T_{\rm re} = 1$ GeV. This choice ensures consistency with the observed present-day magnetic field at large scales, particularly at 1 Mpc.

From Table 5.1, it is evident that for this class of magnetogenesis models to remain free from backreaction and strong coupling issues, the reheating temperature must be relatively

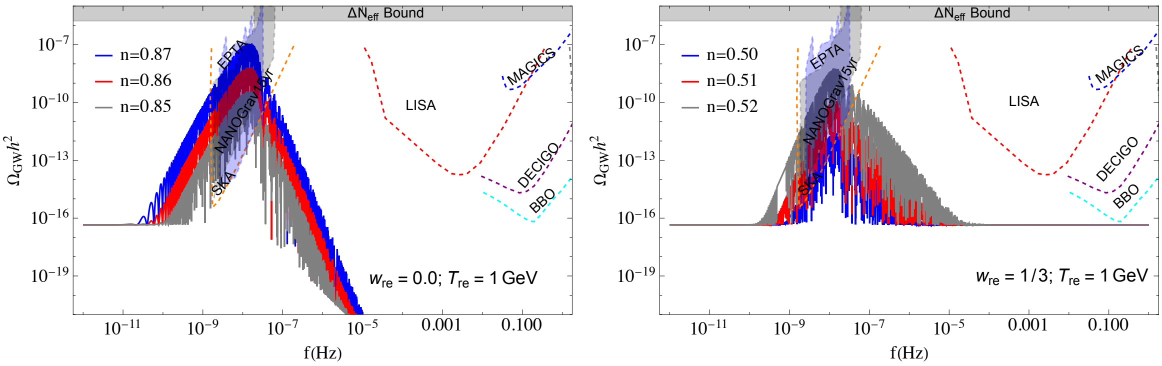

Figure 5.7: Gravitational-wave spectral energy density $\Omega_{\rm GW}h^2$ as a function of frequency f (in Hz) for different values of the coupling parameter n. In the left panel, we show the case of matter-like evolution after inflation, while in the right panel, we present the radiation-like evolution after inflation. In both panels, the reheating temperature is fixed to $T_{\rm re} = 1\,$GeV.

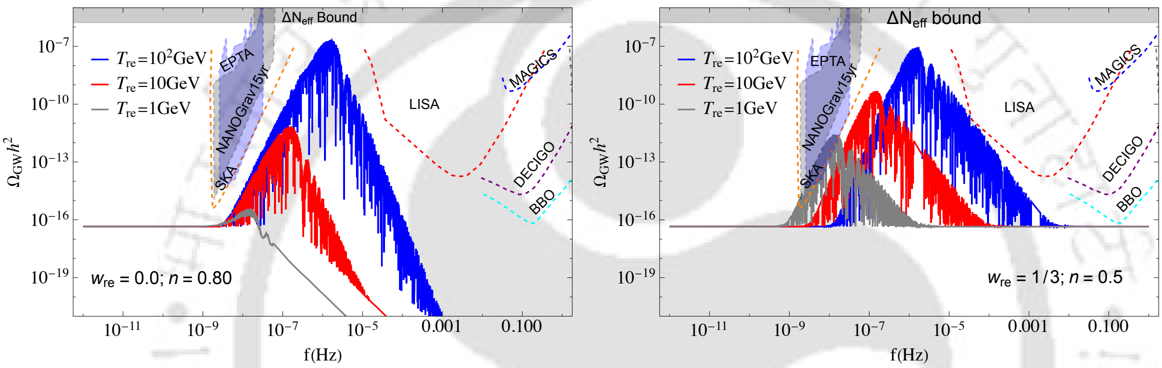

Figure 5.8: Gravitational-wave spectral energy density $\Omega_{\rm GW}h^2$ as a function of frequency f (in Hz) for different reheating scenarios.. In the left panel, we consider a matter-like evolution after inflation with the initial magnetogenesis coupling parameter $n = 0.80$. In the right panel, we consider a radiation-like evolution after inflation with the initial coupling parameter $n = 0.5$. In both panels, three different values of the reheating temperature are shown, $T_{\rm re} = 1$, 10, and $10^2\,$GeV. As the reheating temperature varies, both the amplitude and the peak position of the GW spectrum change accordingly.

low. For the left panel ($w_{\rm re} = 0$), we find that to obtain a reasonable magnetic field strength at 1 Mpc, the coupling parameter must lie within the range $0.8 < n < 0.95$, with the reheating temperature constrained to $10^{-2} \leq T_{\rm re} \leq 10^2$ GeV. Within this parameter range, the generated magnetic fields source a significant secondary GW background, detectable not only by future SKA [334] but also by current PTA observations, including NANOGrav [41], EPTA+IPTA [42], PPTA [43, 44], and CPTA [45].

Although the latest NANOGrav 15-year data suggests a characteristic strain spectral index $\gamma_{\rm CP} = 3.2$ (corresponding to an energy density spectral index $n_{\rm gw} = 1.8$), our magnetogenesis model naturally predicts a strongly blue-tilted magnetic field spectrum, scaling as $\mathcal{P}_B(f) \propto f^{4-2n}$. For instance, choosing $n = 0.85$ gives $\mathcal{P}_B(f) \propto f^{2.3}$. Since for super-horizon modes the secondary GW spectrum follows $\Omega_{\rm GW}(f) \propto f^{2(4-2n)}$, we obtain $\Omega_{\rm GW}(f) \propto f^{4.6}$ at nano-Hz frequencies for $T_{\rm re} = 1$ GeV, indicating a highly blue-tilted GW spectrum.

In the right panel of Fig. 5.7, we consider $w_{\rm re} = 1/3$ with $T_{\rm re} = 1$ GeV. To avoid backreaction effects, we select $n = 0.50, 0.51, 0.52$. These values yield sufficient magnetic fields for detection by future experiments such as SKA. In this case, for super-horizon modes ($k < k_{\rm re}$), the GW spectrum scales as $\Omega_{\rm GW}(f) \propto f^6$ for $n = 0.5$.

Interestingly, we always observe a peak in the GW spectrum around $f \simeq f_{\rm re}$, corresponding to the maximum amplitude of the electromagnetic field at $k \simeq k_{\rm re}$. Identifying this peak frequency could provide insights into the background temperature at the end of reheating. Additionally, we find that the spectral slope of the sub-horizon modes is influenced not only by the coupling parameter n but also by the details of the reheating dynamics. Specifically, for sub-horizon modes, the GW spectrum follows $\Omega_{\rm GW}h^2(f) \propto f^{4(1-n-\alpha)}$, where $\alpha = 2nN_{\rm inf}/(1 + 3w_{\rm re})N_{\rm re}$ depends on the equation of state and reheating temperature. Our analysis indicates that when the reheating dynamics resemble a radiation-dominated background, the resulting magnetic spectrum is more strongly blue-tilted, leading to a correspondingly steeper GW spectrum compared to matter-like reheating scenarios.

In Fig. 5.8, we further explore the impact of reheating temperature by plotting the SED of GWs for $w_{\rm re} = 0.0$ (left) and $w_{\rm re} = 1/3$ (right) for three different reheating temperatures: $T_{\rm re} = 10^2$ GeV (blue), $T_{\rm re} = 10$ GeV (red), and $T_{\rm re} = 1$ GeV (gray). For $w_{\rm re} = 0.0$, we fix $n = 0.80$, while for $w_{\rm re} = 1/3$, we set $n = 0.5$.

Our results show that both the amplitude and peak position of the GW spectrum vary significantly with reheating temperature. A higher reheating temperature implies an earlier end to reheating. To satisfy the condition $f(\eta = \eta_{\rm re}) = 1$, a larger $T_{\rm re}$ requires a higher value of α, which enhances electromagnetic field production during reheating. Consequently, a higher reheating temperature leads to a stronger peak in the magnetic field spectrum (see Fig. 5.5), thereby amplifying the secondary GW background. This trend is clearly illustrated in Fig. 5.8, where increasing $T_{\rm re}$ results in a larger GW amplitude and a shift in the spectral peak.

5.5 Conclusion

The origin of large-scale magnetic fields, with wavelengths exceeding those of galaxies and galaxy clusters, remains an open question in cosmology. While several models have been proposed to explain their genesis, their consistency with observational constraints is still a subject of investigation. In this chapter, we explored a coupling mechanism that can simultaneously address the issue of strong coupling while avoiding backreaction effects, thereby providing a viable explanation for the observed present-day magnetic field strength.

Most studies on this topic assume an arbitrary post-inflationary universe; however, in realistic reheating scenarios, inflation and reheating are strongly correlated, limiting the range of permissible parameter values. Our analysis indicates that achieving the required present-day magnetic field strength is not possible by arbitrarily choosing model parameters. Even when obtaining the desired field strength, many models necessitate an unrealistically low inflationary energy scale. In contrast, we have demonstrated that by carefully selecting coupling parameters and considering specific reheating scenarios, one can successfully generate the observed large-scale magnetic fields without requiring an extremely low inflationary scale.

Many magnetogenesis models suggest that producing sufficiently strong magnetic fields on cosmological scales requires a scale-invariant or nearly scale-invariant spectrum. However, our findings indicate that even a strongly blue-tilted spectral behavior can still account for the observed magnetic field strength. A key requirement for this scenario is a reheating phase characterized by a low reheating temperature. Specifically, for a matter-like reheating scenario ($w_{\rm re} = 0$), we find that in order to satisfy the lower bound on the present-day magnetic field strength for wavelengths larger than 1 Mpc, the reheating temperature must lie within the range $10^{-2} T_{\rm re} < 10^{2}$ GeV, while the coupling parameter n should be within the interval $0.8 < n < 0.95$. Similarly, for a radiation-like reheating scenario ($w_{\rm re} = 1/3$), we find that to generate a sufficiently strong magnetic field on large scales, the coupling parameter must satisfy $0.5 < n < 0.55$, with the reheating temperature constrained to $10^{-2} < T_{\rm re} < 10^{2}$ GeV.

An intriguing outcome of our analysis is that the resulting magnetic field spectrum always exhibits a broken power-law behavior. We further observe that for matter-like reheating scenarios, the produced field, while still consistent with present-day observations, exhibits a smaller blue tilt compared to scenarios with a radiation-like reheating phase ($w_{\rm re} = 1/3$). In both cases, however, our results consistently point toward a low reheating temperature as a key requirement for successful magnetogenesis.

In the second part of this study, we explored a potential observational test for this class of magnetogenesis models via the production of secondary gravitational waves (GWs). Our results show that for suitable model parameters, the generated electromagnetic (EM) field can serve as a significant source of GWs with a distinctive spectral signature. If the present-day magnetic field strength is to be satisfied, the parameter choices lead to a GW spectrum that peaks in the nano-Hz frequency range, making it compatible with the recently observed PTA signals [41–45]. Due to the strongly blue-tilted nature of the magnetic spectrum, the resulting GWs also inherit this characteristic, which can help stabilize the PTA signal within a 2σ limit.

Furthermore, even if we do not aim to explain the present-day large-scale magnetic field strength, our model allows for the generation of strong magnetic fields at smaller scales, which can act as prominent GW sources. Depending on the parameter choices, the resulting GW spectrum could be detectable by future sensitivity curves of LISA [335, 336], DECIGO [340–342], or BBO [337–339]. Notably, we find that generating such strong GWs does not require a low inflationary scale; signals consistent with $H_{\rm e} \simeq 10^{-5} M_{\rm P}$ can still be easily achieved.

The primary objective of this work has been to investigate the impact of reheating dynamics on magnetogenesis models and their implications for the present-day magnetic field strength. Additionally, we have examined how the GW spectrum is influenced by these magnetogenesis scenarios and their associated reheating history. Our results indicate a distinct spectral behavior for the resulting GWs, which varies with the reheating dynamics, allowing for a clear differentiation between different scenarios. Moreover, the strongly blue-tilted GW spectrum predicted by these models makes them easily distinguishable from other sources, providing a potential observational signature for testing magnetogenesis models in the early universe.

Chapter 6

The Magnetic Origin of Primordial Black Holes: A Viable Dark Matter Scenario

6.1 Introduction

Primordial Black Holes (PBHs) are hypothetical black holes that may have formed in the early Universe, well before the emergence of stars and galaxies. They originate from the collapse of overdense regions re-entering the Hubble horizon during the post-inflationary era, seeded by fluctuations generated during inflation as well as post-inflationary dynamics. When the curvature perturbation amplitude exceeds a critical threshold, gravitational collapse leads to PBH formation, a mechanism first proposed by Zel'dovich and Novikov [120] and later developed by Hawking and Carr [121].

Compared to stellar black holes, primordial black holes (PBHs) do not require any stellar progenitors and are instead governed purely by high-energy physics in the early Universe. This makes them unique probes of inflation, reheating, and beyond-standard-model phenomena at energy scales far beyond those accessible to terrestrial particle accelerators.

PBHs have attracted significant attention in recent years due to their potential roles as dark matter candidates [124, 127, 136–141, 189, 351–355], as seeds for supermassive black holes (SMBHs) [356–358], and as contributors to baryogenesis and cosmic radiation through Hawking evaporation [127, 136–141, 353–355].

In addition, PBHs can generate a significant background of secondary gravitational waves, which may be detectable by future gravitational wave experiments [**?**, 359, 360].

Importantly, primordial black hole (PBH) production is highly sensitive to the small-scale primordial curvature power spectrum, which remains largely unconstrained by observations of the CMB and large-scale structure [12, 75, 361, 362]. This lack of constraints opens up the possibility for mechanisms that can significantly enhance perturbations on small scales.

Among the most extensively studied scenarios are inflationary models featuring an ultra-slow-roll (USR) phase [142, 142–147, 156, 183, 191, 195–197, 363]. In such models, the inflaton temporarily undergoes a phase of ultra-slow evolution on a nearly flat potential, leading to a significant amplification of superhorizon curvature perturbations.

Other proposed mechanisms for PBH formation include bubble collisions during first-order phase transitions [157, 158, 364, 365], as well as the collapse of topological defects such as cosmic strings [159–161, 351, 366, 367]. In addition, it has been shown that warm inflation scenarios can also lead to the production of a significant abundance of PBHs [368].

In this chapter, we propose yet another physically motivated alternative mechanism utilizing the well-studied inflationary magnetogenesis model. We show that even without a USR phase, simple magnetic spectra with power law form generated during the early stage of our universe (inflation and during reheating), can enhance curvature perturbations sufficiently to produce PBHs. Most studies on magnetogenesis models focus on matching present-day magnetic field observations at large scales and associated gravitational wave production. However, their impact on primordial curvature perturbations has received comparatively less attention. Interesting to note that the magnetic field at small scales is poorly constrained, similar to the inflationary scalar power spectrum. This freedom motivates us to tune the magnetic spectrum at small scales rather than tuning the inflatonary phase, and enhance the scalar power spectrum. By suitably tuning the magnetic spectrum, we indeed show that the scalar power spectrum can be enhanced sufficiently; therefore, neither an ultra-slow-roll (USR) phase nor other non-standard inflationary dynamics are required, yet a substantial PBH abundance can still be achieved.

In this chapter, we focus on a special class of magnetogenesis model (see [118] for details) that is capable of simultaneously explaining the large-scale magnetic fields observed by various experiments and producing PBHs that can constitute a partial CDM component. Furthermore, for specific parameter choices, they can yield a significant PBH abundance in mass ranges where PBHs could serve as the sole dark matter candidate. We find that the PBH mass is primarily determined by the reheating temperature, while the PBH fractional energy density depends both on the reheating dynamics and the present-day magnetic field.

Magnetic fields are observed across a broad range of astrophysical environments, from kiloparsec (Kpc) to megaparsec (Mpc) length scales, with significant strength. Most intriguing is the presence of a magnetic field in the intergalactic medium (IGM), with length scales even larger than Mpc, and a lower bound on the present-day magnetic field strength around $10^{-17} - 10^{-15}$ G [369, 369–371]. Furthermore, at similar scales, the CMB anisotropies yield an upper bound on the present-day magnetic field strength of order $\sim$ nG [247, 317, 318]. The origin of such large-scale magnetic fields remains one of the most challenging problems in cosmology and has been widely discussed in the literature.

Inflationary magnetogenesis models [13–16, 47, 117, 118, 233, 235–238, 258, 259, 262, 263, 275, 326, 329, 331] are among the most popular scenarios. A typical primordial inflationary magnetogenesis setup is modeled by introducing couplings between the gauge field and scalar or pseudoscalar fields, e.g., $f^2(\phi, R)F_{\mu\nu}F^{\mu\nu}$ [47, 117, 235–238, 258, 259, 262, 263, 316, 372–374], or parity-violating terms like $f^2(\phi, R)F_{\mu\nu}\tilde{F}^{\mu\nu}$ [221, 264–266, 266, 267] Here, R is the Ricci scalar, $F_{\mu\nu} = \partial_\mu A_\nu - \partial_\nu A_\mu$, and A_μ denotes the four-vector potential.

For our present purpose, we consider the simplest non-parity-violating magnetogenesis model. By appropriately choosing the conformal time (η) dependent coupling function $f(\phi, R) = f(\eta)$, we demonstrate that the model can induce large curvature fluctuations leading to primordial black hole (PBH) production, while simultaneously generating a large-scale magnetic field within the observable range. As mentioned earlier, we study scenarios where the produced PBHs survive until today and can act as either fully or partially viable dark matter candidates.

6.2 Model for Magnetogenesis

In this work, we focus on a magnetogenesis scenario in which the induced overdense regions collapse to form primordial black holes (PBHs) within a specific mass window, allowing them to behave as cold dark matter. This requires a mechanism that generates magnetic fields with a peak at intermediate scales, corresponding to the scales relevant for PBH formation within the desired mass range.

As discussed in earlier chapters, the sawtooth-type magnetogenesis model produces a broken power-law magnetic spectrum, where the majority of the electromagnetic energy density is concentrated around $k \simeq k_{\rm re}$. Here, $k_{\rm re}$ denotes the comoving wavenumber corresponding to the horizon scale at the end of reheating.

Since the conformal symmetry-breaking coupling is active during both inflation and reheating, the gauge field experiences continuous excitation across these two phases. However, the dominant contribution to the field amplification arises during the reheating epoch. For simplicity, we parametrize the comoving magnetic and electric fields at the end of reheating using a broken power-law spectrum. Consequently, the corresponding energy spectra exhibit distinct scaling behaviors in different regimes.

In particular, for super-horizon modes ($k < k_{\rm re}$), the spectra scale as [118],

$$\tilde{\mathcal{P}}_{\rm B}(k, \eta_{\rm re}) = \frac{k_{\rm e}^4}{8\pi} \frac{q^1_{n_{\rm B}}(n)}{(\alpha + 1/2)^2} \left(\frac{k_{\rm e}}{k_{\rm re}}\right)^{2(\alpha+1)} \left(\frac{k}{k_{\rm e}}\right)^{n_{\rm B}}, \tag{6.1a}$$

$$\tilde{\mathcal{P}}_{\rm E}(k, \eta_{\rm re}) = \frac{k_{\rm e}^4}{8\pi} \frac{q^1_{n_{\rm B}}(n)}{4} \left(\frac{k_{\rm e}}{k_{\rm re}}\right)^{2\alpha} \left(\frac{k}{k_{\rm e}}\right)^{n_{\rm B}-2}. \tag{6.1b}$$

In the above expression, we note that the electric field exhibits a decaying spectrum compared to the inflationary case, Eq. (5.12), due to the decreasing value of the coupling function during reheating. Whereas for the sub-horizon modes ($k > k_{\rm re}$), the magnetic and electric spectra behave as [118]

$$\tilde{\mathcal{P}}_{\rm B}(k > k_{\rm re}, \eta_{\rm re}) \simeq \frac{k_{\rm e}^4}{4\pi} \frac{q^2_{n_{\rm B}}(n)}{\pi} \left(\frac{k}{k_{\rm e}}\right)^{n_{\rm B}-2(\alpha+1)}, \tag{6.2}$$

$$\tilde{\mathcal{P}}_{\rm E}(k > k_{\rm re}, \eta_{\rm re}) \simeq \frac{k_{\rm e}^4}{4\pi} q^2_{n_{\rm B}}(n) \left(\frac{k}{k_{\rm e}}\right)^{n_{\rm B}-2(\alpha+1)}. \tag{6.3}$$

Where $q^1_{n_{\rm B}}(n)$ and $q^2_{n_{\rm B}}(n)$ is defined as

$$q^1_{n_{\rm B}}(n) = \frac{2^{2n+1}(\alpha - n)^2 \Gamma^2(n + 1/2)}{\cos^2(\pi\alpha)\Gamma^2(1/2 - \alpha)\Gamma^2(\alpha + 1/2)}, \tag{6.4a}$$

$$q^2_{n_{\rm B}}(n) = \frac{2^{2(n+\alpha)}(\alpha - n)^2 \Gamma^2(n + 1/2)}{\cos^2(\pi\alpha)\Gamma^2(1/2 - \alpha)}. \tag{6.4b}$$

After the end of reheating, the universe enters the standard radiation-dominated era, during which the electromagnetic (EM) field regains its gauge-invariant form, and no further amplification of magnetic fields occurs. In this phase, all fundamental particles have already been produced, and the universe exhibits extremely high electrical conductivity. In the high-conductivity limit, the rapid response of charged particles leads to the suppression of electric fields, while the magnetic fields evolve adiabatically. This implies that the comoving magnetic energy density remains constant with time, an assumption valid on sufficiently large scales where magnetohydrodynamic (MHD) effects are negligible.

Backreaction Issue: Throughout the computation, we treated the gauge field as a perturbative component. Hence, the total EM energy density is assumed to remain smaller than the background energy density, i.e., $\rho = 3H^2M_{\rm P}^2$, during both the inflationary and post-inflationary eras. Particularly, the fractional energy density of the EM field at the end of reheating satisfies $\delta_{\rm EM} = \rho_{\rm em}(\eta_{\rm re})/\rho_{\rm bg}(\eta_{\rm re}) \leq 1$, which ensures that the produced EM field energy density always stays below the background energy density, even after reheating. Assuming the electric field decays almost instantaneously due to the high electrical conductivity of the Universe after the end of reheating, while the magnetic field evolves adiabatically, $\rho_{\rm B} \propto a^{-4}$, the $\delta_{\rm em}$ at the end of reheating assumes,

$$\delta_{\rm EM}(\eta_{\rm re}) = \frac{H_{\rm e}^2}{24\pi M_{\rm P}^2}\frac{q^1_{n_{\rm B}}}{2(\alpha+1)-n_{\rm B}}\left(\frac{a_{\rm re}}{a_{\rm e}}\right)^{\frac{2\alpha-n_{\rm B}}{2}} \tag{6.5}$$

To arrive at the above quantity, we have considered EoS during reheating is $w_{\rm re} = 0$. In addition to the above, we need to take into account the additional constraint on reheating temperature $T_{\rm re} > T_{\rm BBN}$, the Big-Bang Nucleosynthesis temperature. We further need to take into account the maximum possible bound on the magnetic field strength at 1 Mpc scale being $\lesssim 1$ nG. To this end, let us point out that in our defined fractional energy density at the end of reheating, we neglected MHD effects, since they are only relevant for modes that remain deep inside the horizon at that epoch [375–377]. Therefore, the total energy density of the produced EM field is not affected by MHD.

Present-day magnetic field and parameter constraints: After reheating, the conformal symmetry of the gauge field is restored, and no further magnetic field production occurs. Once reheating is completed, the universe becomes radiation-dominated with large conductivity. Owing to this high conductivity, the electric field component decays almost instantaneously, while the large-scale modes that remain outside the horizon evolve adiabatically. Therefore, the present-day magnetic field for different scales can be followed from the following relation $a_0^2 B_0 = a_{\rm re}^2 B(\eta_{\rm re})$, and the eq.6.1a

$$B_0(k) = \sqrt{\frac{k_{\rm e}^4 q^1_{n_{\rm B}}}{8\pi}}\left(\frac{k_{\rm e}}{k_{\rm re}}\right)^{\alpha+1}\left(\frac{k}{k_{\rm e}}\right)^{n_{\rm B}/2}. \tag{6.6}$$

We set all the scales k with respect to this. Given the equation of state $w_{\rm re} = 0$ which is the case we will discuss through out the paper, the above constraining equation 6.5 we obtain minimum

$n_{\rm B}$	2.1	2.2	2.3	2.4	2.5	2.6
$T_{\rm re}$ (GeV)	0.01	0.15	4.11	10^2	2.3×10^3	4.8×10^4
$B_0(1\ {\rm Mpc}^{-1})$	2.5×10^{-10}	2.9×10^{-12}	2.8×10^{-14}	2.1×10^{-16}	1.3×10^{-18}	6.4×10^{-21}

Table 6.1: In the table above, we have presented the lower reheating temperature $T_{\rm re}$ (in GeV) to avoid the backreaction due to the excessive production of the gauge field, and we also listed the corresponding present-day magnetic field for the 1 Mpc scales (B_0) in Gauss unit. Here we consider the inflationary energy scale as $H_{\rm e}\simeq10^{-5}M_{\rm P}$ and we consider that the EoS during reheating period is $w_{\rm re}=0$ (matter like evolution).

possible reheating temperature tabulated in Tab.6.1 for a given $n_{\rm B}$ and $H_{\rm e}=10^{-5}M_{\rm P}$, and the corresponding present-day magnetic field strength at the comoving scale of 1 Mpc. For example, $n_{\rm B}=2.1$, we obtain that the minimum reheating temperature would be $T_{\rm re}\simeq0.01$ GeV, consistent with non-backreaction, and the present-day magnetic field turns out to be $\sim10^{-10}$ G, consistent with the observational upper bound.

Eq.6.6 clearly suggests that as $k/k_{\rm re}<1$ for large scale magnetic field, increasing $n_{\rm B}$ reduces the present day value of the magnetic field as $B_0(k)\propto(k/k_{\rm e})^{n_{\rm B}/2}$. Therefore, to remain consistent with current observational bounds, the magnetic spectral index should be $n_{\rm B}>2.1$. Further, if we consider the $n_{\rm B}>2.5$, large-scale magnetic fields can still be generated, but their strength will fall below the present-day lower bound $B_0\gtrsim10^{-19}$ G.

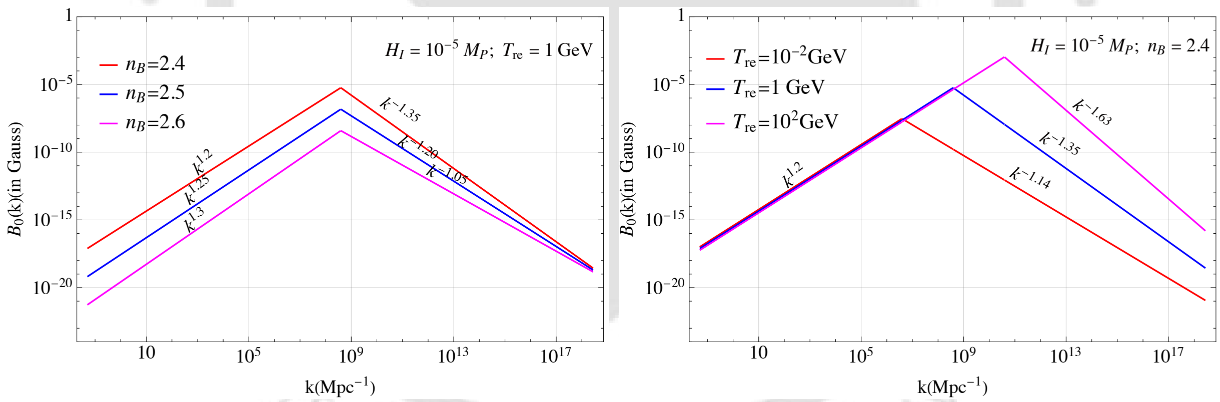

Figure 6.1: In this figure, we present the present-day magnetic field strength $B_0(k)$ (in Gauss) as a function of the comoving wavenumber k (in Mpc^{-1}). The left panel illustrates the dependence of the magnetic field spectrum on the magnetogenesis parameter $n_{\rm B}=4-2n$, with the reheating temperature fixed at $T_{\rm re}=1\,$GeV. In contrast, the right panel shows how the duration of the reheating era influences both the spectral shape and the amplitude of the magnetic field, for a fixed magnetic spectral index $n_{\rm B}=2.4$. In both cases, we assume an average equation of state during reheating of $w_{\rm re}=0$ and the inflationary energy scale as $H_{\rm e}\simeq10^{-5}M_{\rm P}$.

In Fig. 6.1, we present the present-day magnetic field strength $B_0(k)$ (in Gauss) as a function of the comoving wavenumber k (in Mpc^{-1}). The left panel illustrates how $B_0(k)$ depends on the magnetogenesis parameter $n_{\rm B}$, recalling that the magnetic spectral index is given by $n_{\rm B}=4-2n$. For this plot, we fix the reheating temperature to $T_{\rm re}=1\,$GeV, which results in a spectral break in the magnetic spectrum at $k\simeq7.8\times10^8\,{\rm Mpc}^{-1}$. The three colored curves correspond to $n_{\rm B}=2.4$ (red), $n_{\rm B}=2.5$ (blue), and $n_{\rm B}=2.6$ (magenta). For $k<k_{\rm re}$

the magnetic spectrum scales as $B_0 \propto k^{n_{\rm B}/2}$, while for $k > k_{\rm re}$ reheating effects modify the slope to $B_0 \propto k^{n_{\rm B}/2-(\alpha+1)}$. For $n_{\rm B} = 2.4$, this gives a blue-tilted spectrum $B_0 \propto k^{1.2}$ on super-horizon scales and a red-tilted spectrum $B_0 \propto k^{-1.35}$ on sub-horizon scales, as shown in Fig. 6.1. Increasing to $n_{\rm B} = 2.6$ shifts the tilts to $B_0 \propto k^{1.3}$ and $B_0 \propto k^{-1.05}$, respectively.

The right panel of Fig. 6.1 illustrates the impact of reheating duration on $B_0(k)$. For fixed $n_{\rm B}$, the large-scale magnetic field amplitude remains unchanged, while the spectral peak shifts to higher k as the reheating temperature increases. This shift originates from the spectral break at $k \simeq k_{\rm re}$: a higher $T_{\rm re}$ implies a shorter reheating duration, pushing $k_{\rm re}$ toward larger frequencies. Consequently, super-horizon modes preserve their scaling, whereas sub-horizon modes exhibit a $T_{\rm re}$-dependent tilt. For instance, at $T_{\rm re} = 10^{-2}$ GeV the sub-horizon spectrum follows $B_0 \propto k^{-1.63}$, while at $T_{\rm re} = 10^2$ GeV it softens to $B_0 \propto k^{-1.14}$. In both panels we assume $w_{\rm re} = 0$ and $H_{\rm e} \simeq 10^{-5} M_{\rm P}$.

6.3 Induced Curvature Power Spectrum

Primordial magnetic fields (PMFs), if generated in the early universe during inflation or the subsequent reheating phase, not only provide a viable origin for the large-scale magnetic fields observed today, but also act as sources of secondary gravitational waves [117, 220–222, 229, 232–234, 378] and curvature perturbations [325, 326]. In this class of magnetogenesis scenarios considered here, the magnetic field reaches its maximum strength at the end of reheating. Consequently, we should expect that the corresponding curvature perturbation induced by the magnetic field will also peak shortly after reheating. The comoving curvature perturbation on a uniform density hypersurface is defined as $\zeta = -\Phi - \mathcal{H}\frac{\delta\rho}{\rho'}$ [38, 326, 379, 380], where $\mathcal{H} = a'/a$, and prime is with respect to conformal time. Where ρ and $\delta\rho$ are the background energy density and its fluctuation, respectively. There are two ways the produced magnetic field can source the curvature: it can directly contribute from the energy density fluctuations denoted as $\delta\rho = \delta\rho_{\rm B}$ [325, 326], and it can also source the curvature through the anisotropies in the energy-momentum tensor due to the magnetic field via the Bardeen potential Φ [381, 382]. To compute the induced curvature power spectrum due to the magnetic field, we have broken it into two components, one is $\zeta_{\delta\rho_{\rm B}} = -\mathcal{H}\frac{\delta\rho_{\rm B}}{\rho'}$ and the other is $\zeta_\Phi = -\Phi$. The associated curvature power spectrum can be written as

$$P_\zeta(k) = \frac{k^3}{2\pi^2}|\zeta(k)|^2 = P_\zeta^{\delta\rho_B}(k) + P_\zeta^{\Phi}(k) + \mathcal{P}_\zeta^{\Phi\delta\rho_{\rm EM}}(k). \tag{6.7}$$

Here $P_\zeta^{\delta\rho_B}$ indicates the contribution came from the density fluctuation of the magnetic field directly and P_ζ^{Φ} denotes the contributions that came from the anisotropic components of the energy-momentum tensor due to the magnetic field. At the scale of our interest $P_\zeta^{\delta\rho_B} \ll P_\zeta^{\Phi}$, the contribution from the cross term $\mathcal{P}_\zeta^{\Phi\delta\rho_{\rm EM}}(k)$ correlating Φ and $\mathcal{H}\frac{\delta\rho_{\rm EM}}{\rho'}$ will be negligibly small, and we ignore this term ono the term for simplicity.

To compute the curvature spectrum analytically, we utilize the fact that the maximum contribution will come from around the peak of the magnetic power spectrum at $k = k_{\rm re}$, which is near the end of reheating. Therefore, around this scale we define the induced curvature perturbations $\zeta_{\rm B} = -\delta\rho_{\rm B}/4\rho_{\rm ra}$, where we have used $\rho'_{\rm ra} \approx -4\mathcal{H}\rho_{\rm ra}$ with $\rho_{\rm ra}$ being radiation energy density. Interesting to note that as both the magnetic field and radiation energy density dilute as a^{-4} due to background expansion, $\zeta_{\rm B}$ remains constant during the radiation-dominated era. The energy density fluctuations of the magnetic field in Fourier space as [325, 326]

$$\delta\rho_{\rm B} = \int \frac{d^3\mathbf{q}}{(2\pi)^3} B(q) \cdot B(|\mathbf{k}-\mathbf{q}|). \tag{6.8}$$

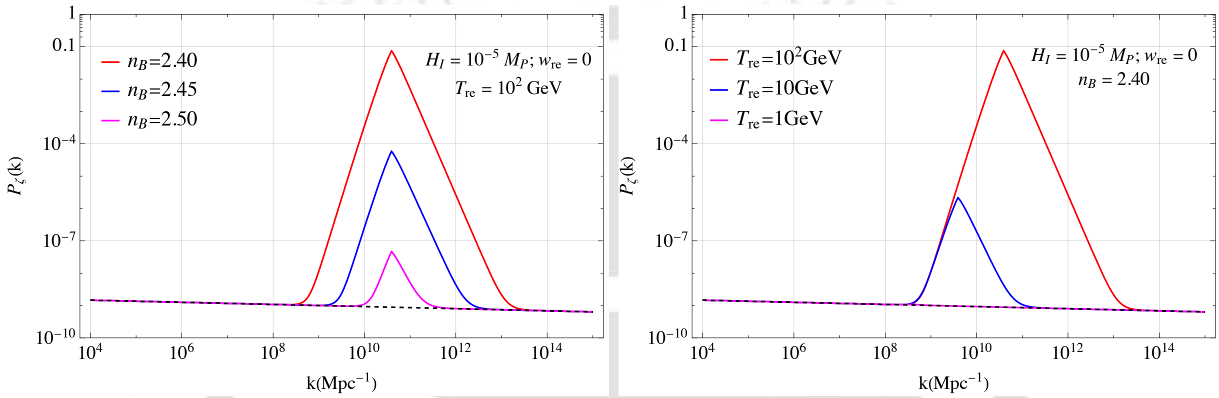

Figure 6.2: Comoving curvature power spectrum $P_\zeta(k)$ shown as a function of the comoving wavenumber $k\,(\mathrm{Mpc}^{-1})$. In the left panel, the dependence on the magnetic spectral index $n_{\rm B}$ is illustrated for a fixed reheating scenario with $(w_{\rm re} = 0, T_{\rm re} = 10^2\,\mathrm{GeV})$. In the right panel, the effect of the reheating duration on $P_\zeta(k)$ is shown, while keeping the equation of state fixed at $w_{\rm re} = 0$ and the magnetic spectral index at $n_{\rm B} = 2.4$. In both panels, the black dashed curve denotes the standard slow-roll inflationary contribution to the curvature power spectrum.

Utilizing this, we can define a two-point correlation function of the magnetic energy density fluctuation as

$$\langle \delta\rho_{\rm B}(\mathbf{k})\delta\rho^*_{\rm B}(\mathbf{k}')\rangle = (2\pi)^3\delta^{(3)}(\mathbf{k}-\mathbf{k}')\frac{2\pi^2}{k^3}P_{\delta\rho_{\rm B}}(k). \tag{6.9}$$

Here $P_{\delta\rho_{\rm B}}(k)$ is the known power spectrum associated with the density fluctuation of the magnetic field. Combining Eq.(6.8) with Eq.(6.9), we get [325, 326]

$$P_{\delta\rho_{\rm B}}(k) = \int \frac{\mathrm{dq}}{q}\int_{-1}^{1} \mathrm{d}\mu \, \frac{(1-\mu^2)\mathcal{P}_{\rm B}(\mathrm{q})\mathcal{P}_{\rm B}(|\mathbf{k}-\mathbf{q}|)}{\left(1+\frac{\mathrm{q}^2}{\mathrm{k}^2}-2\mu\frac{\mathrm{q}}{\mathrm{k}}\right)^{5/2}}, \tag{6.10}$$

where $\mu = \hat{k}\cdot\hat{q} = \cos(\theta)$ where θ is the angle between two vector $\mathbf{k}$ and $\mathbf{q}$. Here we defined $u = q/k$. Now, the induced curvature power spectrum associated with the magnetic energy density fluctuation defined at the end of reheating is

$$P_\zeta^{\delta\rho_B}(k) = \frac{1}{16}\frac{P_{\delta\rho_{\rm B}}(k)}{\rho_{\rm ra}^2}. \tag{6.11}$$

To compute the exact nature of the curvature power spectrum, we have done numerical integration. However, the amplitude of the spectrum at peak frequency can be analytically estimated as

$$A_\zeta \simeq \frac{1}{24}\left(\frac{q^1_{n_{\rm B}}}{24\pi}\right)^2\left(\frac{H_{\rm e}}{M_{\rm P}}\right)^4\left(\frac{a_{\rm re}}{a_{\rm e}}\right)^{2\alpha-n_{\rm B}} \tag{6.12}$$

. Recall that $\delta_{\rm em}(\eta_{\rm re})$ is the fractional energy density of the magnetic field defined at the end of reheating.

Apart from this, we have additional secondary contribution from the modified dynamics of Bardeen potential Φ sourced by the anisotropic component of the magnetic field [381–383]. After the reheating, our standard radiation-dominated era begins, and the peak of the frequency of the magnetic field is now inside the horizon. To track the evolution of the curvature perturbation due to magnetic field anisotropy, we have to solve the Bardeen potential equation in the presence of a source. For simplicity, we ignored the contribution originating from the entropy perturbation due to the magnetic field. In the radiation-dominated era, the evolution of the Bardeen potential sourced by the magnetic anisotropies is simply governed by [381–383]

$$\Phi'' + \frac{4}{\eta}\Phi' + \frac{k^2}{3}\Phi = -\frac{\mathcal{H}^2}{k^2}\left[\frac{k^2}{3} - 2\mathcal{H}'\right]\Pi_{\rm B}\,. \tag{6.13}$$

In the above expression, we made use of $\mathcal{H} = 1/\eta$ during the radiation-dominated phase. Further, $\Pi_{\rm B}(k,\eta)$ is the source term associated with the magnetic field, where $|\Pi_{\rm B}(k)|^2 = \langle \Pi_{\rm B}(k)\Pi^*_{\rm B}(k)\rangle$ is define as [381, 382]

$$|\Pi_{\rm B}(k)|^2 = \frac{36\pi^3}{16\rho^2 a^8}\int \frac{{\rm dq}}{q}\frac{\mathcal{P}_{\rm B}(q)\mathcal{P}_{\rm B}(|\mathbf{k}-\mathbf{q}|)}{|\mathbf{k}-\mathbf{q}|^3}\,\mathcal{F}(k,q,\mu)\,. \tag{6.14}$$

Here $\mathcal{P}_{\rm B}(k)$ is the magnetic power spectrum defined in Eq.(6.1a). Here $\mathcal{F}(k,q,\mu)$ defined as [381]

$$\mathcal{F}(k,q,\mu) = \frac{1+\mu^2+u(2\mu-6\mu^3)+u^2(5-12\mu^2+9\mu^4)}{4(1+u^2-2u\mu)}\,. \tag{6.15}$$

To solve the above Eq.(6.13), we have used the Green's function method, where the solution of the Bardeen potential Φ in the radiation-dominated era can be written as

$$\Phi(k,\eta_\nu) = \int_{\eta_{\rm re}}^{\eta_\nu} {\rm d}\eta_1\left(\frac{\mathcal{G}_{\rm k}(\eta_\nu,\eta_1)}{\eta_1^2}\right)\times\left[\frac{1}{3} - 2\frac{\mathcal{H}'}{{\rm k}^2}\right]\Pi_{\rm B}. \tag{6.16}$$

Here η_ν is the conformal time when the neutrinos are decoupled from the background thermal bath. Recall the fact that as the neutrino's anisotropy balances the magnetic anisotropy, the contribution from the magnetic anisotropy after neutrino decoupling is negligible [349, 350]. Here, the Green's function associated with the differential operator corresponding to the left hand side of the eq.6.13 is

$$\mathcal{G}_k(\eta,\eta_1) = \Theta(\eta-\eta_1)\frac{\pi\sqrt{3}\eta_1}{2\sin(3\pi/2)}\left(\frac{\eta_1}{\eta}\right)^{3/2} \times \left[\mathrm{J}_{3/2}(\tilde{x})\mathrm{J}_{-3/2}(\tilde{x}_1) - \mathrm{J}_{3/2}(\tilde{x}_1)\mathrm{J}_{-3/2}(\tilde{x})\right]. \quad (6.17)$$

In the above we define a new variable $\tilde{x} = \sqrt{3}\,k\eta$. In this magnetogenesis scenario, a magnetic field is produced starting from inflation to the entire period of reheating era, and post-reheating gague field production ceases to exist. Owing to the high electrical conductivity, the electric field decays immediately after the reheating ends, while the magnetic component evolves adiabatically. During radiation domination, both the background and the magnetic field dilute as a^{-4} due to the background expansion, so the quantity $\Pi_{\mathrm{B}}(k,\eta)$ remains constant in time. The amplitude of the comoving magnetic field is constant on super-horizon scales, and it oscillates with constant amplitude for sub-horizon modes (recall that MHD affects modes deep inside the horizon, whereas our interest is primarily at the beginning of the radiation-dominated era [376, 377]). As the peak of wave number are inside the horizon during the radiation dominated era beging as magnetic field get its peak at $k \simeq k_{\mathrm{re}}$, we recall that k_{re} the lowest-mode that can able to re-enter into the horizon at the end of reheating, and PBH is very sensitive and mainly depend on the peak of the curvature power spectrum so if we consider only the dominating term then we can write the power spectrum of the Bardeen potential define as $P_\Phi(k,\eta) = \frac{k^3}{2\pi^2}\Phi^2(k,\eta)$ as

$$P_\Phi(k,\eta) = \frac{k^3}{2\pi^2}\left[-\frac{1}{3}\int_{\eta_{\mathrm{re}}}^{\eta}\frac{\mathrm{d}\eta_1}{\eta_1^2}\mathcal{G}_k(\eta,\eta_1)\right]^2 |\Pi_{\mathrm{B}}(k)|^2\,. \quad (6.18)$$

Exact analytical computing of the curvature power spectrum due to the magnetic anisotropy is quite difficult. We have to do the above integral defined in Eq.(6.18) numerically. At the beginning of the radiation-dominated era, when the peak amplitudes are just inside the horizon, the curvature power spectrum associated with the Bardeen potential is approximated as $P_\zeta^\Phi(k,\eta\simeq\eta_{\mathrm{re}}) \simeq \pi\mathcal{I}^2(\eta,\eta_{\mathrm{re}})P_\zeta^{\delta\rho_{\mathrm{B}}}(k)$, where $\mathcal{I}(\eta,\eta_{\mathrm{re}})$ is define as

$$\mathcal{I}(\eta,\eta_{\mathrm{re}}) = \int_{\eta_{\mathrm{re}}}^{\eta}\frac{\mathrm{d}\eta_1}{\eta_1^2}\mathcal{G}_k(\eta,\eta_{\mathrm{re}}), \quad (6.19)$$

where $P_\zeta^{\delta\rho_{\mathrm{B}}}(k)$ is the induced curvature power spectrum arising from the magnetic-field energy density fluctuations, as defined in Eq. (6.11). For super-horizon scales, the time integral appearing in the source term can be approximated as $\mathcal{I}(\eta,\eta_{\mathrm{re}}) \simeq \ln(\eta/\eta_{\mathrm{re}})$ in a radiation-dominated background. This logarithmic behavior is well known for magnetically induced curvature perturbations [381–383].

In the above analysis, we have considered the contributions from both the electric and magnetic fields. During reheating, these two components coexist, whereas after reheating the large electrical conductivity of the primordial plasma rapidly damps the electric field, leaving only the magnetic field as the surviving component.

For the class of coupling functions considered in this thesis, we always impose $I(\eta) > 1$ in order to avoid the strong-coupling problem. Under this condition, the magnetic field is stronger than the electric field during inflation (see Eq. (5.12)). However, their behaviour changes during the reheating era. We find that on large scales the electric field becomes the dominant component, while on small scales the electric and magnetic fields become comparable. Most importantly, both spectra peak at the same characteristic comoving wavenumber, $k \simeq k_{\rm re}$. Consequently, the peak energy densities stored in the electric and magnetic fields are of the same order of magnitude.

Since the abundance of primordial black holes is mainly determined by the peak of the electromagnetic energy density, both the electric and magnetic fields contribute at a comparable level. Figure 5.3 shows the comoving electric and magnetic power spectra as functions of the comoving wavenumber. It clearly demonstrates that both spectra attain their maximum around $k \simeq k_{\rm re}$.

For simplicity, the analytical calculations presented in this chapter are performed using only the magnetic-field contribution. However, when computing the final primordial black hole abundance, we include the contribution from both the electric and magnetic fields through the total electromagnetic energy density.

As mentioned earlier, we focus on the beginning of the radiation-dominated era, during which primordial black holes (PBHs) are formed. Since, at this epoch, the peak frequency lies inside the horizon, the peak amplitude of the curvature perturbations induced by the magnetic field must be computed numerically at the onset of radiation domination. For instance, choosing $n_{\rm B} = 2.40$ with a reheating temperature $T_{\rm re} = 10^2$ GeV, we obtain $P_\zeta^{\delta\rho_B}(k_{\rm peak}) \simeq 0.11$, while the inflationary contribution is $P_\zeta^{\Phi}(k_{\rm peak}) \simeq 0.014$. On the other hand, for $n_{\rm B} = 2.45$ with the same reheating temperature, the induced curvature power spectrum is significantly suppressed, yielding $P_\zeta^{\delta\rho_B}(k_{\rm peak}) \simeq 8.89 \times 10^{-5}$ and $P_\zeta^{\Phi}(k_{\rm peak}) \simeq 1.08 \times 10^{-5}$.

The spectral behavior of the total curvature power spectrum can be approximated by a broken power-law form. Modes that are far outside the horizon at the end of reheating exhibit a slightly red-tilted spectrum, $P_\zeta(k \ll k_{\rm re}) \propto k^{n_s-1}$, where the inflationary curvature perturbations dominate. Since the electromagnetic field spectrum peaks around $k \simeq k_{\rm re}$, the curvature power spectrum also develops a peak near this scale. For modes that remain just outside the horizon at the end of reheating, the spectrum approximately behaves as $P_\zeta(k \leq k_{\rm re}) \propto k^{2n_{\rm B}}$. In contrast, modes that re-enter the horizon around the end of reheating, i.e. $k \geq k_{\rm re}$, scale as $P_\zeta(k \geq k_{\rm re}) \propto k^{2n_{\rm B}-4(\alpha+1)}$. For modes deep inside the horizon, the magnetic-field contribution becomes subdominant due to the decay of the magnetic energy density, and the spectrum again approaches the inflationary form, $P_\zeta(k \gg k_{\rm re}) \propto k^{n_s-1}$.

Combining these behaviors, the curvature power spectrum can be approximated as

$$P_\zeta(k) \simeq \begin{cases} A_{\rm s}(k/k_*)^{n_s-1} & k_* \le k < k_{\rm SB,1}, \\ A_\zeta(k/k_{\rm re})^{2n_{\rm B}} & k_{\rm SB,1} < k \le k_{\rm re}, \\ A_\zeta(k/k_{\rm re})^{n_{\rm B}-2(\alpha+1)} & k_{\rm re} < k < k_{\rm SB,2}, \\ A_{\rm s}(k/k_*)^{n_s-1} & k_{\rm SB,2} < k < k_{\rm e}, \end{cases} \tag{6.20}$$

Here $A_{\rm s} \simeq 2.1\times10^{-9}$ denotes the amplitude of the curvature power spectrum at CMB scales [12], and A_ζ is defined in Eq. (6.12). $k_{\rm SB,1}$ and $k_{\rm SB,2}$ correspond to the mode associated with the first and second Spectral Breaks (SB) respectively in the above spectrum. For $k > k_{\rm SB,1}$, the secondary (magnetically induced) contribution dominates, while for $k > k_{\rm SB,2}$ the inflationary curvature power spectrum again becomes the dominant component.

In Fig. 6.2, we present the comoving induced curvature power spectrum as a function of the comoving wavenumber k for two distinct scenarios. In the left panel, we fix the reheating dynamics by choosing $w_{\rm re} = 0$ and $T_{\rm re} = 10^2$ GeV. The three different colors correspond to $n_{\rm B} = 2.40, 2.45$, and 2.50. We find that the peak amplitude changes significantly with $n_{\rm B}$ since the magnetic field strength is highly sensitive to the magnetic spectral index. In particular, for fixed reheating scenarios, there exists a threshold value of $n_{\rm B}$ below which the peak amplitude of the induced curvature spectrum can reach $P_\zeta(k_{\rm peak}) \geq 10^{-2}$, providing the conditions necessary for PBH formation.

In the right panel of Fig. 6.2, we show the effect of the reheating duration on the induced curvature power spectrum for a fixed magnetic spectral index $n_{\rm B} = 2.40$. The three colors lines correspond to reheating temperatures $T_{\rm re} = 1,$GeV (magenta), $10,$GeV (blue), and $10^2,$GeV (red). We observe that as $T_{\rm re}$ increases, the peak of the curvature power spectrum shifts toward higher-frequency modes and its amplitude grows. This behavior originates from our chosen coupling prescription, in which the coupling is restored to unity at the end of reheating. Under this condition, the effective post-inflationary coupling α takes larger values for higher $T_{\rm re}$, leading to more efficient gauge field production at the peak wavenumber in high-$T_{\rm re}$ scenarios compared to low-$T_{\rm re}$ ones.

6.4 PBH formation

Primordial black holes (PBHs) are assumed to have formed in the early universe due to the collapse of overdense regions as they re-entered the Hubble horizon. Unlike black holes formed through stellar evolution, PBHs originate from the dynamics of the early universe itself. During the post-inflationary era, sufficiently large curvature perturbations can re-enter the horizon and collapse under their own gravity to form PBHs. The collapse is only efficient if the local density contrast, defined as $\delta = \delta\rho/\rho$, exceeds a critical threshold δ_c. Numerical simulations indicate that in a radiation-dominated background, the threshold value is approximately $\delta_c \sim 0.4$ [174, 175]. If the local perturbation satisfies $\delta \geq \delta_c$, the region can undergo gravitational collapse to form a PBH. In our scenario, we find that the sawtooth-type magnetogenesis model leads to an enhanced magnetic field energy density peaked at the comoving scale $k \simeq k_{\rm re}$. The associated curvature perturbation spectrum reaches a peak amplitude of $\mathcal{P}_\zeta(k \simeq k_{\rm re}) \simeq \mathcal{O}(0.1)$, which is sufficient to trigger PBH formation through gravitational collapse. The mass of the PBHs are typically equal to the horizon mass at the time of horizon re-entry of the corresponding mode, where the horizon mass at the formation time is expressed as $M_H = \frac{4\pi}{3}\rho(t_{\rm h})H^{-3}(t_{\rm h})$, where $t_{\rm h}$ is the cosmic time when the PBHs are formed and $\rho(t_{\rm h})$ is the total background energy density during the formation time. Now, if we consider the efficiency factor accounting for the collapse dynamics, then we can write the PBH mass as $M_{\rm pbh} \simeq 4\pi\gamma_c M_{\rm P}^2 H^{-1}(t_{\rm h})$. We recall that $M_{\rm P} = 1/\sqrt{8\pi G}$ is the reduced Planck mass. Here, $H(t_{\rm h})$ is the Hubble constant during the formation of the PBHs.

The PBH abundance is exponentially sensitive to the peak amplitude of the induced curvature power spectrum, whereas the mass of the PBHs typically depends on the peak frequency of the curvature power spectrum. The fractional energy density of the produced PBHs at the time of formation is quantified as $\beta_{\rm pbh}(M_{\rm pbh}) = \rho_{\rm pbh}(t_{\rm h})/\rho(t_{\rm h})$, where $\rho_{\rm pbh}(t_{\rm h})$ is the initial energy density of the PBHs at the time of formation. Thus, we can express $\beta_{\rm pbh}(M_{\rm pbh})$ as [142–149, 167, 183, 190–197]

$$\beta_{\rm pbh}(M_{\rm pbh}) = \int_{\delta_c}^{\infty} {\rm d}\delta\, P(\delta). \tag{6.21}$$

Here, $P(\delta)$ is the probability distribution of the density contrast δ.

Here $P(\delta)$ is the probability distribution of the density contrast originated from the magnetic field. We recall that the density contrast is defined as $\delta = \delta\rho_{\rm B}/\rho_{\rm rad} \propto B^2$, so the δ is related to the energy density of the electromagnetic field, which depends quadratically on the underlying Gaussian magnetic field and electric field. So we can say that when the density contrast associated with the electromagnetic field is intrinsically non-Gaussian in nature [382]. To capture the full non-Gaussian nature of the distribution function, one can use the MCMC analysis as discussed in [162], but in our computation, we consider a generalized hyperbolic (GH) distribution function, which can be parameterized as

$$P_{\rm NG}(x) = {\rm C_N}\, \exp\left[-\frac{3}{2}\sqrt{1+\frac{x^2}{b^2}}\right], \tag{6.22}$$

where $\rm C_N$ and b are two free parameters, which are fixed by imposing

$$\int_{-\infty}^{\infty} P_{\rm NG}(x)\,{\rm d}x = 1, \qquad \int_{-\infty}^{\infty} x^2 P_{\rm NG}(x)\,{\rm d}x = \sigma_B^2. \tag{6.23}$$

Using these relations, one finds $C = 2.13\sigma_B^{-1}$ and $b = 0.84\,\sigma_B$ [163], where σ_B is the standard deviation of the density fluctuations on the scale corresponding to the mass M. The variance of the smoothed density contrast on the scale $\rm R_l = 1/\mathit{k}$ is

benchmark	BP1	BP2	BP3	BP4	BP5	BP6
$T_{\rm re}$(GeV)	1	1	10^3	10^3	10^5	10^5
$n_{\rm B}$	2.28	2.285	2.5	2.505	2.655	2.66
$B_{0,1\ \rm Mpc}$	7.3×10^{-14}	5.8×10^{-14}	1.4×10^{-18}	1.1×10^{-18}	3.7×10^{-22}	2.8×10^{-22}
$f_{\rm PBH}$	7.5×10^{-4}	5.9×10^{-10}	1.1×10^{-3}	1.4×10^{-11}	1.5×10^{-4}	1.3×10^{-12}

Table 6.2: In the above table, we list representative benchmark points for PBH production, along with the corresponding present-day magnetic field strength at the 1 Mpc scale in Gauss units and the maximum value of $f_{\rm PBH}$ at its peak. To obtain this, we have consider $w_{\rm re}=0$ and the inflationary energy scale $H_{\rm e}\simeq 10^{-5}M_{\rm P}$.

$$\sigma_B^2=\frac{16}{81}\int\frac{\rm dq}{q}(q{\rm R_l})^4W^2{\rm R_l})P_\zeta(q), \tag{6.24}$$

where we commonly used window function $W(k'R)$ as a Gaussian, i.e., $W(k'{\rm R_l})=\exp(-k^2{\rm R_l^2}/2)$ and utilizing this function we get

$$\sigma_B^2({\rm M})=\frac{16}{81}\int_0^\infty\frac{\rm dq}{q}(q{\rm R_l})^4e^{-q^2{\rm R_l^2}}P_\zeta(q). \tag{6.25}$$

Once the behavior of the induced curvature perturbation P_ζ is determined, the initial fractional energy density of PBHs at the time of formation can be computed using Eq. (6.21). We emphasize that the resulting PBH abundance is highly sensitive both to the choice of the probability distribution function $P_{\rm NG}(x)$ and to the critical density contrast δ_c.

It is important to note that the presence of a magnetic field can modify the conventional collapse criterion due to the additional magnetic pressure and its complex, nonlinear interaction with the background plasma. Determining the exact value of the collapse threshold in the presence of magnetic fields would require incorporating all relevant contributions to the collapse equations and solving the full set of relativistic magnetohydrodynamic equations, which is beyond the scope of the present work. Nevertheless, an approximate estimate of δ_c in the presence of magnetic anisotropies has recently been obtained in Ref. [163].

The argument proceeds as follows. Within an isotropic approximation, the total pressure and energy density in the presence of a magnetic field are given by $p_{tot}=p_{\rm rad}+p_B$ and $\rho_{\rm tot}=\rho_{\rm rad}+\rho_B$, respectively, where $r_B=\rho_B/\rho_{\rm rad}$. The corresponding effective equation of state can then be written as $w_{eff}=p_{\rm tot}/\rho_{\rm tot}=c_s^2+\alpha r_B$, where the coefficient α encodes the dynamical evolution of the magnetic field on the relevant length scales. In Ref. [163], the authors analytically estimated $\alpha\approx 2$, although this value is expected to be sensitive to nonlinear magnetohydrodynamic effects.

In view of these theoretical uncertainties, we do not fix a single value of δ_c. Instead, we explore a representative range $\delta_c\in[0.45,\,0.60]$ in our subsequent analysis and examine how variations in δ_c affect both the PBH mass spectrum and the resulting abundance.

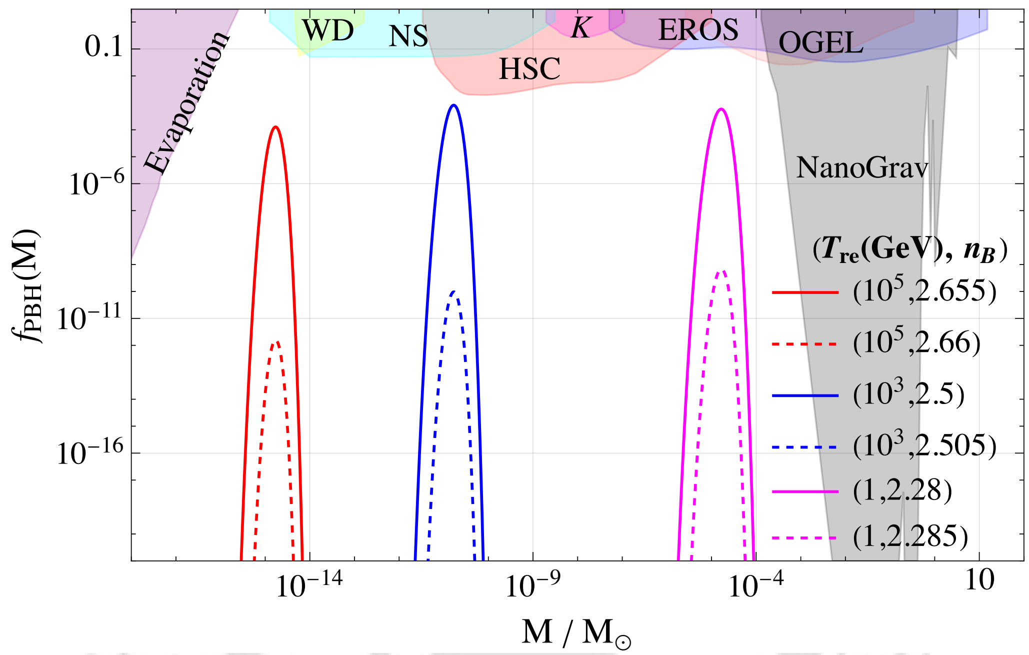

Figure 6.3: In the figure, we show the primordial black hole (PBH) dark matter fraction as a function of PBH mass, expressed in solar-mass units. We consider three fixed reheating temperatures, indicated by different colors. For each temperature, the solid and dashed curves correspond to two different choices of the magnetic spectral index. In all cases, we adopt a critical density contrast of $\delta_c = 0.45$. Table 6.2 lists the corresponding present-day magnetic field strength at the $1\,\mathrm{Mpc}^{-1}$ scale, as well as the peak value of the PBH dark matter fraction.

Now, once we know the behaviour of $P_\zeta(q)$ near the peak, Eq. (2.130) allows us to compute the associated variance of the distribution and thereby determine the initial abundance of PBHs. The mass of the PBHs formed at horizon entry can be expressed as a function of the comoving wavenumber k as

$$M_{\rm pbh} \simeq 1.57 \times 10^{12}\, M_\odot \left(\frac{\gamma_c}{0.2}\right)\left(\frac{106.75}{g_{*,k}(T)}\right)^{1/6} \times \left(\frac{g_{*,\rm eq}(T_0)}{3.81}\right)^{2/3}\left(\frac{1\mathrm{Mpc}^{-1}}{k}\right)^2 . \tag{6.26}$$

Here $g_{*,k}$ is the effective degree of freedom at the time of formation of the PBHs. In our scenarios, the peak of the induced curvature power spectrum is situated at $k \simeq k_{\rm re}$. We recall that $k_{\rm re}$ is the lowest comoving wavenumber that is able to re-enter the horizon at the end of reheating, which mainly depends on the reheating temperature $T_{\rm re}$ through Eq. (2.70). Utilizing the relation, $k_{\rm re} = 3.9\times 10^8\,(T_{\rm re}/1\,\mathrm{GeV})\ \mathrm{Mpc}^{-1}$, if one assumes the reheating temperature being lower than $T_{\rm re} < 10^7\,\mathrm{GeV}$, we can generate PBHs with masses even larger than $M_{\rm pbh} > 10^{15}\,\mathrm{g}$, implying that such PBHs can survive until today and contribute as a cold dark matter (CDM) candidate.

We now define an observable quantity: the present-day mass fraction of dark matter in PBHs as $f_{\rm PBH}(M_{\rm pbh}) = \Omega_{\rm pbh}(M_{\rm pbh})/\Omega_{\rm c}$. Here, $\Omega_{\rm c} \simeq 0.27$ refers to the present-day energy density fraction of cold dark matter in the universe, normalized by the critical density.

After their formation, PBHs behave as non-relativistic matter, meaning their energy density

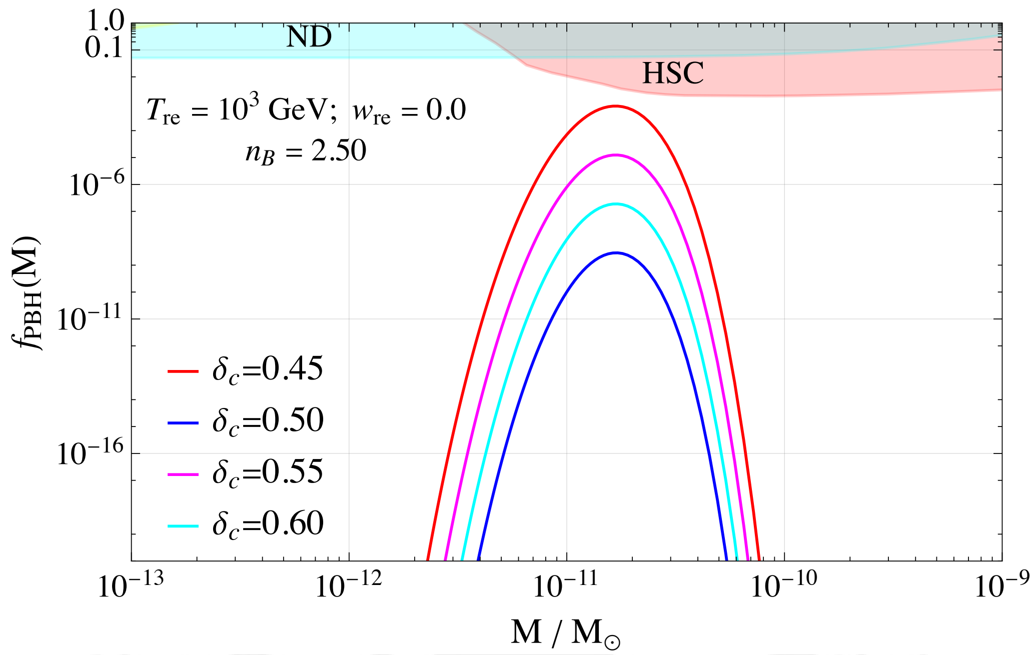

Figure 6.4: In the figure, we plot the primordial black hole (PBH) dark matter fraction as a function of PBH mass in solar-mass units. We illustrate the dependence of the PBH abundance on the threshold value of the density contrast, δ_c, for a fixed reheating parameter with $T_{\rm re} = 10^3$ GeV and $w_{\rm re} = 0$. For all curves, we adopt a magnetic spectral index of $n_{\rm B} = 2.50$.

redshifts as $\rho_{\rm pbh} \propto a^{-3}$, whereas the background radiation energy density redshifts as a^{-4}. As a result, the PBH energy density grows relative to radiation after formation. In our scenarios, since PBHs are produced during the radiation-dominated era, the present-day PBH abundance as a cold dark matter component can be expressed as [146, 147]

$$f_{\rm PBH}(M_{\rm pbh}) = \left(\frac{\gamma_c}{0.2}\right)^{3/2} \left(\frac{\beta_{\rm pbh}(M_{\rm pbh})}{1.46 \times 10^{-8}}\right) \times \left(\frac{g_{*,k}}{g_{*,\rm eq}}\right)^{-1/4} \left(\frac{M_{\rm pbh}}{M_\odot}\right)^{-1/2}. \tag{6.27}$$

Here $g_{*,k} \simeq 106.75$ and $g_{*,\rm eq} = 3.36$ are the relativistic degrees of freedom at the time of PBH formation and matter-radiation equality.

In Tab. 6.2, we present a set of benchmark parameters used to compute the PBH fraction as a dark matter candidate predicted by this model. We consider three distinct values of the reheating temperature, $T_{\rm re} = 1$, 10^3, and 10^5 GeV, assuming a matter-like background during the reheating era. To study the dependence on the magnetic parameters, we adopt two different values of the magnetic spectral index, $n_{\rm B}$, and examine their impact on the present-day PBH fraction.

For each parameter set, we also compute the corresponding present-day magnetic field strength at the 1 Mpc scale. Our results show that the PBH fraction is highly sensitive to the magnetic spectral index, while the present-day magnetic field varies more mildly. This strong sensitivity arises because the initial PBH abundance depends exponentially on the magnetic parameters (as seen in Gaussian-type PDFs); thus, even a small change in $n_{\rm B}$ leads to a substantial variation in the resulting PBH abundance.

In Fig. 6.3, we plot the PBH fractional abundance, $f_{\rm PBH}(M_{\rm pbh})$, as a function of the PBH mass $M_{\rm pbh}$ for the benchmark points listed in Tab. 6.2. For a fixed reheating temperature, the present-day PBH abundance is extremely sensitive to the magnetic spectral index $n_{\rm B}$. We find that PBHs can be produced within specific mass windows that allow them to account for the entire cold dark matter (CDM) abundance. In particular, this occurs for a narrow range of reheating temperatures, 3×10^4 GeV $\lesssim T_{\rm re} \lesssim 10^5$ GeV. As an explicit example, for $T_{\rm re} = 2 \times 10^5\,$GeV and $n_{\rm B} = 2.674$, we obtain $f_{\rm PBH} \simeq 1$ for a corresponding PBH mass $M_{\rm pbh} \simeq 4 \times 10^{-16}\,M_\odot$. For this specific set of parameters, the present-day magnetic field strength evaluated at the 1 Mpc scale is $B_0(1\,{\rm Mpc}) \simeq 1.26 \times 10^{-22}\,$G.

For other reheating temperatures, i.e., $T_{\rm re} < 10^4\,$GeV, although PBHs can be produced over a wider mass range, they typically constitute only a fraction of the observed dark matter abundance. Nevertheless, these scenarios remain consistent with the present-day magnetic field strength inferred from observations. In particular, we find that within the mass range $10^{-12}\,M_\odot \leq M_{\rm pbh} \leq 10^{-1}\,M_\odot$, PBHs can contribute a subdominant fraction of the present-day dark matter abundance while still successfully explaining the observed strength of cosmic magnetic fields.

In the right panel of Fig. 6.4, we show $f_{\rm PBH}$ as a function of the PBH mass for a representative set of reheating and magnetogenesis parameters, where we choose $T_{\rm re} = 10^3$ GeV, $w_{\rm re} = 0$, and a magnetic spectral index $n_{\rm B} = 2.50$ on super-horizon scales. Here we examine the dependence of the PBH abundance on the collapse threshold δ_c. Since PBHs sourced by magnetic fields experience an additional magnetic pressure compared to inflationary curvature perturbations, the effective threshold may differ. However, because the exact value of δ_c for magnetically induced perturbations is not known, we consider four representative values within the range suggested in the literature.

For a fixed reheating scenario, the peak of the magnetic power spectrum—and the associated curvature perturbation amplitude—remains unchanged, so adopting a constant δ_c is justified. Moreover, within the parameter region relevant for simultaneously explaining the present-day magnetic field strength and producing PBHs as a dark matter candidate, δ_c does not vary significantly [163].

6.5 GWs from the Magnetic Field

In the magnetogenesis scenario considered here, a significant magnetic field is generated at small scales near $k \simeq k_{\rm re}$, which can lead to PBH formation. Due to the anisotropies sourced by the magnetic field during the radiation-dominated era, we also expect a substantial production of secondary gravitational waves (SGWs).

In this class of magnetogenesis models, the electromagnetic field can be generated both during inflation and during reheating, with its maximum energy density reached at the end of reheating. Consequently, the largest magnetic-field-induced anisotropies are expected just after the end of reheating. Beyond this point, both the magnetic field and the background radiation energy density dilute as a^{-4}. As shown earlier, for $w_{\rm re} = 0$ (matter-like evolution during reheating), although there is continuous EM field production, the generation of SGWs from the EM field is suppressed compared to that occurring during the radiation-dominated era (see [118] for details).

Gravitational waves (GWs) can also be produced from vacuum fluctuations of spacetime during inflation, when the corresponding modes exit the horizon. This type of tensor fluctuation generation is typically referred to as the primary production of GWs (PGWs), which has a significant impact on large scales. To make this work self-contained, we briefly discuss both PGWs and SGWs in this section. In the presence of the electromagnetic field, the anisotropic stress component of the energy-momentum tensor can source the tensor perturbations, denoted as $h_{ij}(\mathbf{x}, \eta)$. The equation of motion (EoM) of the tensor perturbation is governed by [117, 201, 220–222, 229, 232–234, 384]

$$h''_{ij}(\mathbf{x}, \eta) + 2\mathcal{H}h'_{ij}(\mathbf{x}, \eta) - \nabla^2 h_{ij}(\mathbf{x}, \eta) = \frac{2}{M_{\rm P}^2}\mathcal{P}_{ij}^{lm}T_{lm}, \tag{6.28}$$

where h_{ij} is a traceless tensor, satisfying $\partial^i h_{ij} = h^i_i = 0$. The quantity $\mathcal{H} = a'(\eta)/a(\eta)$ represents the conformal Hubble parameter. The term $\mathcal{P}_{ij}^{lm}$ is the transverse traceless projector, given by $\mathcal{P}_{ij}^{lm} = P_i^l P_j^m - P_{ij}P^{lm}/2$, where $P_{ij} = \delta_{ij} - \partial_i\partial_j/\Delta$. The term T_{lm} represents the spatial part of the energy-momentum tensor of the gauge field.

We can decompose the tensor perturbation $h_{ij}(\mathbf{x}, \eta)$ in terms of their Fourier modes $h^\lambda_{\mathbf{k}}(\eta)$ as

$$h_{ij}(\mathbf{x}, \eta) = \sum_{\lambda=\pm}\int \frac{{\rm d}^3\mathbf{k}}{(2\pi)^3} e^\lambda_{ij}(\mathbf{k}) h^\lambda_{\mathbf{k}}(\eta)\, e^{i\mathbf{k}\cdot\mathbf{x}}, \tag{6.29}$$

where $e^\lambda_{ij}(\mathbf{k})$ is the polarization tensor corresponding to the mode with wave vector $\mathbf{k}$. Here λ denotes the polarization state of the GW, which mainly depends on the nature of the source. In this magnetogeneis model, we have generated a non-helical magnetic field, where both polarization modes are equally amplified from the vacuum, so both polarization states of the produced GWs will have the same contribution. In Fourier space, the equation of motion of the tensor fluctuations is [229, 233]

$$h^{\lambda\prime\prime}_{\mathbf{k}} + 2\mathcal{H}h^{\lambda\prime}_{\mathbf{k}} + k^2 h^\lambda_{\mathbf{k}} = \mathcal{S}(\mathbf{k}, \eta). \tag{6.30}$$

As we have already discussed, as the magnetic field gets its maximum amplified at the end of reheating, the maximum produced anisotropies should be after completion of the reheating. After reheating electric field will decay immediately due to the high electrical conductivity, and the only contribution comes from the magnetic field part. During radiation dominated era, the source term $\mathcal{S}(\eta)$ can be written as [221, 229, 231]

$$\mathcal{S}(\mathbf{k},\eta) = -\frac{2\,e^{ij}_{\lambda}(\mathbf{k})}{M_{\mathrm{P}}^2}\int \frac{\mathrm{d}^3\mathbf{q}}{(2\pi)^3} B_i(\mathbf{q},\eta)B_j(\mathbf{k}-\mathbf{q},\eta). \tag{6.31}$$

Now we can define the two-point correlation function of the tensor fluctuation associated with the tensor power spectrum as

$$P_{\mathrm{T}}(k,\eta) = \sum_{\lambda=\pm}\frac{k^3}{2\pi^2}\langle h^{\lambda}_{\mathbf{k}}(\eta)h^{\lambda *}_{\mathbf{k}'}(\eta)\rangle\delta^{(3)}(\mathbf{k}-\mathbf{k}'). \tag{6.32}$$

Note that in these scenarios, both primary and secondary tensor fluctuations are linearly polarized, which means both polarization modes have the same contribution.

Production of SGWs: After reheating, there is no further production of the magnetic field, as the gauge field restores its conformal nature, and due to the high electrical conductivity, the electric field decays immediately from the universe. So during a radiation-dominated era, the only existing field is the magnetic field, which is responsible for the generation of the secondary gravitational waves. However, the source due to the magnetic field only effectively produces the SGWs up to the neutrino decoupling era, i.e., $\eta = \eta_\nu$, because after neutrino decoupling, they freely travel with very high kinetic energy and consequently dilute the anisotropic stress originated due to the magnetic field [349, 350], and suppress SGW production. Therefore, the production of the secondary gravitational waves due to the magnetic field at the time of neutrino decoupling is [117, 118, 229]

$$\begin{aligned} P_{\mathrm{T}}^{\mathrm{sec}}(k,\eta_\nu) = &\frac{2}{M_{\mathrm{P}}^4 k^4}\times\left(\int_{x_{\mathrm{re}}}^{x_\nu}\mathrm{dx}_1\frac{\mathcal{G}_{\mathrm{k}}(\mathrm{x}_\nu,\mathrm{x}_1)}{\mathrm{a}^2(\mathrm{x}_1)}\right)^2 \\ &\times\int_0^\infty\frac{\mathrm{dq}}{q}\int_{-1}^{1}\mathrm{d}\gamma\frac{\mathcal{F}(\gamma,\mu)\tilde{\mathcal{P}}_{\mathrm{B}}(\mathrm{q},\eta_{\mathrm{re}})\tilde{\mathcal{P}}_{\mathrm{B}}(|\mathbf{k}-\mathbf{q}|,\eta_{\mathrm{re}})}{\left[1+\left(\frac{\mathrm{q}}{\mathrm{k}}\right)^2-2\gamma\frac{\mathrm{q}}{\mathrm{k}}\right]^{3/2}} \end{aligned} \tag{6.33}$$

where we define the Green's function during the radiation-dominated era as [229]

$$\mathcal{G}_k(x_\nu,x_1) = \theta(\eta_\nu-\eta_1)\frac{\eta_1}{\eta_\nu}\sin[k(\eta_1-\eta_\nu)] \tag{6.34}$$

Here $\tilde{\mathcal{P}}_{\mathrm{B}}(k,\eta_{\mathrm{re}}) = a^4(\eta)\mathcal{P}_{\mathrm{B}}(k,\eta_{\mathrm{re}})$ is the comoving magnetic power spectrum during the radiation-dominated era. Now we can write the comoving magnetic power spectrum during radiation radiation-dominant era as [118]

$$\tilde{\mathcal{P}}_{\mathrm{B}}(k,\eta_{\mathrm{re}}) = \frac{k^4|\beta|^2}{8\pi}\left(\frac{k}{k_{\mathrm{e}}}\right)^{-2(\alpha+n+1)}\left(\frac{k}{k_{\mathrm{re}}}\right)J^2_{\alpha+1/2}\left(\frac{k}{k_{\mathrm{re}}}\right) \tag{6.35}$$

Here we deined we define $|\beta|^2 = 2^{2\alpha+1}\Gamma^2(\alpha+1/2)q^1_{n_\mathrm{B}}(n)$, where $q^1_{n_\mathrm{B}}$ is defined in Eq.(6.4a). Now utilizing this in the above Eq.(6.35), we have found that the tensor power spectrum associated with the magnetic field at the time of the neutrino decoupling era as [118]

$$P_\mathrm{T}^{\mathrm{sec}}(k,\eta_\nu) = \frac{k^4|\mathcal{B}|^4}{32\pi^2 M_\mathrm{P}^4}\left(\frac{k}{k_\mathrm{e}}\right)^{-4(n+\alpha+1)} x_{\mathrm{re}}^2\left(\int_{x_{\mathrm{re}}}^{x_\nu} dx_1 \frac{\mathcal{G}_k(x_\nu,x_1)}{a^2(x_1)}\right)^2\int_{u_{\mathrm{min}}}^{u_{\mathrm{max}}}\frac{du}{u}$$
$$\times\int_{-1}^{1} d\mu \frac{f(\mu,\gamma)}{[1+u^2-2u\mu]^{3/2}}u^{3-2(n+\alpha)}(|1-u|)^{3-2(n+\alpha)}\mathrm{J}^2_{\alpha+1/2}(ux_{\mathrm{re}})\mathrm{J}^2_{\alpha+1/2}(|1-u|x_{\mathrm{re}}) \tag{6.36}$$

where we defined $u = q/k$ as a new dimensionless variable$u_{\mathrm{min}} = k_*/k$ and $u_{\mathrm{max}} = k_\mathrm{e}/k$. Here $\mathcal{F}(\gamma,\mu) = (1+\gamma^2)(1+\mu^2)$, with $\gamma = \hat{\mathbf{k}}\cdot\hat{\mathbf{q}}$ and $\mu = \widehat{\mathbf{k}-\mathbf{q}}\cdot\hat{\mathbf{k}}$ [222]. To solve the above integral, we have to perform a numerical integration of the above for the entire range of u (for details, please see [118]).

Present-day GW Spectral Energy Density $\Omega_{\mathrm{GW}}h^2$: Gravitational waves (GWs) weakly interact with matter and can freely propagate without losing their original nature after being produced during a radiation-dominated era. The GW energy density, which scales as $\rho_{\mathrm{GW}} \propto a^{-4}$, can be normalized by the total energy density at the production time, $\rho_c(\eta)$. Presently, this density parameter is given by

$$\Omega_{\mathrm{GW}}(k,\eta) = \frac{\rho_{\mathrm{GW}}(k,\eta)}{\rho_c(\eta)} = \frac{1}{12}\frac{k^2 P_\mathrm{T}(k,\eta)}{a^2(\eta)H^2(\eta)}, \tag{6.37}$$

where $\rho_c(\eta) = 3H^2(\eta)M_\mathrm{P}^2$, with the reduced Planck mass $M_\mathrm{P} \approx 2.43\times 10^{18}$ GeV.

The GW energy density follows the radiation scaling behavior, making modes within the Hubble radius near radiation-matter equality particularly relevant. The present-day energy density parameter $\Omega_{\mathrm{GW}}(k)h^2$ is then given by

$$\Omega_{\mathrm{GW}}h^2(k) \simeq \left(\frac{g_{*,0}}{g_{*,\mathrm{eq}}}\right)^{1/3}\Omega_r h^2\Omega_{\mathrm{GW}}(k,\eta), \tag{6.38}$$

where $\Omega_r h^2 = 4.3\times 10^{-5}$, $g_{*,\mathrm{eq}} \simeq g_{*,0} = 3.35$, and denote relativistic degrees of freedom at equality and today, respectively.

The spectral energy density of gravitational waves (GWs) originating from magnetic fields and from vacuum fluctuations can be distinguished by their distinct characteristics. Depending on whether a given wavenumber is super-horizon or sub-horizon at the end of reheating, the resulting spectral shape will be modified accordingly.

The behavior of primary GWs in a non-instantaneous reheating scenario is well understood. In our case, we consider a matter-like evolution after the end of inflation, with $w_{\mathrm{re}} = 0$. For modes that re-enter the horizon before the end of reheating, the GW amplitude is diluted due to the background expansion, resulting in a red-tilted spectrum with $\Omega^{\mathrm{pri}}_{\mathrm{GW}}(f > f_{\mathrm{re}}) \propto f^{-2}$.

Here, $f = 2\pi/k$. On the other hand, modes that remain well outside the horizon at the end of reheating exhibit a scale-invariant spectrum, since the tensor power spectrum generated during inflation is itself scale-invariant, originating from vacuum fluctuations in a de Sitter background. Therefore, the PGW spectrum can be expressed as [117–119, 207, 229]

$$\Omega_{\rm GW}^{\rm pri}h^2(f) \simeq \frac{\Omega_{\rm r}h^2}{6}\frac{H_{\rm e}^2}{M_{\rm P}^2} \times \begin{cases} 1 & f < f_{\rm re} \\ \mathcal{D}\left(\frac{f}{f_{\rm re}}\right)^{-2} & f_{\rm re} < f < f_{\rm end} \end{cases} \tag{6.39}$$

where $\mathcal{D} \simeq 6/\pi^{1/2} \simeq \mathcal{O}(1)$ [117, 229].

Similarly, the SGWs sourced by the magnetic field exhibit a broken power-law spectrum, reflecting the broken power-law nature of the magnetic field itself. In analogy to the PGW case, the spectral behavior of SGWs generated by the magnetic field can be expressed as [118]

$$\begin{aligned}\Omega_{\rm GW}^{\rm sec}h^2(f) \simeq& \frac{\Omega_{\rm r}h^2}{6}\left(\frac{H_{\rm e}}{M_{\rm P}}\right)^4\left(\frac{a_{\rm e}}{a_{\rm re}}\right)^2\mathcal{I}^2(\eta_{\rm re},\eta_\nu) \\ &\times \begin{cases} \mathcal{A}_1\left(\frac{f_{\rm end}}{f_{\rm re}}\right)^{4(\alpha+1)}\left(\frac{f}{f_{\rm end}}\right)^{2n_{\rm B}} & f_{\rm cmb} < f < f_{\rm re} \\ \mathcal{A}_2\left(\frac{f_{\rm end}}{f_{\rm re}}\right)^{2n_{\rm B,2}}\left(\frac{f}{f_{\rm end}}\right)^{-2n_{\rm B,2}} & f_{\rm re} < f < f_{\rm end} \end{cases}\end{aligned} \tag{6.40}$$

Here we define $n_{\rm B,2} = 2(\alpha+1) - n_{\rm B}$ with

$$\mathcal{A}_1 = \frac{|\mathcal{B}|^4 2^{-4(n+1/2)}}{144\,\pi^2(4-2n)\Gamma^4(\alpha+1/2)}, \tag{6.41a}$$

$$\mathcal{A}_2 = \frac{|\mathcal{B}|^4}{360\,\pi^4}\frac{1}{2(n+\alpha)-2}, \tag{6.41b}$$

Here, $\mathcal{I}(\eta_\nu, \eta_{\rm re})$ is defined as [229]

$$\mathcal{I}(\eta_{\rm re},\eta_\nu) = \int_{x_{\rm re}}^{x_\nu} dx_1 \frac{\sin(x_1 - x_\nu)}{x_1}. \tag{6.42}$$

It is evident that the GW spectral index is simply twice the magnetic spectral index when the GWs are sourced by the magnetic field. This follows from the relation $\Omega_{\rm GW}^{\rm sec}(k) \propto \tilde{\mathcal{P}}_{\rm B}^2(k)$, with the dominant production occurring during the radiation-dominated era. The only additional scale dependence arises logarithmically from the factor $\mathcal{I}^2(\eta_\nu, \eta_{\rm re})$, since both the background and source energy densities dilute as a^{-4}. In Fig. 6.5, we present the present-day spectral energy density $\Omega_{\rm GW}h^2(f)$ of GWs as a function of comoving frequency f (Hz) for six benchmark points (BPs) listed in Tab. 6.2. For BP1 (red solid line) and BP2 (red dashed line), the GW spectra exhibit nearly identical amplitudes and shapes. This similarity arises because, for a fixed reheating temperature, a small change in the magnetic spectral index does not significantly alter the magnetic field strength, and consequently, the corresponding GW amplitude remains almost unchanged. However, as shown in Fig. 6.3, the PBH abundance is highly sensitive to the magnetic spectral index. A similar trend is observed for the other benchmark points.

In Fig. 6.5, the three different colors correspond to three distinct reheating temperatures,

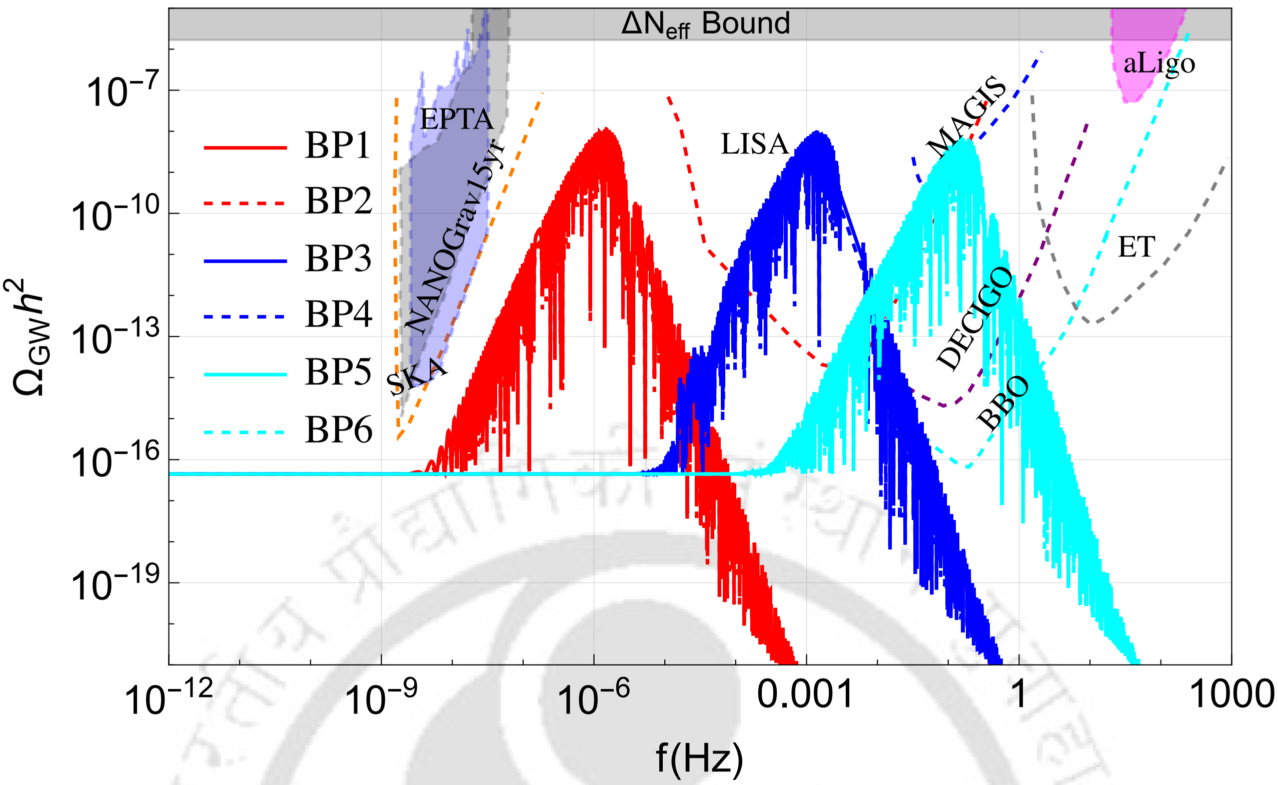

Figure 6.5: In this figure, we present the present-day spectral energy density of GWs, $\Omega_{\rm GW}h^2(f)$ sourced by the magnetic field, as a function of the observable frequency f (Hz) for six benchmark points (BPs) listed in Tab. 6.2.

$T_{\rm re} = 1$ GeV (red), $T_{\rm re} = 10^3$ GeV (blue), and $T_{\rm re} = 10^5$ GeV (cyan), as listed in Tab. 6.2. Since the GW spectral energy density scales as the fourth power of the magnetic field amplitude, $\Omega_{\rm GW} \propto B^4$, a small variation in the magnetic spectral index $n_{\rm B}$ does not lead to a significant change in the magnetic field strength (see Eq. (6.41a)). As discussed earlier, the magnetic field amplitude is sensitive to the magnetogenesis parameter n; however, small variations in its value do not significantly modify the resulting magnetic field strength (see Tab. 6.2). Consequently, the corresponding change in the GW spectrum, which depends on the magnetic field amplitude, is relatively mild, in contrast to the PBH abundance, which exhibits a much stronger sensitivity, as also evident from Tab. 6.2.

As an explicit example, for $T_{\rm re} = 1\,$GeV and $n_{\rm B} = 2.28$, we find that the GW amplitude at the peak frequency is $\Omega_{\rm GW}h^2(f_{\rm peak}) \simeq 2.05 \times 10^{-9}$, whereas for a slightly larger value $n_{\rm B} = 2.285$, the peak amplitude decreases to $\Omega_{\rm GW}h^2(f_{\rm peak}) \simeq 9.92 \times 10^{-10}$. In contrast, for the same set of parameters, the present-day dark matter abundance shows a dramatic change: $f_{\rm PBH}(f_{\rm peak}) \simeq 7.56 \times 10^{-4}$ for $n_{\rm B} = 2.28$, while for $n_{\rm B} = 2.285$ it is reduced to $f_{\rm PBH}(f_{\rm peak}) \simeq 5.9 \times 10^{-10}$.

The peak frequency of the induced GW spectrum depends sensitively on the reheating temperature, as the peak of the magnetic power spectrum is reheating-temperature dependent. Lower reheating temperatures correspond to a larger horizon size at the end of reheating, which in turn shifts the GW peak toward lower frequencies. Thus, decreasing $T_{\rm re}$ moves the peak of the

GW spectrum to smaller frequency bands. For the benchmark parameter sets considered here, the peak amplitudes of the GW spectrum remain nearly identical. This is because achieving PBH formation requires a comparable magnetic energy density perturbation, typically $\delta\rho_B/\rho \simeq 0.1$, across the parameter space. However, the initial PBH abundance depends exponentially on the peak amplitude of the magnetically induced curvature perturbations, making the PBH fraction highly sensitive to even a small shift in $n_{\rm B}$.

Therefore, if PBHs are sourced by primordial magnetic fields, an associated GW background is always generated alongside them. Importantly, the spectral shape of these magnetically induced GWs [118,221,229,231] is qualitatively different from that of GWs produced by curvature perturbations, offering a distinct observational signature [183, 209, 384].

Comparison with scalar-induced GWs: In this scenario, primordial magnetic fields source gravitational waves (GWs) through two distinct mechanisms. First, the anisotropic stress of the magnetic field directly sources tensor perturbations. Second, the curvature perturbations induced by the magnetic field act as a secondary source for tensor modes, giving rise to scalar-induced gravitational waves (SIGWs). Since these two mechanisms are physically distinct, the resulting GW spectra exhibit different behaviors across frequency ranges.

In this work, we have focused so far on the magnetic field-induced GW production. The scalar perturbation should also induce the gravitational wave. Due to its secondary nature with respect to the magnetic spectrum, its contribution to GW is expected to be subdominant. For comparison, however, we provide an analytical estimate of the scalar-induced GWs, following Refs. [215, 385]. A precise determination of the GW spectrum over the full frequency range, including its amplitude and detailed spectral features, requires a full numerical solution of the tensor perturbation equations, as performed in Refs. [142, 167, 183, 190–197, 384].

For our present purpose of comparison, we restrict our to the spectral range $k_{\rm SB,1} < k < k_{\rm SB,2}$, where the secondary curvature perturbations dominate over the primary one. Within this window, the curvature power spectrum can be parameterized as [215, 385]

$$P_\zeta(k) \simeq \mathcal{A}_\zeta \times \begin{cases} (k/k_{\rm re})^{n_{\rm IR}} & k < k_{\rm re} \\ (k/k_{\rm re})^{-n_{\rm UV}} & k > k_{\rm re} \end{cases} \tag{6.43}$$

Here, $n_{\rm IR} = 2n_{\rm B}$ characterizes the infrared spectral tilt near the peak ($k < k_{\rm re}$), while $n_{\rm UV} = 2(\alpha+1) - n_{\rm B}$ denotes the ultraviolet spectral tilt ($k > k_{\rm re}$). The peak amplitude $\mathcal{A}_\zeta$ is defined in Eq. (6.12).

We focus on the region of parameter space in which the model can simultaneously explain the observed large-scale magnetic field strength and generate a sufficient abundance of primordial black holes (PBHs) in the mass range compatible with cold dark matter. In this regime, we consistently find $n_{\rm IR} > 3/2$ and $n_{\rm UV} < 4$. As an illustrative example, for the benchmark point BP1 with $n_{\rm B} = 2.28$, $w_{\rm re} = 0$, and $T_{\rm re} = 1\,{\rm GeV}$, we obtain $n_{\rm IR} = 4.56$ and $n_{\rm UV} = 3.058$. For this class of parameters, the GW spectrum sourced by curvature perturbations can be written as [215, 385]

$$\Omega_{\rm GW}^{\rm cur}h^2 \propto \mathcal{A}_\zeta^2 \times \begin{cases} (f/f_{\rm re})^3 & f < f_{\rm re} \\ (f/f_{\rm re})^{-4(\alpha+1)+2n_{\rm B}} & f > f_{\rm re} \end{cases} \tag{6.44}$$

Here, $\Omega_{\rm GW}^{\rm cur}h^2$ denotes the present-day spectral energy density of gravitational waves sourced by the curvature power spectrum.

Comparing Eq.(6.40) with Eq.(6.44), we find that for modes outside the horizon at the end of reheating ($f < f_{\rm re}$), the GW spectrum sourced by the magnetic field scales as $\Omega_{\rm GW}^{\rm sec}(f) \propto f^{2n_{\rm B}}$, whereas the scalar-induced GW spectrum behaves as $\Omega_{\rm GW}^{\rm cur} \propto f^3$. For modes inside the horizon ($f > f_{\rm re}$), both spectra follow the same scaling, $\Omega_{\rm GW}^{\rm sec} \propto f^{-4(\alpha+1)+2n_{\rm B}}$. The peak amplitude of the GW spectrum originating from the magnetic field is larger than the contribution arising from scalar perturbations. Near the peak, the ratio of the peak amplitudes due to the magnetic field and the scalar perturbations can be estimated as $\Omega_{\rm GW}^{\rm mag}(f_{\rm re})/\Omega_{\rm GW}^{\rm cur}(f_{\rm re}) \sim \mathcal{O}(10^2)$.

6.6 Conclusion

A wide range of mechanisms for primordial black hole (PBH) formation have been proposed in the literature, including enhancements in inflationary perturbations [142, 142–147, 183, 191, 195–197, 384], bubble collisions in first-order phase transitions [157, 158, 364, 365], cosmic-string collapse [159–161, 351, 366, 367], and scalar-field fragmentation [386, 387]. However, none of these scenarios currently enjoys direct observational support regarding the true origin of PBHs. In this chapter, we have explored an alternative and well-motivated pathway for PBH formation in a mass window compatible with PBHs constituting the cold dark matter (CDM).

In our framework, primordial magnetic fields are generated through a sawtooth-type coupling, which naturally yields a broken power-law magnetic power spectrum while avoiding the usual backreaction and strong-coupling issues. This structure imprints a corresponding broken power-law feature in the induced curvature perturbation spectrum, with the peak scale determined by the reheating dynamics. We have shown that, for a suitable choice of model parameters and reheating temperature, the same magnetogenesis setup can both account for the observed large-scale magnetic fields and produce sufficiently enhanced density fluctuations to generate PBHs.

Since PBH formation is exponentially sensitive to the peak amplitude of curvature perturbations, and in this scenario directly linked to the peak amplitude of the primordial magnetic field, the model naturally predicts a sizable stochastic gravitational-wave (GW) background sourced by magnetic anisotropic stresses. The spectral shape of these secondary GWs is governed by the magnetic spectral index, making it qualitatively distinct from the spectrum produced by curvature perturbations [142, 167, 183, 190–197, 384]. For appropriate parameter choices, the predicted GW signals fall within the target sensitivity of future experiments such as LISA [335, 336], DECIGO [340–342], BBO [337–339], and SKA [334], and may also help explain the PTA signals reported in recent observations [41–45].

Furthermore, both the PBH mass function and the peak frequency of the induced GW spectrum depend sensitively on the reheating temperature. Thus, a joint observation of a characteristic GW peak together with a PBH mass range compatible with CDM could provide key information about reheating and the underlying magnetic power spectrum. Multi-messenger constraints—combining PBH abundance, GW observations, and large-scale magnetic-field measurements—are therefore essential to fully test this class of magnetogenesis scenarios.

In summary, this chapter demonstrates that a unified magnetogenesis framework can simultaneously generate observable primordial magnetic fields, produce distinctive gravitational-wave signatures, and provide a viable mechanism for PBH formation. This connection between early-Universe magnetic fields and present-day dark matter abundance offers a promising target for upcoming observational probes.

Chapter 7

Minimal Magnetogenesis: The Role of Inflationary Perturbations and ALPs, and Its Gravitational Wave Signatures

7.1 Introduction

In the previous chapters, we have discussed scenarios of early Universe magnetogenesis, focusing on mechanisms that explain the origin of large-scale magnetic fields while avoiding issues such as strong coupling and backreaction. In many such models, the generation of significant magnetic fields requires an additional coupling with the gauge sector, where the coupling function evolves rapidly with time [47, 117, 118, 229, 233, 235, 237, 238, 258, 259, 262]. However, to explain the large-scale magnetic fields observed in galaxies and clusters of galaxies [85, 388–390], as well as those inferred in cosmic voids from γ-ray observations [248, 250, 251] or constrained by the CMB anisotropies [245, 246, 251, 391], it is not always necessary to invoke an inflationary or post-inflationary origin (e.g., during reheating).

Despite their significance, a consistent generation mechanism for primordial magnetic fields (PMFs) remains elusive. Several astrophysical and cosmological models have been proposed. Astrophysical mechanisms typically require seed fields of the order of 10^{-22} G, which are then amplified by the galactic dynamo effect [392]. To explain the origin of such seed fields, cosmological mechanisms have been considered, including phase transitions in the early universe [393–395], magnetic monopoles [396], and breaking conformal invariance through couplings to the inflaton field [47, 235, 237, 238, 258, 259, 262, 263, 275, 330]. Other proposals include signatures of multi-inflationary models [397] and cosmological vector perturbations [398].

This chapter mainly focuses on the inflationary magnetogenesis mechanism with a minimally coupled electromagnetic field. We emphasize that our approach sharply contrasts with conventional inflationary magnetogenesis scenarios involving explicit conformal breaking in the electromagnetic sector. The electromagnetic field in four dimensions is inherently conformally invariant, which prohibits the production of classical gauge fields from the quantum vacuum in a conformally flat inflationary background. Therefore, non-minimal electromagnetic theories are typically introduced to achieve non-trivial field production by explicitly breaking conformal invariance through non-trivial gauge kinetic functions.

Such models are broadly classified into two distinct categories based on the polarization properties of the gauge field: non-helical $f_1(\eta)FF$ models [47, 235, 237, 238, 258, 259, 262], and helical $f_1(\eta)F\tilde{F}$ models [264–266, 315]. Apart from the well-known axion ($\mathfrak{a}$)–photon coupling $\mathfrak{a}\,F\tilde{F}$ [221, 275, 275–278], most other forms of gauge kinetic functions lack robust physical motivation and are often introduced in an ad hoc manner.

Despite these challenges, a substantial body of work has explored explicit breaking of conformal invariance in the electromagnetic sector (see [238] and references therein). However, such approaches face several unresolved issues, including the strong coupling problem, backreaction effects, and ultraviolet incompleteness, which complicate the construction of consistent magnetogenesis models. Most existing frameworks aim to generate magnetic fields of the required strength on Mpc scales directly from inflation, motivating the present work.

In this chapter, we propose a **two-stage process** for the generation of large-scale magnetic fields. The primary objective of this approach is to formulate a minimal magnetogenesis model within the established framework of inflation and axion electrodynamics. As discussed earlier, due to the conformal nature of the background, the growth of electromagnetic fields is suppressed in a conformally flat Friedmann–Lemaître–Robertson–Walker (FLRW) universe. However, if the background deviates from conformal flatness, gauge fields can be generated gravitationally without invoking additional non-minimal couplings.

Such possibilities have been explored in anisotropic cosmological models, such as Bianchi-type universes [399], where the metric is not conformally flat. In these scenarios, large-scale magnetic fields can be generated from the quantum vacuum [400]. However, they raise fundamental questions regarding the realization of anisotropy during inflation. Instead, we adopt the framework proposed in [310], where conformal flatness is dynamically broken by inflationary metric perturbations.

In the **first stage** of our mechanism, a minimally coupled gauge field propagates through this perturbed background. The metric perturbations induce mixing between positive and negative frequency modes, leading to the gravitational production of a classical electromagnetic field from the quantum vacuum at all scales. Since this process is sourced by perturbations, the resulting field strength is naturally Planck suppressed and proportional to the amplitude of inflationary curvature perturbations.

In the **second stage**, during subsequent cosmological evolution, the generated magnetic field interacts with a homogeneous oscillating axion background. The axion is a well-motivated extension of the standard model, introduced to solve the strong CP problem [401], and also arises naturally in string theory [402]. It originates from the spontaneous breaking of a global U(1) symmetry and can remain light due to non-perturbative effects. If initially misaligned, the axion evolves into a homogeneous oscillating field at later times, which can resonantly amplify the pre-existing seed magnetic field. This mechanism leads to the production of a helical electromagnetic spectrum.

We compute the power spectrum of the generated magnetic fields, considering different scalar perturbation spectra, and analyze the relation between curvature perturbations and magnetic field strength. The evolution of the magnetic field is followed across various cosmological epochs, including inflation, reheating, radiation domination, and matter domination. During the matter-dominated era, after recombination, when the Universe becomes electrically neutral, an oscillating axion field with suitable mass can excite gauge field modes at Mpc scales, resulting in present-day magnetic field strengths consistent with observations.

Furthermore, we compute the stochastic gravitational waves (GWs) generated by the late-time excitation of gauge fields due to axion oscillations. These GWs can leave observable imprints on the GW spectrum at CMB scales, potentially detectable by future experiments such as CMB-S4 [403, 404]. Since the generated magnetic fields are helical, they act as sources of chiral GWs.

Additionally, the magnetic field spectrum exhibits a peak whose position depends on the axion mass, leading to a distinctive feature in the GW spectrum. Such features may imprint observable signatures on the CMB, providing a potential probe of this mechanism. A detailed analysis of these observational imprints is left for future work.

In Section 7.3, we explore how, after the recombination epoch, the presence of ultralight axions (ULAs) can lead to a resonant amplification of the seed gauge field generated by the inflationary curvature power spectrum to an observationally favored value at Mpc scale. Section 7.4 discusses the potential detection of this mechanism through the secondary gravitational waves generated from the resonantly produced magnetic field in the homogeneous oscillating axion background. Finally, in Section 7.5, we summarize our key findings.

7.2 First stage: Magnetogensis from curvature power spectrum

7.2.1 Generalities

In the standard scenario, the conformal flatness of the background and conformal invariance of the electromagnetic field conspire in preventing the production of the electromagnetic field during inflation. However, in the presence of curvature perturbations, the conformal flatness of the background is dynamically broken, leading to the generation of primordial magnetic fields. In this section, we explore the evolution of the gauge field in such a scenario following the reference [310], where curvature-induced modifications to the electromagnetic action allow for efficient field amplification. So we begin with the following equation

$$\mathcal{S} = \int d^4x\, \sqrt{-g}\left[\frac{M_{pl}^2}{2}R + \frac{1}{2}\partial^\mu\varphi\partial_\mu\varphi - V(\varphi) - \frac{1}{4}F_{\mu\nu}F^{\mu\nu}\right]. \tag{7.1}$$

Now, finding the equation of motion for the gauge field, we arrive at,

$$\partial_\nu\left(\frac{\delta\mathcal{L}_{EM}}{\partial\partial_\mu A_\nu}\right) = \partial_\nu\left(\frac{\partial\sqrt{-g}F_{\mu\nu}F^{\mu\nu}}{\partial\partial_\mu A_\nu}\right) = \frac{\partial}{\partial x^\mu}[\sqrt{-g}g^{\alpha\mu}g^{\beta\nu}F_{\alpha\beta}] = 0, \tag{7.2}$$

To begin with, we consider the following perturbed flat FLRW metric,

$$ds^2 = a^2(\eta)\left[-(1+2\Psi)d\eta^2 + (1+2\Phi)\delta_{ij}dx^i dx^j\right] \tag{7.3}$$

In this background, for $\nu = 0$, we find,

$$\frac{\partial}{\partial x^i}\left[(1-2\Phi)(\partial_i A_0 - \partial_0 A_i)\right] = 0, \tag{7.4}$$

and for $\nu = i$ we get,

$$\frac{\partial}{\partial \eta}\left[(1-2\Phi)(\partial_i A_0 - \partial_0 A_i)\right] + \frac{\partial}{\partial x^j}\left[(1+2\Phi)(\partial_j A_i - \partial_i A_j)\right] = 0. \tag{7.5}$$

In addition, we have considered the Coulomb gauge condition $\vec{\nabla}\cdot\vec{A} = 0$. In the limit of vanishing anisotropic stress, we further assume $\Psi = -\Phi$. From the above expression, it is clear that in the presence of Φ, the gauge field should amplify itself from the vacuum sourced by the metric perturbation. If we assume that in the asymptotic past, all the modes were well inside the horizon and choose the well-known Bunch-Davis (BD) vacuum, we can write

$$A_\mu^{\mathbf{k},\lambda}(x) \xrightarrow[\eta\to-\infty]{} A_\mu^{(0)\mathbf{k},\lambda}(x) = \frac{1}{\sqrt{2k}}\epsilon_\mu(\mathbf{k},\lambda)e^{i(\vec{k}\cdot\mathbf{x}-k\eta)}, \tag{7.6}$$

where $\epsilon_\mu(\mathbf{k},\lambda)$ is the polarization vector for gauge field. Now, after inflation starts, an inhomogeneous background is formed, and in the presence of a non-vanishing metric perturbation Φ, the gauge field is excited from the BD vacuum. Therefore, in the asymptotic future, this solution will behave as a linear superposition of positive and negative frequency modes with different momentum and polarization. We can express this gauge field as

$$A_\mu^{\mathbf{k},\lambda}(x) \xrightarrow[\eta\to\infty]{} \sum_{\lambda'}\sum_{q}\left(\alpha_{\mathbf{k}}^{\lambda\lambda'}(q,\eta)\frac{\epsilon_{\mathbf{q}}^{\lambda}}{\sqrt{2q}}e^{i(\mathbf{q}\cdot\mathbf{x}-q\eta)} + \beta_{\mathbf{k}}^{\lambda\lambda'}(\mathbf{q},\eta)\frac{\epsilon_{\mathbf{q}}^{\lambda*}}{\sqrt{2q}}e^{-i(\mathbf{q}\cdot\mathbf{x}-q\eta)}\right). \tag{7.7}$$

Here, '$\alpha_{\mathbf{k}}^{\lambda\lambda'}$' and '$\beta_{\mathbf{k}}^{\lambda\lambda'}$' can be taken to be as the well-known Bogolyubov coefficients, and we can easily determine the expression order by order in terms of metric perturbation. In order to compute $\beta_{\mathbf{k}}^{\lambda\lambda'}(q,\eta)$, we expand the gauge field as $A_\mu^{\mathbf{k},\lambda}(\mathbf{q},\eta) = A_\mu^{(0)\mathbf{k},\lambda}(\mathbf{q},\eta) + A_\mu^{(1)\mathbf{k},\lambda}(\mathbf{q},\eta) + \cdots$. Here, $A_\mu^{(0)\mathbf{k},\lambda}$ is the solution of the gauge field in the absence of perturbation. Utilizing this with Eqs. (7.4)(7.5) (7.6), we get the equation of motion of the gauge field in Fourier space as

$$\frac{d^2}{d\eta^2}A_i^{(1)\mathbf{k},\lambda}(\mathbf{q},\eta) + q^2 A_i^{(1)\mathbf{k},\lambda}(\mathbf{q},\eta) = J_i^{\mathbf{k},\lambda}(\mathbf{q},\eta), \tag{7.8}$$

where the source term $J_i^{\mathbf{k},\lambda}(\mathbf{q},\eta)$ takes the following form [233, 310],

$$\begin{aligned} J_i^{\mathbf{k},\lambda}(\mathbf{q},\eta) = -\sqrt{2q}\Bigg[&\left(i\Phi'(\mathbf{k}+\mathbf{q},\eta) + \frac{q^2-\mathbf{k}\cdot\mathbf{q}}{q}\Phi(\mathbf{k}+\mathbf{q},\eta)\right)\epsilon_{i\mathbf{k}}^{\lambda}e^{-iq\eta} \\ &+ (\epsilon_{\mathbf{k}}^{\lambda}\cdot\mathbf{q})\Phi(\mathbf{k}+\mathbf{q},\eta)\frac{k_i}{k}e^{-iq\eta} - i\frac{\epsilon_{\mathbf{k}}^{\lambda}\cdot\mathbf{q}}{q^2}\frac{\partial}{\partial\eta}\left[\Phi(\mathbf{k}+\mathbf{q},\eta)e^{-ik\eta}\right]\mathbf{q}_i\Bigg]. \end{aligned} \tag{7.9}$$

Detailed calculations are given in the Appendix A.2. Now, we solve the above equation using the Green's function method, and we can write the solution of the gauge field as

$$A_i^{\mathbf{k},\lambda}(\mathbf{q},\eta) = \frac{\epsilon_{i\mathbf{k}}^{\lambda}}{\sqrt{2k}}\delta(\mathbf{k}-\mathbf{q})e^{-ik\eta} + \frac{1}{2}\int_{\eta_i}^{\eta_f} J_i^{\mathbf{k},\lambda}(\mathbf{q},\eta)\mathcal{G}_q(\eta_f,\eta')d\eta', \tag{7.10}$$

where $\mathcal{G}_q(\eta_f,\eta')$ is the Greens function of Eq.(7.8). The first term of Eq.(7.10) is due to the homogeneous part of Eq.(7.8) and can be assumed as quantum fluctuations as long as they are inside the horizon during inflation. Now the Green's function of the corresponding Eq.(7.8) is $\mathcal{G}_q(\eta_f,\eta') = \Theta(\eta_f-\eta')\sin(q(\eta_f-\eta'))/q$. Utilizing this in Eq.(7.10) and compared with Eq.(7.7) it is straight forward to obtain the Bogoliubov coefficient $\beta_{\mathbf{k}}^{\lambda\lambda'}(\mathbf{q},\eta)$ as,

$$\beta_{\mathbf{k}}^{\lambda\lambda'}(\mathbf{q},\eta) = -\sum_i \frac{i}{\sqrt{2q}}\int_{\eta_i}^{\eta_f} \epsilon_{i\mathbf{q}}^{\lambda*} J_i^{\mathbf{k},\lambda}(\mathbf{k}+\mathbf{q},\eta')e^{-iq\eta'}d\eta'. \tag{7.11}$$

Where η_i and η_f are the initial time when the source is active and the final time, respectively. Once we know the behavior of the metric fluctuation, then from the above integral we can easily compute the total number of photons created with the comoving wave number q, and the expression is given by $N_q = \sum_{\lambda\lambda'}\sum_k \left|\beta_{\mathbf{k}}^{\lambda\lambda'}(\mathbf{q},\eta)\right|^2$. In the continuum limit, we can write the total number of photons in terms of the power spectrum as (see detailed calculation in appendix A.2)

$$N_k = \sum_{\lambda\lambda'}\int \frac{d^3q}{(2\pi)^3}\Phi_0^2(|\mathbf{k}+\mathbf{q}|)\mathcal{D}(k,q), \tag{7.12}$$

where we introduce

$$\mathcal{D}(k,q) = \left|\int d\eta' \left\{\left(i\mathcal{C}'(|\mathbf{k}+\mathbf{q}|\eta') + \frac{q^2-\mathbf{k}\cdot\mathbf{q}}{q}\mathcal{C}(|\mathbf{k}+\mathbf{q}|\eta')\right)(\epsilon_{\mathbf{k}}^{\lambda}\cdot\epsilon_{\mathbf{q}}^{\lambda'}) + \frac{(\epsilon_{\mathbf{k}}^{\lambda}\cdot\mathbf{q})(\epsilon_{\mathbf{q}}^{\lambda'}\cdot\mathbf{k})}{q^2}\mathcal{C}(|\mathbf{k}+\mathbf{q}|\eta')\right\}\right|^2. \tag{7.13}$$

Here, $\mathcal{C}(k\eta)$ can be identified as the transfer function defined as $\Phi(q,\eta) = \Phi_0(q)\mathcal{C}(q\eta)$, and $\mathcal{C}'(q\eta) = d\mathcal{C}/d\eta$. Typically the scalar power spectrum is expressed as $P_\Phi(\mathbf{k}+\mathbf{q}) = (|\mathbf{k}+\mathbf{q}|)^3\Phi_0^2(|\mathbf{k}+\mathbf{q}|)/2\pi^2$. As we have seen, the last term of Eq.(7.9) does not contribute to the number spectrum due to the transversality condition of the polarization vectors.

Defining the Present-day magnetic field Strength:

Once we compute the total photon number density for the comoving wave number 'k', then we can immediately compute the magnetic energy density in terms of the scalar power spectrum stored in the mode 'k' at any instant of time as

$$\mathcal{P}_{\rm B}(k,\eta) = \frac{\partial \rho_{\rm B}(\eta)}{\partial \ln(k)} = \left(\frac{k}{a(\eta)}\right)^4 N_k(\eta) = \left(\frac{k}{a(\eta)}\right)^4 \sum_{\lambda\lambda'} \int \frac{d^3q}{(2\pi)^3}\left(\frac{q}{k}\right)\frac{2\pi^2 P_\Phi(\mathbf{k}+\mathbf{q})}{(|\mathbf{k}+\mathbf{q}|)^3}\mathcal{D}(k,q) \tag{7.14}$$

here '$a(\eta)$' is the scale factor defined at 'η'. After the production of the gauge field, it evolves adiabatically, and due to the expansion of our universe, the magnetic energy density dilutes as a^{-4}. If there is no additional source for the magnetic field during the subsequent evolution, we can define the present-day magnetic field as

$$B_0(k) = \left(\frac{k}{a(\eta_0)}\right)^2 \sqrt{N_k}, \tag{7.15}$$

We set $a(\eta_0) = 1$ to define the present-day scale factor.

7.2.2 Generation of the magnetic field during the inflation era

In this subsection, we describe the evolution of the magnetic field power spectrum and number density during inflation. Considering a simple slow-roll type inflation with minimally coupled potential, one can write the solution for Φ following [405],

$$\Phi^{''} + 2\left(\mathcal{H} - \frac{\varphi^{''}}{\varphi}\right)\Phi^{'} - \nabla^2\Phi + 2\left(\mathcal{H}^{'} - \mathcal{H}\frac{\varphi^{''}}{\varphi}\right)\Phi = 0, \tag{7.16}$$

where $\mathcal{H}$ is the Hubble parameter with respect to conformal time η, and $'$ indicates the derivative with respect to η. It is more convenient to revert to physical time 't'. In the sub-horizon scale, the solution is oscillatory in time. In the superhorizon scale, considering the background equation of motion, slow roll conditions during inflation, and rewriting in terms of physical time, one gets

$$\Phi \equiv -A\frac{\dot{H}}{H^2} \sim \frac{A}{16\pi G}\left(\frac{V_{,\varphi}}{V}\right)^2. \tag{7.17}$$

Or, in terms of the curvature perturbation $\mathcal{R}$,

$$\Phi \sim \frac{\sqrt{\epsilon}}{2\sqrt{k^3}}\frac{H}{M_p} \sim \epsilon\mathcal{R}, \tag{7.18}$$

where ϵ is the slow-roll parameter during inflation which suppresses Φ during inflation. Further, in terms of the equation of state, on superhorizon scales [405],

$$\mathcal{R} = \frac{\frac{2}{3}H^{-1}\dot{\Phi} + \Phi}{(1+w)} + \Phi \tag{7.19}$$

Despite the suppression from ϵ, one can still compute the total number of photons generated due to inflation purely arising from the metric fluctuations $\sim \Phi$ contribution as

$$N_k = \sum_{\lambda\lambda'} \int \frac{d^3\mathbf{q}}{(2\pi)^3} \epsilon^2 \Phi_0^2(|\mathbf{k}+\mathbf{q}|)\mathcal{D}(k,q), \tag{7.20}$$

where $\mathcal{D}(k,q)$ is a function of the momenta and the transfer function, as previously mentioned. Φ oscillates and decays on sub-horizon scales, and the contribution is negligible. on super-horizon scales the behavior depends on that of ϵ, as $\mathcal{R}$ is roughly constant. For the simple quadratic potential, nearly scale-invariant power spectrum, we begin with splitting the above integral into two limit $\int_{k_*}^{k_e} \mathrm{dq} = \int_{\mathrm{k}_*}^{\mathrm{k}} \mathrm{dq} + \int_{\mathrm{k}}^{\mathrm{k_e}} \mathrm{dq}$, where the limits indicate the peak wavenumber and the wavenumber corresponding to the CMB, and we can write N_k as

$$N_k \simeq \int_{k_*}^{k} \frac{\mathrm{dq}}{q}\frac{q}{k}\frac{q^3}{2\pi^2}\epsilon^2\mathcal{R}^2(k)\times\mathcal{O}(1) + \int_{k}^{k_e} \frac{\mathrm{dq}}{q}\frac{q}{k}\frac{q^3}{2\pi^2}\epsilon^2\mathcal{R}^2(k)\times\mathcal{O}(1), \tag{7.21}$$

and the magnetic power spectrum takes the form,

$$\mathcal{P}_{\mathrm{B}}(k,\eta_{\mathrm{e}}) \simeq \frac{k^3 k_*}{a^4(\eta_{\mathrm{e}})}\frac{\epsilon^2 A_s}{n_s}\left\{\left(\frac{k_{\mathrm{e}}}{k_*}\right)^{n_s}\right\}, \tag{7.22}$$

We can further consider an ultra-slow-roll type inflationary scenario, where the enhanced curvature power spectrum is generated due to the ultra-slow-roll phase, and the comoving curvature power spectrum is parameterized as

$$P_{\mathcal{R}}(k) = A_s\left(\frac{k}{k_*}\right)^{n_s-1} + A_0\ \mathrm{Exp}\left[-\frac{(k-k_p)^2}{\delta\times k_p^2}\right], \tag{7.23}$$

Here $A_s \simeq 2.1\times10^{-9}$ is the amplitude of the scalar curvature power spectrum observed by Planck, and n_s is the scalar spectral index [11]. Here, A_0 is the amplitude of the curvature power spectrum at peak wavenumber, and δ is the dimensionless parameter that sets the spectral shape of the curvature near the peak. k_{p} is the position of the peak of the curvature power spectrum. In this case, we get two contributions to the number density - from the usual nearly-scale invariant term in the first part in 7.23, and the PBH-type enhancement in the second term. Hence, the total number density is of the form,

$$N_k \simeq \frac{\epsilon^2 A_s}{n_s}\left(\frac{k_*}{k}\right)\left\{\left(\frac{k_{\mathrm{e}}}{k_*}\right)^{n_s} + \frac{A_0 n_s\sqrt{\pi\delta}}{A_s}\left(\frac{k_{\mathrm{p}}}{k_*}\right)\left[1+\mathrm{Erf}\left(\frac{k_{\mathrm{p}}-k}{k_{\mathrm{p}}\sqrt{\delta}}\right)\right]\right\}. \tag{7.24}$$

As we see, the total number produced for co-moving wavenumber k scales as $N_k \propto k^{-1}$. The energy density of the produced magnetic field per logarithmic wavenumber is defined as $\rho_{\mathrm{B}}(k,\eta) = (k/a(\eta))^4 N_k(\eta)$. Or we can define the comoving magnetic energy density as $\tilde{\rho_{\mathrm{B}}}(k,\eta) = k^4 N_k(\eta)$. Now, at the end of inflation, the magnetic energy store per logarithmic k

is

$$\mathcal{P}_{\mathrm{B}}(k,\eta_{\mathrm{e}}) \simeq \frac{k^3 k_*}{a^4(\eta_{\mathrm{e}})}\frac{\epsilon^2 A_s}{n_s}\left\{\left(\frac{k_{\mathrm{e}}}{k_*}\right)^{n_s} + \frac{A_0 n_s\sqrt{\pi\delta}}{A_s}\left(\frac{k_{\mathrm{p}}}{k_*}\right)\left[1+\mathrm{Erf}\left(\frac{k_{\mathrm{p}}-k}{k_{\mathrm{p}}\sqrt{\delta}}\right)\right]\right\}. \tag{7.25}$$

7.2.3 Generation of magnetic field for post-inflationary evolution

As shown above, the magnetic power spectrum at any given time is proportional to the inflationary scalar power spectrum. After the end of inflation, this scalar power spectrum evolves into the curvature power spectrum, which can, in principle, influence the post-inflationary evolution of the gauge field.

In the high-conductivity limit, however, the production of gauge fields by any source term becomes highly suppressed. During reheating, the generation of charged particles—and hence the development of conductivity- depends on the specific model describing how the inflaton decays into Standard Model particles. In simple perturbative reheating scenarios, the energy density remains largely dominated by the inflaton field for most of the duration, making the behavior of conductivity during this phase uncertain.

If conductivity develops rapidly after inflation and is assumed to affect all comoving modes k uniformly, then any further gauge field production would be strongly suppressed. Given the lack of precise knowledge about the evolution of conductivity during reheating, we assume a small but nonzero electric conductivity during this phase. Full conductivity is considered to be established only after the inflaton has completely decayed and the universe becomes thermalized, entering a radiation-dominated epoch.

In this section, we consider different possible inflationary spectra consistent with CMB and explore their impact on the present-day magnetic field strength. Before we do that, we provide a quick summary of the post-inflation evolution of the scalar perturbation Φ. For this, let us assume that after inflation, the universe is filled with a fluid of equation of state w_{re}, and the energy density of the fluid evolves as $H^2 \propto \rho_\varphi \propto a^{-3(1+w_{\mathrm{re}})}$. For example, the reheating phase corresponds to $w = w_{\mathrm{re}}$, radiation domination corresponds to $w_{\mathrm{re}} = 1/3$. In the linear order in perturbation theory, the equation of motion (EoM) for Φ after inflation in Fourier space is given by [217]

$$\Phi'' + \frac{4+2\beta}{1+\beta}\mathcal{H}\Phi' + k^2\Phi = 0, \tag{7.26}$$

Here $\beta = (1-3w_{\mathrm{re}})/(1+3w_{\mathrm{re}})$ and the solution of the above equation is well known and takes the form [217],

$$\Phi(k,\eta) = \Phi_0(k)2^{\beta+3/2}\Gamma[\beta+5/2](k\eta)^{-\beta-3/2}J_{\beta+3/2}(k\eta) = \mathcal{C}_{\mathrm{T}}(k\eta)\Phi_0(k). \tag{7.27}$$

Where the primordial part $\Phi_0(k)$ is set by inflationary dynamics, and is related to the curvature perturbation on co-moving constant energy slices, and $\mathcal{C}_{\mathrm{T}}(k\eta)$ is the transfer function associated with a given post-inflationary phase with an equation of state w.

We can now write the primordial scalar power spectrum $P_\Phi(k)$ in terms of comoving curvature power spectrum $P_\mathcal{R}(k)$ as

$$P_\Phi(k,\eta) = \left(\frac{2+\beta}{3+2\beta}\right)^2 |\mathcal{C}_\mathrm{T}(k\eta)|^2 \, P_\mathcal{R}(k). \tag{7.28}$$

As long as a particular mode is outside the horizon during the phase under consideration, namely in the $k\eta << 1$ limit (super-horizon limit), the transfer function freezes to unity $|\mathcal{C}_\mathrm{T}(k\eta)|^2 \simeq 1$, and we have,

$$P_\Phi(k < \mathcal{H}^{-1},\eta) \simeq \left(\frac{2+\beta}{3+2\beta}\right)^2 P_\mathcal{R}(k). \tag{7.29}$$

It is clear that the spectrum of Φ becomes constant at the super-horizon scale and can be directly identified with the inflationary power spectrum up to an equation state-dependent factor. This is well known to be directly imprinted in the CMB temperature anisotropies and yields robust constraints, particularly in the early stages of inflation. On the contrary, the sub-horizon modes, when entering the horizon during the phase under consideration, can undergo non-trivial evolution, and the spectrum changes according to

$$P_\Phi(k > \mathcal{H}^{-1},\eta) \simeq \frac{2^{2(\beta+2)}\Gamma^2(\beta+5/2)}{2\pi}(k\eta)^{-2(\beta+2)} P_\mathcal{R}(k). \tag{7.30}$$

The value of $\beta(w_\mathrm{re})$ assumes the value in between $-1/2 \leq \beta \leq 1$. Hence, the comoving power spectrum always decays after the modes' reentry during the post-inflationary epoch. Further, an important point to realize is that CMB temperature anisotropies do not provide any constraint on the spectrum of those sub-horizon modes, and therefore, the later stage of inflationary dynamics remains poorly constrained. This particular fact leads to a possibility of modifying the later stage of inflationary dynamics that can modify the scalar power spectrum at small scales with large amplitude [142, 167, 183, 190–197]. Such enhancement in the curvature spectrum causes large density perturbations and produces primordial black holes (PBH), which is widely discussed as a potential dark matter candidate [183, 208, 209]. We will later see that those PBH-like power spectra indeed help increase the magnetic field strength on large scales.

In this section, we, therefore, explore those different types of inflationary spectra and their role in modifying the strength of large-scale magnetic fields. We further study the effect of the post-inflationary era, such as reheating with the generic equation of state w_re. Inflation is governed by the slow-rolling inflaton field with a nearly constant potential. In such an inflaton background, the curvature power spectrum assumes a power law form. For long-wavelength modes, CMB fixes two parameters of the power law spectrum. However, as we pointed out earlier, a high-frequency curvature power spectrum is poorly constrained, and

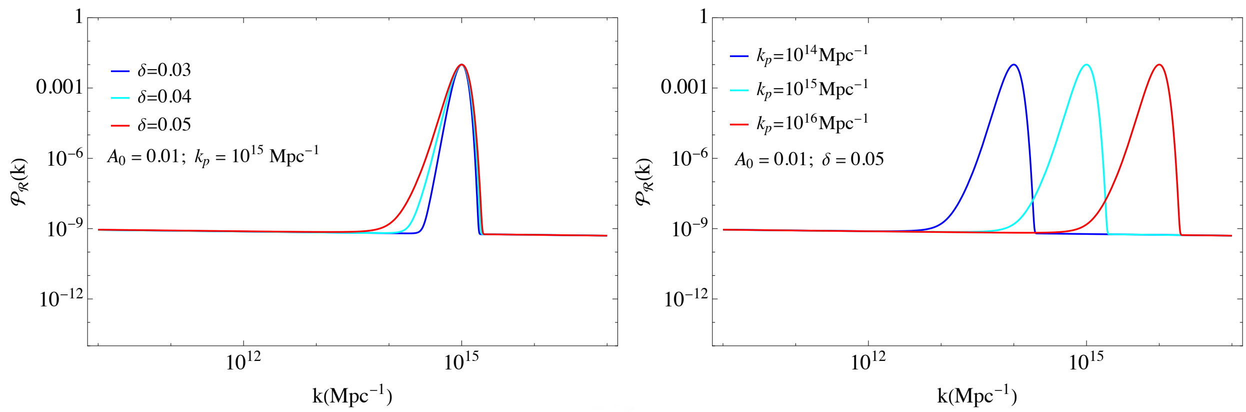

Figure 7.1: In this figure, we illustrate the behavior of the curvature power spectrum for different scenarios. In the left panel, we show how the spectral shape depends on the parameter δ, represented by three colors. In the right panel, we demonstrate how the spectral peak shifts depending on the peak wave number, denoted as $k_{\rm p}$, for a fixed value of $\delta = 0.05$. In both figures, we set the amplitude to $A_0 = 0.01$, the scalar amplitude to $\mathcal{A}_s \simeq 2.1 \times 10^{-9}$, and the spectral index to $n_s = 0.965$.

hence, we parameterized the full inflationary spectrum in the following way [165],

$$P_{\mathcal{R}}(k) = A_s \left(\frac{k}{k_*}\right)^{n_s-1} + A_0 \ \mathrm{Exp}\left[-\frac{(k-k_{\rm p})^2}{\delta \times k_{\rm p}^2}\right], \tag{7.31}$$

The first part of the spectrum is well constrained by CMB at the pivot scale $k_* = 0.05\mathrm{Mpc}^{-1}$ with amplitude $A_s = 2.1 \times 10^{-9}$, and scalar spectral index $n_s = 0.9649 \pm 0.0042$ at 68% CL [11]. The second part of the spectrum peaked around $k_{\rm p} >> k_*$; we parameterize by an exponential function keeping all the essential features of the PBH spectrum studied in the literature [183, 194–196, 200, 208, 209]. This essentially features an exponential amplification of curvature perturbations on small scales. By properly tuning the amplitude parameter A_0, one can achieve a magnitude of the power spectrum $P_{\mathcal{R}}(k)$ as high as $\mathcal{O}(10^{-2} - 10^{-1})$. Such a high value is critical for PBH formation in the subsequent evolution. The width of the spectrum is controlled by δ. To remain consistent with CMB observations, we maintain the following constraint $\delta^{-1} \leq \ln(A_0/A_s)$ throughout our analysis.

Utilizing the above curvature spectrum Eq.7.31 into the expression of magnetic power spectrum Eq.7.14, we find the following approximate analytic expression for the present-day magnetic power spectrum as:

$$\begin{aligned}\mathcal{P}_{\rm B}(k,\eta_0) &= \mathcal{P}_{\rm B}^{\rm inf}(k,\eta_e)\left(\frac{a_{\rm e}}{a_0}\right)^4 \\ &\simeq \frac{8\pi^2 H_{\rm e}^4}{9}\left(\frac{k}{k_{\rm e}}\right)^3\left(\frac{a_{\rm e}}{a_0}\right)^4\left(\frac{2+\beta}{3+2\beta}\right)^2\left[\frac{A_s}{n_s}\left(\frac{k_{\rm e}}{k_*}\right)^{n_s-1} + \frac{1}{2}\sqrt{\pi\delta}\frac{A_0 k_{\rm p}}{k_{\rm e}}\left(1+\mathrm{Erf}\left[\frac{k_{\rm p}-k}{k_{\rm p}\sqrt{\delta}}\right]\right)\right]\end{aligned} \tag{7.32}$$

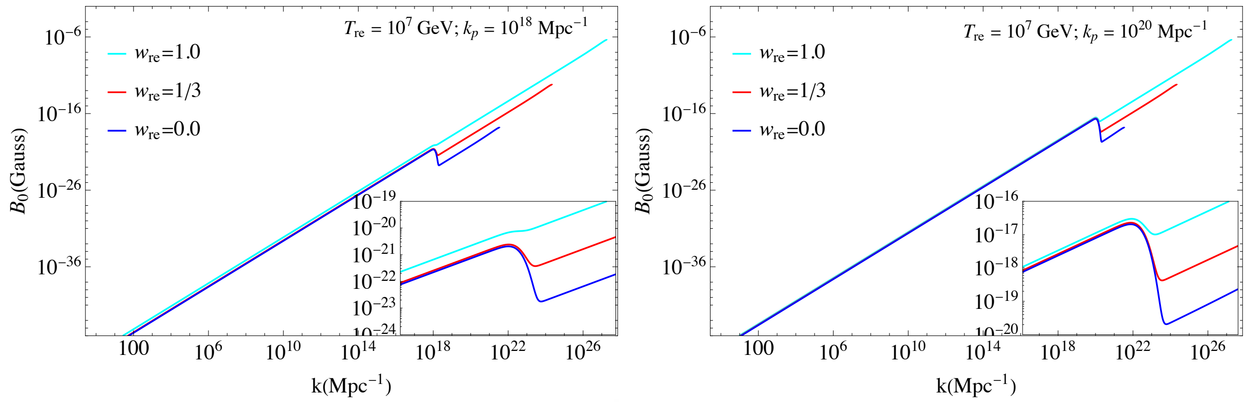

Figure 7.2: In these figures, we present the present-day magnetic field strength as a function of the comoving wavenumber k (in Mpc^{-1}). We consider a fixed reheating temperature of $T_{\mathrm{re}} = 10^7\,\mathrm{GeV}$, with the three different colors corresponding to different values of the equation of state parameter during reheating: $w_{\mathrm{re}} = 0.0$, $w_{\mathrm{re}} = 1/3$, and $w_{\mathrm{re}} = 1.0$. The left panel corresponds to a curvature power spectrum peak at $k_{\mathrm{p}} = 10^{18}\,\mathrm{Mpc}^{-1}$, while the right panel shows the result for $k_{\mathrm{p}} = 10^{20}\,\mathrm{Mpc}^{-1}$. In both figures, we set the amplitude of the curvature power spectrum peak to $A_0 = 0.1$. For the slow-roll type curvature power spectrum, we use $A_s \simeq 2.1 \times 10^{-9}$ with a spectral index of $n_s = 0.965$.

Here, (a_{e}/a_0) takes care of the dilution factor of the magnetic energy density due to background expansion from its inflationary counterpart $\mathcal{P}_{\mathrm{B}}^{\mathrm{inf}}(k, \eta_e)$ defined at the end of inflation.

Note that $k_* < k_{\mathrm{p}} < k_e$, and the PBH spectrum amplitude $A_0 \gg A_s \sim 10^{-9}$. This immediately suggests that across all scales for $k < k_{\mathrm{p}}$, the magnetic spectrum behaves as $\mathcal{P}_{\mathrm{B}}(k) \propto A_0 k_{\mathrm{p}} k^3$. The large-scale magnetic field strength is controlled by the amplitude A_0 of the small-scale modification of the PBH spectrum and its peak frequency k_{p}. For small wavelength modes, $(k > k_{\mathrm{p}})$, as the spectrum amplitude reduces to the primordial one (see Fig.(7.1)), the magnetic spectrum reduces to $\mathcal{P}_{\mathrm{B}}(k) \propto A_s k^3$ with reduced amplitude. In summary, we find the present-day magnetic field strength as a function of the amplitude of the inflationary power spectrum, as,

$$B_0 = \sqrt{\mathcal{P}_{\mathrm{B}}(k, \eta_0)} \propto \begin{cases} \sqrt{A_0 k_{\mathrm{p}}}\, k^{\frac{3}{2}} & \text{for} \quad k < k_{\mathrm{p}} \\ \sqrt{A_s}\, k^{\frac{3}{2}} & \text{for} \quad k > k_{\mathrm{p}} \end{cases}. \tag{7.33}$$

Whereas near the peak scale, the magnetic field strength shows a fall in strength due to the Error function, and it exhibits a spectral break. However, the peak in the magnetic spectrum near k_p occurs only if $k_{\mathrm{p}} \geq A_s k_{\mathrm{p}}/n_s\sqrt{\pi}\delta$. All the aforementioned features observed from the analytic form of the magnetic spectrum are depicted in Figs. (7.2), (7.3), and (7.4).

At this stage, we provide some numerical estimates to gain insight into the magnetic field strength defined at the comoving scale of 1 Mpc. We consider the case where the curvature power spectrum is peaked at $k \simeq k_{\mathrm{e}}$. Since the post-inflationary dynamics depend on the parameters of the inflationary model, we express all relevant quantities in terms of two reheating parameters: the equation of state (EoS) w_{re} and the reheating temperature T_{re}

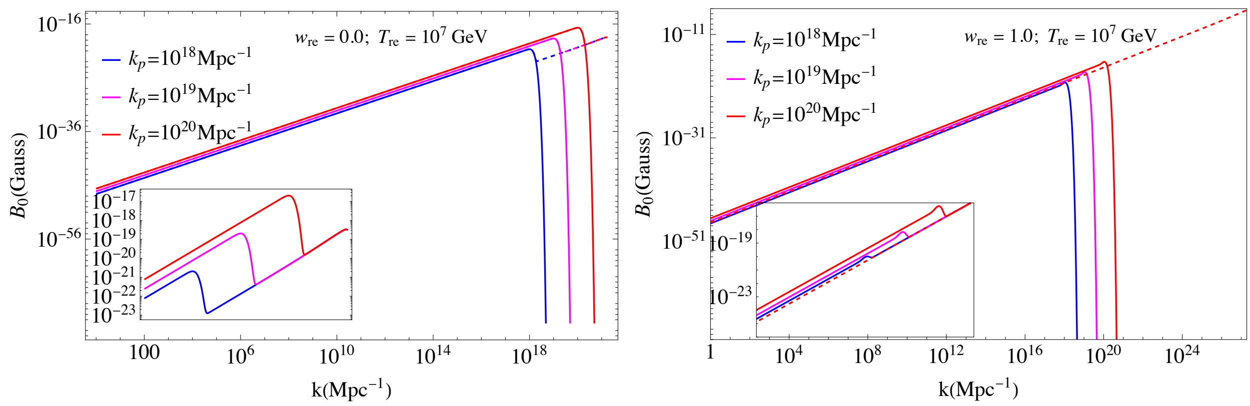

Figure 7.3: This figures show the present-day magnetic field strength, $B_0(k)$, as a function of the comoving wavenumber k (in Mpc^{-1}), for two different values of the equation of state parameter during reheating: $w_{\rm re} = 0.0$ (left) and $w_{\rm re} = 1.0$ (right). In both cases, the reheating temperature is fixed at $T_{\rm re} = 10^7$ GeV. Each figure includes three curves, with different colors representing three distinct values of the peak scale $k_{\rm p}$ of the curvature power spectrum. In both figures, we set the amplitude of the curvature power spectrum peak to $A_0 = 0.1$. For the slow-roll type curvature power spectrum, we use $A_s \simeq 2.1 \times 10^{-9}$ with a spectral index of $n_s = 0.965$.

(see Eqs. (2.70)(2.69) for the relationship between them). For a matter-dominated reheating phase with $w_{\rm re} = 0$, the magnetic field strength at the end of inflation turned out to be $B^{\rm inf} = \sqrt{\mathcal{P}_{\rm B}^{\rm inf}(k = 1{\rm Mpc}, \eta_e)} \simeq 2.93 \times 10^{16}$ G. In the radiation-dominated case with $w_{\rm re} = 1/3$, we find $B^{\rm inf} \simeq 4.29 \times 10^{10}$ G, while for a kination-dominated era with $w_{\rm re} = 1$, the magnetic field strength is reduced to $B^{\rm inf} \simeq 6.25 \times 10^4$ G.

Following their production, the magnetic fields dilute as a^{-2} due to the expansion of the Universe. Consequently, the present-day magnetic field strength depends on the post-inflationary evolution. Agian at 1 Mpc scale for $w_{\rm re} = 0$, we obtain $B_0 \simeq 3.76 \times 10^{-47}$ G; for a radiation-like reheating phase ($w_{\rm re} = 1/3$), $B_0 \simeq 3.81 \times 10^{-45}$ G; and for a kination-like phase ($w_{\rm re} = 1$), the present-day strength becomes $B_0 \simeq 3.94 \times 10^{-43}$ G. In all these estimates, we assume that the reheating phase ends when the background temperature reaches $T_{\rm re} \simeq 10^4$ GeV.

In Fig.7.2, we have numerically plotted the present-day magnetic field strength $B_0(k)$ as a function of the wave number k for a Gaussian-type curvature power spectrum, as defined in Eq. (7.31). We consider three sample equations of state (EoS): $w_{\rm re} = 0, 1/3,$ and 1. In both panels, the reheating temperature of the universe is fixed at $T_{\rm re} = 10^7$ GeV. The left panel corresponds to $k_p = 10^{18}$ Mpc^{-1}, while the right panel corresponds to $k_p = 10^{20}$ Mpc^{-1}. The strength of the magnetic field recovers our analytical expectation $B_0 \propto k^{3/2}$ with a very mild direct dependence on the reheating equation of state.

As discussed earlier, the cutoff wavenumber $k_{\rm e}$ depends on the reheating dynamics and the specific inflationary model under consideration (see Eq. (2.69)). In general, a higher equation of state parameter ($w_{\rm re} > 1/3$) corresponds to a shorter duration of the reheating phase compared to a matter-like phase ($w_{\rm re} < 1/3$) and due to this the produced magnetic field strength is dependent on the duration of the reheating dynamics. Since the magnetic field generated in such mechanisms is scale-dependent, and the comoving magnetic field amplitude scales as $B_0 \propto k^{3/2}$, the total magnetic energy density is sensitive to the details of the post-inflationary evolution. From our analysis, we find that while the magnetic field strength at large scales does exhibit dependence on the reheating dynamics, the effect is not significant enough to account for the present-day observed magnetic field strength at cosmological scales, but the total magnetic energy density is strongly dependent on the reheating dynamics.

Similarly, in Fig. 7.3, we plot the present-day magnetic field $B_0(k)$ as a function of the comoving wavenumber k for two different reheating scenarios. The left panel corresponds to $w_{\rm re} = 0$ with $T_{\rm re} = 10^7$ GeV, while the right panel corresponds to $w_{\rm re} = 1$ with $T_{\rm re} = 10^7$ GeV. Three different colors indicate different values of the peak wavenumber: $k_p = 10^{18}, 10^{19},$ and 10^{20} Mpc^{-1}. We observe that the magnetic field strength for scales $k < k_p$ indeed increases with the peak wave number k_p, following the relation $B_0(k < k_p) \propto k_p^{1/2}$, as we derived from Eq. (7.33). The dashed lines represent the contribution to the magnetic field from the first term in the curvature power spectrum in Eq. (7.31), which enables magnetic field generation even at scales $k > k_p$.

The PBH-induced curvature power spectrum leads to a significant enhancement in the magnetic power spectrum compared to the conventional inflationary scalar power spectrum. Notably, this enhancement extends to all super-horizon modes smaller than the mode k_p. From Eq. (7.33), the total enhancement factor from the PBH-type curvature spectrum can be expressed as $(A_0 k_p n_s)/(k_{\rm e} A_s)$, where A_0 is the peak amplitude of the curvature perturbations, A_s is the scalar amplitude, and n_s is the spectral index constrained by CMB observations. The maximum enhancement occurs when the peak frequency is aligned with $k_{\rm e}$ (i.e., $k_p \simeq k_{\rm e}$), giving an overall enhancement factor of $(A_0 n_s)/A_s$. For example, if $A_0 = 1$ (the maximum allowed curvature amplitude), $n_s = 0.965$ (the central value from CMB constraints), and $A_s \simeq 2.2 \times 10^{-9}$, the enhancement factor is approximately 4.4×10^8. For purely inflationary spectrum, the magnetic field strength at 1 Mpc scale can be calculated as $\sim 10^{-45}$ Gauss. However, PBH spectrum can enhance that value to a maximum $\sim 10^{-41}$ Gauss. This is indeed a significant enhancement, but much below the current observational bound $\sim 10^{-18}$ Gauss.

In Fig. 7.4, we present the present-day magnetic field strength as a function of wavelength λ, expressed in Mpc units. This plot focuses on large-scale magnetic fields, covering a range from 10 Mpc to 0.1 Kpc. We consider three different values of the equation-of-state parameter during reheating: $w_{\rm re} = 0$ (left), $w_{\rm re} = 1/3$ (middle), and $w_{\rm re} = 1$ (right). For each case, we show results for two different reheating temperatures: $T_{\rm re} = 10^{10}\,$GeV (cyan) and $T_{\rm re} = 1\,$GeV (blue). The colored bands represent the range between the maximum and minimum magnetic field strengths generated due to the curvature power spectrum. Solid lines correspond to magnetic fields sourced by the standard slow-roll-type curvature power spectrum, while dashed lines correspond to those sourced by an enhanced curvature power spectrum. To maximize the enhancement, we choose the peak of the curvature spectrum to lie near $k_p \simeq k_{\rm e}$, as the amplified magnetic field scales as $B_0 \propto k_{\rm e}^{1/2}$. The shaded vertical regions in the plot indicate

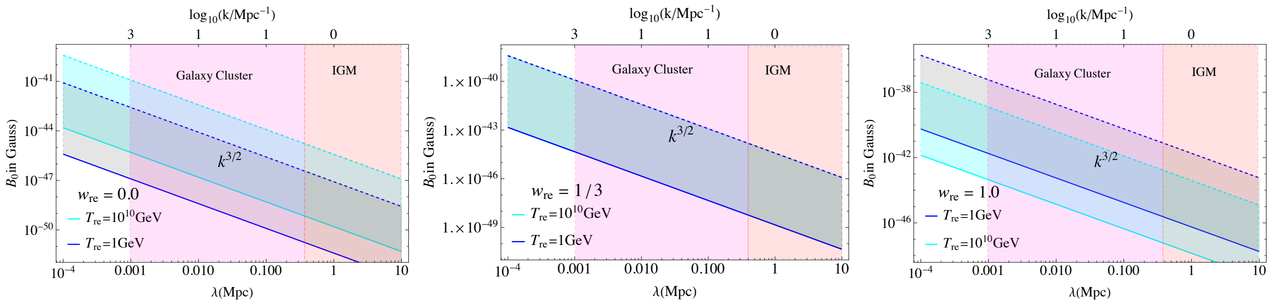

Figure 7.4: The above figures show the present-day magnetic field strength, B_0 (in Gauss), as a function of the observable wavelength λ (in Mpc) for three different values of the reheating equation-of-state parameter: $w_{\rm re} = 0.0$ (left), $w_{\rm re} = 1/3$ (middle), and $w_{\rm re} = 1.0$ (right). The two shaded color bands correspond to two different reheating temperatures: $T_{\rm re} = 1\,\mathrm{GeV}$ (blue) and $T_{\rm re} = 10^{10}\,\mathrm{GeV}$ (cyan). Solid lines represent the magnetic field spectrum generated from a simple slow-roll-type curvature power spectrum, while dashed lines correspond to the PBH-type curvature power spectrum, where the peak is located near the scale $k_{\rm e}$, i.e., $k_{\rm p} \simeq k_{\rm e}$. In all plots, we have fixed the maximum amplitude of the curvature power spectrum to be $A_0 = 1.0$. The vertical shaded regions indicate the characteristic length scales of the intergalactic medium (IGM) and galaxy clusters.

different physical length scales. We observe that for higher reheating temperatures, the large-scale magnetic fields sourced by the curvature power spectrum become significantly stronger. In particular, the field strength can be enhanced by up to four orders of magnitude for larger values of $w_{\rm re}$. Notably, in the radiation-like reheating scenario ($w_{\rm re} = 1/3$), the post-inflationary background evolves like a radiation fluid, making the total duration of the post-inflationary era largely independent of the reheating temperature. In contrast, for matter-like or kination-like reheating scenarios, the duration of the reheating era depends strongly on $T_{\rm re}$, as the background energy density dilutes more slowly (matter-like) or more rapidly (kination-like) compared to the magnetic field energy density. This relative dilution plays a crucial role in determining the final magnetic field strength observed today. We find that for both $w_{\rm re} = 0.0$ and $w_{\rm re} = 1.0$, the present-day magnetic field strength depends on the duration of the reheating era, whereas for $w_{\rm re} = 1/3$, it does not exhibit such dependence. Further, we observe a contrasting behavior in the dependence of magnetic field strength on the reheating temperature. For $w_{\rm re} < 1/3$, the magnetic field strength today increases with increasing reheating temperature (see the left panel of Fig. 7.4), while for $w_{\rm re} > 1/3$, the trend reverses: the magnetic field strength decreases with increasing reheating temperature (see the right panel of Fig. 7.4).

This opposite behavior can be understood as follows:

$$\mathcal{P}_{\rm B}(k,\eta_0) \propto \frac{a_e^4}{a_0^4} = \frac{a_e^4}{a_{\rm re}^4}\frac{a_{\rm re}^4}{a_0^4} \sim e^{-4N_{re}}\frac{T_0^4}{T_{re}^4} = \left(\frac{\pi^2 g_{\rm re} T_{\rm re}^4}{90 H_{\rm e}^2 M_{\rm P}^2}\right)^{\frac{4}{3(1+w_{\rm re})}} \frac{T_0^4}{T_{re}^4} \sim H_{\rm e}^{-\frac{8}{3(1+w_{\rm re})}} T_{\rm re}^{\frac{4-12w_{\rm re}}{3(1+w_{\rm re})}}. \quad (7.34)$$

Therefore, for the radiation-like reheating phase, the present-day magnetic field turns out to be independent of reheating temperature. Further for $w_{\rm re} = 0$, the present day magnetic field $B_0 = \sqrt{\mathcal{P}_{\rm B}(k)} \propto T_{\rm re}^{2/3}$, and for $w_{\rm re} = 1$, $B_0 \propto T_{\rm re}^{-4/3}$. We recover all those behaviors numerically

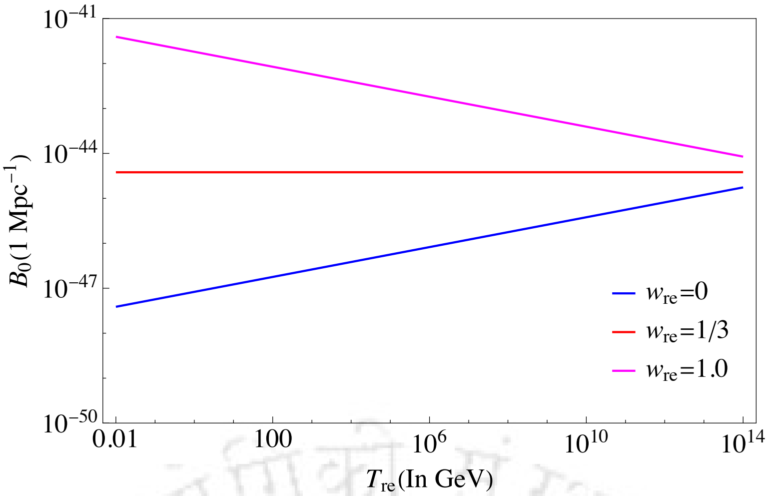

Figure 7.5: In the above figure, we have shown how the present-day magnetic field depends on the reheating temperature (effectively determined by the duration of the reheating periods) for three different values of effective equation of state $w_{\rm re} = 0,\ 1/3,\ \&\ 1.0$ denoted by three different colored lines. Here we consider the peak of the curvature perturbation situated near the $k_{\rm e}$ to get the maximum enhancement. In all cases, we consider the amplitude of the peak curvature power spectrum to be $A_0 \simeq 1.0$ in order to investigate the maximum possible enhancement of the magnetic field due to the curvature power spectrum.

as depicted in Figs.(7.4)(7.5).In Fig. 7.4, we observe that there are no visible spectral breaks, unlike in Fig. 7.2 or Fig. 7.3. This is primarily due to the range of scales considered in this plot. Our focus here is on large-scale magnetic fields and understanding how their present-day strength depends on reheating dynamics. To maximize the enhancement, we assume that the peak of the curvature power spectrum lies at smaller scales, close to $k_{\rm e}$. Since the spectral break in the magnetic field spectrum typically appears near the peak of the curvature power spectrum, and this peak lies outside the range of scales shown in Fig. 7.4, the spectral break is not visible here. However, if we were to plot the magnetic field spectrum at smaller scales, we would observe similar spectral break features as seen in Fig. 7.2 and Fig. 7.3.

In Fig. (7.5), we plot the present-day magnetic field strength defined at the comoving scale of 1 Mpc for three different reheating equations of state, $w_{\rm re} = 0.0,\ 1/3$, and 1.0, represented by three distinct colors. As observed, in the case of matter-like reheating ($w_{\rm re} = 0$), decreasing the reheating temperature $T_{\rm re}$ leads to a corresponding decrease in the present-day magnetic field strength. This behavior can be attributed to the fact that, for a matter-like expansion, achieving the same reheating temperature requires a longer duration of reheating. A lower reheating temperature implies a prolonged reheating phase, leading to greater dilution of the magnetic field.

Similarly, for kination-like reheating ($w_{\rm re} = 1$), where the background dilutes more rapidly, the duration of reheating required to reach a given $T_{\rm re}$ is shorter. Consequently, for a fixed reheating temperature, changing the equation of state results in significant variations in the present-day magnetic field strength, as illustrated in Fig. (7.5). The explicit dependence of the magnetic field strength on the reheating temperature is given in Eq.(7.34).

Magnetic field dominated universe: Bound on $T_{\rm re}$: So far, we have discussed the generation of a magnetic field from the curvature perturbations. While the magnetic field produced on large scales is generally modest in strength compared to that predicted by alternative mechanisms, the associated total energy density can still be substantial.

The magnetic energy density at conformal time η is given by

$$\rho_{\rm B}(\eta) = \int_{k_*}^{k_{\rm e}} \frac{{\rm d}k}{k}\,\rho_{\rm B}(k,\eta) = \frac{8\pi^2 H_{\rm e}^4}{9}\left(\frac{a_{\rm e}}{a}\right)^4\left(\frac{2+\beta}{3+2\beta}\right)^2\left[\frac{A_s}{n_s}\left(\frac{k_{\rm e}}{k_*}\right)^{n_s-1}+\frac{1}{2}\sqrt{\pi\delta}\frac{A_0 k_p}{k_{\rm e}}\right], \qquad (7.35)$$

where $H_{\rm e}$ is the Hubble parameter during inflation in conformal time, and $a_{\rm e}$ is the scale factor at the end of inflation. In this expression, we have taken the ultraviolet (UV) cutoff for the magnetic field spectrum to be $k_{\rm e}$, which represents the highest comoving wavenumber that can be excited by inflationary fluctuations.

During inflation, all perturbation modes originate in the Bunch-Davies vacuum while deeply inside the horizon (i.e., $k \gg aH$). As the Universe expands and these modes cross the horizon (i.e., when $k = aH$), they undergo a quantum-to-classical transition and their amplitudes become effectively frozen under adiabatic conditions. Since both metric and curvature perturbations arise from inflaton field fluctuations, the largest wavenumber that can be influenced corresponds to the maximum scale $k_{\rm e}$, which denotes the highest mode to exit the horizon before the end of inflation.

After their production, magnetic fields evolve adiabatically, diluting as a^{-4} due to cosmic expansion. In contrast, during reheating, the energy density of the inflaton field—which dominates the background until reheating ends—scales as $a^{-3(1+w_{\rm re})}$. For inflationary models with a stiff equation of state ($w_{\rm re} > 1/3$) during reheating, the background energy density dilutes faster than the magnetic field energy density. This leads to an effective enhancement of the magnetic field's fractional energy density, scaling as $a^{3w_{\rm re}-1}$.

We define the fractional magnetic energy density at the end of reheating as $\delta_{\rm B} = \rho_{\rm B}(\eta = \eta_{\rm re})/\rho(\eta = \eta_{\rm re})$, where $\rho(\eta)$ is the total background energy density. Using Eq. (7.35) and the expression for the reheating energy density, we obtain

$$\delta_B(\eta = \eta_{\rm re}) \simeq \frac{8\pi^2}{27}\left(\frac{H_{\rm e}}{M_{\rm P}}\right)^2\left(\frac{2+\beta}{3+2\beta}\right)^2\left[\frac{A_s}{n_s}\left(\frac{k_{\rm e}}{k_*}\right)^{n_s-1}+\frac{1}{2}\sqrt{\pi\delta}\frac{A_0 k_p}{k_{\rm e}}\right]\left(\frac{T_{\rm max}}{T_{\rm re}}\right)^{\frac{4(3w_{\rm re}-1)}{3(1+w_{\rm re})}}. \qquad (7.36)$$

Here, $T_{\rm max}$ denotes the maximum temperature of the universe, which depends on the inflationary energy scale. For instance, assuming $H_{\rm e} \simeq 10^{-5} M_{\rm P}$, we obtain $T_{\rm max} \simeq 10^{15}$ GeV.

As evident from the expression above, for reheating scenarios with $w_{\rm re} > 1/3$, the fractional energy density increases as the reheating temperature $T_{\rm re}$ decreases. Conversely, for $w_{\rm re} < 1/3$, the fractional energy density decreases with decreasing $T_{\rm re}$. For instance, in the case of kination ($w_{\rm re} = 1$), the scaling becomes $\delta_{\rm B}(T > T_{\rm re}) \propto T^{-4/3}$.

To avoid a universe dominated by magnetic fields, the reheating temperature must be bounded from below by the condition $\delta_B = 1$. In Fig. (7.6), we present the minimum allowed reheating temperature as a function of the equation of state parameter $w_{\rm re}$, for two different values of the peak scale of the curvature power spectrum. The gray curve corresponds to $k_p \simeq k_e$, while the blue curve represents $k_p \simeq 10^{25}\,\mathrm{Mpc}^{-1}$. For comparison, the cyan curve shows the result obtained using a simple slow-roll type curvature power spectrum as defined in Eq. (7.31).

We find that for $w_{\rm re} = 1.0$, in order to avoid a magnetic field–dominated universe before the completion of reheating, the minimum reheating temperature must satisfy $T_{\rm re} \gtrsim T_{\rm min} \simeq 4.3 \times 10^8\,\mathrm{GeV}$. In all cases, we consider the amplitude of the peak of the curvature power spectrum to be $A_0 \sim 0.1$.

Although we have explored the possibility of post-inflationary enhancement of gauge fields, such amplification is constrained by the conductivity of the early Universe. On small scales, it is indeed possible to enhance the curvature power spectrum in scenarios with low conductivity. However, in the presence of a highly conducting plasma, the post-inflationary production of gauge fields sourced by curvature perturbations is significantly suppressed. Even with a primordial black hole (PBH)-type curvature power spectrum, the magnetic field can at most be amplified by a factor of $\sim 10^5$, which remains far below current observational limits.

Given that our primary objective is to account for the large-scale magnetic fields with coherence lengths larger than 1 Mpc, this post-inflationary mechanism alone is insufficient. Additional dynamics are required to amplify magnetic fields on these large scales. In the following, we discuss how ultra-light axion-like particles (ALPs) can lead to further enhancement of the gauge field, particularly during the Dark Ages. During this epoch, ALPs re-enter the horizon and begin to oscillate, sourcing gauge fields efficiently through their coupling to photons.

It is important to note that post-inflationary amplification due to curvature perturbation is not strictly necessary for the secondary stage of gauge-field production. The same present-day magnetic field spectrum can be achieved even in the case of a simple slow-roll curvature power spectrum, provided that the axion-photon coupling constant is sufficiently large.

7.3 **Second stage:** Resonant amplification from oscillating ALPs after photon decoupling

In our previous section, we observed that inhomogeneous metric perturbation during inflation generates a large-scale magnetic field. However, as it is a second-order effect in perturbation, the strength turned out to be insufficient for the current observed bound. In this section, we therefore explore the second phase of gauge field production via ultralight Axion or Axion-like particles (ALPs). Axion is a pseudo-Nambu-Goldstone boson, which can naturally be very light due to the underlying shift symmetry of the system. It couples with the gauge field via the parity-violating coupling $\mathfrak{a} F\tilde{F}$ term. Let us suppose the axion is initially misaligned from its true vacuum. In that case, it can dynamically evolve into an oscillatory state, and the

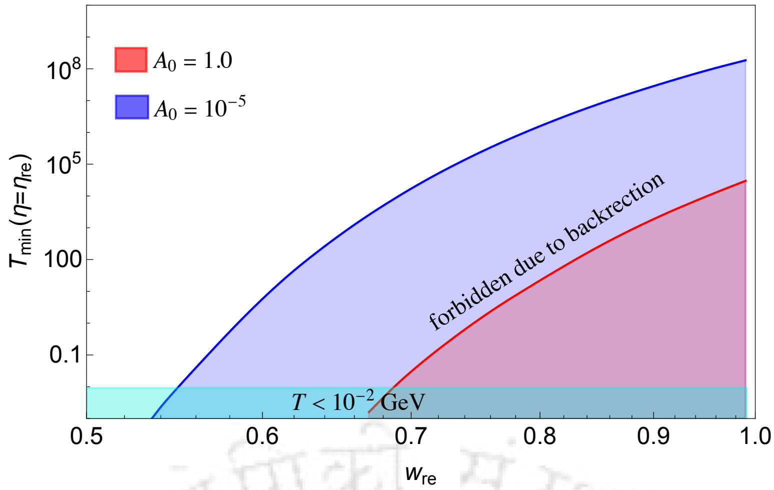

Figure 7.6: In the figure above, we plot the minimum background temperature, $T_{\rm min}$ (in GeV), as a function of the equation of state parameter during reheating, $w_{\rm re}$. The quantity $T_{\rm min}$ denotes the temperature below which the magnetic energy density exceeds the inflaton energy density, corresponding to the shaded region in the plot. We consider two scenarios for the curvature power spectrum, characterized by different peak scales: the gray curve corresponds to $k_p = k_{\rm e}$. Note that $k_{\rm e}$ is the mode which exits the horizon at the end of inflation. The blue curve represents $k_p = 10^{25}\,{\rm Mpc}^{-1}$. Here the cyan line illustrates the case of a slow-roll type curvature power spectrum. The red-shaded region marks the lower bound on the reheating temperature, given by $T_{\rm re} \simeq T_{\rm BBN} \simeq 0.01\,{\rm GeV}$, to ensure consistency with the Big Bang Nucleosynthesis.

coupled gauge field can be copiously produced if appropriate resonance conditions are satisfied. In this section, we will utilize this mechanism in the cosmological background and explore the possibility of resonant magnetic field production at a very large scale.

However, it is important to realize that after the inflation, the universe becomes filled with highly conducting plasma, and hence, any non-vanishing electric field propagating through it quickly decays due to the rapid response of free charges, and the magnetic field freezes into a constant value. The decay time scale is closely tied to the characteristic frequency of the plasma, which determines the interplay between the charge density oscillations and field dynamics. Any electric field mode frequency larger than the plasma frequency expressed as $\omega_p = (4\pi q^2 n_q/m_q)^{1/2}$ quickly decays within the time scale $\tau \propto \omega_p^{-1}$. Here, n_q is the number density of particles of charge q, and m_q is its mass. In the post-inflationary universe, the charge density is expected to be very large; therefore, production of the gauge field from any external source, such as an oscillating axion, may always seem to remain suppressed due to high conductivity.

Thanks to the recombination era in the early universe, the phase after the recombination, well known as the Dark Ages of the universe, comes to our rescue. Recombination is the phase during which neutral hydrogen and Helium are formed, and the plasma frequency becomes negligibly small. This significantly reduces the decay timescale so that the gauge field can no longer feel the conductivity. It is in this era that we will discuss the production of gauge fields due to axion-photon coupling. The Lagrangian density of the axion-photon system is given by

$$\mathcal{L} = -\frac{1}{2}\partial_\mu \mathfrak{a} \partial^\mu \mathfrak{a} - V(\mathfrak{a}) - \frac{1}{4}F_{\mu\nu}F^{\mu\nu} - \frac{\alpha}{4f_a}\mathfrak{a}\, F_{\mu\nu}\tilde{F}^{\mu\nu}\,, \tag{7.37}$$

where α is the dimensionless coupling parameter and f_a is the decay constant of the axion field denoted as '$\mathfrak{a}$'. Here $V(\mathfrak{a})$ is the potential of the axion (or ALPs) fields. The potential for axion-like particles (ALPs) is typically modeled as

$$V(\mathfrak{a}) = (m_a\, f_a)^2 \left[1 - \cos\left(\frac{\mathfrak{a}}{f_a}\right)\right]. \tag{7.38}$$

Here, m_a is the mass of the axion field. The axion is assumed to be a purely classical homogeneous field that rolls down to the minima of its potential. The equation of motion (EoM) for the homogeneous mode of the axion field $\mathfrak{a}$ and the Fourier modes of the gauge field A_λ in the FLRW background are given by [277, 406]

$$\mathfrak{a}'' + 2\mathcal{H}\mathfrak{a}' + a^2 V_{,\mathfrak{a}} = \frac{a^2\alpha}{f_a}\langle \mathbf{E}\cdot\mathbf{B}\rangle, \tag{7.39}$$

$$A_\lambda''(k,\eta) + \left(k^2 - \lambda\frac{\alpha k \mathfrak{a}'}{f_a}\right) A_\lambda(k,\eta) = 0, \tag{7.40}$$

Here, λ denotes the polarization index of the gauge field. It is important to note that the above two equations are valid only in the absence of photon scattering, and hence they are applicable during the post-recombination epoch up to reionization. The term on the right-hand side of the first equation, which describes the backreaction of a gauge field production, can be expressed as [277]

$$\langle \mathbf{E}\cdot\mathbf{B}\rangle = -\frac{1}{8\pi^2}\int \frac{dk}{k}\left(\frac{k}{a}\right)^4 \sum_{\lambda=\pm}\left[\frac{1}{k}\frac{d}{d\eta}\left(|\sqrt{2k}A_\lambda|^2\right)\right]. \tag{7.41}$$

Nevertheless, we will work in the parameter regime where such backreaction is small. A detailed study will be done in our future publication. From the homogeneous axion equation, one can quickly realize that when the dynamical Hubble parameter becomes close to the axion mass, the axion oscillates around its minimum, and we define the associated scale to as $k_{\rm osc} = a_{\rm osc}H_{\rm osc}$. Since the universe is matter-dominated by this time, we also see the scale factor evolving during this period as $a(\eta) = a_{\rm osc}(\eta/\eta_{\rm osc})^2 = a_{\rm osc}(x/x_{\rm osc})^2$. In terms of the dimensionaless time $x = k_{\rm osc}\eta$, and field variable $\psi = \mathfrak{a}/f_a$, we rewrite the above equation as ,

$$\frac{\partial^2\psi}{\partial x^2} + \frac{4}{x}\frac{\partial\psi}{\partial x} + \frac{m_a^2}{H_{\rm osc}^2}\left(\frac{x}{x_{\rm osc}}\right)^4 \sin\psi = 0, \tag{7.42a}$$

$$\frac{\partial^2 A_\lambda}{\partial x^2} + \left(\frac{k^2}{k_{\rm osc}^2} - \lambda\alpha\frac{k}{k_{\rm osc}}\frac{\partial\psi}{\partial x}\right) A_\lambda = 0. \tag{7.42b}$$

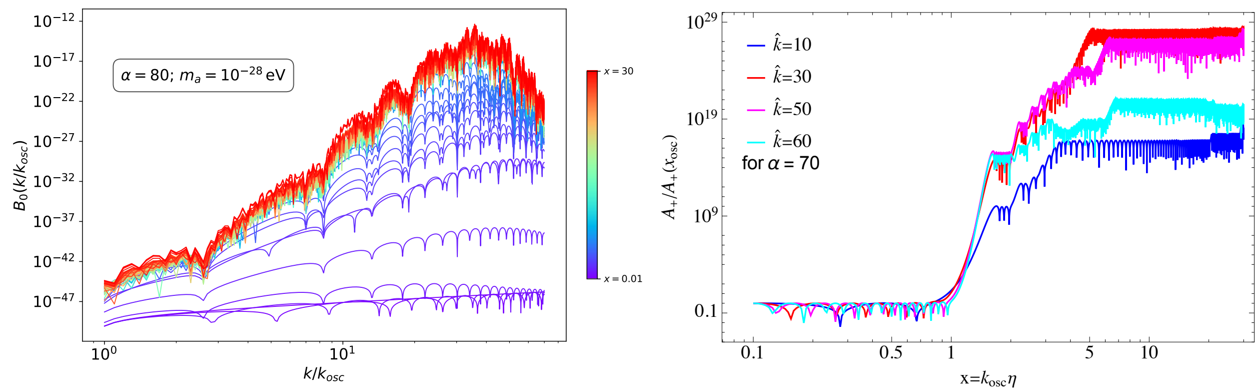

Figure 7.7: In the left panel, we present the time evolution of the comoving magnetic field as a function of the comoving wavenumber normalized by $k_{\rm osc}$, for a fixed value of the coupling $\alpha = 80$ and axion mass $m_a = 10^{-28}$ eV. The side color bar indicates the time evolution of the comoving magnetic field, starting from $x = k_{\rm osc}\eta \simeq 0.1$ and evolving up to $x \simeq 30$. At the initial time $x \simeq 0.1$, all relevant wavenumbers lie outside the horizon. The initial condition for the gauge field is set based on the inflationary production discussed earlier, which provides the seed configuration for subsequent evolution. When we set the initial magnetic field strength, then we simply consider a slow-roll type inflationary curvature power spectrum with $A_s \simeq 2.1 \times 10^{-9}$ with $n_s \simeq 0.965$. In the right panel, we show the late-time growth of the gauge field, normalized by its initial value, as a function of the dimensionless time variable $x = k_{\rm osc}\eta$. This plot corresponds to $\alpha = 70$, and we define the dimensionless wavenumber $\hat{k} = k/k_{\rm osc}$.

As stated earlier, we assume the axion to be frozen in at $\psi = 1.0$ and $\dot{\psi} = 0$ until the Hubble parameter becomes close to its mass after the recombination era. Once the condition $m_\chi \simeq 3H$ is met, the axion starts to oscillate in a neutral matter-dominated phase, leading to tachyonic enhancement of the gauge field production. We should remember that such production can continue to occur until the universe becomes reionized. Utilizing the entropy conservation, the oscillation scale at present can be easily calculated to be,

$$\frac{k_{\rm osc}}{a_0} \simeq \left(\frac{43 g_{s,*}(T_{\rm osc})}{11}\right)^{1/3} \frac{T_0 m_a}{3T_{\rm osc}} \simeq 0.01\,{\rm Mpc}^{-1} \left(\frac{m_a}{10^{-28}\,{\rm eV}}\right), \tag{7.43}$$

where $T_{\rm osc}$ is the temperature of the thermal bath when the axion starts to oscillate, and we can express this as a function of axion mass m_a as

$$T_{\rm osc} = \left(\frac{10}{g_{s,*}(T_{\rm eq})} \frac{m_a^2 M_{\rm P}^2}{T_{\rm eq}}\right)^{1/3} \simeq 0.28\,{\rm eV} \left(\frac{m_a}{10^{-28}\,{\rm eV}}\right)^{1/3}. \tag{7.44}$$

Here, $g_*(T_{\rm eq}) \simeq g_{s,*}(T_{\rm osc}) \simeq 3.36$ represents the number of relativistic degrees of freedom at the time of matter-radiation equality with the radiation temperature defined as $T_{\rm eq} \sim 0.8$ eV. Note the temperature of the radiation at the time of photon decoupling is defined as $T_{\rm rec} \simeq 3000{\rm K} \sim 0.26$ eV, and at the present time is defined as $T_0 = 2.7$ K $= 2.348 \times 10^{-4}$ eV. As pointed out earlier, after this, the universe became dominated by non-relativistic matter, mostly with neutral hydrogen. However, subsequently, cosmic reionization began when the

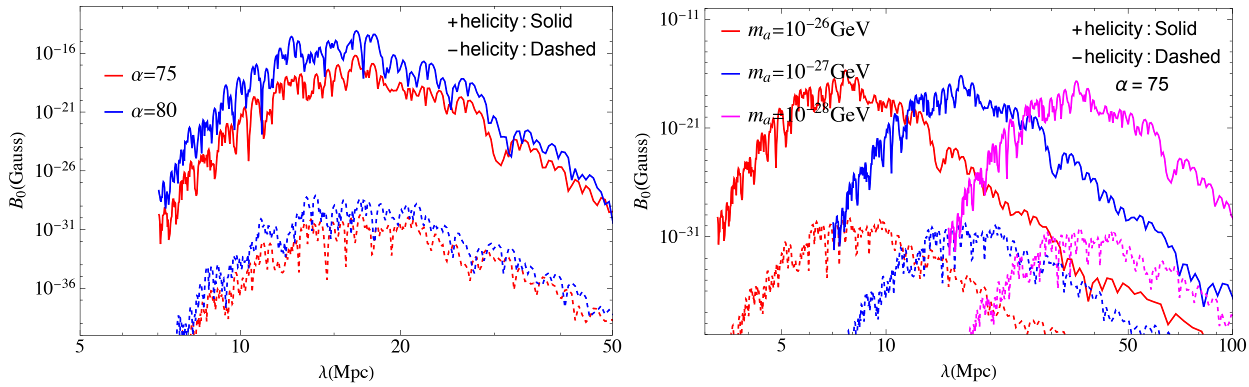

Figure 7.8: Present-day magnetic field strength B_0 (in Gauss unit) as a function of the comoving length scale λ (in Mpc). **Left panel:** Variation of B_0 for two different values of the coupling constant, $\alpha = 75$ (blue) and $\alpha = 80$ (magenta), with a fixed axion mass $m_a = 10^{-28}$ eV. **Right panel:** Dependence of B_0 on the axion mass, shown for $m_a = 10^{-28}$ eV (blue), 10^{-29} eV (magenta) and 10^{-30} eV (red), with a fixed coupling constant $\alpha = 80$. In both panels, solid lines represent positive-helicity (+) modes, while dashed lines correspond to negative-helicity (−) modes. For both spectra, we assume that the initial magnetic fields were generated during inflation due to a slow-roll-type curvature power spectrum, characterized by $A_s \simeq 2.1 \times 10^{-9}$ and $n_s \simeq 0.965$.

first stars formed, and early galaxies and quasars ionized most of the intergalactic medium. The temperature of the background radiation at the onset of reionization can be estimated to be in the range $T_{\rm reion} \simeq 0.002 - 0.005$ eV. And the time between these two distinct phases is known as the Dark Ages. As we are particularly interested in the production of gauge fields during the Dark Ages, the axion mass is required to lie within the range 10^{-28}–10^{-31} eV. The corresponding background temperatures at which the axion field begins to oscillate are given by $T_{\rm osc}(m_a = 10^{-28}\,{\rm eV}) \sim 0.28\,{\rm eV}$ and $T_{\rm osc}(m_a = 10^{-31}\,{\rm eV}) \sim 0.003\,{\rm eV}$, respectively. Utilizing Eqs. (7.43) and (7.44), we can compute the corresponding wavenumbers of modes that undergo excitation due to axion oscillations. Our analysis indicates that during the Dark Ages, characteristic length scales in the range 1 Mpc to 10^3 Mpc can be excited.

Analytical Spectral behaviors of Magnetic fields:

We can rewrite the EoM of the gauge field Eq.(7.42b) in the following fashion

$$\frac{\partial^2 A_\lambda}{\partial x^2} + \kappa^2 A_\lambda = 0\,, \quad \text{with} \quad \kappa = \sqrt{\left(\frac{k^2}{k_{\rm osc}^2} - \lambda\alpha \frac{k}{k_{\rm osc}}\frac{\partial \psi}{\partial x}\right)}\,. \tag{7.45}$$

Each mode evolves with an effective, time-dependent frequency denoted by κ. This implies that modes with long wavelengths, those satisfying the condition $k/k_{\rm osc} < |\lambda\alpha\psi'(x)|$, can experience exponential growth. During a matter-dominated era, the axion field $\psi(x)$ evolves as $\psi(x) = \psi_0 \sin(x^3)/x^3$, and consequently $\psi'(x) \sim 3\psi_0 \cos(x^3)/x$. Substituting this into the instability condition, one finds the mode $k_{\rm max} \sim (3\,\alpha\psi_0 k_{\rm osc})/x_{\rm osc}$, which represents the maximum wavenumber susceptible to the instability induced by axion oscillations. Modes with $k_{\rm osc} < k < k_{\rm max}$ are unstable and can grow due to the tachyonic instability, although this growth is limited to a finite range of frequencies determined by the dynamics of the background expansion. Employing the WKB approximation, the gauge field solution in the tachyonic regime, where $\kappa^2 < 0$, is given by

$$A_\lambda(x) = \frac{C_1}{\sqrt{|\kappa(x)|}} e^{\beta_c(x)} \,, \quad \text{where} \quad \beta_c(x) = \int_{x_{\rm osc}}^{x} \sqrt{\left(\frac{k^2}{k_{\rm osc}^2}\right) - \alpha \frac{k}{k_{\rm osc}} \frac{\partial \psi}{\partial x'}} dx' \,. \tag{7.46}$$

As $\kappa > 0$, the last term of the above equation is oscillatory in nature. Note that axion is frozen until $x_{\rm osc}$, we can safely set the the initial condition at $x = x_{\rm osc}$, $A(x = x_{\rm osc}) = A_{\rm osc}$, where $A_{\rm osc}$ is the initial amplitude of the gauge field produced due to the inflationary curvature perturbation discussed in the beginning. Now, utilizing the initial condition, we get the approximate solution of the gauge field as

$$A_\lambda(x) = A_{\rm osc}(k) \left(\frac{|\kappa(x_{\rm osc})|}{|\kappa(x)|}\right)^{1/2} e^{\beta_c(x)} \,. \tag{7.47}$$

Here, β_c quantifies the enhancement of the gauge field during axion oscillations. It is important to note that the two polarization modes, $\lambda = \pm$, experience instability at different times. As a result, the produced electromagnetic field acquires a helical nature.

Now, utilizing the Eq.(7.32) and Eq.(7.47), we can immediately compute the spectral behavior of the present-day magnetic field at large scale as

$$B_0 = \sqrt{\mathcal{P}_{B_0}(k)} \propto k^2 A_\lambda(x_0) \propto k^{3/2} e^{\beta_c(k,\lambda,\alpha)} \,. \tag{7.48}$$

This is one of the main results of the present paper. We can also estimate the maximum amplitude of the produced magnetic field by finding the maximum value of β_c.

Fig. (7.7) illustrates the evolution of the generated magnetic field. The left panel shows the time evolution of the comoving magnetic field spectrum as a function of $k/k_{\rm osc}$, for a coupling constant $\alpha = 80$. In this analysis, the axion mass is fixed at $m_a = 10^{-28}\,$eV. The color bar represents the dimensionless time variable x. As time progresses, we observe that the magnetic field spectrum initially grows and eventually saturates, indicating the end of significant amplification. The right panel shows the time evolution of individual magnetic field modes as a function of the dimensionless time variable $x = k_{\rm osc}\eta$, for a fixed coupling parameter $\alpha = 70$. It indicates the resonant growth of the gauge field in the oscillating axion background. Once the axion oscillation amplitude reduces sufficiently, the growth ceases to exist.

To study the spectral behavior of the magnetic field, we plot the present-day field strength $B_0(\lambda)$ as a function of comoving wavelength λ (in Mpc) in Fig. (7.8). The left panel shows results for two values of the coupling parameter: $\alpha = 80$ (blue) and $\alpha = 75$ (magenta). Solid lines represent the positive helicity modes (A_+), while dashed lines indicate the negative helicity modes (A_-). For this plot, we fix the axion-like particle (ALP) mass at $m_a = 10^{-28}\,$eV. As expected, a stronger coupling (α) leads to greater magnetic field amplification. We also observe a difference between the two helicity modes. This is because each mode experiences instability at different times, leading to different amplification levels.

The right panel of Fig. (7.8) explores how the magnetic field spectrum changes with the ALP mass. Here, we vary the mass over three values: $m_a = 10^{-28}$, 10^{-29}, and 10^{-30} eV, while keeping the coupling fixed at $\alpha = 80$. As before, solid lines correspond to A_+ modes, and dashed lines to A_- modes. We find that lighter ALPs shift the peak of the magnetic field spectrum to larger length scales. This shift occurs because lighter ALPs start oscillating later in cosmic history, when longer wavelengths have already entered the horizon. As a result, gauge fields with larger wavelengths are excited more efficiently..

In Fig. (7.9), we plot the present-day magnetic field strength as a function of wavelength for the same coupling constant $\alpha = 80$, using the same three values of the ALP mass. Since these relatively light ALPs begin oscillating after photon decoupling, they preferentially amplify gauge fields on the corresponding length scales, as shown in the figure. We also include current observational bounds on large-scale magnetic fields for comparison. From the plot, it is clear that for coupling values $\alpha > 70$, the ALPs can boost magnetic field strengths on Mpc scales to levels consistent with all existing constraints. Specifically, for $\alpha = 80$, the maximum field strength achieved at around 1 Mpc is $B_0(\sim 1\,\mathrm{Mpc}) \sim 10^{-10}$ Gauss. Although larger values of the coupling parameter $\alpha > 80$ can be considered, they tend to produce a significant amount of gravitational waves (GWs) at CMB scales. This may lead to a violation of current bounds on the tensor-to-scalar ratio. The final section will discuss the gravitational wave spectrum in detail.

Computing the Relic Density of the Axion:

The initial energy density of the axion can be approximated as

$$\rho_{\mathfrak{a}}(T_{\rm osc}) \simeq \frac{1}{2} m_a^2 f_a^2 \theta_i^2, \tag{7.49}$$

where f_a is the decay constant of the axion, and θ_i is the initial misalignment angle.

The energy density redshifts to the present day due to the expansion of the background universe. Axions begin to oscillate when the background temperature equals $T_{\rm osc}$, i.e., $T \simeq T_{\rm osc}$. For $T < T_{\rm osc}$, the axion behaves like non-relativistic matter, and its energy density dilutes as $\rho_\chi \propto a^{-3}$.

Assuming that no significant entropy production occurs after reheating, which is a reasonable approximation of the conservation of entropy, $s(T)a^3 = \text{const}$, allows us to express the redshift factor as

$$\frac{a_{\rm osc}}{a_0} = \frac{T_0}{T_{\rm osc}} \left(\frac{g_*(T_0)}{g_*(T_{\rm osc})} \right)^{1/3}, \tag{7.50}$$

where $g_*(T)$ is the effective number of entropy degrees of freedom at temperature T.

The relic density parameter $\Omega_{\mathfrak{a}} h^2$ is define as $\Omega_{\mathfrak{a}} h^2 = \rho_{\mathfrak{a}}(T_0)/\rho_{\rm cri}(T_0)$. Now utilizing Eq.(7.50), we can find that

$$\Omega_{\mathfrak{a}} h^2 \simeq 0.12\, \theta_i^2 \left(\frac{f_a}{10^{12}\ \mathrm{GeV}}\right)^2 \left(\frac{m_a}{10^{-5}\ \mathrm{eV}}\right)^{1/2} . \tag{7.51}$$

As previously discussed, at early times when $H \gg m_a$, the axion field remains in the slow-roll regime with $\dot{\mathfrak{a}} \approx 0$. In this phase, the equation of state of the axion is given by $w_{\mathfrak{a}} = P_{\mathfrak{a}}/\rho_{\mathfrak{a}} \approx -1$, indicating that the field behaves as a dark energy component. Here, $\rho_{\mathfrak{a}}$ and $P_{\mathfrak{a}}$ represent the energy density and pressure of the background axion field, respectively. At later times, when $H \ll m_a$, the field undergoes coherent oscillations around the potential minimum, leading to an equation of state that oscillates around zero. Consequently, the energy density follows the scaling relation $\rho_{\mathfrak{a}} \propto a^{-3}$, which is characteristic of non-relativistic matter. This implies that after the onset of oscillations, the axion behaves as a dark matter-like component. However, note that in the axion mass range of our interest $m_a \leq 10^{-28}$ eV, the onset of oscillations $a_{\rm osc} > a_{\rm eq}$ occurs much later compared to the matter-radiation equality. Therefore, axions cannot constitute the entirety of the dark matter component of the universe. Observational constraints from galaxy surveys place an upper bound on the relic density of axions, $\Omega_{\mathfrak{a}} h^2 < 0.004$, for axion masses in the range 10^{-31} eV $< m_a < 10^{-28}$ eV at 95% confidence level [407]. Utilizing the abundance equation for the axion Eq.(7.51), one obtains a constraint on the axion decay constant,

$$f_a \lesssim 9.42 \times 10^{16}\, (10^{-28}\mathrm{eV}/m_a)^{1/4}\, \mathrm{GeV}. \tag{7.52}$$

Here we assume the initial angle of misalignment $\theta_i \simeq 1$. Specifically, for ultralight axions in this mass range, we find that the maximum allowed decay constant is $f_a < 9.42 \times 10^{16}$ GeV for $m_a = 10^{-28}$ eV, and that is sub-Planckian.

In our analysis, we restrict the coupling parameter to $\alpha < 100$ to ensure the generation of sufficiently strong primordial magnetic fields while remaining within the regime where back-reaction is under control. This choice of α, together with the corresponding values of f_a, is also consistent with the current upper bound on the axion–photon coupling, $g_{a\gamma} = \alpha/f_a \ll 5.8 \times 10^{-11}$ GeV^{-1} [408]. Moreover, the resulting magnetic field strength is consistent with the current observational constraints on large-scale magnetic fields [252–257, 391].

To avoid the backreaction problem, we further restrict our analysis to the parameter region where the total energy density of the produced gauge field always remains smaller than the energy density of the axion field. For coupling strengths $\alpha \gtrsim 85$, the energy density of the gauge field becomes comparable to that of the axion, and the backreaction on the axion dynamics can no longer be neglected. A proper treatment of this regime requires solving the full coupled system including the backreaction effects. In that case, larger values of α can be considered. Although the magnetic field strength at CMB scales does not change significantly, the resulting magnetic field spectrum becomes considerably broader.

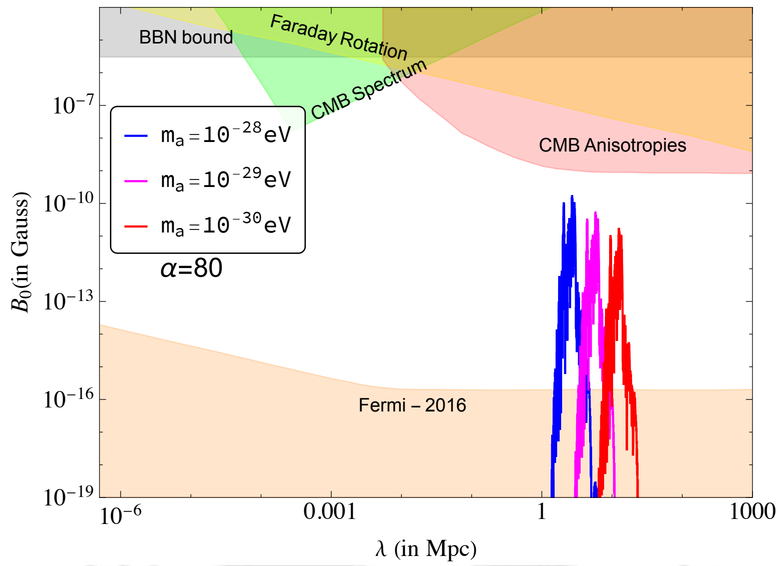

Figure 7.9: In the figure, we have plotted the present-day magnetic field strength (in Gauss) as a function of the length scale (λ) along with different observational bounds. Here, we consider a fixed coupling parameter $\alpha = 80$ with different colors indicating three different masses of the axion field.

7.4 Secondary Gravitational Waves due to Magnetic Fields

The presence of primordial magnetic fields in the early universe can serve as a crucial source of gravitational waves. Metric perturbations induce anisotropic stress associated with helical or non-helical magnetic fields, thereby generating a stochastic gravitational wave background (SGWB). This mechanism provides unique insights into the dynamics of axions and gauge fields.

As discussed, in the presence of ultralight axion-like particles (ALPs), the gauge field can be excited due to the oscillations of ALPs via a $\mathfrak{a}F\tilde{F}$ coupling. This excitation can significantly contribute to the production of gravitational waves.

Considering the tensor fluctuations, the FLRW metric can be written as

$$ds^2 = a^2(\eta)\left[-d\eta^2 + (\delta_{ij} + h_{ij})dx^i dx^j\right] . \tag{7.53}$$

The tensor mode h_{ij} is the traceless tensor, i.e., $\partial^i h_{ij} = h^i_i = 0$. In Fourier space, the equation of motion for the gravitational wave amplitude 'h', for either polarization h_+ or h_-, becomes [220–222, 232, 234, 409]:

$$h''_{\mathbf{k}} + 2\mathcal{H}h'_{\mathbf{k}} + k^2 h_{\mathbf{k}} = \mathcal{S}_\lambda(\mathbf{k}, \eta), \tag{7.54}$$

where $\mathcal{S}_\lambda$ is the source term. Here, we consider electromagnetic fields as the source term, which can be written as [220–222, 229, 232, 234, 409]

$$\mathcal{S}_\lambda(\mathbf{k},\eta) = -\frac{1}{a^2(\eta)}\int \frac{d^3q}{(2\pi)^{3/2}} e_\lambda^{ij}(\mathbf{k})\Big\{A_i'(\mathbf{q},\eta)A_j'(|\mathbf{k}-\mathbf{q}|,\eta) \\ -\epsilon^{iab}q_a A_b(\mathbf{q},\eta)\epsilon^{icd}(k-q)_c A_d(|\mathbf{k}-\mathbf{q}|,\eta)+\dots\Big\}. \tag{7.55}$$

Here $e_\lambda^{ij}(\mathbf{k})$ is the polarization tensor corresponding to the mode with wave vector '$\mathbf{k}$' and the polarization index λ. ϵ^{iab} is the three dimensional flat space Levi-civita symbol. As our source is helical so we chose circular polarization basis which can be define as $e_\lambda^{ij} = -\frac{1}{2}\left(\hat{e}^1 \pm i\ \hat{e}^2\right)_i \times \left(\hat{e}^1 \pm i\ \hat{e}^2\right)_j$, [222]. Here $\hat{e}^1$ & $\hat{e}^2$ are a set of mutually orthonormal basis vectors of our coordinate system. Whereas the tensor power spectrum $P_{\rm T}(k,\eta)$ is define as $P_{\rm T}(k,\eta) = \frac{k^3}{2\pi^2}\left|h_{\mathbf{k}}(k,\eta)\right|^2$ [117, 119, 220–222, 229, 230, 232, 234, 409]. It is convenient to express the tensor power spectrum as the sum of two components: one arising from vacuum fluctuations and the other from source terms. These two contributions are uncorrelated, so we write them as:

$$P_{\rm T}(k,\eta) = P_{\rm T}^{\rm pri}(k,\eta) + P_{\rm T}^{\rm sec}(k,\eta), \tag{7.56}$$

where $P_{\rm T}^{\rm pri}(k,\eta)$ refers to vacuum production, and $P_{\rm T}^{\rm sec}(k,\eta)$ is due to the EM field. The primary one is produced due to quantum fluctuations, which are well-known and near CMB scale; the spectrum remains scale invariant (for instance, see [204–207, 229]). Here, we mainly focus on the secondary productions of the GWs due to late time dynamics, and we can write the tensor power spectrum induced by the EM field in terms of the electromagnetic power spectrum as [229]

$$P_{\rm T}^{\rm sec}(k,\eta_0) = \frac{2}{M_{\rm P}^4}\int_0^\infty \frac{dq}{q}\int_{-1}^{1} d\mu \frac{\mathcal{F}(\mu,\beta,\lambda)}{[1+(q/k)^2-2\mu(q/k)]^{3/2}} \\ \times\left[\int_{\eta_{\rm osc}}^{\eta_f} d\eta_1 a^2(\eta_1)\mathcal{G}_{\mathbf{k}}(\eta_f,\eta_1)\mathcal{P}_{\rm B}{}^{1/2}(q,\eta_1)\mathcal{P}_{\rm B}{}^{1/2}(|\mathbf{k}-\mathbf{q}|,\eta_1)\right]^2. \tag{7.57}$$

The resonant production of the gauge field due to the oscillating axion is typically narrowly peaked both in time and momentum. Therefore, we perform the above integral Eq.(7.54) within $\eta_{\rm osc}$ and η_f from the beginning and end of gauge field production. Beyond this point, the magnetic field energy density dilutes as a^{-4} due to the expansion of the background universe. Here $\mathcal{G}_{\mathbf{k}}(\eta,\eta_1)$ is the Green's function associated with Eq.(7.54), and the Green's function in the matter-dominated phase is written as [229]

$$\mathcal{G}_{\mathbf{k}}^{\rm ra}(k,\eta,\eta_1) = \Theta(\eta-\eta_1)\frac{1}{k}\frac{x_1}{x^3}\left\{-(x-x_1)\cos(x-x_1)+(1+xx_1)\sin(x-x_1)\right\}, \tag{7.58}$$

where we have defined $x = k\eta$ is a dimensionless variable.

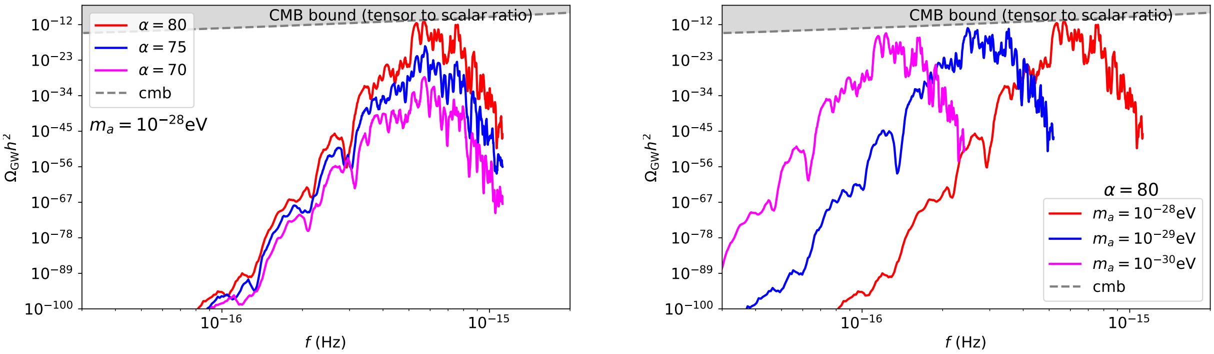

Figure 7.10: In the figure above, we present the spectrum of stochastic gravitational waves (SGWs) induced by the magnetic field generated through the oscillation of axion-like particles (ALPs) at late times, after recombination. The quantity $\Omega_{\rm GW}h^2$ is plotted as a function of the comoving frequency f (in Hz). The left panel illustrates the SGW spectrum for a fixed axion mass, $m_a = 10^{-28}$ eV, with different colors representing various values of the coupling parameter α. In the right panel, we explore the dependence of the SGW spectrum on the ALP mass while keeping the coupling parameter fixed at $\alpha = 80$. In both panels, the gray-shaded region denotes the CMB bound on the tensor-to-scalar ratio. The black dotted line in both figures is the future CMB-S4 observation of the tensor-to-scalar ratio corresponding to $r \simeq 10^{-4}$. For both spectra, we assume that the initial magnetic fields were generated during inflation due to a slow-roll-type curvature power spectrum, characterized by $A_s \simeq 2.1 \times 10^{-9}$ and $n_s \simeq 0.965$.

The tensor power spectrum is proportional to $B_0^4(k)$ and can be expressed as

$$P_{\rm T}^{\rm sec}(k,\eta_f) \propto \frac{B_0^4(k)x_{\rm eq}^8}{M_{\rm P}^4 k^4 a_{\rm eq}^4}\,\mathcal{F}_{n_{\rm B}}(k) \times \overline{\mathcal{I}^2(k,\eta_{\rm osc},\eta_f)}\,, \tag{7.59}$$

where $\overline{\mathcal{I}^2(k,\eta_{\rm osc},\eta_f)}$ carry the time integral part and $\mathcal{F}_{n_{\rm B}}(k)$ carry the momentum integral part of the above Eq.(7.57). Here, the $\overline{\mathcal{I}^2(k,\eta_{\rm osc},\eta_f)}$ is the oscillation average of the time integral part. In the above, we have replaced the scale factor during the matter-dominated era as $a(\eta) = a_{\rm eq}(\eta/\eta_{\rm eq})^2$.

Now the dimensionless spectral energy density (SED) of secondary GWs *today* (i.e., at η_0) is defined as $\Omega_{\rm GW}(k,\eta_0) = \rho_{\rm gw}(k,\eta_0)/3H_0^2M_{\rm P}^2$, where H_0 denotes the present value of the Hubble parameter. We can further express the SED of SGWs in terms of radiation energy density as [229]

$$\Omega_{\rm GW}h^2 \simeq \Omega_{\rm ra}^0 h^2\ \Omega_{\rm GW}(k,\eta_f)\,, \tag{7.60}$$

where $\Omega_{\rm ra}^0 h^2 \simeq 4.3 \times 10^{-5}$, fractional radiation energy density at present time.

In Fig. (7.10), we present the present-day gravitational wave (GW) spectrum as a function of the observable frequency f (in Hz) for two different scenarios.

In the left panel of Fig. (7.10), we illustrate the dependence of the stochastic gravitational wave (SGW) spectrum on the coupling parameter α for a fixed axion-like particle (ALP) mass,

$m_a = 10^{-28}$ eV. We observe that as the coupling strength increases, the amplitude of the GW spectrum also increases, making it potentially detectable by future CMB experiments [404]. However, the overall shape of the spectrum remains unchanged, and in all cases, the peak appears at the same position. This behavior arises because the peak position of the GW spectrum is determined by the magnetic field spectrum, which, in turn, depends on the ALP mass.

In the right panel of Fig. (7.10), we plot $\Omega_{\rm GW}h^2$ as a function of f (in Hz), where different colors represent different values of the ALP mass, which oscillates after recombination. Here, we fix the coupling constant at $\alpha = 80$. We observe that varying the ALP mass leads to a significant shift in the peak position of the GW spectrum. This is expected, as a lower ALP mass implies a later onset of oscillations, and only those modes that re-enter the horizon during this period experience tachyonic instability. Additionally, we find that decreasing the ALP mass results in a gradual decrease in the peak amplitude of the GW spectrum for the same coupling $\alpha = 80$. This effect can be attributed to the initial spectral behavior of the magnetic field, which originates from inflationary curvature perturbations. In this study, we have also found that the generated magnetic field exhibits a helical nature, which naturally implies the production of helical gravitational waves (GWs). This results in an asymmetry between the two polarization modes of the tensor power spectrum, leading to a distinctive signature in the B-mode polarization of the cosmic microwave background (CMB). If future CMB experiments, such as CMB-S4 [404], detect any helical features, it will serve as a clear indication of the existence of a helical magnetic field. Moreover, such a detection could indirectly probe the presence of ultralight axion-like particles.

Furthermore, we find that consistency with the tensor-to-scalar ratio constraints from Planck 2018 [11] imposes a strong bound on the coupling parameter α. Specifically, we observe that $\alpha = 80$ leads to significant GW production at CMB scales, whereas values exceeding $\alpha > 80$ would immediately violate the current observational constraints on the tensor-to-scalar ratio.

7.5 Conclusion

Observations across different astrophysical and cosmological scales indicate that our universe is fully magnetized. However, explaining the origin of these cosmic magnetic fields remains a significant challenge. A natural mechanism for generating such fields is highly desirable, yet existing models often face issues such as strong coupling or backreaction. Even in cases where these issues are circumvented, the generation of large-scale magnetic fields typically requires non-trivial couplings with the gauge field, whose origins remain elusive.

In this chapter, we address this issue by investigating the generation of magnetic fields across all relevant length scales from curvature perturbations. These perturbations naturally arise from quantum fluctuations during inflation. In the presence of curvature, the spacetime metric exhibits deviations from perfect spatial flatness, and these metric fluctuations can break the conformal flatness property of the background, leading to non-trivial gauge field production at higher orders in perturbation theory. Exploiting this breaking, we first derive how curvature-induced metric fluctuations induce gauge field production and determine their impact on the resulting magnetic field spectrum. As expected, the resulting magnetic field strength remains small due to the relatively small amplitude, as it was generated gravitationally. Interestingly, we find that a primordial black hole (PBH)-type curvature power spectrum can enhance the magnetic field strength by up to a fourth order of magnitude compared to the case with a simple slow-roll type curvature power spectrum. For example, we consider a scale non-invariant power spectrum with a peak frequency k_p, typically associated with the formation of primordial black holes (PBHs). For wavenumbers $k < k_p$, the magnetic field strength becomes sensitive to the peak frequency of the curvature perturbations, resulting in an amplification of the magnetic field by up to four orders of magnitude, even at Cosmic Microwave Background (CMB) scales. We found present day strength of the magnetic field follows $B_0 \propto \sqrt{A_0 k_p} k^{\frac{3}{2}}$ for $k < k_p$, and $\sqrt{A_s} k^{\frac{3}{2}}$ for $k > k_p$. For a PBH-type spectrum, if we assume $A_0 \simeq 1$, the maximum magnetic field strength on the 1 Mpc scale is found to be of the order $B_0 \sim 10^{-41}$ G, whereas for a slow-roll type curvature spectrum, the corresponding strength is approximately $B_0 \sim 10^{-45}$ G. Moreover, a distinct scaling behavior emerges in the magnetic field spectrum, which follows a power-law dependence $B(k) \propto k^{3/2}$. The total energy density associated with the generated magnetic field is found to be substantial and may have a significant impact on the evolution of the early universe.

Additionally, we explore the effects of the post-inflationary reheating phase on the evolution of gauge fields. Our analysis reveals that non-trivial reheating scenarios can significantly enhance gauge field production. In scenarios where the reheating equation-of-state parameter satisfies $w_{\rm re} > 1/3$, we find that the magnetic field can carry a significant fraction of the total energy density. This enhancement has the potential to influence the standard predictions of Big Bang Nucleosynthesis (BBN). In particular, we demonstrate that in kination-like reheating scenarios with $w_{\rm re} = 1.0$ and a background temperature of $T \sim 10^8$ GeV , the energy density of the magnetic field can surpass that of the inflaton. Such a situation could lead to a magnetically dominated universe during the post-inflationary epoch, thereby altering the dynamics of BBN and the subsequent thermal history of the universe.

As previously discussed, the gravitationally generated magnetic fields sourced by inflationary curvature perturbations are typically too weak on large scales ($\sim$ Mpc) to meet current observational bounds. Therefore, additional dynamics are required to further amplify these seed magnetic fields at later times. In this context, we explore the possibility of axion-photon coupling as a mechanism for such enhancement. Axions naturally couple to gauge fields through the Chern-Simons term $\frac{\alpha\,\mathfrak{a}}{f_a} F\tilde{F}$, where α is the dimensionless coupling constant and f_a is the axion decay constant. When the axion field begins to oscillate, which occurs when the Hubble parameter satisfies $3H \simeq m_a$ (with m_a denoting the axion mass), a tachyonic instability is induced in the gauge field sector. We find that for coupling constants in the range $60 < \alpha < 80$

and axion masses 10^{-31} eV $\lesssim\ m_a \lesssim 10^{-28}$ eV, the gauge fields originally generated by inflationary curvature perturbations can be significantly amplified. As a result, the magnetic field strength can reach values as high as $B_0 \sim 10^{-10}$ G on Mpc scales.

In the final section, we analyze the generation of secondary gravitational waves (SGWs) induced by magnetic fields in the presence of axions. Our results indicate a substantial production of SGWs, with amplitudes potentially within the sensitivity reach of future Cosmic Microwave Background (CMB) experiments, such as CMB-S4. To remain consistent with current observational bounds on the tensor-to-scalar ratio, we find that the axion-photon coupling strength must satisfy $\alpha \leq 80$. An intriguing feature of this mechanism is the natural generation of helical magnetic fields, which in turn lead to the production of helical gravitational waves. The future detection of helical B-mode polarization in the CMB would provide compelling evidence for the presence of such helical magnetic fields, thereby lending support to the proposed amplification mechanism. Moreover, we observe that the axion mass plays a crucial role in determining the peak frequency of the resulting gravitational wave spectrum. This mass-dependent feature imprints a distinctive signature on the CMB power spectrum, offering a promising observational channel to probe the existence of ultra-light axions through precision CMB measurements.

Chapter 8

Conclusions and Outlook

8.1 Conclusions

The magnetic field is one of the key components of our Universe. A wide range of observations indicate that the Universe is permeated by magnetic fields on different length scales. Several mechanisms have been proposed in the literature to explain the origin of these cosmic magnetic fields, including scenarios with an inflationary origin [47, 235–237, 258, 259, 262–267, 270, 275, 311, 327, 328, 331, 372, 388, 389, 410], post-inflationary processes such as cosmological phase transitions [231, 284–286], and mechanisms involving topological defects [287, 303–307, 309, 411, 412]. Astrophysical mechanisms have also been suggested; however, such scenarios face difficulties in explaining the origin of magnetic fields in cosmic voids, which have been inferred from high-energy gamma-ray observations [319–321].

Among the proposed scenarios, inflationary magnetogenesis is often considered one of the most promising mechanisms for explaining magnetic fields on very large scales. Nevertheless, most models of inflationary magnetogenesis suffer from well-known problems such as the strong coupling and backreaction issues [235,236,238]. Furthermore, in much of the existing literature, it is commonly assumed that the Universe becomes radiation-dominated immediately after the end of inflation, implying that the inflaton field decays instantaneously into radiation. In such a scenario, the conductivity of the Universe rapidly becomes very large, leading to the rapid decay of the electric field, while the magnetic field on superhorizon scales evolves adiabatically.

Although the instantaneous reheating scenario provides a convenient approximation, in a realistic situation the decay of the inflaton field and the subsequent thermalization of the Universe require a finite amount of time. Since inflation and reheating are closely connected, non-trivial reheating dynamics can leave observable imprints on several cosmological relics, including the present-day abundance of dark matter, the spectrum of gravitational waves, as well as the strength and spectrum of cosmic magnetic fields.

The reheating phase therefore plays a crucial role in the thermal history of the Universe. During this epoch, the Universe transitions from a cold inflationary phase to a hot plasma state, and all fundamental particles are produced, thereby establishing the appropriate initial conditions for Big Bang Nucleosynthesis (BBN). Because reheating occurs at very early times and the relevant dynamics predominantly take place on very small scales, it is extremely challenging to probe this epoch using large-scale cosmological observations such as the cosmic microwave background (CMB). As a result, there are currently no strong observational constraints on the detailed dynamics of reheating, and its observational signatures remain largely unexplored.

In this thesis, we address two main questions: how the post-inflationary dynamics during the reheating era can leave observable imprints on large-scale magnetic fields, and how the dynamics of reheating may be probed through future gravitational wave observations.

In Chap. 4, we discussed the non-trivial effects of reheating dynamics on large-scale magnetic fields and their observational signatures in the gravitational wave spectrum. In this chapter, we consider a simple Ratra-type magnetogenesis model with the coupling $\mathcal{L}_{\rm EM} \supset \frac{1}{4} f_1^2(\phi) F_{\mu\nu} F^{\mu\nu}$ [316], which can generate non-helical magnetic fields [117, 118, 235, 236, 238]. To explain the large-scale magnetic fields observed in cosmic voids, it has been shown that this class of models typically suffers from either the strong coupling problem or the backreaction problem.

In this work, we demonstrate that if post-inflationary energy transfer from the electric field to the magnetic field is allowed, both the strong coupling and backreaction problems can be alleviated, while still successfully explaining the observed large-scale magnetic fields. This energy conversion is effective only for those modes that remain outside the horizon during the reheating era. Moreover, the efficiency of this energy transfer crucially depends on the electrical conductivity of the Universe during reheating, which must remain sufficiently small [117].

To illustrate this effect, we consider two extreme limiting cases. In the first scenario, we assume vanishing electrical conductivity, whereas in the second scenario we consider infinite electrical conductivity. In the case of zero electrical conductivity, both the electric and magnetic fields are present during the reheating era. To avoid the strong coupling problem, we work in the regime where the electric field dominates during inflation. In this situation, the electric energy density on large scales can transfer its energy to the magnetic field, thereby enhancing the large-scale magnetic field strength. The efficiency of this conversion depends on two main factors: the initial energy difference between the electric and magnetic components on the relevant large scales, and the duration of the reheating phase.

On the other hand, in the limit of infinite electrical conductivity, the electric field decays almost instantaneously and is effectively erased from the Universe. As a result, no further conversion of electric energy into magnetic energy can occur during reheating.

In the second part of this chapter, we discuss the possible detection of this class of magnetogenesis models through gravitational wave observations. We find that the post-inflationary dynamics not only modify the spectral behavior of the present-day gravitational wave spectrum but can also significantly enhance its overall amplitude, particularly in scenarios where the reheating phase is characterized by a stiff equation of state, $w_{\rm re} > 1/3$. Interestingly, the resulting gravitational wave spectra can intersect the projected sensitivity curves of future detectors and may therefore be detectable by experiments such as LISA, DECIGO, and BBO.

In Chap. 5, we discussed an alternative magnetogenesis scenario in which the gauge field production continues even after inflation. In particular, we considered a sawtooth-type coupling that allows the generation of electromagnetic fields during both the inflationary and post-inflationary phases. In the previous chapter, we assumed that the magnetic field is generated only during inflation, after which a partial conversion of electric field energy density into magnetic field energy density may occur during reheating, while the total comoving electromagnetic energy density remains conserved.

In contrast, in this scenario we consider a coupling that allows the continuous production of electromagnetic fields during both phases. This type of model is particularly appealing because it can simultaneously avoid the strong coupling and backreaction problems. In our previous analysis, we found that explaining the observed large-scale magnetic fields, even after accounting for post-inflationary energy conversion, requires the reheating equation of state to satisfy $w_{\rm re} \geq 1/3$. However, if the post-inflationary evolution follows a matter-like behavior with an average equation of state $w_{\rm re} = 0$, then even for the lowest possible reheating temperature, $T_{\rm re} = 0.01$ GeV, the maximum present-day magnetic field strength that can be achieved is only $B_0(1\ \mathrm{Mpc}) \simeq 10^{-28}$ Gauss. This implies that, for a matter-like post-inflationary evolution with vanishing electrical conductivity, the Ratra-type magnetogenesis model cannot successfully explain the large-scale magnetic fields.

Motivated by this limitation, we therefore investigated the sawtooth-type coupling scenario. We find that, with an appropriate choice of the coupling parameters and reheating dynamics, it is possible to generate a significant amount of large-scale magnetic fields, sufficient to explain the lower bounds inferred from gamma-ray observations.

In addition, we studied the production of secondary gravitational waves generated in this class of magnetogenesis models. Our analysis shows that these scenarios can produce a substantial gravitational wave background that may be detectable by future gravitational wave experiments. We also find that the resulting present-day gravitational wave spectrum exhibits notable differences compared to the previous scenario. Therefore, detecting such gravitational wave signals and analyzing their spectral properties may provide a powerful way to distinguish between different magnetogenesis models.

In the first two works, we discussed how primordial magnetic fields can generate a significant amount of secondary gravitational waves (SGWs). In Chap. 6, we explore another important consequence of the presence of primordial magnetic fields. In particular, we study an alternative mechanism for primordial black hole (PBH) formation, in which primordial magnetic fields can generate a significant abundance of PBHs within the mass window where they may serve as viable dark matter candidates.

For this purpose, we consider a specific magnetogenesis model discussed in Chap. 5, which produces an electromagnetic spectrum with a broken power-law behavior. In this model, both the electric and magnetic spectra exhibit a peak at $k \simeq k_{\rm re}$. Here $k_{\rm re}$ denotes the comoving wavenumber that re-enters the horizon at the end of the reheating era. In this scenario, most of the electromagnetic energy density is concentrated near this peak scale, i.e., $k \simeq k_{\rm re}$.

Since the electromagnetic field is treated as a perturbative component, it can act as a source of density perturbations. If the magnetic energy density near the peak constitutes a few percent of the background energy density, it can generate sufficiently large density fluctuations around this scale. These overdensities can subsequently collapse and lead to the formation of PBHs.

Interestingly, we find that the position of the peak in the magnetic field spectrum depends on the reheating temperature $T_{\rm re}$. Therefore, by tuning the reheating parameters, the peak position of the spectrum can be shifted. Since the PBH mass is determined by the horizon mass at the time of horizon re-entry, the mass of the resulting PBHs is directly related to the position of this peak scale. By tuning the reheating temperature, we can produce the PBHs within the mass window where they can be treated as a dark matter candidate. Most interesting, we have found that tehre have specific temperature window, where we can generate PBHs within the mass range, where it can be the entire dark matter abundance. Here, we also discuss the possible source of detecting this PBH formation mechanism, and we have found that the produced GWs can easily be detected by future GW experiments.

In Chap. 7, we discuss another alternative mechanism for generating large-scale magnetic fields through the axion–photon coupling. In a flat FLRW background, the electromagnetic field is conformally invariant in nature. Therefore, in the absence of any additional coupling to the gauge field, electromagnetic fields cannot be efficiently generated during inflation. However, if the spacetime metric itself is perturbed, the conformal invariance of the gauge field can be naturally broken at higher order [233, 310]. In this work, we therefore consider the production of gauge fields sourced directly by metric fluctuations.

Since no explicit coupling is introduced by hand, the gauge field can be viewed as being gravitationally coupled at higher order, which naturally breaks the conformal symmetry and excites the gauge field from the vacuum. This process typically leads to a blue-tilted magnetic spectrum, where the large-scale magnetic field scales as $B_0 \propto k^{3/2}$ [233, 310]. However, this mechanism is not very efficient in generating large-scale magnetic fields. This is because the effect arises from second-order corrections, and the amplitude of inflationary perturbations on large scales is extremely small.

We also investigate the effect of the post-inflationary evolution on this generation mechanism, as well as how enhanced curvature perturbations can influence the production of gauge fields. Our analysis shows that inflationary metric scalar perturbations can indeed generate large-scale magnetic fields; however, their strength can reach at most $B_0 \simeq 10^{-40}$ Gauss. In contrast, high-energy gamma-ray observations indicate that the lower bound on the large-scale magnetic field is $B_0(1\ \mathrm{Mpc}) \leq 10^{-17}$ Gauss. Therefore, this mechanism alone cannot explain the origin of the observed large-scale magnetic fields.

To address this limitation, we consider a late-time enhancement of the magnetic field in the presence of ultra-light axions or axion-like particles (ALPs) during the Dark Ages. During this epoch, the Universe was predominantly filled with neutral hydrogen and helium, resulting in a significant decrease in both the conductivity and the temperature of the cosmic plasma. Consequently, the mean free path of photons becomes sufficiently large. If ultra-light axions with mass $m_a \leq 10^{-27}$ eV are present, they begin to oscillate during the Dark Ages.

As is well known, electromagnetic fields can couple to axions or axion-like particles through the interaction $\mathcal{L}_{\rm EM} \supset \frac{\alpha}{f_\phi}\phi F_{\mu\nu}\tilde{F}^{\mu\nu}$. In the presence of this coupling, the oscillation of the axion field can transfer its kinetic energy into electromagnetic energy density, thereby enhancing the gauge field. We find that when the coupling parameter satisfies $\alpha > 70$, the oscillations of the axion field can significantly amplify the magnetic field on length scales consistent with present-day observations.

We also discuss possible observational signatures of this mechanism. In particular, these signals may be detectable through future CMB experiments such as CMB-S4 via measurements of the B-mode polarization. In addition, we analyze the spectrum of secondary gravitational waves produced by these magnetic fields. Interestingly, this mechanism can generate fully helical magnetic fields, and consequently the resulting gravitational waves are also helical in nature. Detecting such a helical signal on CMB scales would therefore provide a direct signature of helical magnetic fields and an indirect probe of this class of magnetogenesis scenarios.

8.2 Future Outlook

Evolution of magnetic field in full MHD system during reheating: In our previous studies, we have primarily focused on the evolution of primordial magnetic fields during the post-inflationary era in scenarios with non-instantaneous reheating. Our analysis has demonstrated that the dynamics of the reheating phase can leave significant imprints on both the evolution of the magnetic field and the present-day gravitational wave (GW) spectrum. In most of our analyses, we considered two extreme limits for the electrical conductivity of the Universe during reheating, namely vanishing electrical conductivity and extremely high electrical conductivity.

Since our primary interest has been on large-scale modes, these scales typically remain outside the horizon during the reheating era, and their evolution can therefore be reliably described within linear perturbation theory. However, the evolution of modes that lie inside the horizon during reheating remains largely unexplored. In particular, when the inflaton field continuously decays into radiation, the plasma dynamics may significantly affect the behavior of electromagnetic fields on subhorizon scales. Understanding this evolution requires a more complete treatment that incorporates the full magnetohydrodynamic (MHD) dynamics of the system. Therefore, a natural and important extension of the present work is to study the evolution of primordial magnetic fields by solving the full MHD equations during the reheating era, with the goal of understanding how subhorizon magnetic field modes evolve in a dynamically evolving plasma background.

Ultra light PBHs from inflationary magnetogenesis scenarios: Another promising direction arises from the connection between inflationary magnetogenesis and primordial black hole (PBH) formation. In this thesis, we have shown that post-inflationary magnetogenesis scenarios can generate PBHs under certain conditions, potentially within the mass range where they can act as viable dark matter candidates. More generally, several inflationary magnetogenesis models predict the significant amplification of electromagnetic fields during inflation. If the generated electromagnetic fields become sufficiently strong, they can source additional curvature perturbations.

While the amplitude of curvature perturbations on CMB scales is tightly constrained by observations, inflation naturally produces fluctuations on a wide range of scales. In particular, if the electromagnetic field spectrum is blue tilted, the induced perturbations remain consistent with CMB constraints on large scales while potentially becoming large on much smaller scales. In such cases, the induced curvature perturbations at small scales can reach amplitudes as large as $\mathcal{P}_{\mathcal{R}}(k >> k_*) \sim \mathcal{O}(0.01)$. When this occurs, the enhanced density fluctuations may collapse gravitationally upon horizon re-entry, leading to the formation of ultra-light PBHs. Exploring this connection between inflationary magnetogenesis, small-scale curvature perturbations, and PBH formation therefore represents an exciting avenue for future investigation.

Chapter A

Appendix

A.1 Computation of Friedmann equations

Here, we briefly describe how, from the two Friedmann equations, one can obtain the continuity equation of the fluid. If we take the time derivative of the 2nd Friedmann equation Eq.(2.14), we get

$$2H\dot{H} = \frac{8\pi \mathrm{G_N}}{3}\dot{\rho} + \frac{2k}{a^2}H \tag{A.1}$$

If we take the time derivative of the Hubble parameter with respect to cosmic time t, then we have

$$\dot{H} = \frac{\ddot{a}}{a} - H^2 \tag{A.2}$$

Now, replace the 2nd Friedmann equation in the above, and we get

$$\dot{H} = -\frac{4\pi \mathrm{G_N}}{3}(\rho + 3P) + \frac{\Lambda_g}{3} - H^2 \tag{A.3}$$

Replace the above Eq.(A.3) in Eq.(A.1), we get

$$\dot{\rho} + H(\rho + 3P) = \frac{3}{4\pi \mathrm{G_N}}H\left(\frac{\Lambda_g}{3} - H^2 - \frac{k}{a^2}\right) = -2H\rho \tag{A.4}$$

$$\dot{\rho} + 3H(\rho + P) = 0 \tag{A.5}$$

A.2 Detailed calculation of gauge field generation in inflationary perturbed background

We first begin with the action of the background Lagrangian and then perturb the fields and the metric,

$$S = \int d^4x\, \sqrt{-g}\left[\frac{M_{pl}^2}{2}R + \frac{1}{2}\partial^\mu\varphi\partial_\mu\varphi - V(\varphi) - \frac{1}{4}F_{\mu\nu}F^{\mu\nu}\right]. \tag{A.6}$$

Now, finding the equation of motion for the gauge field, we arrive at,

$$\partial_\nu\left(\frac{\delta\mathcal{L}_{EM}}{\partial\partial_\mu A_\nu}\right) = \partial_\nu\left(\frac{\partial\sqrt{-g}F_{\mu\nu}F^{\mu\nu}}{\partial\partial_\mu A_\nu}\right) = \frac{\partial}{\partial x^\mu}[\sqrt{-g}g^{\alpha\mu}g^{\beta\nu}F_{\alpha\beta}] = 0, \tag{A.7}$$

Expressing the gauge field in terms of Fourier modes,

$$A_i = \int \frac{d^4x}{(2\pi)^{3/2}} \epsilon_i^\lambda A_{\mathbf{k}}^\lambda e^{i(\mathbf{k}\cdot\mathbf{x}-k\eta)} \tag{A.8}$$

The equation of motion of the gauge field mode in the presence of the metric fluctuations in Fourier space is governed by

$$A_{\mathbf{k}}^{\lambda''} + A_{\mathbf{k}}^\lambda = \frac{1}{k^2}\mathcal{J}_{\mathbf{k}}^\lambda(x), \tag{A.9}$$

Here, the prime ($'$) is defined as the derivative with respect to the new dimensionless variable $x = k\eta$, and $J_i^{\mathbf{k},\lambda}(\eta)$ is the source due to metric fluctuations. [1] Now, the solution of the homogeneous part of the above Eq.(A.8) is

$$A_{\mathbf{k}}^\lambda = C_1\cos(k\eta) + C_2\sin(k\eta). \tag{A.10}$$

Considering two independent solutions, we can contract the Green's function,

$$\mathrm{G}_k(x,x_1) = \Theta(x-x_1)\frac{A_{\mathbf{k},1}^\lambda(x)A_{\mathbf{k},2}^\lambda(x_1) - A_{\mathbf{k},1}^\lambda(x_1)A_{\mathbf{k},2}^\lambda(x)}{A_{\mathbf{k},1}^{\lambda'}(x_1)A_{\mathbf{k},2}^\lambda(x_1) - A_{\mathbf{k},1}^\lambda(x_1)A_{\mathbf{k},2}^{\lambda'}(x_1)} \tag{A.11}$$

$$= \Theta\frac{A_{\mathbf{k},1}^\lambda(x)A_{\mathbf{k},2}^\lambda(x_1) - A_{\mathbf{k},1}^\lambda(x_1)A_{\mathbf{k},2}^\lambda(x)}{-C_1C_2} = \Theta(x-x_1)\sin(x-x_1). \tag{A.12}$$

Now the solution of the above equations is,

$$A_{\mathbf{k}}^\lambda = A_{\mathbf{k}}^{\mathrm{vac}} + \frac{1}{k^2}\int dx_1 G_k(x,x_1)\mathcal{J}_{\mathbf{k}}^\lambda(x_1) = A_{\mathbf{k}}^{\mathrm{vac}} + \frac{1}{k}\int d\eta_1 \sin k(\eta-\eta_1) J_i^{\mathbf{k},\lambda}(\eta_1) \tag{A.13}$$

We are assuming that metric perturbations vanish before inflation starts so that we can define an appropriate initial conformal vacuum state. Because of the presence of the inhomogeneous background in the asymptotic future, this solution will behave as a linear superposition of positive and negative frequency modes with different momentum and different polarizations, i.e.

$$A_k^\lambda(\eta\to\infty)\sum_{\lambda'}\sum_q \left(\alpha_{\mathbf{k}}^{\lambda\lambda'}(q,\eta)\frac{\epsilon_{\mathbf{q}}^\lambda}{\sqrt{2q}}e^{i(\mathbf{q}\cdot\mathbf{x}-q\eta)} + \beta_{\mathbf{k}}^{\lambda\lambda'}(\mathbf{q},\eta)\frac{\epsilon_{\mathbf{q}}^{\lambda*}}{\sqrt{2q}}e^{-i(\mathbf{q}\cdot\mathbf{x}-q\eta)}\right), \tag{A.14}$$

here $\alpha_{\mathbf{k}}^{\lambda\lambda'}$ & $\beta_{\mathbf{k}}^{\lambda\lambda'}$ are the Bogoliubov coefficient to the first order in the metric perturbations. Now comparing this expression with Eq.(A.8), it is straight forward to obtain the Bogoliubov coefficient $\beta_{\mathbf{k}}^{\lambda\lambda'}(q,\eta)$, which is given by,

$$\beta_{\mathbf{k}}^{\lambda\lambda'}(q,\eta) = -\frac{i}{\sqrt{2k}}\sum_i\int_{\eta_i}^{\eta}\epsilon_{i\mathbf{q}}^{\lambda*}J_i^{\mathbf{k},\lambda}(\mathbf{k}+\mathbf{q},\eta_1)e^{-ik\eta_1}d\eta_1. \tag{A.15}$$

[1] We use the following convention $\tilde{F}(\vec{q},\eta) = \frac{1}{(2\pi)^{3/2}}\int d^3x\, e^{i\vec{q}\vec{x}}F(\vec{x},\eta)$.

Now the total number of photon created with comoving wave number 'k/a' is defined as

$$N_{\mathbf{k}}(\eta) = \sum_{\lambda,\lambda'}\sum_{q}\left|\beta_{\mathbf{k}}^{\lambda\lambda'}(q,\eta)\right|^2 = \int_{k_*}^{k_e}\frac{d^3q}{(2\pi)^3}\left|\beta_{\mathbf{k}}^{\lambda\lambda'}\right|^2 = \int_{k_*}^{k}\frac{d^3q}{(2\pi)^3}\left|\beta_{\mathbf{k}}^{\lambda\lambda'}\right|^2 + \int_{k}^{k_e}\frac{d^3q}{(2\pi)^3}\left|\beta_{\mathbf{k}}^{\lambda\lambda'}\right|^2. \tag{A.16}$$

The electromagnetic source term $J_i^{\mathbf{k},\lambda}$ is sourced by the metric fluctuations Φ and it can be written as [310]

$$J_i^{\mathbf{k},\lambda} = -\sqrt{2q}\left[\left(i\Phi'(\mathbf{k}+\mathbf{q},\eta) + \frac{q^2-\mathbf{k}\cdot\mathbf{q}}{q}\Phi(\mathbf{k}+\mathbf{q},\eta)\right)\epsilon_{i\mathbf{q}}^{\lambda}e^{-iq\eta} + (\epsilon_{\mathbf{q}}^{\lambda}\cdot\mathbf{k})\Phi(\mathbf{k}+\mathbf{q},\eta)\frac{\mathbf{q}_i}{q}e^{-iq\eta}\right.$$
$$\left.\underbrace{-i\frac{\epsilon_{\mathbf{q}}^{\lambda}\cdot\mathbf{k}}{q^2}\frac{\partial}{\partial\eta}\left[\Phi(\mathbf{k}+\mathbf{q},\eta)e^{-ik\eta}\right]\mathbf{k}_i}\right]. \tag{A.17}$$

Last term of the above equation does not contribute to the $\beta_{\mathbf{k}}^{\lambda\lambda'}$ because of the transverse condition of the polarization vectors. So for the further calculations we drop this term, multiplying this with the polarization vector and taking the modulus square, we get

$$\left|\epsilon_{\mathbf{k}}^{\lambda}\cdot J^{\mathbf{k},\lambda'}\right|^2 = 2q\left[|\Phi'(\mathbf{k}+\mathbf{q},\eta)|^2 + \left(\frac{q^2-\mathbf{k}\cdot\mathbf{q}}{q}\right)^2\Phi^2(\mathbf{k}+\mathbf{q},\eta)(\epsilon_{\mathbf{q}}^{\lambda'}\cdot\epsilon_{\mathbf{k}}^{\lambda})^2\right.$$
$$\left.+\frac{(\epsilon_{\mathbf{q}}^{\lambda'}\cdot\mathbf{k})^2(\epsilon_{\mathbf{k}}^{\lambda}\cdot\mathbf{q})^2}{q^2}\Phi^2(\mathbf{k}+\mathbf{q},\eta)\right], \tag{A.18}$$

$$= \frac{4\pi^2 q}{|\mathbf{k}+\mathbf{q}|^3}\left[\left(P_{\Phi'}(\mathbf{k}+\mathbf{q},\eta) + \left(\frac{q^2-\mathbf{k}\cdot\mathbf{q}}{q}\right)^2 P_{\Phi}(\mathbf{k}+\mathbf{q},\eta)\right)(\epsilon_{\mathbf{q}}^{\lambda'}\cdot\epsilon_{\mathbf{k}}^{\lambda})^2\right.$$
$$\left.+\frac{(\epsilon_{\mathbf{q}}^{\lambda'}\cdot\mathbf{k})^2(\epsilon_{\mathbf{k}}^{\lambda}\cdot\mathbf{q})^2}{q^2}P_{\Phi}(\mathbf{k}+\mathbf{q},\eta)\right], \tag{A.19}$$

here P_Φ & $P_{\Phi'}$ are defined as

$$P_\Phi(\mathbf{k}+\mathbf{q},\eta) = \mathcal{P}_\Phi^i(|\mathbf{k}+\mathbf{q}|)\mathcal{C}^2(|\mathbf{k}+\mathbf{q})\eta);\ P_{\Phi'}(\mathbf{k}+\mathbf{q},\eta) == \mathcal{P}_\Phi^i(|\mathbf{k}+\mathbf{q}|)\mathcal{C}'^2(|\mathbf{k}+\mathbf{q})\eta). \tag{A.20}$$

In the above integral we kept only those therm which are contributing in the number spectrum. Now we can write the number spectrum as

$$N_k = \sum_{\lambda\lambda'}\int\frac{d^3q}{(2\pi)^3}\left(\frac{q}{k}\right)\Phi_0^2(|\mathbf{k}+\mathbf{q}|)\mathcal{D}(k,q), \tag{A.21}$$

where we define

$$\mathcal{D}(k,q) = \left| \int d\eta' \left\{ \left(i\mathcal{C}'(|\mathbf{k}+\mathbf{q}|\eta') + \frac{q^2 - \mathbf{k}\cdot\mathbf{q}}{q}\mathcal{C}(|\mathbf{k}+\mathbf{q}|\eta') \right)(\epsilon^{\lambda}_{\mathbf{k}}\cdot\epsilon^{\lambda'}_{\mathbf{q}}) + \frac{(\epsilon^{\lambda}_{\mathbf{k}}\cdot\mathbf{q})(\epsilon^{\lambda'}_{\mathbf{q}}\cdot\mathbf{k})}{q^2}\mathcal{C}(|\mathbf{k}+\mathbf{q}|\eta') \right\} \right|^2. \tag{A.22}$$

A.3 PBH mass if they form during the reheating era

At the time of horizon crossing $k = aH$, so we can write $H(t_{\rm h}) = k/a(t_{\rm h})$. Now we have to eliminate $a(t_{\rm h})$ in favour of a background quantity or a known quantity. So to do that, we write

$$\frac{a}{a_{\rm re}} = \left(\frac{H}{H_{\rm re}}\right)^{-2/3(1+w_{\rm re})} \tag{A.23}$$

where we have used $H \propto a^{-3(1+w_{\rm re})/2}$.

So at the time of horizon crossing, we insert the above expression for a and get

$$k = aH = Ha_{\rm re}\left(\frac{H}{H_{\rm re}}\right)^{-2/3(1+w_{\rm re})} \tag{A.24}$$

$$= a_{\rm re}H^{\frac{1+3w_{\rm re}}{3(1+w_{\rm re})}}H_{\rm re}^{\frac{2}{3(1+w_{\rm re})}} \tag{A.25}$$

$$\frac{k}{a_0} = \frac{a_{\rm re}}{a_0}H^{\frac{1+3w_{\rm re}}{3(1+w_{\rm re})}}H_{\rm re}^{\frac{2}{3(1+w_{\rm re})}} \tag{A.26}$$

After the end of reheating, the entropy of the universe remains conserved, and we can relate the reheating temperature and the present-day temperature through the following

$$a_{\rm re}T_{\rm re} = a_{\rm eq}T_{\rm eq}\left(\frac{g_{*,eq}}{g_{*,re}}\right)^{1/3} \tag{A.27}$$

Now utilizing eq.(A.27) in the above Eq.(A.26), we get

$$\frac{k}{a_0} = \left(\frac{a_{\rm eq}}{a_0}\right)\frac{T_{\rm eq}}{T_{\rm re}}\left(\frac{g_{*,\rm eq}}{g_{s,\rm re}}\right)^{1/3}H^{\frac{1+3w_{\rm re}}{3(1+w_{\rm re})}}H_{\rm re}^{\frac{2}{3(1+w_{\rm re})}} = \frac{T_0}{T_{\rm re}}\left(\frac{g_{*,\rm eq}}{g_{s,\rm re}}\right)^{1/3}H^{\frac{1+3w_{\rm re}}{3(1+w_{\rm re})}}H_{\rm re}^{\frac{2}{3(1+w_{\rm re})}} \tag{A.28}$$

Now we can replace $H_{\rm re}$ by the $T_{\rm re}$. At the end of reheating, the reheating temperature and the radiation energy are related as

$$\rho_{\rm ra} = 3H_{\rm re}^2M_{\rm P}^2 = \frac{\pi^2 g_{s,\rm re}}{30}T_{\rm re}^4 \tag{A.29}$$

$$H_{\rm re} = \left(\frac{\pi g_{s,\rm re}}{90}\right)^{1/2}\frac{T_{\rm re}^2}{M_{\rm P}} \tag{A.30}$$

Now we can rewrite Eq.(A.28) as

$$H^{-1} = \left[\left(\frac{g_{*,\mathrm{eq}}}{g_{s,\mathrm{re}}}\right)^{1/3} \frac{T_0}{k}\right]^{\frac{3(1+w_{\mathrm{re}})}{1+3w_{\mathrm{re}}}} \left(\frac{1}{T_{\mathrm{re}}}\right)^{\frac{3(1+w_{\mathrm{re}})}{1+3w_{\mathrm{re}}}} H_{\mathrm{re}}^{\frac{2}{1+3w_{\mathrm{re}}}} \tag{A.31}$$

Now replace the value of H_{re} from eq.(A.30), in the above we get

$$H^{-1} = \left[\left(\frac{g_{*,\mathrm{eq}}}{g_{s,\mathrm{re}}}\right)^{1/3} \frac{T_0}{k}\right]^{\frac{3(1+w_{\mathrm{re}})}{1+3w_{\mathrm{re}}}} \left(\frac{1}{T_{\mathrm{re}}}\right)^{\frac{3(1+w_{\mathrm{re}})}{1+3w_{\mathrm{re}}}} \left(\frac{\pi^2 g_{s,\mathrm{re}}}{90}\right)^{\frac{1}{1+3w_{\mathrm{re}}}} \left(\frac{T_{\mathrm{re}}^2}{M_{\mathrm{P}}}\right)^{\frac{2}{1+3w_{\mathrm{re}}}} \tag{A.32}$$

$$= \frac{1}{M_{\mathrm{P}}} \left(\frac{\pi^2 g_{*,\mathrm{eq}}}{90}\right)^{\frac{1}{1+3w_{\mathrm{re}}}} \left(\frac{T_0}{k}\right)^{\frac{3(1+w_{\mathrm{re}})}{1+3w_{\mathrm{re}}}} \left(\frac{g_{*,\mathrm{eq}}}{g_{s,\mathrm{re}}}\right)^{\frac{w_{\mathrm{re}}}{1+3w_{\mathrm{re}}}} \left(\frac{T_{\mathrm{re}}}{M_{\mathrm{P}}}\right)^{\frac{1-3w_{\mathrm{re}}}{1+3w_{\mathrm{re}}}} \tag{A.33}$$

Whereas the PBH's mass at the time of horizon crossing is

$$M_{\mathrm{pbh}} = 4\pi\gamma M_{\mathrm{P}}^2 H^{-1} \tag{A.34}$$

$$= 4\pi\gamma M_{\mathrm{P}} \left(\frac{\pi^2 g_{*,\mathrm{eq}}}{90}\right)^{\frac{1}{1+3w_{\mathrm{re}}}} \left(\frac{T_0}{k}\right)^{\frac{3(1+w_{\mathrm{re}})}{1+3w_{\mathrm{re}}}} \left(\frac{g_{*,\mathrm{eq}}}{g_{s,\mathrm{re}}}\right)^{\frac{w_{\mathrm{re}}}{1+3w_{\mathrm{re}}}} \left(\frac{T_{\mathrm{re}}}{M_{\mathrm{P}}}\right)^{\frac{1-3w_{\mathrm{re}}}{1+3w_{\mathrm{re}}}} \tag{A.35}$$

Now, if we want to express the PBH's mass in terms of solar mass units, then we have found

$$M_{\mathrm{pbh}} \simeq 5.486 \times 10^{-39} M_{\odot} \left(\frac{\gamma}{0.2}\right) \left(\frac{\pi^2 g_{*,\mathrm{eq}}}{90}\right)^{\frac{1}{1+3w_{\mathrm{re}}}} \left(\frac{T_0}{k}\right)^{\frac{3(1+w_{\mathrm{re}})}{1+3w_{\mathrm{re}}}} \left(\frac{g_{*,\mathrm{eq}}}{g_{s,\mathrm{re}}}\right)^{\frac{w_{\mathrm{re}}}{1+3w_{\mathrm{re}}}} \left(\frac{T_{\mathrm{re}}}{M_{\mathrm{P}}}\right)^{\frac{1-3w_{\mathrm{re}}}{1+3w_{\mathrm{re}}}} \tag{A.36}$$

where we have used $M_{\mathrm{P}} = 1/\sqrt{8\pi G} \simeq 4.31 \times 10^{-9}\,\mathrm{kg} \simeq 2.183 \times 10^{-39} M_{\odot}$, where $1\,M_{\odot} \simeq 1.9985 \times 10^{30}\,\mathrm{kg}$.

A.4 Post-inflationary contributions to the secondary tensor power spectrum

The PMFs are expected to have been generated during inflation due to a non-conformal coupling. We shall assume that the conformal symmetry of the electromagnetic action is restored at the end of inflation. As a result, the electromagnetic modes simply oscillate post-inflation, apart from the diluting factor that arises due to the expansion of the universe. The tensor modes $h_{\mathbf{k}}^{\lambda}(\eta)$ are governed by the equation (see, for instance, Refs. [220–222])

$$h_{\boldsymbol{k}}^{\lambda\prime\prime} + 2\frac{a'}{a} h_{\boldsymbol{k}}^{\lambda\prime} + k^2 h_{\boldsymbol{k}}^{\lambda} = \mathcal{S}_{\boldsymbol{k}}^{\lambda}, \tag{A.37}$$

where the source term $\mathcal{S}_{\boldsymbol{k}}^{\lambda}$ is given by

$$\mathcal{S}_{\boldsymbol{k}}^{\lambda}(\eta) = -\frac{2}{M_{\rm pl}^2} e_{\lambda}^{ij}(\boldsymbol{k}) \int \frac{{\rm d}^3\mathbf{q}}{(2\pi)^{3/2}} [E_i(\mathbf{q},\eta)E_j(\mathbf{k}-\mathbf{q},\eta) + B_i(\mathbf{q},\eta)B_j(\mathbf{k}-\mathbf{q},\eta)]. \tag{A.38}$$

The Green's function corresponding to Eq. (A.37) satisfies the differential equation

$$\mathcal{G}_{\mathbf{k}}''(\eta,\eta_1) + 2\mathcal{H}\mathcal{G}_{\mathbf{k}}'(\eta,\eta_1) + k^2\mathcal{G}_{\mathbf{k}}(\eta,\eta_1) = \delta^{(1)}(\eta-\eta_1). \tag{A.39}$$

The Green's function during the epochs of reheating and radiation domination can be easily obtained to be

$$G_k^{\rm re}(\eta,\eta_1) = \theta(\eta-\eta_1)\frac{\pi\eta^l\eta_1^{1-l}}{2\sin(l\pi)}\left[J_l(k\eta)J_{-l}(k\eta_1) - J_{-l}(k\eta)J_l(k\eta_1)\right], \tag{A.40a}$$

$$G_k^{\rm ra}(\eta,\eta_1) = \theta(\eta-\eta_1)\frac{\eta_1}{k\eta}\sin[k(\eta_1-\eta)], \tag{A.40b}$$

where $l = (1-\delta)/2$ with $\delta = 4/(1+3w_{\rm re})$.

Evidently, at the time of decoupling of the neutrinos η_ν, the tensor perturbations generated by the magnetic fields can be expressed as

$$h_\lambda(\mathbf{k},\eta_\nu) = \int_{\eta_{\rm e}}^{\eta_{\rm re}} {\rm d}\eta_1 {\rm G}_{\rm k}^{\rm re}(\eta_{\rm re},\eta_1)\mathcal{S}_{\mathbf{k}}(\eta_1) + \int_{\eta_{\rm re}}^{\eta_\nu} {\rm d}\eta_1 {\rm G}_{\rm k}^{\rm ra}(\eta_\nu,\eta_1)\mathcal{S}_{\mathbf{k}}(\eta_1). \tag{A.41}$$

Since we have assumed that the electric fields are sub-dominant post-inflation, we find that the tensor power spectrum [as defined in Eq. (2.195)] can be expressed as

$$\mathcal{P}_{\rm SEC}(k,\eta_\nu) = \frac{2a_{\rm e}^8}{M_{\rm pl}^4}\left[\int_{\eta_{\rm e}}^{\eta_{\rm re}} \frac{{\rm d}\eta_1}{a^2(\eta_1)} G_k^{\rm re}(\eta_{\rm re},\eta_1) + \int_{\eta_{\rm re}}^{\eta_\nu} \frac{d\eta_1}{a^2(\eta_1)} G_k^{\rm ra}(\eta_\nu,\eta_1)\right]^2 \int_0^\infty \frac{\rm dq}{q}\int_{-1}^{1} \frac{{\rm d}\mu {\rm f}(\mu,\beta)\mathcal{P}_{\rm B}^{\rm I}({\rm q})\mathcal{P}_{\rm B}^{\rm I}(|\mathbf{k}-\mathbf{q}|)}{[1+(q/k)^2 - 2\mu(q/k)]^{3/2}} \tag{A.42}$$

$$\simeq \frac{2a_{\rm e}^8}{M_{\rm pl}^4 k^4}\left[\mathcal{C}_{\rm re}^2(x_{\rm re},x_{\rm e}) + \mathcal{C}_{\rm ra}^2(x_\nu,x_{\rm re})\right]\int_0^\infty \frac{\rm dq}{q}\int_{-1}^{1} \frac{{\rm d}\mu {\rm f}(\mu,\beta)\mathcal{P}_{\rm B}^{\rm I}({\rm q})\mathcal{P}_{\rm B}^{\rm I}(|\mathbf{k}-\mathbf{q}|)}{[1+(q/k)^2 - 2\mu(q/k)]^{3/2}}, \tag{A.43}$$

where we have set $x = k\eta$, and the quantities $\mathcal{C}_{\rm re}(x_{\rm e},x_{\rm re})$ and $\mathcal{C}_{\rm re}(x_{\rm e},x_\nu)$ are given by

$$\mathcal{C}_{\rm re}(x_{\rm re},x_{\rm e}) = k\int_{x_{\rm e}}^{x_{\rm re}} \frac{{\rm d}x_1}{a^2(x_1)} G_k^{\rm re}(x_{\rm re},x_1) = \frac{kx_{\rm e}^\delta}{a_{\rm e}^2}\int_{x_{\rm e}}^{x_{\rm re}} {\rm dx_1 x_1^{-\delta} G_k^{re}(x_{re},x_1)} = \frac{{\rm x_e^\delta}}{{\rm a_e^2}}\mathcal{C}_{\rm m,re}({\rm x_{re}},{\rm x_e}), \tag{A.44a}$$

$$\mathcal{C}_{\rm ra}(x_\nu,x_{\rm re}) = k\int_{x_{\rm re}}^{x_\nu} \frac{{\rm d}x_1}{a^2(x_1)} G_k^{\rm ra}(x_\nu,x_1) = \frac{kx_{\rm re}^2}{a_{\rm re}^2}\int_{x_{\rm re}}^{x_\nu} {\rm d}x_1 x_1^{-2} G_k^{\rm ra}(x_\nu,x_1) = \frac{x_{\rm re}^2}{a_{\rm re}^2}\mathcal{C}_{\rm r}^{\rm ra}(x_\nu,x_{\rm re}). \tag{A.44b}$$

In arriving at the final expressions above, we have made use of the following forms of the scale factor during the epochs of reheating and radiation domination:

$$a(\eta) = \begin{cases} a_{\rm e}(x/x_{\rm e})^{\delta/2} & \text{for } \eta_{\rm e} \leq \eta \leq \eta_{\rm re}, \\ a_{\rm re}(x/x_{\rm re}) & \text{for } \eta_{\rm re} \leq \eta \leq \eta_{\rm eq}, \end{cases} \tag{A.45}$$

where $\eta_{\rm eq}$ represents the conformal time corresponding to the epoch of radiation-matter equality.

Calculating $\mathcal{C}_{\rm re}(x_{\rm re}, x_{\rm e})$ and $\mathcal{C}_{\rm ra}(x_\nu, x_{\rm re})$

Let us now compute the quantities $\mathcal{C}_{\rm re}(x_{\rm e}, x_{\rm re})$ and $\mathcal{C}_{\rm re}(x_{\rm re}, x_\nu)$ during the epochs of reheating and radiation domination. During reheating, upon using the functional form (A.40a) for the Green's function, the indefinite integral in Eq. (A.44a) can be evaluated to be

$$\begin{aligned}\mathcal{C}_{\rm m,re}(x, x_1) &= k\int {\rm dx_1 x_1^{-\delta} G_k^{re}(x, x_1)} = \frac{\pi {\rm x^l}}{2{\rm sin(l}\pi)}\int {\rm dx_1 x_1^{1-l-\delta}}\,[{\rm J_l(x)J_{-l}(x_1) - J_{-l}(x)J_l(x_1)}] \\ &= 2^{-2-l}x^l x_1^{2-2l-\delta}\left\{\frac{\Gamma(-l)\Gamma[1-(\delta/2)]}{\Gamma[2-(\delta/2)]}x_1^{2l}J_{-l}(x)\,{}_1F_2[1-(\delta/2); 1+l, 2-(\delta/2); -(x_1^2/4)]\right. \\ &\left.+\,4^l\frac{\Gamma(l)\Gamma[1-l-(\delta/2)]}{\Gamma[2-l-(\delta/2)]}J_l(x){}_1F_2[1-l-(\delta/2); 1-l, 2-l-(\delta/2); -(x_1^2/4)]\right\},\end{aligned} \tag{A.46}$$

where ${}_1F_2(a, b, c, z)$ denotes the hypergeometric function. Similarly, upon substituting the Green's function (A.40b) during the radiation dominated epoch in Eq. (A.44b) and carrying out the integral, we obtain that

$$\mathcal{C}_{\rm r}^{\rm ra}(x_\nu, x_{\rm re}) = k\int_{x_{\rm re}}^{x_\nu} {\rm dx_1 x_1^{-2} G_k^{ra}(x_\nu, x_1)} = \frac{1}{\rm x_\nu}\int_{\rm x_{re}}^{\rm x_\nu}\frac{\rm dx_1}{\rm x_1}\sin({\rm x}_\nu - {\rm x}_1) = \frac{1}{\rm x_\nu}\mathcal{I}({\rm x}_\nu, {\rm x_{re}}). \tag{A.47}$$

For convenience, we break the above integral into two domains, i.e. $k < k_\nu$ and $k_\nu < k < k_{\rm re}$. In these cases, the integral $\mathcal{I}(x_\nu, x_{\rm re})$ reduces to

$$\mathcal{I}(x_\nu, x_{\rm re}) \simeq \begin{cases} [\gamma_{\rm E} + \ln(k/k_{\rm re})]\,(k/k_\nu) & \text{for } k < k_\nu, \\ \gamma_{\rm E} + \ln(k/k_{\rm re}) & \text{for } k_\nu < k < k_{\rm re}, \end{cases} \tag{A.48}$$

where $\gamma_{\rm E} = 0.577$ is the Euler's constant.

Contributions to the secondary tensor power spectrum

At the end of reheating, the secondary tensor power spectrum induced by the magnetic fields can be expressed as

$$\begin{aligned}
P_{\rm SEC}^{\lambda,\rm re}(k,\eta_{\rm re}) &= \frac{2a_{\rm e}^8}{M_{\rm pl}^4 k^4}\left[\mathcal{C}_{\rm m,re}(x_{\rm e},x_{\rm re})\right]^2 \int_0^\infty \frac{{\rm d}q}{q}\int_{-1}^{1}\frac{{\rm d}\mu f(\mu,\beta)\mathcal{P}_{\rm B}^{\rm I}({\rm q})\mathcal{P}_{\rm B}^{\rm I}(|\mathbf{k}-\mathbf{q}|}{[1+(q/k)^2-2\mu(q/k)]^{3/2}}\\
&= \frac{2H_{\rm e}^4}{M_{\rm pl}^4}\left(\frac{a_{\rm e}^2\mathcal{B}}{k_{\rm e}^2}\right)^4\left(\frac{k}{k_{\rm e}}\right)^{2(\delta+n_{\rm B}-2)}\left[\mathcal{C}_{\rm re}(x_{\rm e},x_{\rm re})\right]^2\mathcal{F}_{n_{\rm B}}(k), \qquad \text{(A.49)}
\end{aligned}$$

where $\mathcal{F}_{n_{\rm B}}(k)$ is defined as

$$\begin{aligned}
\mathcal{F}_{n_{\rm B}}(k) &= \int_{k_*}^{k_{\rm e}}\frac{{\rm d}q}{q}\int_{-1}^{1}{\rm d}\mu\frac{({\rm q/k})^{\rm n_B}f(\mu,\beta)}{[1+({\rm q/k})^2-2\mu({\rm q/k})]^{(3-{\rm n_B})/2}}\\
&\simeq \frac{16}{3n_{\rm B}}\left[1-\left(\frac{k_*}{k}\right)^{n_{\rm B}}\right]+\frac{2\alpha}{3}\left[\left(\frac{k_{\rm e}}{k}\right)^{2n_{\rm B}-3}-1\right]. \qquad \text{(A.50)}
\end{aligned}$$

In a similar fashion, the contribution to the secondary tensor power spectrum due to the magnetic fields during the epoch of radiation domination can be expressed as

$$\begin{aligned}
P_{\rm SEC}^{\lambda,\rm ra}(k,\eta_\nu) &= \frac{2a_{\rm e}^8}{M_{\rm pl}^4 k^4}\frac{x_{\rm re}^4}{a_{\rm re}^4}\left[\mathcal{C}_{\rm r}^{\rm ra}(x_{\rm re},x_\nu)\right]^2 \int_0^\infty \frac{{\rm d}q}{q}\int_{-1}^{1}\frac{{\rm d}\mu f(\mu,\beta)\mathcal{P}_{\rm B}^{\rm I}({\rm q})\mathcal{P}_{\rm B}^{\rm I}(|\mathbf{k}-\mathbf{q}|}{[1+(q/k)^2-2\mu(q/k)]^{3/2}}\\
&= \frac{2H_{\rm e}^4}{M_{\rm pl}^4}\left(\frac{x_{\rm re}}{x_{\rm e}}\right)^4\left(\frac{a_{\rm e}}{a_{\rm re}}\right)^4\left(\frac{a_{\rm e}^2\mathcal{B}}{k_{\rm e}^2}\right)^4\left(\frac{k}{k_{\rm e}}\right)^{2n_{\rm B}}\left[\mathcal{C}_{\rm r}^{\rm ra}(x_{\rm re},x_\nu)\right]^2\mathcal{F}_{n_{\rm B}}(k). \qquad \text{(A.51)}
\end{aligned}$$

Lastly, the contribution due to the cross-term in the secondary tensor power spectrum can be expressed as

$$\begin{aligned}
P_{\rm T,s}^{\rm c}(k) &= \frac{4a_{\rm e}^8}{M_{\rm pl}^4 k^4}\mathcal{C}_{\rm re}(x_{\rm e},x_{\rm re})\,\mathcal{C}_{\rm ra}(x_{\rm re},x_\nu)\int_0^\infty \frac{{\rm d}q}{q}\int_{-1}^{1}\frac{{\rm d}\mu f(\mu,\beta)\mathcal{P}_{\rm B}^{\rm I}({\rm q})\mathcal{P}_{\rm B}^{\rm I}(|\mathbf{k}-\mathbf{q}|}{[1+(q/k)^2-2\mu(q/k)]^{3/2}}\\
&= \frac{4H_{\rm e}^4}{M_{\rm pl}^4}\left(\frac{a_{\rm e}^2\mathcal{B}}{k_{\rm e}^2}\right)^4\left(\frac{a_{\rm e}}{a_{\rm re}}\right)^2\left(\frac{k}{k_{\rm e}}\right)^{2n_{\rm B}+\delta-2}\mathcal{C}_{\rm m,re}(x_{\rm e},x_{\rm re})\,\mathcal{C}_{\rm r}^{\rm ra}(x_{\rm re},x_\nu)\mathcal{F}_{n_{\rm B}}(k). \qquad \text{(A.52)}
\end{aligned}$$

We find that this cross-term is subdominant when compared to the other two terms [i.e. those given by Eqs. (A.49) and (A.51)]. It is for this reason that, in Eq. (A.43), we have dropped this term in the final expression for the secondary tensor power spectrum.

Spectral shape of $\Omega_{\rm GW}$ for $k < k_{\rm re}$ and $k \gg k_{\rm re}$

Over wave numbers such that $k \ll k_{\rm re}$, we can consider the limit wherein $x_{\rm e} \ll x_{\rm re} \ll 1$. In such a case, we find that the quantity $\mathcal{C}_{\rm m,re}(x_{\rm re},x_{\rm e})$ simplifies to be

$$\lim_{k\ll k_{\rm re}}\mathcal{C}_{\rm m,re}(x_{\rm re},x_{\rm e}) \simeq \frac{1}{(1-\delta)^2}\left\{\frac{2}{1+2\delta}-\frac{2}{2-\delta}\left[1-\left(\frac{k_{\rm re}}{k_{\rm e}}\right)^{2-\delta}\right]\right\}\left(\frac{k}{k_{\rm re}}\right)^{2-\delta}. \qquad \text{(A.53)}$$

Similarly, when $k \gg k_{\rm re}$, for $w_{\rm re} > 1/3$, the quantity $\mathcal{C}_{\rm m,re}(x_{\rm re}, x_{\rm e})$ reduces to

$$\lim_{k\gg k_{\rm re}} \mathcal{C}_{\rm m,re}(x_{\rm re}, x_{\rm e}) \simeq \sqrt{\frac{2}{\pi}}\frac{2^{(1-\delta)/2}}{(1-\delta)}\Gamma[(3-\delta)/2]\Gamma[(\delta-1)/2]x_{\rm re}^{-\delta/2}\biggl\{\frac{\Gamma[(1-\delta)/2]}{\Gamma(\delta/2)}\cos\left[x_{\rm re}-(2-\delta)\pi/4\right] \\ -\frac{2}{2-\delta}\cos\left[x_{\rm re}-\delta\pi/4\right]\biggr\}, \tag{A.54}$$

whereas, for $w_{\rm re} < 1/3$, the quantity simplifies to

$$\lim_{k\gg k_{\rm re}} \mathcal{C}_{\rm m,re}(x_{\rm e}, x_{\rm re}) \simeq \sqrt{\frac{2}{\pi}}\frac{2^{(\delta-3)/2}}{(1-\delta)}\frac{\Gamma[(\delta-1)/2]\Gamma[1-(\delta/2)]}{\Gamma[2-(\delta/2)]}x_{\rm re}^{-\delta/2}x_{\rm e}^{2-\delta}\cos\left[-x_{\rm re}+\delta\pi/4\right] \\ \simeq \sqrt{\frac{2}{\pi}}\frac{2^{(\delta-3)/2}\Gamma[\frac{\delta-1}{2}]}{(1-\delta)(1-\delta/2)}x_{\rm re}^{-\delta/2}x_{\rm e}^{2-\delta}\cos[x_{\rm re}-(2-\delta)\pi/4]. \tag{A.55}$$

At the end of reheating, the power spectrum of secondary GWs generated due to the magnetic fields can be parametrized as

$$P_{\rm SEC}^{\lambda,{\rm re}}(k,\eta_{\rm re}) = \frac{2H_{\rm e}^4}{M_{\rm pl}^4}\left(\frac{a_{\rm e}^2\mathcal{B}}{k_{\rm e}^2}\right)^4\left(\frac{k}{k_{\rm e}}\right)^{2(\delta+n_{\rm B}-2)}\mathcal{F}_{n_{\rm B}}(k)\,\mathcal{C}^2(x_{\rm re},x_{\rm e}). \tag{A.56}$$

On substituting Eq. (A.53) in this expression, for $k \ll k_{\rm re}$, we obtain that

$$P_{\rm SEC}^{\lambda,{\rm re}}(k,\eta_{\rm re}) \simeq \mathcal{A}_1\left(\frac{\mathcal{B}a_{\rm e}^2}{k_{\rm e}^2}\right)^4\left(\frac{H_{\rm e}}{M_{\rm pl}}\right)^4\left(\frac{k_{\rm re}}{k_{\rm e}}\right)^{2(\delta-2)}\left(\frac{k}{k_{\rm e}}\right)^{2n_{\rm B}}\mathcal{F}_{n_{\rm B}}(k). \tag{A.57}$$

Similarly, on utilizing Eqs. (A.54) and (A.55), for $k > k_{\rm re}$, we obtain the following expressions

$$P_{\rm SEC}^{\lambda,{\rm re}}(k,\eta_{\rm re}) \simeq \mathcal{A}_2\left(\frac{\mathcal{B}a_{\rm e}^2}{k_{\rm e}^2}\right)^4\left(\frac{H_{\rm e}}{M_{\rm pl}}\right)^4\left(\frac{k_{\rm re}}{k_{\rm e}}\right)^{2(\delta-2)}\left(\frac{k}{k_{\rm re}}\right)^{-2-|n_w|}\left(\frac{k}{k_{\rm e}}\right)^{2n_{\rm B}}\mathcal{F}_{n_{\rm B}}(k), \tag{A.58a}$$

$$P_{\rm SEC}^{\lambda,{\rm re}}(k,\eta_{\rm re}) \simeq \mathcal{A}_3\left(\frac{\mathcal{B}a_{\rm e}^2}{k_{\rm e}^2}\right)^4\left(\frac{H_{\rm e}}{M_{\rm pl}}\right)^4\left(\frac{k_{\rm re}}{k_{\rm e}}\right)^{2(\delta-2)}\left(\frac{k}{k_{\rm re}}\right)^{-2-|n_w|}\left(\frac{k}{k_{\rm e}}\right)^{2n_{\rm B}}\mathcal{F}_{n_{\rm B}}(k), \tag{A.58b}$$

when $w_{\rm re} > 1/3$ and $w_{\rm re} < 1/3$, respectively. The quantities $\mathcal{A}_1$, $\mathcal{A}_2$ and $\mathcal{A}_3$ that appear in the above expressions are given by

$$\mathcal{A}_1 = \frac{2}{(1-\delta)^4}\left\{\frac{2}{1+2\delta}-\frac{2}{2-\delta}\left[1-\left(\frac{k_{\rm re}}{k_{\rm e}}\right)^{2-\delta}\right]\right\}^2, \tag{A.59a}$$

$$\mathcal{A}_2 = \frac{2^{(3-\delta)}\Gamma^2[(3-\delta)/2]\Gamma^2[(\delta-1)/2]}{\pi(1-\delta)^2}\biggl\{\frac{\Gamma[(1-\delta)/2]}{\Gamma(\delta/2)}\cos\left[(k/k_{\rm re})-(2-\delta)\pi/4\right] \\ -\frac{2}{2-\delta}\cos\left[(k/k_{\rm re})-\delta\pi/4\right]\biggr\}^2, \tag{A.59b}$$

$$\mathcal{A}_3 = \frac{2^{\delta-1}\Gamma^2[(\delta-1)/2]}{\pi(1-\delta)^2(1-\delta/2)^2}\left(\frac{k_{\rm re}}{k_{\rm e}}\right)^{2(2-\delta)}\cos^2[(k/k_{\rm re})-\delta\pi/4]. \tag{A.59c}$$

A.4.1 Computing the tensor power spectrum for $k > k_{\rm re}$:

We now turn our attention to scenarios where all relevant modes are deep inside the horizon before the end of reheating, i.e., $k > k_{\rm re}$, which corresponds to $x_{\rm re} > 1$. In this regime, the tensor power spectrum sourced by the magnetic field for modes $k > k_{\rm re}$ can be expressed as

$$\begin{aligned}P_{\rm T}^{\rm sec}(k > k_{\rm re}, \eta_\nu) = \frac{k^4|\mathcal{B}|^4}{32\pi^2 M_{\rm P}^4}\left(\frac{k}{k_{\rm e}}\right)^{-4(n+\alpha+1)} x_{\rm re}^2 \left(\int_{x_{\rm re}}^{x_\nu} dx_1 \frac{\mathcal{G}_{\bf k}(x_\nu, x_1)}{a^2(x_1)}\right)^2 \\ \times \left\{\int_{u_{\rm min}}^1 \frac{du}{u}\int_{-1}^1 d\mu f(\mu,\gamma) u^{3-2(n+\alpha)} {\rm J}_{\alpha+1/2}^2(ux_{\rm re}){\rm J}_{\alpha+1/2}^2(x_{\rm re}) \right. \\ \left. + \int_1^{u_{\rm max}} \frac{du}{u^4}\int_{-1}^1 d\mu f(\mu,\gamma) u^{6-4(n+\alpha)} {\rm J}_{\alpha+1/2}^4(ux_{\rm re})\right\}\end{aligned} \quad (A.60)$$

$$\begin{aligned}P_{\rm T}^{\rm sec}(k > k_{\rm re}, \eta_\nu) = \frac{k^4|\mathcal{B}|^4}{32\pi^2 M_{\rm P}^4}\left(\frac{k}{k_{\rm e}}\right)^{-4(n+\alpha+1)} x_{\rm re}^2 \left(\int_{x_{\rm re}}^{x_\nu} dx_1 \frac{\mathcal{G}_{\bf k}(x_\nu, x_1)}{a^2(x_1)}\right)^2 \\ \times \left\{F_{uu}^3(k > k_{\rm re}, \eta_{\rm re}) + F_{uu}^4(k > k_{\rm re}, \eta_{\rm re})\right\}\end{aligned} \quad (A.61)$$

where we defined

$$F_{uu}^3(k > k_{\rm re}, \eta_{\rm re}) = \int_{u_{\rm min}}^1 \frac{du}{u}\int_{-1}^1 d\mu f(\mu,\gamma) u^{3-2(n+\alpha)} {\rm J}_{\alpha+1/2}^2(ux_{\rm re}){\rm J}_{\alpha+1/2}^2(x_{\rm re} > 1) \quad (A.62)$$

$$F_{uu}^4(k > k_{\rm re}, \eta_{\rm re}) = \int_1^{u_{\rm max}} \frac{du}{u^4}\int_{-1}^1 d\mu f(\mu,\gamma) u^{6-4(n+\alpha)} {\rm J}_{\alpha+1/2}^4(ux_{\rm re}) \quad (A.63)$$

Similarly, we first perform the μ integral and rewrite the above integral as

$$F_{uu}^3(k > k_{\rm re}, \eta_{\rm re}) = \frac{8}{3}\int_{u_{\rm min}}^1 \frac{du}{u} u^{3-2(n+\alpha)} {\rm J}_{\alpha+1/2}^2(ux_{\rm re}){\rm J}_{\alpha+1/2}^2(x_{\rm re} > 1) \quad (A.64)$$

$$= \frac{8}{3}\int_{u_{\rm min}}^1 du u^{2-2(n+\alpha)} {\rm J}_{\alpha+1/2}^2(ux_{\rm re}){\rm J}_{\alpha+1/2}^2(x_{\rm re} > 1) \quad (A.65)$$

$$F_{uu}^4(k > k_{\rm re}, \eta_{\rm re}) = \frac{16}{15}\int_1^{u_{\rm max}} \frac{du}{u^4} u^{6-4(n+\alpha)} {\rm J}_{\alpha+1/2}^4(ux_{\rm re} >> 1) \quad (A.66)$$

$$= \frac{16}{15}\int_1^{u_{\rm max}} du u^{2-4(n+\alpha)} {\rm J}_{\alpha+1/2}^4(ux_{\rm re} >> 1) \quad (A.67)$$

From Fig. (A.1), it is evident that for $k > k_{\rm re}$, the dominant contribution arises entirely from the first integral, i.e., F_{uu}^3 defined in Eq. (A.65). Hence, we neglect the second integral, F_{uu}^4, as its contribution is subdominant. To gain an analytical understanding of the GW spectral

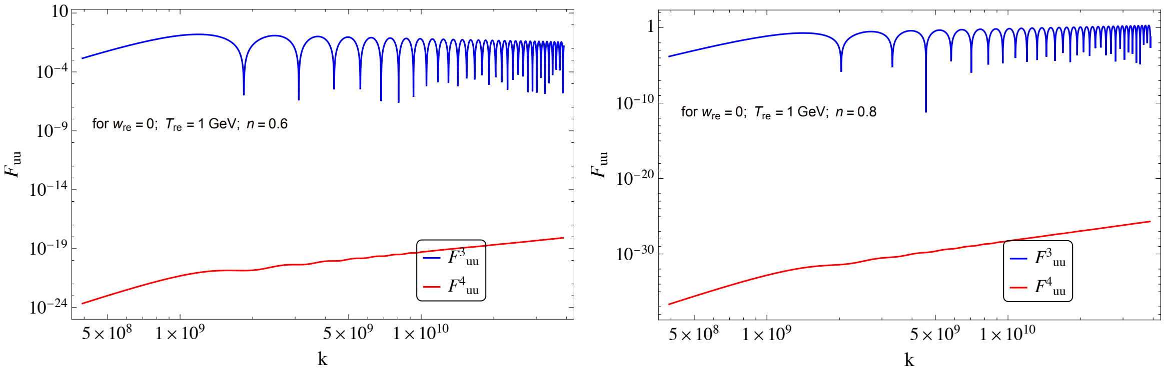

Figure A.1: In this figure, we have shown how the numerical and analytical estimate is consistence with each other for a specific set of parameters.

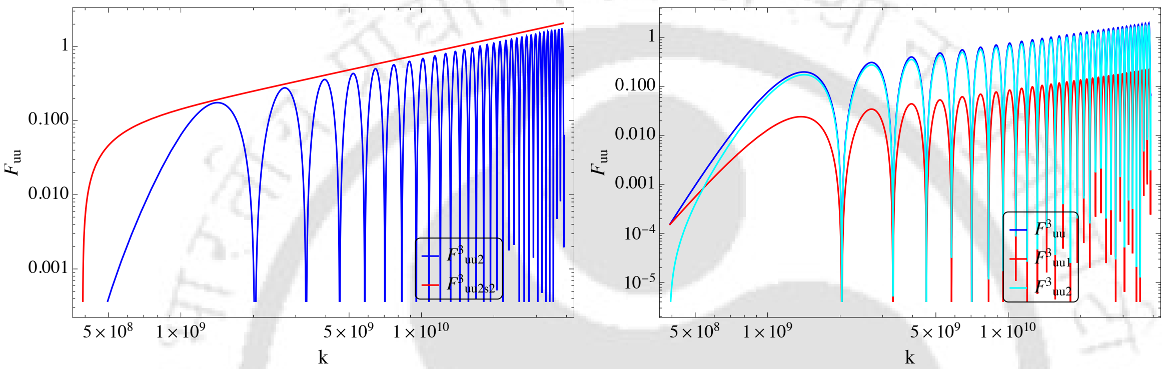

Figure A.2: In this figure, we have shown how the numerical and analytical estimates are consistent for a specific set of parameters.

behavior, we now decompose the above integral into two parts as

$$F^3_{uu}(k > k_{\rm re}, \eta_{\rm re}) = \frac{8}{3}\left\{\int_{u_{\min}}^{k_{\rm re}/k} du u^{2-2(n+\alpha)} \mathrm{J}^2_{\alpha+1/2}(ux_{\rm re})\mathrm{J}^2_{\alpha+1/2}(x_{\rm re} > 1) + \int_{k_{\rm re}/k}^{1} du u^{2-2(n+\alpha)} \mathrm{J}^2_{\alpha+1/2}(ux_{\rm re})\mathrm{J}^2_{\alpha+1/2}(x_{\rm re} > 1)\right\} \tag{A.68}$$

$$F^3_{uu}(k > k_{\rm re}, \eta_{\rm re}) = F^3_{uu,1}(k > k_{\rm re}, \eta_{\rm re}) + F^3_{uu,2}(k > k_{\rm re}, \eta_{\rm re}) \tag{A.69}$$

where we defined

$$F^3_{uu,1}(k > k_{\rm re}, \eta_{\rm re}) = \frac{8}{3}\int_{u_{\min}}^{k_{\rm re}/k} du u^{2-2(n+\alpha)} \mathrm{J}^2_{\alpha+1/2}(ux_{\rm re})\mathrm{J}^2_{\alpha+1/2}(x_{\rm re} > 1) \tag{A.70}$$

$$F^3_{uu,2}(k > k_{\rm re}, \eta_{\rm re}) = \frac{8}{3}\int_{k_{\rm re}/k}^{1} du u^{2-2(n+\alpha)} \mathrm{J}^2_{\alpha+1/2}(ux_{\rm re})\mathrm{J}^2_{\alpha+1/2}(x_{\rm re} > 1) \tag{A.71}$$

As shown in Fig. A.2, we find that the last integral provides the best fit to the full numerical result. Therefore, we retain only the last integral for further analytical estimations. Since we are focusing on the modes that remain inside the horizon at the end of reheating, i.e., $k > k_{\rm re}$, and the integration range extends from $k_{\rm re}/k$ to 1, the above expression can be further simplified as

$$F^3_{uu,2}(k > k_{\rm re}, \eta_{\rm re}) = \frac{8}{3}\frac{4}{\pi^2}\frac{1}{x^2_{\rm re}}\int_{k_{\rm re}/k}^{1} du u^{1-2(n+\alpha)} \tag{A.72}$$

$$= \frac{8}{3}\frac{4}{\pi^2}\frac{1}{x^2_{\rm re}}\frac{1}{2-2(n+\alpha)}\left\{1 - \left(\frac{k_{\rm re}}{k}\right)^{2-2(n+\alpha)}\right\} \tag{A.73}$$

However, as we have seen, to ensure consistency with the full numerical amplitude, we need to include an overall numerical prefactor. We find that this prefactor is approximately 0.2. Therefore, the final analytical expression for the integral becomes

$$F^3_{uu}(k > k_{\rm re}) \simeq \frac{64}{30\pi^2}\frac{1}{2-2(n+\alpha)}\frac{1}{x^2_{\rm re}}\left\{1 - \left(\frac{k_{\rm re}}{k}\right)^{2-2(n+\alpha)}\right\} \tag{A.74}$$

Bibliography

[1] LIGO Scientific, Virgo collaboration, *Observation of Gravitational Waves from a Binary Black Hole Merger*, *Phys. Rev. Lett.* **116** (2016) 061102 [1602.03837].

[2] LIGO Scientific, Virgo collaboration, *Properties of the Binary Black Hole Merger GW150914*, *Phys. Rev. Lett.* **116** (2016) 241102 [1602.03840].

[3] LIGO Scientific, Virgo collaboration, *GW150914: The Advanced LIGO Detectors in the Era of First Discoveries*, *Phys. Rev. Lett.* **116** (2016) 131103 [1602.03838].

[4] LIGO Scientific, Virgo collaboration, *GW150914: First results from the search for binary black hole coalescence with Advanced LIGO*, *Phys. Rev. D* **93** (2016) 122003 [1602.03839].

[5] LIGO Scientific, VIRGO collaboration, *GW170104: Observation of a 50-Solar-Mass Binary Black Hole Coalescence at Redshift 0.2*, *Phys. Rev. Lett.* **118** (2017) 221101 [1706.01812].

[6] LIGO Scientific, Virgo collaboration, *Upper Limits on the Stochastic Gravitational-Wave Background from Advanced LIGO's First Observing Run*, *Phys. Rev. Lett.* **118** (2017) 121101 [1612.02029].

[7] G.F.e.a.C.C. Smoot, *Structure in the cobe differential microwave radiometer first-year maps*, *Astrophys. J. Lett.* **396** (1992) L1.

[8] J.C.e.a.C.C. Mather, *Measurement of the cosmic microwave background spectrum by the cobe firas instrument*, *Astrophys. J.* **420** (1994) 439.

[9] C.L.e.a.W.C. Bennett, *First-year wilkinson microwave anisotropy probe (wmap) observations: Preliminary maps and basic results*, *Astrophys. J. Suppl.* **148** (2003) 1 [astro-ph/0302207].

[10] E.e.a.W.C. Komatsu, *Seven-year wilkinson microwave anisotropy probe (wmap) observations: Cosmological interpretation*, *Astrophys. J. Suppl.* **192** (2011) 18 [1001.4538].

[11] Planck collaboration, *Planck 2018 results. VI. Cosmological parameters*, *Astron. Astrophys.* **641** (2020) A6 [1807.06209].

[12] Planck collaboration, *Planck 2018 results. X. Constraints on inflation*, *Astron. Astrophys.* **641** (2020) A10 [1807.06211].

[13] A.H. Guth, *The Inflationary Universe: A Possible Solution to the Horizon and Flatness Problems*, *Phys. Rev. D* **23** (1981) 347.

[14] A.D. Linde, *A New Inflationary Universe Scenario: A Possible Solution of the Horizon, Flatness, Homogeneity, Isotropy and Primordial Monopole Problems*, *Phys. Lett. B* **108** (1982) 389.

[15] A. Albrecht and P.J. Steinhardt, *Cosmology for Grand Unified Theories with Radiatively Induced Symmetry Breaking*, *Phys. Rev. Lett.* **48** (1982) 1220.

[16] A.A. Starobinsky, *A New Type of Isotropic Cosmological Models Without Singularity*, *Phys. Lett. B* **91** (1980) 99.

[17] A.R. Liddle, P. Parsons and J.D. Barrow, *Formalizing the slow-roll approximation in inflation*, *Phys. Rev. D* **50** (1994) 7222.

[18] V.F. Mukhanov and G.V. Chibisov, *Quantum fluctuations and a nonsingular universe*, *JETP Lett.* **33** (1981) 532.

[19] A.A. Starobinsky, *Dynamics of phase transition in the new inflationary universe scenario*, *Phys. Lett. B* **117** (1982) 175.

[20] V.C. Rubin and W.K. Ford, *Rotation of the andromeda nebula from a spectroscopic survey of emission regions*, *Astrophys. J.* **159** (1970) 379.

[21] V.C. Rubin, W.K. Ford and N. Thonnard, *Rotational properties of 21 sc galaxies with a large range of luminosities and radii*, *Astrophys. J.* **238** (1980) 471.

[22] A. Bosma, *The Distribution and Kinematics of Neutral Hydrogen in Spiral Galaxies*, Ph.D. thesis, University of Groningen, 1978.

[23] D.e.a. Clowe, *A direct empirical proof of the existence of dark matter*, *Astrophys. J. Lett.* **648** (2006) L109 [astro-ph/0608407].

[24] R.e.a. Massey, *Dark matter maps reveal cosmic scaffolding*, *Nature* **445** (2007) 286 [astro-ph/0701594].

[25] C.e.a.M.C. Alcock, *The macho project: Microlensing results from 5.7 years of lmc observations*, *Astrophys. J.* **542** (2000) 281 [astro-ph/0001272].

[26] P.e.a.E.-C. Tisserand, *Limits on the macho content of the galactic halo from the eros-2 survey*, *Astron. Astrophys.* **469** (2007) 387 [astro-ph/0607207].

[27] G. Bertone, D. Hooper and J. Silk, *Particle dark matter: Evidence, candidates and constraints*, *Phys. Rept.* **405** (2005) 279 [hep-ph/0404175].

[28] G. Bertone and T. Tait, M. P., *A new era in the search for dark matter*, *Nature* **562** (2018) 51 [1810.01668].

[29] A.G.e.a. Riess, *Observational evidence from supernovae for an accelerating universe and a cosmological constant*, *Astron. J.* **116** (1998) 1009 [astro-ph/9805201].

[30] S.e.a. Perlmutter, *Measurements of ω and λ from 42 high-redshift supernovae*, *Astrophys. J.* **517** (1999) 565 [astro-ph/9812133].

[31] D.J.e.a. Eisenstein, *Detection of the baryon acoustic peak in the large-scale correlation function of sdss luminous red galaxies*, *Astrophys. J.* **633** (2005) 560 [astro-ph/0501171].

[32] M.e.a. Tegmark, *Cosmological parameters from sdss and wmap*, *Phys. Rev. D* **69** (2004) 103501 [astro-ph/0310723].

[33] S. Weinberg, *Cosmology*, Oxford University Press (2008).

[34] P.J.E. Peebles and B. Ratra, *The cosmological constant and dark energy*, *Rev. Mod. Phys.* **75** (2003) 559 [astro-ph/0207347].

[35] S. Weinberg, *The cosmological constant problem*, *Rev. Mod. Phys.* **61** (1989) 1.

[36] J. Martin, *Everything you always wanted to know about the cosmological constant problem*, *Comptes Rendus Physique* **13** (2012) 566 [1205.3365].

[37] C.e.a. Cheung, *The effective field theory of inflation*, *JHEP* **03** (2008) 014 [0709.0293].

[38] D. Baumann, *Tasi lectures on inflation*, *arXiv:0907.5424* (2009) .

[39] Y.e.a.P.C. Akrami, *Planck 2018 results. ix. constraints on primordial non-gaussianity*, *Astron. Astrophys.* **641** (2020) A9 [1805.09291].

[40] E.W. Kolb and M.S. Turner, *The Early Universe*, vol. 69 (1990), 10.1201/9780429492860.

[41] NANOGrav collaboration, *The NANOGrav 15 yr Data Set: Evidence for a Gravitational-wave Background*, *Astrophys. J. Lett.* **951** (2023) L8 [2306.16213].

[42] A. et al, *The second data release from the European Pulsar Timing Array I. The dataset and timing analysis*, *arXiv e-prints* (2023) arXiv:2306.16224 [2306.16224].

[43] D.J. Reardon et al., *Search for an Isotropic Gravitational-wave Background with the Parkes Pulsar Timing Array*, *Astrophys. J. Lett.* **951** (2023) L6 [2306.16215].

[44] A. Zic et al., *The Parkes Pulsar Timing Array third data release*, *Publ. Astron. Soc. Austral.* **40** (2023) e049 [2306.16230].

[45] H. Xu et al., *Searching for the Nano-Hertz Stochastic Gravitational Wave Background with the Chinese Pulsar Timing Array Data Release I*, *Res. Astron. Astrophys.* **23** (2023) 075024 [2306.16216].

[46] L.M. Widrow, *Origin of galactic and extragalactic magnetic fields*, *Rev. Mod. Phys.* **74** (2002) 775 [astro-ph/0207240].

[47] R. Durrer and A. Neronov, *Cosmological Magnetic Fields: Their Generation, Evolution and Observation*, *Astron. Astrophys. Rev.* **21** (2013) 62 [1303.7121].

[48] A.D. Sakharov, *Violation of cp invariance, c asymmetry, and baryon asymmetry of the universe*, *JETP Lett.* **5** (1967) 24.

[49] A. Riotto and M. Trodden, *Recent progress in baryogenesis*, *Ann. Rev. Nucl. Part. Sci.* **49** (1999) 35 [hep-ph/9901362].

[50] M. Drewes, J.U. Kang and U.R. Mun, *CMB constraints on the inflaton couplings and reheating temperature in α-attractor inflation*, *JHEP* **11** (2017) 072 [1708.01197].

[51] D.S. Zharov, O.O. Sobol and S.I. Vilchinskii, *Reheating acts on starobinsky and higgs inflation*, 2025.

[52] M.R. Haque, S. Pal and D. Paul, *Act dr6 insights on the inflationary attractor models and reheating*, 2025.

[53] L. Liu, Z. Yi and Y. Gong, *Reconciling higgs inflation with act observations through reheating*, 2025.

[54] M. Drewes, L. Ming and I. Oldengott, *LiteBIRD and CMB-S4 sensitivities to reheating in plateau models of inflation*, *JCAP* **05** (2024) 081 [2303.13503].

[55] L. Dai, M. Kamionkowski and J. Wang, *Reheating constraints to inflationary models*, *Physical Review Letters* **113** (2014) .

[56] M.R. Haque, S. Pal and D. Paul, *ACT DR6 Insights on the Inflationary Attractor models and Reheating*, 2505.01517.

[57] L. Kofman, A.D. Linde and A.A. Starobinsky, *Towards the theory of reheating after inflation*, *Phys. Rev. D* **56** (1997) 3258 [hep-ph/9704452].

[58] B.A. Bassett, S. Tsujikawa and D. Wands, *Inflation dynamics and reheating*, *Reviews of Modern Physics* **78** (2006) 537–589.

[59] J.L. Cook, E. Dimastrogiovanni, D.A. Easson and L.M. Krauss, *Reheating predictions in single field inflation*, *JCAP* **04** (2015) 047 [1502.04673].

[60] P. Adshead, P. Ralegankar and J. Shelton, *Reheating in two-sector cosmology*, *Journal of High Energy Physics* **2019** (2019) .

[61] M. Kawasaki, K. Kohri and N. Sugiyama, *MeV scale reheating temperature and thermalization of neutrino background*, *Phys. Rev. D* **62** (2000) 023506 [astro-ph/0002127].

[62] M.A. Amin, M.P. Hertzberg, D.I. Kaiser and J. Karouby, *Nonperturbative Dynamics Of Reheating After Inflation: A Review*, *Int. J. Mod. Phys. D* **24** (2014) 1530003 [1410.3808].

[63] Y. Shtanov, J.H. Traschen and R.H. Brandenberger, *Universe reheating after inflation*, *Phys. Rev. D* **51** (1995) 5438 [hep-ph/9407247].

[64] BICEP, Keck collaboration, *Improved Constraints on Primordial Gravitational Waves using Planck, WMAP, and BICEP/Keck Observations through the 2018 Observing Season*, *Phys. Rev. Lett.* **127** (2021) 151301 [2110.00483].

[65] BICEP2, Keck Array collaboration, *BICEP2 / Keck Array x: Constraints on Primordial Gravitational Waves using Planck, WMAP, and New BICEP2/Keck Observations through the 2015 Season*, *Phys. Rev. Lett.* **121** (2018) 221301 [1810.05216].

[66] SDSS collaboration, *Detection of the Baryon Acoustic Peak in the Large-Scale Correlation Function of SDSS Luminous Red Galaxies*, *Astrophys. J.* **633** (2005) 560 [astro-ph/0501171].

[67] eBOSS collaboration, *Completed SDSS-IV extended Baryon Oscillation Spectroscopic Survey: Cosmological implications from two decades of spectroscopic surveys at the Apache Point Observatory*, *Phys. Rev. D* **103** (2021) 083533 [2007.08991].

[68] T.J. Clarke, E.J. Copeland and A. Moss, *Constraints on primordial gravitational waves from the Cosmic Microwave Background*, *JCAP* **10** (2020) 002 [2004.11396].

[69] Particle Data Group Collaboration collaboration, *Review of particle physics*, *Phys. Rev. D* **110** (2024) 030001.

[70] A.G. Riess et al., *A Comprehensive Measurement of the Local Value of the Hubble Constant with 1 km s^{-1} Mpc^{-1} Uncertainty from the Hubble Space Telescope and the SH0ES Team*, *Astrophys. J. Lett.* **934** (2022) L7 [2112.04510].

[71] BOSS collaboration, *The clustering of galaxies in the completed SDSS-III Baryon Oscillation Spectroscopic Survey: Observational systematics and baryon acoustic oscillations in the correlation function*, *Mon. Not. Roy. Astron. Soc.* **464** (2017) 1168 [1607.03145].

[72] B.D. Fields, P. Molaro and S. Sarkar, *Big-bang nucleosynthesis*, *Particle Data Group Review* (2020) [1912.01132].

[73] B.M.S. Hansen et al., *An age constraint from the globular cluster m4*, *Nature* **500** (2013) 51.

[74] D.J. Fixsen, *The Temperature of the Cosmic Microwave Background*, *Astrophys. J.* **707** (2009) 916 [0911.1955].

[75] DES collaboration, *Dark Energy Survey Year 3 results: Cosmological constraints from galaxy clustering and weak lensing*, *Phys. Rev. D* **105** (2022) 023520 [2105.13549].

[76] R.J. Cooke, M. Pettini and C.C. Steidel, *One Percent Determination of the Primordial Deuterium Abundance*, *Astrophys. J.* **855** (2018) 102 [1710.11129].

[77] Y.I. Izotov, T.X. Thuan and N.G. Guseva, *A new determination of the primordial He abundance using the He I 10830 AA emission line: cosmological implications*, *Mon. Not. Roy. Astron. Soc.* **445** (2014) 778 [1408.6953].

[78] G. Mangano, G. Miele, S. Pastor, T. Pinto, O. Pisanti and P.D. Serpico, *Relic neutrino decoupling including flavor oscillations*, *Nucl. Phys. B* **729** (2005) 221 [hep-ph/0506164].

[79] I. Esteban, M.C. Gonzalez-Garcia, M. Maltoni, T. Schwetz and A. Zhou, *The fate of hints: updated global analysis of three-flavor neutrino oscillations*, *JHEP* **09** (2020) 178 [2007.14792].

[80] S. Weinberg, *Cosmology*, Oxford University Press (2008).

[81] S. Dodelson, *Modern Cosmology*, Academic Press (2003).

[82] V. Mukhanov, *Physical Foundations of Cosmology*, Cambridge University Press (2005).

[83] D.W. Hogg et al., *Cosmic homogeneity demonstrated with luminous red galaxies*, *Astrophysical Journal* **624** (2005) 54 [astro-ph/0411197].

[84] O.F. Piattella, *Lecture Notes in Cosmology*, UNITEXT for Physics, Springer, Cham (2018), 10.1007/978-3-319-95570-4, [1803.00070].

[85] M.S. Turner and L.M. Widrow, *Inflation Produced, Large Scale Magnetic Fields*, *Phys. Rev. D* **37** (1988) 2743.

[86] Atacama Cosmology Telescope collaboration, *The Atacama Cosmology Telescope: DR6 power spectra, likelihoods and ΛCDM parameters*, *JCAP* **11** (2025) 062 [2503.14452].

[87] L. Senatore, *Lectures on Inflation*, in *Theoretical Advanced Study Institute in Elementary Particle Physics: New Frontiers in Fields and Strings*, pp. 447–543, 2017, DOI [1609.00716].

[88] M. Lemoine, J. Martin and P. Peter, eds., *Inflationary cosmology* (2008), 10.1007/978-3-540-74353-8.

[89] J. Martin, *Inflation and precision cosmology*, 2003.

[90] J. Martin, *Inflationary cosmological perturbations of quantum-mechanical origin*, in *Lecture Notes in Physics*, p. 199–244, Springer-Verlag DOI.

[91] L. Sriramkumar, *An introduction to inflation and cosmological perturbation theory*, 2009.

[92] A. Linde, *Inflationary Cosmology after Planck 2013*, in *100e Ecole d'Ete de Physique: Post-Planck Cosmology*, pp. 231–316, 2015, DOI [1402.0526].

[93] D. Baumann, *Cosmological inflation: Theory and observations*, *Advanced Science Letters* **2** (2009) 105–120.

[94] D. Baumann, *Primordial Cosmology*, *PoS* **TASI2017** (2018) 009 [1807.03098].

[95] D. Baumann and H.V. Peiris, *Cosmological Inflation: Theory and Observations*, *Adv. Sci. Lett.* **2** (2009) 105 [0810.3022].

[96] R. Brandenberger, *Initial conditions for inflation — A short review*, *Int. J. Mod. Phys. D* **26** (2016) 1740002 [1601.01918].

[97] R. Kallosh and A. Linde, *Polynomial α-attractors*, *JCAP* **04** (2022) 017 [2202.06492].

[98] D. Maity and P. Saha, *CMB constraints on dark matter phenomenology via reheating in Minimal plateau inflation*, *Phys. Dark Univ.* **25** (2019) 100317 [1804.10115].

[99] P. Saha, S. Anand and L. Sriramkumar, *Accounting for the time evolution of the equation of state parameter during reheating*, *Phys. Rev. D* **102** (2020) 103511 [2005.01874].

[100] P. Saha and Y. Urakawa, *Potential surge preheating: enhanced resonance from potential features*, *JCAP* **04** (2025) 061 [2412.17359].

[101] J. Martin, T. Papanikolaou, L. Pinol and V. Vennin, *Metric preheating and radiative decay in single-field inflation*, *JCAP* **05** (2020) 003 [2002.01820].

[102] S. Antusch, D.G. Figueroa, K. Marschall and F. Torrenti, *Characterizing the postinflationary reheating history: Single daughter field with quadratic-quadratic interaction*, *Phys. Rev. D* **105** (2022) 043532 [2112.11280].

[103] F. Dux, A. Florio, J. Klarić, A. Shkerin and I. Timiryasov, *Preheating in Palatini Higgs inflation on the lattice*, *JCAP* **09** (2022) 015 [2203.13286].

[104] R. Mahbub and S.S. Mishra, *Oscillon formation from preheating in asymmetric inflationary potentials*, *Phys. Rev. D* **108** (2023) 063524 [2303.07503].

[105] R. Allahverdi, R. Brandenberger, F.-Y. Cyr-Racine and A. Mazumdar, *Reheating in Inflationary Cosmology: Theory and Applications*, *Ann. Rev. Nucl. Part. Sci.* **60** (2010) 27 [1001.2600].

[106] M. Kawasaki, K. Kohri and N. Sugiyama, *Cosmological constraints on late time entropy production*, *Phys. Rev. Lett.* **82** (1999) 4168 [astro-ph/9811437].

[107] M.R. Haque and D. Maity, *Gravitational reheating*, *Phys. Rev. D* **107** (2023) 043531.

[108] T. Hasegawa, N. Hiroshima, K. Kohri, R.S.L. Hansen, T. Tram and S. Hannestad, *MeV-scale reheating temperature and thermalization of oscillating neutrinos by radiative and hadronic decays of massive particles*, *JCAP* **12** (2019) 012 [1908.10189].

[109] S. Hannestad, *What is the lowest possible reheating temperature?*, *Physical Review D* **70** (2004) .

[110] A. Ghosh and D. Ghosh, *Time evolution of the equation of state during perturbative reheating and its impact on the inflationary tensor perturbation spectrum*, *Nucl. Phys. B* **1018** (2025) 116976 [2411.02052].

[111] D. Choi, S. Jeon and J.-O. Gong, *Weakly model-independent determination of total expansion during inflation*, 2509.21850.

[112] S. Antusch, K. Marschall and F. Torrenti, *Equation of state during (p)reheating with trilinear interactions*, *JCAP* **11** (2025) 002 [2507.13465].

[113] L. Dai, M. Kamionkowski and J. Wang, *Reheating constraints to inflationary models*, *Phys. Rev. Lett.* **113** (2014) 041302.

[114] M.R. Haque, D. Maity and R. Mondal, *Thermal and nonthermal dark matters with gravitational neutrino reheating*, *Phys. Rev. D* **111** (2025) 063546 [2408.12450].

[115] M.R. Haque, D. Maity and R. Mondal, *Gravitational neutrino reheating*, *Phys. Rev. D* **109** (2024) 063543 [2311.07684].

[116] A. Chakraborty, M.R. Haque, D. Maity and R. Mondal, *Inflaton phenomenology via reheating in light of primordial gravitational waves and the latest BICEP/Keck data*, *Phys. Rev. D* **108** (2023) 023515 [2304.13637].

[117] S. Maiti, D. Maity and R. Srikanth, *Probing reheating phase via nonhelical magnetogenesis and secondary gravitational waves*, *Phys. Rev. D* **112** (2025) 063552 [2505.13623].

[118] S. Maiti, *Magnetogenesis from a sawtooth coupling: Gravitational wave probe of reheating*, *Phys. Rev. D* **112** (2025) 043536 [2506.06183].

[119] A. Chakraborty, S. Maiti and D. Maity, *Probing a nonminimal coupling through superhorizon instability and secondary gravitational waves*, *Phys. Rev. D* **111** (2025) 083505 [2408.07767].

[120] Y.B. Zel'dovich and I.D. Novikov, *The Hypothesis of Cores Retarded during Expansion and the Hot Cosmological Model*, *Sov. Astron.* **10** (1967) 602.

[121] S. Hawking, *Gravitationally collapsed objects of very low mass*, *Mon. Not. Roy. Astron. Soc.* **152** (1971) 75.

[122] B.J. Carr and S.W. Hawking, *Black holes in the early universe*, *Mon. Not. Roy. Astron. Soc.* **168** (1974) 399.

[123] B.J. Carr, *The primordial black hole mass spectrum*, *Astrophysical Journal* **201** (1975) 1.

[124] B. Carr and F. Kuhnel, *Primordial Black Holes as Dark Matter: Recent Developments*, *Ann. Rev. Nucl. Part. Sci.* **70** (2020) 355 [2006.02838].

[125] M. Riajul Haque, E. Kpatcha, D. Maity and Y. Mambrini, *Primordial black hole reheating*, *Phys. Rev. D* **108** (2023) 063523 [2305.10518].

[126] N. Bernal, C.S. Fong, Y.F. Perez-Gonzalez and J. Turner, *Rescuing high-scale leptogenesis using primordial black holes*, *Phys. Rev. D* **106** (2022) 035019 [2203.08823].

[127] K. Schmitz and X.-J. Xu, *Wash-in leptogenesis after the evaporation of primordial black holes*, *Phys. Lett. B* **849** (2024) 138473 [2311.01089].

[128] S. Wang, Y.-F. Wang, Q.-G. Huang and T.G.F. Li, *Constraints on the primordial black hole abundance from the first advanced ligo observation run using the stochastic gravitational-wave background*, *Phys. Rev. Lett.* **120** (2018) 191102.

[129] A.D. Dolgov and D. Ejlli, *Relic gravitational waves from light primordial black holes*, *Phys. Rev. D* **84** (2011) 024028 [1105.2303].

[130] E. Bagui and S. Clesse, *A boosted gravitational wave background for primordial black holes with broad mass distributions and thermal features*, *Phys. Dark Univ.* **38** (2022) 101115 [2110.07487].

[131] M. Sasaki, T. Suyama, T. Tanaka and S. Yokoyama, *Primordial Black Hole Scenario for the Gravitational-Wave Event GW150914*, *Phys. Rev. Lett.* **117** (2016) 061101 [1603.08338].

[132] D. Ghosh and A.K. Mishra, *Gravitation wave signal from asteroid mass primordial black hole dark matter*, *Phys. Rev. D* **109** (2024) 043537.

[133] T. Papanikolaou, X.-C. He, X.-H. Ma, Y.-F. Cai, E.N. Saridakis and M. Sasaki, *New probe of non-Gaussianities with primordial black hole induced gravitational waves*, *Phys. Lett. B* **857** (2024) 138997 [2403.00660].

[134] T. Papanikolaou, S. Banerjee, Y.-F. Cai, S. Capozziello and E.N. Saridakis, *Primordial black holes and induced gravitational waves in non-singular matter bouncing cosmology*, *JCAP* **06** (2024) 066 [2404.03779].

[135] U. Kumar, *Primordial gravitational wave background as a probe of primordial black holes*, *Phys. Rev. D* **112** (2025) 084027.

[136] A. Ireland, S. Profumo and J. Scharnhorst, *Primordial gravitational waves from black hole evaporation in standard and nonstandard cosmologies*, *Phys. Rev. D* **107** (2023) 104021 [2302.10188].

[137] J. Kalita and D. Maity, *Revisiting PBH Accretion, Evaporation and Their Cosmological Consequences*, 2512.07291.

[138] S. Das, M.R. Haque, J. Kalita, R. Karmakar and D. Maity, *Impact of general relativistic accretion on primordial black holes*, *Phys. Rev. D* **112** (2025) 123540 [2505.15419].

[139] P. Athron, M. Chianese, S. Datta, R. Samanta and N. Saviano, *Impact of memory-burdened black holes on primordial gravitational waves in light of Pulsar Timing Array*, *JCAP* **05** (2025) 005 [2411.19286].

[140] M. Gross, Y. Mambrini, E. Kpatcha, M.O. Olea-Romacho and R. Roshan, *Gravitational wave production during reheating: From the inflaton to primordial black holes*, *Phys. Rev. D* **111** (2025) 035020 [2411.04189].

[141] S. Profumo, L. Brown, C. Ewasiuk, S. Ricarte and H. Su, *Maximal gravitational wave signal from asteroid-mass primordial black hole mergers at resonant microwave cavities*, *Phys. Rev. D* **111** (2025) 063072 [2410.15400].

[142] J. Garcia-Bellido and E. Ruiz Morales, *Primordial black holes from single field models of inflation*, *Phys. Dark Univ.* **18** (2017) 47 [1702.03901].

[143] H. Motohashi and W. Hu, *Primordial Black Holes and Slow-Roll Violation*, *Phys. Rev. D* **96** (2017) 063503 [1706.06784].

[144] C.T. Byrnes, P.S. Cole and S.P. Patil, *Steepest growth of the power spectrum and primordial black holes*, *JCAP* **06** (2019) 028 [1811.11158].

[145] G. Ballesteros, J. Beltran Jimenez and M. Pieroni, *Black hole formation from a general quadratic action for inflationary primordial fluctuations*, *JCAP* **06** (2019) 016 [1811.03065].

[146] R.N. Raveendran, K. Parattu and L. Sriramkumar, *Enhanced power on small scales and evolution of quantum state of perturbations in single and two field inflationary models*, *Gen. Rel. Grav.* **54** (2022) 91 [2206.05760].

[147] H.V. Ragavendra, P. Saha, L. Sriramkumar and J. Silk, *Primordial black holes and secondary gravitational waves from ultraslow roll and punctuated inflation*, *Phys. Rev. D* **103** (2021) 083510 [2008.12202].

[148] M. Braglia, D.K. Hazra, F. Finelli, G.F. Smoot, L. Sriramkumar and A.A. Starobinsky, *Generating PBHs and small-scale GWs in two-field models of inflation*, *JCAP* **08** (2020) 001 [2005.02895].

[149] A. Karam, N. Koivunen, E. Tomberg, V. Vaskonen and H. Veermäe, *Anatomy of single-field inflationary models for primordial black holes*, *JCAP* **03** (2023) 013 [2205.13540].

[150] E. Bugaev and P. Klimai, *Axion inflation with gauge field production and primordial black holes*, *Phys. Rev. D* **90** (2014) 103501 [1312.7435].

[151] C. Unal, A. Papageorgiou and I. Obata, *Axion-gauge dynamics during inflation as the origin of pulsar timing array signals and primordial black holes*, *Phys. Lett. B* **856** (2024) 138873 [2307.02322].

[152] E. Erfani, *Primordial Black Holes Formation from Particle Production during Inflation*, *JCAP* **04** (2016) 020 [1511.08470].

[153] C. Chen, A. Ghoshal, G. Tasinato and E. Tomberg, *Stochastic axionlike curvaton: Non-Gaussianity and primordial black holes without a large power spectrum*, *Phys. Rev. D* **111** (2025) 063539 [2409.12950].

[154] O. Özsoy and G. Tasinato, *Inflation and Primordial Black Holes*, *Universe* **9** (2023) 203 [2301.03600].

[155] O. Özsoy and G. Tasinato, *Consistency conditions and primordial black holes in single field inflation*, *Phys. Rev. D* **105** (2022) 023524 [2111.02432].

[156] N. Bhaumik and R.K. Jain, *Primordial black holes dark matter from inflection point models of inflation and the effects of reheating*, *JCAP* **01** (2020) 037 [1907.04125].

[157] S.W. Hawking, I.G. Moss and J.M. Stewart, *Bubble collisions in the very early universe*, *Phys. Rev. D* **26** (1982) 2681.

[158] S.G. Rubin, A.S. Sakharov and M.Y. Khlopov, *The Formation of primary galactic nuclei during phase transitions in the early universe*, *J. Exp. Theor. Phys.* **91** (2001) 921 [hep-ph/0106187].

[159] S.W. Hawking, *Black Holes From Cosmic Strings*, *Phys. Lett. B* **231** (1989) 237.

[160] A. Polnarev and R. Zembowicz, *Formation of Primordial Black Holes by Cosmic Strings*, *Phys. Rev. D* **43** (1991) 1106.

[161] R.R. Caldwell and B. Allen, *Cosmological constraints on cosmic-string gravitational radiation*, *Phys. Rev. D* **45** (1992) 3447.

[162] S. Saga, H. Tashiro and S. Yokoyama, *Limits on primordial magnetic fields from primordial black hole abundance*, *JCAP* **05** (2020) 039 [2002.01286].

[163] A. Kushwaha and T. Suyama, *Constraining small-scale primordial magnetic fields from the abundance of primordial black holes*, *JCAP* **12** (2024) 012 [2405.19693].

[164] S. Maiti and D. Maity, *The Magnetic Origin of Primordial Black Holes: A Viable Dark Matter Scenario*, 2508.19217.

[165] R.-g. Cai, S. Pi and M. Sasaki, *Gravitational Waves Induced by non-Gaussian Scalar Perturbations*, *Phys. Rev. Lett.* **122** (2019) 201101 [1810.11000].

[166] G. Franciolini, A. Iovino, Junior., V. Vaskonen and H. Veermae, *Recent Gravitational Wave Observation by Pulsar Timing Arrays and Primordial Black Holes: The Importance of Non-Gaussianities*, *Phys. Rev. Lett.* **131** (2023) 201401 [2306.17149].

[167] J.S. Bullock and J.R. Primack, *NonGaussian fluctuations and primordial black holes from inflation*, *Phys. Rev. D* **55** (1997) 7423 [astro-ph/9611106].

[168] S. Young and C.T. Byrnes, *Primordial black holes in non-Gaussian regimes*, *JCAP* **08** (2013) 052 [1307.4995].

[169] C.T. Byrnes, E.J. Copeland and A.M. Green, *Primordial black holes as a tool for constraining non-Gaussianity*, *Phys. Rev. D* **86** (2012) 043512 [1206.4188].

[170] M. Sasaki, T. Suyama, T. Tanaka and S. Yokoyama, *Primordial black holes—perspectives in gravitational wave astronomy*, *Class. Quant. Grav.* **35** (2018) 063001.

[171] C. Germani and I. Musco, *Abundance of Primordial Black Holes Depends on the Shape of the Inflationary Power Spectrum*, *Phys. Rev. Lett.* **122** (2019) 141302 [1805.04087].

[172] A. Escrivà, *Simulation of primordial black hole formation using pseudo-spectral methods*, Phys. Dark Univ. **27** (2020) 100466 [1907.13065].

[173] A. Escrivà, C. Germani and R.K. Sheth, *Analytical thresholds for black hole formation in general cosmological backgrounds*, JCAP **01** (2021) 030 [2007.05564].

[174] A. Escrivà, C. Germani and R.K. Sheth, *Universal threshold for primordial black hole formation*, Phys. Rev. D **101** (2020) 044022 [1907.13311].

[175] T. Papanikolaou, *Toward the primordial black hole formation threshold in a time-dependent equation-of-state background*, Phys. Rev. D **105** (2022) 124055.

[176] T. Harada, C.-M. Yoo and K. Kohri, *Threshold of primordial black hole formation*, Phys. Rev. D **88** (2013) 084051 [1309.4201].

[177] M. Shibata and M. Sasaki, *Black hole formation in the Friedmann universe: Formulation and computation in numerical relativity*, Phys. Rev. D **60** (1999) 084002 [gr-qc/9905064].

[178] S. Raatikainen, S. Räsänen and E. Tomberg, *Primordial black hole compaction function from stochastic fluctuations in ultraslow-roll inflation*, Phys. Rev. Lett. **133** (2024) 121403.

[179] J. Yang, X. Wang, X.-H. Ma, D. Zhang, S.-F. Yan, A. Ilyas et al., *Compaction function analysis of cmb μ distortion constraints on primordial black holes*, Phys. Rev. D **111** (2025) 043522.

[180] M. Kawasaki and H. Nakatsuka, *Effect of nonlinearity between density and curvature perturbations on the primordial black hole formation*, Phys. Rev. D **99** (2019) 123501 [1903.02994].

[181] C. Germani and R.K. Sheth, *Nonlinear statistics of primordial black holes from Gaussian curvature perturbations*, Phys. Rev. D **101** (2020) 063520 [1912.07072].

[182] S. Maity, N. Bhaumik, M.R. Haque, D. Maity and L. Sriramkumar, *Constraining the history of reheating with the NANOGrav 15-year data*, JCAP **01** (2025) 118 [2403.16963].

[183] H.V. Ragavendra, P. Saha, L. Sriramkumar and J. Silk, *Primordial black holes and secondary gravitational waves from ultraslow roll and punctuated inflation*, Phys. Rev. D **103** (2021) 083510.

[184] H.V. Ragavendra and L. Sriramkumar, *Observational Imprints of Enhanced Scalar Power on Small Scales in Ultra Slow Roll Inflation and Associated Non-Gaussianities*, Galaxies **11** (2023) 34 [2301.08887].

[185] S.W. Hawking, *Particle Creation by Black Holes*, *Commun. Math. Phys.* **43** (1975) 199.

[186] D.N. Page, *Particle emission rates from a black hole. ii. massless particles from a rotating hole*, *Phys. Rev. D* **14** (1976) 3260.

[187] B.J. Carr, K. Kohri, Y. Sendouda and J. Yokoyama, *New cosmological constraints on primordial black holes*, *Phys. Rev. D* **81** (2010) 104019 [0912.5297].

[188] B. Carr, K. Kohri, Y. Sendouda and J. Yokoyama, *Constraints on primordial black holes*, *Rept. Prog. Phys.* **84** (2021) 116902 [2002.12778].

[189] G. Sato-Polito, E.D. Kovetz and M. Kamionkowski, *Constraints on the primordial curvature power spectrum from primordial black holes*, *Phys. Rev. D* **100** (2019) 063521 [1904.10971].

[190] M.Y. Khlopov and A.G. Polnarev, *PRIMORDIAL BLACK HOLES AS A COSMOLOGICAL TEST OF GRAND UNIFICATION*, *Phys. Lett. B* **97** (1980) 383.

[191] J. Garcia-Bellido, A.D. Linde and D. Wands, *Density perturbations and black hole formation in hybrid inflation*, *Phys. Rev. D* **54** (1996) 6040 [astro-ph/9605094].

[192] J. Yokoyama, *Chaotic new inflation and formation of primordial black holes*, *Phys. Rev. D* **58** (1998) 083510 [astro-ph/9802357].

[193] M. Kawasaki, N. Sugiyama and T. Yanagida, *Primordial black hole formation in a double inflation model in supergravity*, *Phys. Rev. D* **57** (1998) 6050 [hep-ph/9710259].

[194] N. Bhaumik and R.K. Jain, *Small scale induced gravitational waves from primordial black holes, a stringent lower mass bound, and the imprints of an early matter to radiation transition*, *Phys. Rev. D* **104** (2021) 023531 [2009.10424].

[195] M. Solbi and K. Karami, *Primordial black holes and induced gravitational waves in k-inflation*, *JCAP* **08** (2021) 056 [2102.05651].

[196] D.G. Figueroa, S. Raatikainen, S. Rasanen and E. Tomberg, *Implications of stochastic effects for primordial black hole production in ultra-slow-roll inflation*, *JCAP* **05** (2022) 027 [2111.07437].

[197] D. Frolovsky, S.V. Ketov and S. Saburov, *E-models of inflation and primordial black holes*, *Front. in Phys.* **10** (2022) 1005333 [2207.11878].

[198] S. Young, C.T. Byrnes and M. Sasaki, *Calculating the mass fraction of primordial black holes*, *JCAP* **07** (2014) 045 [1405.7023].

[199] K. Ando, K. Inomata and M. Kawasaki, *Primordial black holes and uncertainties in the choice of the window function*, *Phys. Rev. D* **97** (2018) 103528 [1802.06393].

[200] H.V. Ragavendra, L. Sriramkumar and J. Silk, *Could PBHs and secondary GWs have originated from squeezed initial states?*, *JCAP* **05** (2021) 010 [2011.09938].

[201] A. Bhaumik, T. Papanikolaou and A. Ghoshal, *Vector induced gravitational waves sourced by primordial magnetic fields*, *JCAP* **08** (2025) 054 [2504.10477].

[202] V. Acquaviva, N. Bartolo, S. Matarrese and A. Riotto, *Second order cosmological perturbations from inflation*, *Nucl. Phys. B* **667** (2003) 119 [astro-ph/0209156].

[203] D. Baumann, P.J. Steinhardt, K. Takahashi and K. Ichiki, *Gravitational Wave Spectrum Induced by Primordial Scalar Perturbations*, *Phys. Rev. D* **76** (2007) 084019 [hep-th/0703290].

[204] A.A. Starobinsky, *Spectrum of relict gravitational radiation and the early state of the universe*, *JETP Lett.* **30** (1979) 682.

[205] L.P. Grishchuk, *Amplification of gravitational waves in an istropic universe*, *Zh. Eksp. Teor. Fiz.* **67** (1974) 825.

[206] M.C. Guzzetti, N. Bartolo, M. Liguori and S. Matarrese, *Gravitational waves from inflation*, *Riv. Nuovo Cim.* **39** (2016) 399 [1605.01615].

[207] M.R. Haque, D. Maity, T. Paul and L. Sriramkumar, *Decoding the phases of early and late time reheating through imprints on primordial gravitational waves*, *Phys. Rev. D* **104** (2021) 063513 [2105.09242].

[208] J. Adams, B. Cresswell and R. Easther, *Inflationary perturbations from a potential with a step*, *Phys. Rev. D* **64** (2001) 123514.

[209] H. Di and Y. Gong, *Primordial black holes and second order gravitational waves from ultra-slow-roll inflation*, *JCAP* **07** (2018) 007 [1707.09578].

[210] C. Fu, P. Wu and H. Yu, *Scalar induced gravitational waves in inflation with gravitationally enhanced friction*, *Phys. Rev. D* **101** (2020) 023529 [1912.05927].

[211] G. Domènech and J. Tränkle, *Gravitational waves induced by matter isocurvature in general cosmologies*, *JCAP* **12** (2025) 017 [2509.02122].

[212] G. Domènech, S. Pi, A. Wang and J. Wang, *Induced gravitational wave interpretation of PTA data: a complete study for general equation of state*, *JCAP* **08** (2024) 054 [2402.18965].

[213] S. Balaji, G. Domènech and G. Franciolini, *Scalar-induced gravitational wave interpretation of PTA data: the role of scalar fluctuation propagation speed*, *JCAP* **10** (2023) 041 [2307.08552].

[214] S. Balaji, G. Domenech and J. Silk, *Induced gravitational waves from slow-roll inflation after an enhancing phase*, *JCAP* **09** (2022) 016 [2205.01696].

[215] G. Domènech, *Scalar Induced Gravitational Waves Review*, *Universe* **7** (2021) 398 [2109.01398].

[216] G. Domènech and M. Sasaki, *Approximate gauge independence of the induced gravitational wave spectrum*, *Phys. Rev. D* **103** (2021) 063531 [2012.14016].

[217] G. Domènech, S. Pi and M. Sasaki, *Induced gravitational waves as a probe of thermal history of the universe*, *JCAP* **08** (2020) 017 [2005.12314].

[218] G. Domènech, *Induced gravitational waves in a general cosmological background*, *Int. J. Mod. Phys. D* **29** (2020) 2050028 [1912.05583].

[219] E. Dimastrogiovanni, M. Fasiello, A. Malhotra and G. Tasinato, *Enhancing gravitational wave anisotropies with peaked scalar sources*, *JCAP* **01** (2023) 018 [2205.05644].

[220] L. Sorbo, *Parity violation in the Cosmic Microwave Background from a pseudoscalar inflaton*, *JCAP* **06** (2011) 003 [1101.1525].

[221] C. Caprini and L. Sorbo, *Adding helicity to inflationary magnetogenesis*, *JCAP* **10** (2014) 056 [1407.2809].

[222] R. Sharma, K. Subramanian and T.R. Seshadri, *Gravitational wave generation in a viable scenario of inflationary magnetogenesis*, *Phys. Rev. D* **101** (2020) 103526 [1912.12089].

[223] V. Mukhanov, H. Feldman and R. Brandenberger, *Theory of cosmological perturbations*, *Physics Reports* **215** (1992) 203.

[224] H. Kodama and M. Sasaki, *Cosmological Perturbation Theory*, *Prog. Theor. Phys. Suppl.* **78** (1984) 1.

[225] A. Riotto, *Inflation and the theory of cosmological perturbations*, *ICTP Lect. Notes Ser.* **14** (2003) 317 [hep-ph/0210162].

[226] R.H. Brandenberger, *Lectures on the theory of cosmological perturbations*, *Lect. Notes Phys.* **646** (2004) 127 [hep-th/0306071].

[227] K.A. Malik and D. Wands, *Cosmological perturbations*, *Phys. Rept.* **475** (2009) 1 [0809.4944].

[228] D. Langlois, *Lectures on inflation and cosmological perturbations*, *Lect. Notes Phys.* **800** (2010) 1 [1001.5259].

[229] S. Maiti, D. Maity and L. Sriramkumar, *Constraining inflationary magnetogenesis and reheating via GWs in light of PTA data*, 2401.01864.

[230] A. Hoory, J. Martin, A. Paul and L. Sriramkumar, *Primary gravitational waves at high frequencies I: Origin of suppression in the power spectrum*, 2512.03959.

[231] C. Caprini and D.G. Figueroa, *Cosmological Backgrounds of Gravitational Waves*, *Class. Quant. Grav.* **35** (2018) 163001 [1801.04268].

[232] S. Okano and T. Fujita, *Chiral Gravitational Waves Produced in a Helical Magnetogenesis Model*, *JCAP* **03** (2021) 026 [2005.13833].

[233] S. Maiti, D. Maity and R. Srikanth, *Minimal magnetogenesis: The role of inflationary perturbations and ALPs, and their gravitational wave signatures*, *Phys. Rev. D* **112** (2025) 043535 [2504.15400].

[234] A. Ito and J. Soda, *Primordial Gravitational Waves Induced by Magnetic Fields in an Ekpyrotic Scenario*, *Phys. Lett. B* **771** (2017) 415 [1607.07062].

[235] K. Subramanian, *The origin, evolution and signatures of primordial magnetic fields*, *Rept. Prog. Phys.* **79** (2016) 076901 [1504.02311].

[236] R. Sharma, S. Jagannathan, T.R. Seshadri and K. Subramanian, *Challenges in Inflationary Magnetogenesis: Constraints from Strong Coupling, Backreaction and the Schwinger Effect*, *Phys. Rev. D* **96** (2017) 083511 [1708.08119].

[237] M.R. Haque, D. Maity and S. Pal, *Probing the reheating phase through primordial magnetic field and CMB*, *Phys. Rev. D* **103** (2021) 103540 [2012.10859].

[238] S. Tripathy, D. Chowdhury, R.K. Jain and L. Sriramkumar, *Challenges in the choice of the nonconformal coupling function in inflationary magnetogenesis*, *Phys. Rev. D* **105** (2022) 063519 [2111.01478].

[239] S.P. Corbà and L. Sorbo, *Correlated scalar perturbations and gravitational waves from axion inflation*, *JCAP* **10** (2024) 024 [2403.03338].

[240] M. Teuscher, R. Durrer, K. Martineau and A. Barrau, *A universal scaling law for gravitational waves induced during inflation*, 2512.14670.

[241] A. Fletcher, *Magnetic fields in nearby galaxies*, *arXiv preprint arXiv:1104.2427* (2011) .

[242] R. Beck, *Magnetic fields in spiral galaxies*, The Astronomy and Astrophysics Review **24** (2016) 4.

[243] M. Haverkorn, J.C. Brown, B.M. Gaensler and N.M. McClure-Griffiths, *The outer scale of turbulence in the magneto-ionized Galactic interstellar medium*, *Astrophys. J.* **680** (2008) 362 [0802.2740].

[244] P. Kronberg, Q. Dufton, H. Li and S. Colgate, *Magnetic energy of the intergalactic medium from galactic black holes*, *The Astrophysical Journal* **560** (2001) 178.

[245] D. Paoletti, J. Chluba, F. Finelli and J. Rubiño-Martín, *Constraints on primordial magnetic fields from their impact on the ionization history with planck 2018*, *Monthly Notices of the Royal Astronomical Society* **517** (2022) 3916.

[246] A. Zucca, Y. Li and L. Pogosian, *Constraints on Primordial Magnetic Fields from Planck combined with the South Pole Telescope CMB B-mode polarization measurements*, *Phys. Rev. D* **95** (2017) 063506 [1611.00757].

[247] BICEP2, Keck Arrary collaboration, *BICEP2 / Keck Array IX: New bounds on anisotropies of CMB polarization rotation and implications for axionlike particles and primordial magnetic fields*, *Phys. Rev. D* **96** (2017) 102003 [1705.02523].

[248] MAGIC collaboration, *A lower bound on intergalactic magnetic fields from time variability of 1ES 0229+200 from MAGIC and Fermi/LAT observations*, *Astron. Astrophys.* **670** (2023) A145 [2210.03321].

[249] K. Takahashi, M. Mori, K. Ichiki and S. Inoue, *Lower bounds on intergalactic magnetic fields from simultaneously observed gev–tev light curves of the blazar mrk 501*, *The Astrophysical Journal Letters* **744** (2011) L7.

[250] T.C. Arlen, V.V. Vassilev, T. Weisgarber, S.P. Wakely and S.Y. Shafi, *Intergalactic magnetic fields and gamma-ray observations of extreme tev blazars*, *The Astrophysical Journal* **796** (2014) 18.

[251] T.C. Arlen, V.V. Vassiliev, T. Weisgarber, S.P. Wakely and S.Y. Shafi, *Intergalactic Magnetic Fields and Gamma Ray Observations of Extreme TeV Blazars*, *Astrophys. J.* **796** (2014) 18 [1210.2802].

[252] I. Vovk, A.M. Taylor, D. Semikoz and A. Neronov, *Fermi/LAT observations of 1ES 0229+200: implications for extragalactic magnetic fields and background light*, *Astrophys. J. Lett.* **747** (2012) L14 [1112.2534].

[253] F. Tavecchio, G. Ghisellini, L. Foschini, G. Bonnoli, G. Ghirlanda and P. Coppi, *The intergalactic magnetic field constrained by Fermi/LAT observations of the TeV blazar 1ES 0229+200*, *Mon. Not. Roy. Astron. Soc.* **406** (2010) L70 [1004.1329].

[254] C.D. Dermer, M. Cavadini, S. Razzaque, J.D. Finke, J. Chiang and B. Lott, *Time Delay of Cascade Radiation for TeV Blazars and the Measurement of the Intergalactic Magnetic Field*, *Astrophys. J. Lett.* **733** (2011) L21 [1011.6660].

[255] K. Dolag, M. Kachelriess, S. Ostapchenko and R. Tomas, *Lower limit on the strength and filling factor of extragalactic magnetic fields*, *Astrophys. J. Lett.* **727** (2011) L4 [1009.1782].

[256] A. Neronov and I. Vovk, *Evidence for strong extragalactic magnetic fields from Fermi observations of TeV blazars*, *Science* **328** (2010) 73 [1006.3504].

[257] A.M. Taylor, I. Vovk and A. Neronov, *Extragalactic magnetic fields constraints from simultaneous GeV-TeV observations of blazars*, *Astron. Astrophys.* **529** (2011) A144 [1101.0932].

[258] A. Kandus, K.E. Kunze and C.G. Tsagas, *Primordial magnetogenesis*, *Phys. Rept.* **505** (2011) 1 [1007.3891].

[259] R.J.Z. Ferreira, R.K. Jain and M.S. Sloth, *Inflationary magnetogenesis without the strong coupling problem*, *JCAP* **10** (2013) 004 [1305.7151].

[260] R.J.Z. Ferreira, R.K. Jain and M.S. Sloth, *Inflationary Magnetogenesis without the Strong Coupling Problem II: Constraints from CMB anisotropies and B-modes*, *JCAP* **06** (2014) 053 [1403.5516].

[261] C.T. Byrnes, L. Hollenstein, R.K. Jain and F.R. Urban, *Resonant magnetic fields from inflation*, *JCAP* **03** (2012) 009 [1111.2030].

[262] T. Kobayashi, *Primordial Magnetic Fields from the Post-Inflationary Universe*, *JCAP* **05** (2014) 040 [1403.5168].

[263] Y. Li and L.-Y. Zhang, *Inflationary magnetogenesis with a self-consistent coupling function*, *Mod. Phys. Lett. A* **37** (2022) 2250069.

[264] L. Campanelli, *Helical Magnetic Fields from Inflation*, *Int. J. Mod. Phys. D* **18** (2009) 1395 [0805.0575].

[265] R.K. Jain, R. Durrer and L. Hollenstein, *Generation of helical magnetic fields from inflation*, *J. Phys. Conf. Ser.* **484** (2014) 012062 [1204.2409].

[266] R. Sharma, K. Subramanian and T.R. Seshadri, *Generation of helical magnetic field in a viable scenario of inflationary magnetogenesis*, *Phys. Rev. D* **97** (2018) 083503 [1802.04847].

[267] K. Bamba, S.D. Odintsov, T. Paul and D. Maity, *Helical magnetogenesis with reheating phase from higher curvature coupling and baryogenesis*, *Phys. Dark Univ.* **36** (2022) 101025 [2107.11524].

[268] H. Bazrafshan Moghaddam, E. McDonough, R. Namba and R.H. Brandenberger, *Inflationary magneto-(non)genesis, increasing kinetic couplings, and the strong coupling problem*, *Class. Quant. Grav.* **35** (2018) 105015 [1707.05820].

[269] M.M. Anber and L. Sorbo, *N-flationary magnetic fields*, *JCAP* **10** (2006) 018 [astro-ph/0606534].

[270] A. Benevides, A. Dabholkar and T. Kobayashi, *To B or not to B: Primordial magnetic fields from Weyl anomaly*, *JHEP* **11** (2018) 039 [1808.08237].

[271] D. Green and T. Kobayashi, *Constraints on Primordial Magnetic Fields from Inflation*, *JCAP* **03** (2016) 010 [1511.08793].

[272] S. Chakraborty, S. Pal and S. SenGupta, *Hilltop Inflation and Generation of Helical Magnetic Field*, *Universe* **8** (2022) 26 [1810.03478].

[273] A. Kushwaha and S. Shankaranarayanan, *Helical magnetic fields from Riemann coupling lead to baryogenesis*, *Phys. Rev. D* **104** (2021) 063502 [2103.05339].

[274] A. Kushwaha and S. Shankaranarayanan, *Helical magnetic fields from Riemann coupling*, *Phys. Rev. D* **102** (2020) 103528 [2008.10825].

[275] P. Adshead, J.T. Giblin, T.R. Scully and E.I. Sfakianakis, *Magnetogenesis from axion inflation*, *JCAP* **10** (2016) 039 [1606.08474].

[276] K. Choi, H. Kim and T. Sekiguchi, *Late-time magnetogenesis driven by axionlike particle dark matter and a dark photon*, *Phys. Rev. Lett.* **121** (2018) 031102.

[277] T. Patel, H. Tashiro and Y. Urakawa, *Resonant magnetogenesis from axions*, *JCAP* **01** (2020) 043 [1909.00288].

[278] A. Brandenburg, O. Iarygina, E.I. Sfakianakis and R. Sharma, *Magnetogenesis from axion-SU(2) inflation*, *JCAP* **12** (2024) 057 [2408.17413].

[279] H.V. Ragavendra, G. Tasinato and L. Sriramkumar, *Chiral gravitational waves from multi-phase magnetogenesis*, 2602.16575.

[280] B. Atkins, D. Chowdhury, A. Marriott-Best and G. Tasinato, *Inflationary magnetogenesis beyond slow-roll and its induced gravitational waves*, *Phys. Rev. D* **112** (2025) 063534 [2507.01772].

[281] M. Peloso and L. Sorbo, *Instability in axion inflation with strong backreaction from gauge modes*, *JCAP* **01** (2023) 038 [2209.08131].

[282] T. Kobayashi and R.K. Jain, *Impact of Helical Electromagnetic Fields on the Axion Window*, *JCAP* **03** (2021) 025 [2012.00896].

[283] J.M. Quashnock, A. Loeb and D.N. Spergel, *Magnetic Field Generation During the Cosmological QCD Phase Transition*, *Astrophys. J. Lett.* **344** (1989) L49.

[284] C. Caprini and R. Durrer, *Gravitational waves from stochastic relativistic sources: Primordial turbulence and magnetic fields*, *Phys. Rev. D* **74** (2006) 063521 [astro-ph/0603476].

[285] T. Kahniashvili, G. Gogoberidze and B. Ratra, *Polarized cosmological gravitational waves from primordial helical turbulence*, *Phys. Rev. Lett.* **95** (2005) 151301.

[286] T. Kahniashvili, L. Campanelli, G. Gogoberidze, Y. Maravin and B. Ratra, *Gravitational radiation from primordial helical inverse cascade magnetohydrodynamic turbulence*, *Phys. Rev. D* **78** (2008) 123006.

[287] T. Vachaspati, *Magnetic fields from cosmological phase transitions*, *Phys. Lett. B* **265** (1991) 258.

[288] M. Hindmarsh and A. Everett, *Magnetic fields from phase transitions*, *Phys. Rev. D* **58** (1998) 103505 [astro-ph/9708004].

[289] G. Baym, D. Bödeker and L. McLerran, *Magnetic fields produced by phase transition bubbles in the electroweak phase transition*, *Phys. Rev. D* **53** (1996) 662.

[290] K. Enqvist and P. Olesen, *On primordial magnetic fields of electroweak origin*, *Phys. Lett. B* **319** (1993) 178 [hep-ph/9308270].

[291] J. Ahonen and K. Enqvist, *Magnetic field generation in first order phase transition bubble collisions*, *Phys. Rev. D* **57** (1998) 664.

[292] A. Brandenburg, K. Enqvist and P. Olesen, *Large-scale magnetic fields from hydromagnetic turbulence in the very early universe*, *Phys. Rev. D* **54** (1996) 1291.

[293] T. Vachaspati, *Progress on cosmological magnetic fields*, *Rept. Prog. Phys.* **84** (2021) 074901 [2010.10525].

[294] B. Cheng and A.V. Olinto, *Primordial magnetic fields generated in the quark-hadron transition*, *Phys. Rev. D* **50** (1994) 2421.

[295] G. Sigl, A.V. Olinto and K. Jedamzik, *Primordial magnetic fields from cosmological first order phase transitions*, *Phys. Rev. D* **55** (1997) 4582.

[296] A. Brandenburg and K. Subramanian, *Astrophysical magnetic fields and nonlinear dynamo theory*, *Phys. Rept.* **417** (2005) 1 [astro-ph/0405052].

[297] M. Christensson, M. Hindmarsh and A. Brandenburg, *Inverse cascade in decaying three-dimensional magnetohydrodynamic turbulence*, *Phys. Rev. E* **64** (2001) 056405.

[298] C. Caprini, R. Durrer and G. Servant, *The stochastic gravitational wave background from turbulence and magnetic fields generated by a first-order phase transition*, *JCAP* **12** (2009) 024 [0909.0622].

[299] A. Brandenburg, K. Enqvist and P. Olesen, *Large scale magnetic fields from hydromagnetic turbulence in the very early universe*, *Phys. Rev. D* **54** (1996) 1291 [astro-ph/9602031].

[300] C. Caprini and R. Durrer, *Gravitational wave production: A Strong constraint on primordial magnetic fields*, Phys. Rev. D **65** (2001) 023517 [astro-ph/0106244].

[301] A. Roper Pol, C. Caprini, A. Neronov and D. Semikoz, *Gravitational wave signal from primordial magnetic fields in the Pulsar Timing Array frequency band*, Phys. Rev. D **105** (2022) 123502 [2201.05630].

[302] A. Vilenkin and E.P.S. Shellard, *Cosmic Strings and Other Topological Defects*, Cambridge University Press (1994).

[303] T. Vachaspati and A. Vilenkin, *Large-scale structure from wiggly cosmic strings*, Phys. Rev. Lett. **67** (1991) 1057.

[304] K. Dimopoulos, *Primordial magnetic fields from superconducting cosmic strings*, Phys. Rev. D **57** (1998) 4629 [hep-ph/9706513].

[305] S. Sau and S. Sanyal, *Generation of magnetic fields in cosmic string wakes*, PoS **ICHEP2020** (2021) 607.

[306] J.P. Ostriker, A.C. Thompson and E. Witten, *Cosmological Effects of Superconducting Strings*, Phys. Lett. B **180** (1986) 231.

[307] S. Nayak, S. Sau and S. Sanyal, *Evolution of magnetic fields in cosmic string wakes*, Astropart. Phys. **146** (2023) 102805 [2204.13303].

[308] T.W.B. Kibble and A. Vilenkin, *Phase equilibration in bubble collisions*, Phys. Rev. D **52** (1995) 679 [hep-ph/9501266].

[309] J.P. Preskill, *Cosmological production of superheavy magnetic monopoles*, Phys. Rev. Lett. **43** (1979) 1365.

[310] A.L. Maroto, *Primordial magnetic fields from metric perturbations*, Phys. Rev. D **64** (2001) 083006.

[311] T. Kobayashi and M.S. Sloth, *Early Cosmological Evolution of Primordial Electromagnetic Fields*, Phys. Rev. D **100** (2019) 023524 [1903.02561].

[312] S.Y. Choi, J.S. Shim and H.S. Song, *Factorization and polarization in linearized gravity*, Phys. Rev. D **51** (1995) 2751 [hep-th/9411092].

[313] C. Caprini, M.C. Guzzetti and L. Sorbo, *Inflationary magnetogenesis with added helicity: constraints from non-gaussianities*, Class. Quant. Grav. **35** (2018) 124003 [1707.09750].

[314] T. Kahniashvili, A. Brandenburg, R. Durrer, A.G. Tevzadze and W. Yin, *Scale-invariant helical magnetic field evolution and the duration of inflation*, JCAP **12** (2017) 002 [1610.03139].

[315] A. Talebian, A. Nassiri-Rad and H. Firouzjahi, *Primordial helical magnetic fields from inflation?*, *Phys. Rev. D* **105** (2022) 023528 [2111.02147].

[316] B. Ratra, *Cosmological 'seed' magnetic field from inflation*, *Astrophys. J. Lett.* **391** (1992) L1.

[317] D. Paoletti, F. Finelli and F. Paci, *The full contribution of a stochastic background of magnetic fields to CMB anisotropies*, *Mon. Not. Roy. Astron. Soc.* **396** (2009) 523 [0811.0230].

[318] Planck collaboration, *Planck 2015 results. XIX. Constraints on primordial magnetic fields*, *Astron. Astrophys.* **594** (2016) A19 [1502.01594].

[319] A. Neronov and I. Vovk, *Evidence for strong extragalactic magnetic fields from fermi observations of tev blazars*, *Science* **328** (2010) 73.

[320] W. Essey, S. Ando and A. Kusenko, *Determination of intergalactic magnetic fields from gamma ray data*, *Astropart. Phys.* **35** (2011) 135 [1012.5313].

[321] S. Saga, H. Tashiro and S. Yokoyama, *Limits on primordial magnetic fields from direct detection experiments of gravitational wave background*, *Phys. Rev. D* **98** (2018) 083518.

[322] C. Caprini, R. Durrer and T. Kahniashvili, *Cosmic microwave background and helical magnetic fields: The tensor mode*, *Phys. Rev. D* **69** (2004) 063006.

[323] I. Sendra and T.L. Smith, *Improved limits on short-wavelength gravitational waves from the cosmic microwave background*, *Phys. Rev. D* **85** (2012) 123002.

[324] T.J. Clarke, E.J. Copeland and A. Moss, *Constraints on primordial gravitational waves from the cosmic microwave background*, *Journal of Cosmology and Astroparticle Physics* **2020** (2020) 002.

[325] T. Fujita and S. Yokoyama, *Higher order statistics of curvature perturbations in IFF model and its Planck constraints*, *JCAP* **09** (2013) 009 [1306.2992].

[326] T. Fujita and R. Namba, *Pre-reheating magnetogenesis in the kinetic coupling model*, *Phys. Rev. D* **94** (2016) 043523.

[327] T. Kobayashi and M.S. Sloth, *Early cosmological evolution of primordial electromagnetic fields*, *Phys. Rev. D* **100** (2019) 023524.

[328] D. Maity, S. Pal and T. Paul, *Effective Theory of Inflationary Magnetogenesis and Constraints on Reheating*, *JCAP* **05** (2021) 045 [2103.02411].

[329] H.J. Hortúa and L. Castañeda, *Power spectrum of post-inflationary primordial magnetic fields*, *Phys. Rev. D* **90** (2014) 123520 [1405.1786].

[330] M.S. Turner and L.M. Widrow, *Inflation-produced, large-scale magnetic fields*, *Phys. Rev. D* **37** (1988) 2743.

[331] T. Papanikolaou, C. Tzerefos, S. Capozziello and G. Lambiase, *Gravitational-wave signatures of gravito-electromagnetic couplings*, *JCAP* **01** (2025) 051 [2408.17259].

[332] L. Lentati et al., *European Pulsar Timing Array Limits On An Isotropic Stochastic Gravitational-Wave Background*, *Mon. Not. Roy. Astron. Soc.* **453** (2015) 2576 [1504.03692].

[333] NANOGrav collaboration, *The NANOGrav 12.5 yr Data Set: Search for an Isotropic Stochastic Gravitational-wave Background*, *Astrophys. J. Lett.* **905** (2020) L34 [2009.04496].

[334] G. Janssen et al., *Gravitational wave astronomy with the SKA*, *PoS* **AASKA14** (2015) 037 [1501.00127].

[335] P. Amaro-Seoane et al., *eLISA/NGO: Astrophysics and cosmology in the gravitational-wave millihertz regime*, *GW Notes* **6** (2013) 4 [1201.3621].

[336] E. Barausse et al., *Prospects for Fundamental Physics with LISA*, *Gen. Rel. Grav.* **52** (2020) 81 [2001.09793].

[337] J. Crowder and N.J. Cornish, *Beyond LISA: Exploring future gravitational wave missions*, *Phys. Rev. D* **72** (2005) 083005 [gr-qc/0506015].

[338] V. Corbin and N.J. Cornish, *Detecting the cosmic gravitational wave background with the big bang observer*, *Class. Quant. Grav.* **23** (2006) 2435 [gr-qc/0512039].

[339] J. Baker et al., *Space Based Gravitational Wave Astronomy Beyond LISA*, *Bull. Am. Astron. Soc.* **51** (2019) 243 [1907.11305].

[340] N. Seto, S. Kawamura and T. Nakamura, *Possibility of direct measurement of the acceleration of the universe using 0.1-Hz band laser interferometer gravitational wave antenna in space*, *Phys. Rev. Lett.* **87** (2001) 221103 [astro-ph/0108011].

[341] S. Kawamura et al., *The Japanese space gravitational wave antenna: DECIGO*, *Class. Quant. Grav.* **28** (2011) 094011.

[342] A. Suemasa, K. Nakagawa and M. Musha, *Highly frequency-stabilized laser for space gravitational wave detector DECIGO/DPF*, *Proc. SPIE Int. Soc. Opt. Eng.* **10563** (2017) 105632V.

[343] M. Punturo et al., *The Einstein Telescope: A third-generation gravitational wave observatory*, *Class. Quant. Grav.* **27** (2010) 194002.

[344] B. Sathyaprakash et al., *Scientific Objectives of Einstein Telescope*, *Class. Quant. Grav.* **29** (2012) 124013 [1206.0331].

[345] D. Blas and A.C. Jenkins, *Bridging the μHz Gap in the Gravitational-Wave Landscape with Binary Resonances*, *Phys. Rev. Lett.* **128** (2022) 101103 [2107.04601].

[346] J.W. Foster, D. Blas, A. Bourgoin, A. Hees, M. Herrero-Valea, A.C. Jenkins et al., *Discovering μHz gravitational waves and ultra-light dark matter with binary resonances*, 2504.15334.

[347] J. Martin and J. Yokoyama, *Generation of Large-Scale Magnetic Fields in Single-Field Inflation*, *JCAP* **01** (2008) 025 [0711.4307].

[348] Planck collaboration, *Planck 2015 results. XIII. Cosmological parameters*, *Astron. Astrophys.* **594** (2016) A13 [1502.01589].

[349] A. Lewis, *Cmb anisotropies from primordial inhomogeneous magnetic fields*, *Phys. Rev. D* **70** (2004) 043011.

[350] KAGRA, Virgo, LIGO Scientific collaboration, *Upper limits on the isotropic gravitational-wave background from Advanced LIGO and Advanced Virgo's third observing run*, *Phys. Rev. D* **104** (2021) 022004 [2101.12130].

[351] S. Balaji, M. Fairbairn and M.O. Olea-Romacho, *Magnetogenesis with gravitational waves and primordial black hole dark matter*, *Phys. Rev. D* **109** (2024) 075048 [2402.05179].

[352] D. Borah and I. Saha, *Filtered cogenesis of PBH dark matter and baryons*, *JCAP* **08** (2025) 008 [2502.12248].

[353] A. Boudon, B. Bose, H. Huang and L. Lombriser, *Baryogenesis through asymmetric Hawking radiation from primordial black holes as dark matter*, *Phys. Rev. D* **103** (2021) 083504 [2010.14426].

[354] J. Auffinger, *Primordial black hole constraints with Hawking radiation—A review*, *Prog. Part. Nucl. Phys.* **131** (2023) 104040 [2206.02672].

[355] D. Borah, S. Jyoti Das and I. Saha, *Dark matter from phase transition generated PBH evaporation with gravitational waves signatures*, *Phys. Rev. D* **110** (2024) 035014 [2401.12282].

[356] R. Bean and J. Magueijo, *Could supermassive black holes be quintessential primordial black holes?*, *Phys. Rev. D* **66** (2002) 063505 [astro-ph/0204486].

[357] S. Clesse and J. García-Bellido, *Massive Primordial Black Holes from Hybrid Inflation as Dark Matter and the seeds of Galaxies*, *Phys. Rev. D* **92** (2015) 023524 [1501.07565].

[358] B. Carr and J. Silk, *Primordial Black Holes as Generators of Cosmic Structures*, *Mon. Not. Roy. Astron. Soc.* **478** (2018) 3756 [1801.00672].

[359] N. Bhaumik, A. Ghoshal, R.K. Jain and M. Lewicki, *Distinct signatures of spinning PBH domination and evaporation: doubly peaked gravitational waves, dark relics and CMB complementarity*, *JHEP* **05** (2023) 169 [2212.00775].

[360] LISA Cosmology Working Group collaboration, *Primordial black holes and their gravitational-wave signatures*, *Living Rev. Rel.* **28** (2025) 1 [2310.19857].

[361] SDSS collaboration, *Cosmological parameters from SDSS and WMAP*, *Phys. Rev. D* **69** (2004) 103501 [astro-ph/0310723].

[362] R. Khatri and R.A. Sunyaev, *Forecasts for CMB μ and i-type spectral distortion constraints on the primordial power spectrum on scales $8 \lesssim k \lesssim 10^4 Mpc^{-1}$ with the future Pixie-like experiments*, *JCAP* **06** (2013) 026 [1303.7212].

[363] N. Bhaumik, R.K. Jain and M. Lewicki, *Ultralow mass primordial black holes in the early Universe can explain the pulsar timing array signal*, *Phys. Rev. D* **108** (2023) 123532 [2308.07912].

[364] S. Ge, J. Guo and J. Liu, *New mechanism for primordial black hole formation from the qcd axion*, *Phys. Rev. D* **109** (2024) 123030.

[365] W.-Y. Ai, L. Heurtier and T.H. Jung, *Primordial black holes from an interrupted phase transition*, 2409.02175.

[366] S. Balaji, J. Gonçalves, D. Marfatia, A.P. Morais and R. Pasechnik, *Primordial black holes and magnetic fields in conformal neutrino mass models*, 2505.08011.

[367] S. Balaji, J. Silk and Y.-P. Wu, *Induced gravitational waves from the cosmic coincidence*, *JCAP* **06** (2022) 008 [2202.00700].

[368] R. Arya, R.K. Jain and A.K. Mishra, *Primordial black holes dark matter and secondary gravitational waves from warm Higgs-G inflation*, *JCAP* **02** (2024) 034 [2302.08940].

[369] A.M. Taylor, I. Vovk and A. Neronov, *Extragalactic magnetic fields constraints from simultaneous GeV-TeV observations of blazars*, *aap* **529** (2011) A144 [1101.0932].

[370] M.S. Pshirkov, P.G. Tinyakov and F.R. Urban, *New limits on extragalactic magnetic fields from rotation measures*, *Phys. Rev. Lett.* **116** (2016) 191302.

[371] A. Neronov and I. Vovk, *Evidence for Strong Extragalactic Magnetic Fields from Fermi Observations of TeV Blazars*, *Science* **328** (2010) 73 [1006.3504].

[372] V. Demozzi, V. Mukhanov and H. Rubinstein, *Magnetic fields from inflation?*, *JCAP* **08** (2009) 025 [0907.1030].

[373] K. Dimopoulos, A. Ghoshal and T. Papanikolaou, *Is inflationary magnetogenesis sensitive to the postinflationary history?*, *Phys. Rev. D* **111** (2025) 083550.

[374] C. Cecchini and M. Rinaldi, *Inflationary helical magnetic fields with a sawtooth coupling*, *Phys. Dark Univ.* **40** (2023) 101212 [2301.07699].

[375] A. Brandenburg, Y. He and R. Sharma, *Simulations of Helical Inflationary Magnetogenesis and Gravitational Waves*, *Astrophys. J.* **922** (2021) 192 [2107.12333].

[376] A. Brandenburg and R. Sharma, *Simulating Relic Gravitational Waves from Inflationary Magnetogenesis*, *Astrophys. J.* **920** (2021) 26 [2106.03857].

[377] R. Sharma and A. Brandenburg, *Low frequency tail of gravitational wave spectra from hydromagnetic turbulence*, *Phys. Rev. D* **106** (2022) 103536 [2206.00055].

[378] U. Kumar, *Primordial Gravitational Wave Background as a Probe of the Primordial Black Holes*, 2507.10033.

[379] B.A. Bassett, S. Tsujikawa and D. Wands, *Inflation dynamics and reheating*, *Rev. Mod. Phys.* **78** (2006) 537 [astro-ph/0507632].

[380] D. Wands, K.A. Malik, D.H. Lyth and A.R. Liddle, *A New approach to the evolution of cosmological perturbations on large scales*, *Phys. Rev. D* **62** (2000) 043527 [astro-ph/0003278].

[381] J.R. Shaw and A. Lewis, *Massive neutrinos and magnetic fields in the early universe*, *Phys. Rev. D* **81** (2010) 043517.

[382] S. Saga, H. Tashiro and S. Yokoyama, *Limits on primordial magnetic fields from primordial black hole abundance*, *Journal of Cosmology and Astroparticle Physics* **2020** (2020) 039.

[383] C. Bonvin, C. Caprini and R. Durrer, *Magnetic fields from inflation: The cmb temperature anisotropies*, *Phys. Rev. D* **88** (2013) 083515.

[384] R. Saito and J. Yokoyama, *Gravitational-wave background as a probe of the primordial black-hole abundance*, *Phys. Rev. Lett.* **102** (2009) 161101.

[385] V. Atal and G. Domènech, *Probing non-Gaussianities with the high frequency tail of induced gravitational waves*, *JCAP* **06** (2021) 001 [2103.01056].

[386] E. Cotner, A. Kusenko and V. Takhistov, *Primordial black holes from inflaton fragmentation into oscillons*, *Phys. Rev. D* **98** (2018) 083513.

[387] E. Cotner, A. Kusenko, M. Sasaki and V. Takhistov, *Analytic Description of Primordial Black Hole Formation from Scalar Field Fragmentation*, *JCAP* **10** (2019) 077 [1907.10613].

[388] D. Grasso and H.R. Rubinstein, *Magnetic fields in the early universe*, *Phys. Rept.* **348** (2001) 163 [astro-ph/0009061].

[389] M. Giovannini, *The Magnetized universe*, *Int. J. Mod. Phys. D* **13** (2004) 391 [astro-ph/0312614].

[390] P.P. Kronberg, Q.W. Dufton, H. Li and S.A. Colgate, *Magnetic energy of the intergalactic medium from galactic black holes*, *Astrophys. J.* **560** (2001) 178 [astro-ph/0106281].

[391] K. Takahashi, M. Mori, K. Ichiki and S. Inoue, *Lower Bounds on Intergalactic Magnetic Fields from Simultaneously Observed GeV-TeV Light Curves of the Blazar Mrk 501*, *Astrophys. J. Lett.* **744** (2012) L7 [1103.3835].

[392] A. Brandenburg and E. Ntormousi, *Galactic Dynamos*, *Annual Review of Astronomy and Astrophysics* **61** (2023) 561 [2211.03476].

[393] M. Hindmarsh and A. Everett, *Magnetic fields from phase transitions*, *Phys. Rev. D* **58** (1998) 103505.

[394] T. Kahniashvili, A.G. Tevzadze, A. Brandenburg and A. Neronov, *Evolution of Primordial Magnetic Fields from Phase Transitions*, *Phys. Rev. D* **87** (2013) 083007 [1212.0596].

[395] J. Ellis, M. Fairbairn, M. Lewicki, V. Vaskonen and A. Wickens, *Intergalactic Magnetic Fields from First-Order Phase Transitions*, *JCAP* **09** (2019) 019 [1907.04315].

[396] M.V. Medvedev and A. Loeb, *Plasma Constraints on the Cosmological Abundance of Magnetic Monopoles and the Origin of Cosmic Magnetic Fields*, *JCAP* **06** (2017) 058 [1704.05094].

[397] Y. Li and L.-Y. Zhang, *Inflationary magnetogenesis of primordial magnetic fields with multiple vector fields*, *Mod. Phys. Lett. A* **38** (2023) .

[398] P. Carrilho and K.A. Malik, *Magnetogenesis from isocurvature initial conditions*, *Journal of Cosmology and Astroparticle Physics* **2019** (2019) 028–028.

[399] S.L. Parnovsky, *The big bang could be anisotropic. the case of bianchi i model*, *Classical and Quantum Gravity* **40** (2023) 135005.

[400] S. Pal, D. Maity and T.Q. Do, *Magnetogenesis from an anisotropic universe*, *Phys. Rev. D* **109** (2024) 083507 [2311.07685].

[401] F. Wilczek, *Problem of strong p and t invariance in the presence of instantons*, *Phys. Rev. Lett.* **40** (1978) 279.

[402] P. Svrcek and E. Witten, *Axions in string theory*, *Journal of High Energy Physics* **2006** (2006) 051–051.

[403] M. Drewes and L. Ming, *Connecting Cosmic Inflation to Particle Physics with LiteBIRD, CMB-S4, EUCLID, and SKA*, *Phys. Rev. Lett.* **133** (2024) 031001 [2208.07609].

[404] CMB-S4 collaboration, *CMB-S4: Forecasting Constraints on Primordial Gravitational Waves*, *Astrophys. J.* **926** (2022) 54 [2008.12619].

[405] V.F. Mukhanov, H.A. Feldman and R.H. Brandenberger, *Theory of cosmological perturbations*, *physrep* **215** (1992) 203.

[406] R. Brandenberger, J. Fröhlich and H. Jiao, *Cosmological magnetic fields from ultralight dark matter*, 2025.

[407] A. Laguë, J.R. Bond, R. Hložek, K.K. Rogers, D.J.E. Marsh and D. Grin, *Constraining ultralight axions with galaxy surveys*, *JCAP* **01** (2022) 049 [2104.07802].

[408] CAST Collaboration collaboration, *New upper limit on the axion-photon coupling with an extended cast run with a xe-based micromegas detector*, *Phys. Rev. Lett.* **133** (2024) 221005.

[409] C. Caprini and R. Durrer, *Gravitational wave production: A strong constraint on primordial magnetic fields*, *Phys. Rev. D* **65** (2001) 023517.

[410] J. Martin and J. Yokoyama, *Generation of large scale magnetic fields in single-field inflation*, *Journal of Cosmology and Astroparticle Physics* **2008** (2008) 025.

[411] R.H. Brandenberger, A.-C. Davis, A.M. Matheson and M. Trodden, *Superconducting cosmic strings and primordial magnetic fields*, *Phys. Lett. B* **293** (1992) 287 [hep-ph/9206232].

[412] K. Horiguchi, K. Ichiki and N. Sugiyama, *Primordial magnetic fields from the string network*, *PTEP* **2016** (2016) 083E02 [1601.01059].